Parametric Radio Channel Estimation and Robust Localization

Li, Xuhong

2022

Document Version:
Publisher's PDF, also known as Version of record

Parametric Radio Channel Estimation and Robust Localization

Xuhong Li

Lund 2022

Series of licentiate and doctoral theses
No. 146
ISSN 1654-790X146
ISBN 978-91-8039-279-2 (print)
ISBN 978-91-8039-280-8 (pdf)

This thesis is produced by using the LaTeX Documentation System
Printed in Sweden by *Tryckeriet i E-huset*, Lund.

Department of Electrical and Information Technology
Lund University, Box 118, SE-221 00 Lund, Sweden

To my dear family

Popular Science

Location awareness has become an integral part of almost all mobile devices and applications that are used in our daily life. We rely on navigation apps to know the surrounding traffic status and find the less congested route to work or grocery stores. We can easily identify locations of missing items via Internet-of-Things (IoT) positioning tags. In retail, knowing consumers' movement patterns enables the stores to optimize product placement and perform proximity marketing and advertisements. Location information also helps to realize health and behavioral monitoring improving nursing and medical services for elder adults and people with disabilities. Moreover, high precision location information is critical for many emerging applications such as intelligent transportation systems, augmented/virtual reality, etc, and it can also enhance the communication service itself in fifth generation (5G)-and-beyond networks.

At this moment, you probably already think of "global positioning system" (GPS), the most well-known positioning system. In open areas it provides accuracy at meter-level for most civilian applications. However, when you are indoor or in dense urban environments where the direct "sight" between satellites and your mobile device is blocked by buildings, the accuracy and robustness of GPS services are severely degraded and not sufficient for many existing applications, not mentioning emerging applications requiring centermeter level position information. This thesis focuses on the research topic "*how to use wireless signals that are exchanged between terrestrial radio infrastructures for positioning as a complement or substitute of existing localization systems.*" The signals may refer to the signals exchanged between your mobile phone and base stations, your tablet computer and WiFi router, or between IoT devices.

Radio signals reach receiving devices via direct paths or reflections from surrounding objects, for instance walls, trees or even vehicles passing by. By using proper mathematic tools, we can analyze the distance, directional and other environment-related characteristics of radio waves and use them for positioning. In practice, useful radio signals are always corrupted by noise and the achievable accuracy of a positioning solution mainly depends on "*how fine*

you can distinguish individual radio waves and sense the changes of their characteristics from noisy received signals."

The 5G-and-beyond radio systems continue to develop towards higher frequency ranges, wider signal bandwidths, and massive antenna arrays which can contain a few hundreds of co-operating antennas. With these nice devices, it's like having a "high-resolution microscope" for observing the characteristics of radio waves—sensing abilities are greatly boosted, which makes centimeter-level accuracy positioning possible. Note that "massive" does not only describe the number of antennas, but also implies the complexity level of the signal processing process where we analyze useful information of radio waves from noise-corrupted signals. A major part of this thesis is about "*How to take advantage of massive antenna systems for positioning in practice?*". More specifically, we proposed mathematical algorithms that can be generally applied for efficient and accurate estimation of radio wave information using measurements from radio systems with massive antennas. Furthermore, we demonstrated the positioning performance with estimated path information using real measurements from our testbed at Lund University.

Besides the radio networks that serve human-to-human/device communications, position information can also benefit the applications for IoT networks dedicated for machine-type communications. "Things" may refer to the temperature meters in the wild collecting data for meteorologist, the tire pressure monitors on your vehicles, or the sensors in your apartment alerting you in case of break-in, etc. Low-power consumption is a common feature of many IoT devices since they need to survive on a battery for a long time, even up to a number of years. Therefore, these devices don't "wake up" and transmit signals as frequent as devices of other radio networks, for example your smart phone. Moreover, IoT devices are normally limited in size and manufacturing cost, therefore they don't have nice features like large bandwidths or massive antennas. The second part of the thesis is about "*How to make the best of the limited resources from IoT networks for positioning?*"

Radio-based positioning is a broad research topic and there is no single solution. With all the works in this thesis, ranging from algorithm design to radio signal measurements, we would like to exploit the potential of existing/future radio networks for positioning, and demonstrate the possibilities both theoretically and practically.

Abstract

Robust and accurate localization using radio signals for scenarios such as indoor and dense urban areas is of great importance, but challenging due to multipath propagation and dynamic channel conditions. This thesis explores a few interesting topics in this research field both theoretically and experimentally, which are summarized in the following.

The first topic focuses on the estimation of local geometry related information conveyed in specular multipath components (MPCs) from channel observations for multipath-assisted localization and mapping. In dynamic scenarios, the number of existing specular MPCs (model-order) as well as their parameters, e.g., distances, angles and amplitudes, are both unknown and time-varying. The estimation quality of above unknown information largely influences the achievable accuracy and robustness of a localization solution.

The 5G-and-beyond radio systems exploit large-scale antenna arrays with up to a few hundred elements enabling superior resolvability of MPCs in angular subspace. We present an extended Kalman filter-based sequential parametric channel estimator exploiting phase information of MPCs and demonstrate the potential of using massive multiple-input multiple-output (MIMO) systems with standard cellular bandwidth for high-accuracy localization and mapping. Furthermore, it is noted that most of the existing parametric channel estimators essentially consider the model-order detection, data association, and sequential estimation of MPC parameters, but solve them in separate blocks. We proposes a belief propagation (BP)-based algorithm which formulates all the problems in a joint Bayesian framework, and obtains the marginal posterior probability density functions (PDFs) in an approximate but computationally efficient manner by running sum-product algorithm on the factor graph representation of the joint problem formulation. Moreover, the use of amplitude information further enables the reliable detection of "weak" MPCs with very low signal-to-noise ratios. Results using real radio measurements demonstrate the excellent performance of the proposed algorithms in realistic and challenging scenarios.

The second topic concerns about received signal strength (RSS)-based localization solutions for long-range outdoor IoT networks. Such networks mostly

serve applications with low-power, low-rate and low-cost features, therefore dedicated localization solutions should have low complexity and minimum infrastructural needs. To make the best use of the limited resources, we present a localization solution which fuses both range and angle information extracted from non-coherent RSS measurements, and it is designed to be adaptive to dynamic propagation conditions by sequentially estimating the time-varying path-loss exponents for different anchors together with the target position.

Preface

This doctoral thesis is comprised of two parts. The first part gives an overview of the research field in which I have been working during my Ph.D. studies and a brief summary of my contribution in the research field. The second part is composed of six papers that constitute my main scientific work, including:

[**T1**] X. Li, K. Batstone, K. Åström, M. Oskarsson, C. Gustafson and F. Tufvesson, "Robust Phase-based Positioning using Massive MIMO with Limited Bandwidth," in *Proc. IEEE 28th Annu. Int. Symp. Pers., Indoor, Mobile Radio Commun. (PIMRC)*, Montreal, Canada, pp. 1-7, Oct. 2017.

[**T2**] X. Li, E. Leitinger, M. Oskarsson, K. Åström and F. Tufvesson, "Massive MIMO-Based Localization and Mapping Exploiting Phase Information of Multipath Components," *IEEE Trans. Wireless Commun.*, vol. 18, no. 9, pp. 4254–4267, Sept. 2019.

[**T3**] X. Li, M. Abou Nasa, F. Rezaei and F. Tufvesson, "Target Tracking using Signal Strength Differences for Long-Range IoT Networks," in *Proc. IEEE Int. Conf. Commun. Workshops (ICC Workshops)*, Dublin, Ireland, Jun. 2020, pp. 1–6.

[**T4**] X. Li, E. Leitinger and F. Tufvesson, "RSS-based Localization of Low-Power IoT Devices Exploiting AoA and Range Information," in *Proc. Asilomar*, Pacific Grove, CA, USA, Oct. 2020, pp. 651-656.

[**T5**] X. Li, E. Leitinger and F. Tufvesson, "Detection and Tracking of Multipath Channel Parameters Using Belief Propagation," in *Proc. Asilomar*, Pacific Grove, CA, USA, Oct. 2020, pp. 1083-1089.

[**T6**] X. Li, E. Leitinger, A. Venus and F. Tufvesson, "Sequential Detection and Estimation of Multipath Channel Parameters Using Belief Propagation," *IEEE Trans. Wireless Commun.*, 2022, doi: 10.1109/TWC.2022.3165856.

The included papers are referenced in Part I using labels in the form [T#], to distinguish them from conventional references to work of others.

During my Ph.D. study, I have also presented research outcomes as a temporary documents (TD) in the European Cooperation in Science and Technology (COST) action (CA15104) and contributed to the publications in the following that are not included in the thesis.

- X. Li, K. Batstone, K. Åström, M. Oskarsson, C. Gustafson and F. Tufvesson, "Robust Phase-based Positioning using Massive MIMO with Limited Bandwidth," in COST CA15104 Technical Meeting, TD(17)04032, Lund, Sweden, May 2017.
- J. Vieira, E. Leitinger, M. Sarajlic, X. Li and F. Tufvesson, "Deep Convolutional Neural Networks for Massive MIMO FingerprintBased Positioning," in *IEEE 28th Annual International Symposium on Personal, Indoor, and Mobile Radio Communications (PIMRC)*, Montreal, QC, Canada, Oct. 2017
- J. Flordelis, X. Li, O. Edfors, and F. Tufvesson, "Massive MIMO extensions to the COST 2100 channel model: Modeling and validation," *IEEE Trans. Wireless Commun.*, vol. 19, no. 1, pp. 380–394, Jan. 2020.
- K. Witrisal, C. Anton-Haro, S. Grebien, W. Joseph, E. Leitinger, X. Li, J. A. Del Peral-Rosado, D. Plets, J. Vilà-Valls, T. Wilding, "Chapter 9 - localization and tracking", in *Inclusive Radio Communications for 5G and Beyond*, C. Oestges and F. Quitin, Eds., Academic Press, 2021, pp. 253-293.

Acknowledgements

This long journey as a PhD student has been full of excitement, challenge, joy, and most of all, gratitude to all the wonderful people who helped to make this thesis possible.

My sincere gratitude goes to my supervisor Prof. Fredrik Tufvesson for providing me this life changing opportunity to study in this nice group. Thank you for all the inspiring discussions and encouragement, and for all the resources and great support so that I can pursue the research topics that I am interested in. Thanks for always being patient and having faith in my work.

My utmost gratitude goes to my co-supervisor Dr. Erik Leitinger, without whom this whole thing would be literally "mission impossible". It is truly an honor and a precious experience to work with Erik, who is very knowledgeable, encouraging and supportive. Those countless detailed and inspiring discussions on basic mathematic problems, algorithms, academic writing, etc, have led me into the fun and fascinating world of research, and continuously encourage me to become a better researcher—diligent and rigorous in work, active and creative in thought. Thank you for always being there for questions and for being super patient even when seeing my "nodding head + confusing face" in the early days. Thank you!

I am grateful to my dear colleagues and friends at EIT—my two amazing officemates Saeedeh and Juan, José Flordelis and Hu Sha for a lot of discussions and help with measurements in the early stage of my study, Associate Prof. Michael Lentmaier for proofreading this thesis, my "Doraemon" friend Siyu who just can fix/build anything and always shares interesting ideas, Haorui for exploring restaurants on Fridays, Sara, Christian, Anders, João, Muris, Fredrik Rusek, Ove, Liang, Hemanth, Liu Yangxurui, MinKeun, Umar, Michiel Sandra, Jesús, Erik Bengtsson, Meifang, Xiang, Dino, Aleksei, Neharika, Hedieh, Juan Sanchez, Russell, Junshi, Guoda, Xuesong, Andreia, Vincent, Wei, Makambi, Ashkan, Dimitrios, Ghassan, Nafiseh, Carl, Atif, and those I may have forgotten to include, for all the joyful moments together. I would also like to thank my colleagues and friends from the WASP project, in particular Alexandre Martins, thank you for the warm greetings and interesting talks in the office,

and your kind help on the cameras, etc, and I knew sometimes I got stuck into the boring stuff so that I forgot the important things. I would like to extend my gratitude to administrative and technical staff, Linda Bienen, Elisabeth Nordström, Elisabeth Ohlsson, Anne Andersson, Pia Bruhn and Erik Jonsson for helping out whenever I asked for.

I am also grateful to my co-authors, Prof. Kalle Åström, Associate Prof. Magnus Oskarsson and Kenneth Batstone from the Centre for Mathematical Sciences, and Alexander Venus from the Graz University of Technology, Austria, for all the interesting collaborations and fruitful discussions.

My deepest gratefulness goes to my family—my parents, my lovely little sister, and my dear grandparents, for their endless love, support, and trust in everything I do.

亲爱的爸爸妈妈，可爱妹妹，姥姥姥爷，你们的爱和鼓励
是我不断前行的强大动力！ 사랑해요

Most importantly, I would like to thank my beloved husband Xiaodong. It is your love and support that give me the courage to never give up during this adventure, and we together achieve all of this. In those stressful days, thank you for being my cheer up leader, my superman who just takes care of everything.

Xuhong Li
Lund, May 2022

List of Acronyms and Abbreviations

2D	Two-Dimensional
3D	Three-Dimensional
5G	Fifth Generation
AoA	Angle-of-Arrival
AoD	Angle-of-Departure
AWGN	Additive White Gaussian Noise
BP	Belief Propagation
CRLB	Cramér–Rao Lower Bound
CIR	Channel Impulse Response
CT	Coordinated Turn
DA	Data Association
DMC	Dense Multipath Component
EADF	Effective Aperture Distribution Function
EKF	Extended Kalman Filter
EM	Expectation-Maximization
FIM	Fisher Information Matrix
GPS	Global Positioning System
GSSM	Geometry-Based Stochastic Signal Model
iid	Independent and Identically Distributed
IoT	Internet-of-Things
IMM	Interacting Multiple Model

KF	Kalman Filter
LoS	Line-of-Sight
LPWAN	Low-Power Wide Area Network
MIMO	Multiple-Input Multiple-Output
MISO	Multiple-Input Single-Output
ML	Maximum-Likelihood
MPC	Multipath Component
MAP	Maximum A-Posteriori
MDL	Minimum Description Length
MNFA	Mean Number of False Alarms
NCV	Nearly-Constant Velocity
NLoS	Non LoS
OSPA	Optimal Subpattern Assignment
PA	Physical Anchor
PDF	Probability Density Function
PDP	Power Delay Profile
PF	Particle Filter
PLE	Path-Loss Exponent
PLM	Path-Loss Model
RRC	Root-Raised-Cosine
RSS	Received Signal Strength
RSSD	RSS Difference
SAGE	Space-Alternating Generalized Expectation-Maximization
SLAM	Simultaneous Localization and Mapping
SNR	Signal-to-Noise Ratio
SPA	Sum-Product Algorithm
SIMO	Single-Input Multiple-Output
UWB	Ultra-Wideband
WLAN	Wireless Local-Area Network
VA	Virtual Anchor

Contents

Part I

Overview of the Research Field

Chapter 1

Introduction

Location-based services encompass a wide range of applications used in our daily lives, such as navigation assistance, product or service discovery, and critical services like emergency response. In open outdoor scenarios, location awareness is mostly enabled by global navigation satellite systems (GNSS) [1], where the global positioning system (GPS) is the most well-known example. Nevertheless, GNSS reception is impaired by strong signal attenuation from buildings and by the multipath effect in challenging environments such as urban canyons or indoor. Dedicated substitute or supplement localization[1] solutions that are able to seamlessly provide high-accuracy and robust services under various and challenging conditions are required by existing and emerging application scenarios, for examples intelligent transportation systems [3], aerial vehicles, assisted living [4], smart factory [5].

1.1 Wireless Localization Technologies

Existing wireless localization technologies can be roughly grouped into the following categories based on their physical sensing mechanisms:

- Optical systems, such as camera-based systems and laser scanners built upon angle information and/or range information.
- Acoustic systems [6] use sound to determine the distance and direction of its source or reflectors. The systems can be active or passive and work in different mediums, e.g., gases, liquids or even solids.

[1] According to [2], *positioning* describes the determination of the coordinates of an object in a defined coordinate system, while *localization* refers to the position of an object relative to topological relations. These terms are used interchangeably in this thesis.

- Radio-based systems [3], [5], [7], [8], which rely on the transmission and reception of radio signals for position estimation.
- Inertial sensors, which capture the dynamical state of a system, e.g., acceleration, angular rate, etc. Examples include inertial measurement unit (IMU) using a combination of gyroscopes and magnetometers. IMU data enables motion tracking of mobile nodes and is usually combined with other measurements by means of sensor fusion.

For challenging environments or complex application cases, it is usually difficult for a single technology to deliver adequate accuracy and robustness, therefore a diversity of technologies are often combined in a data fusion framework. A comprehensive overview of existing localization technologies are given in [9]. This thesis focuses on radio-based technologies.

Radio-based localization systems typically consist of a number of anchor nodes at known locations, and one or more mobile target nodes whose positions need to be estimated. These nodes act as transmitters or receivers based on the technologies used. Localization is performed either by directly using the received signals or by following a two-stage process, i.e., measurement collection and measurement processing with localization algorithms. For two-stage methods, measurements refer to position-dependent information extracted from radio signals exchanged between nodes. The following is a brief overview on the inter-node measurements and corresponding localization methods.

- Radio visibility, which is used in proximity (range-free) methods to detect the presence of a target around an anchor instead of calculating the exact position coordinates of the target.
- Time-of-arrival (ToA), time-of-flight (ToF) or time-difference-of-arrival (TDoA), can be exploited in range-based positioning methods. The time synchronization between nodes is critical to obtain accurate ToAs, ToFs, however the requirement can be relaxed for methods using TDoAs.
- Angle-of-arrivals (AoAs) are typically obtained by using phased antenna arrays at nodes, and the accuracy of AoA measurements mainly depends on the array aperture and signal-to-noise ratio (SNR).
- RSS measurements can be used in fingerprinting methods [10], [11], or in range-based [12], [13] methods where ranging is performed by exploiting a path-loss model (PLM) [13].

The basic principles of the range- and angle-based positioning schemes are illustrated in Fig. 2.1 using three anchors in a two-dimensional (2D) scenario. Under the simplified assumption of no measurement errors, the user position is the intersection of corresponding circles around the anchors with ranges as

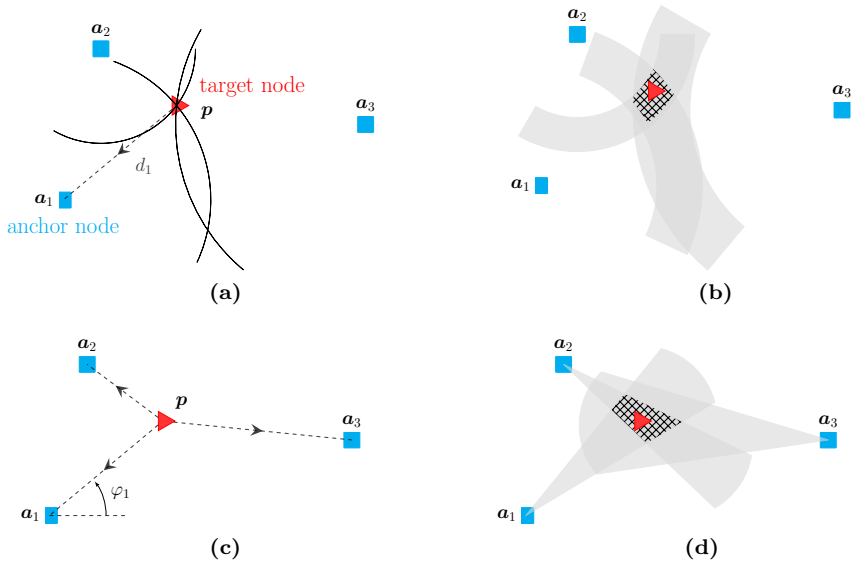

Figure 1.1: The basic principles of the range-based positioning methods (a), (b), and angle-based positioning methods (c), (d). (a) intersection point of circles which are centered at the anchors with perfect range measurements as the radii (e.g., d_1); (b) intersection area of noisy range measurements; (c) intersection point of directional lines from the anchors based on the perfect AoA measurements, e.g., φ_1; (d) intersection area of noisy angle measurements.

the radii in Fig. 1.1a, or the intersection of directional lines in Fig. 1.1c. Since measurements are always noisy in practice, the intersection point spreads out to the intersection area of noisy measurements as shown in Fig. 1.1b and Fig. 1.1d, thus estimation methods are needed. The achievable accuracy of range-based algorithms depends primarily on the employed signal bandwidth and the SNR. Angle-based systems normally have higher hardware complexity since phased antenna arrays are typically required. Comparably, range-based methods are more commonly used. In the afore mentioned scenario, the associations from measurements to anchors are assumed as known prior. In practice, localization and simultaneous localization and mapping (SLAM) problems are often complicated by the association uncertainty (see for Section 3.3.2).

1.2 Radio-based Localization

Nowadays, many research works focus on using signals from terrestrial wireless networks to develop localization and navigation systems that work where satel-

lite system fails. In general, such signals are designed for data communication, not for localization purposes.

A few typical examples of the radio networks available for localization are cellular networks, wireless local-area networks (WLANs), ultra-wideband (UWB)-based systems [14], [15], radio frequency identification (RFID) technology, and wireless sensor networks (WSNs). Cellular networks provide limited temporal and spatial resolution due to limited bandwidth (typically 20 MHz in LTE) and small scale antenna arrays (e.g., $2 \times 2, 4 \times 4$) applied. Hence, for positioning purpose they can serve as supplement to GNSS to improve startup performance and robustness when satellite signals are weak or unavailable, but cannot deliver satisfactory accuracies as standalone systems in a straight forward manner.

1.2.1 Localization for 5G and IoT Networks

The 5G-and-beyond mobile communication systems [8], [16]–[18] deliver enhanced and new features for localization, which can significantly improve existing location-based services and enable new use cases with strict requirements in terms of accuracy, latency, availability, reliability, etc. Specifically, 5G-and-beyond systems exploit new radio spectra, in particular the millimeter (mm)-wave spectrum above 24 GHz, to meet the increased demands for data rates. Large bandwidths available within these spectra tremendously improve the resolvability in delay/distance subspace. Furthermore, higher carrier frequencies lead to smaller antenna elements which makes it possible to accommodate more elements within an antenna array of same or even reduced physical size. The use of large antenna arrays with up to a few hundred elements (massive MIMO) is one of the key features of 5G systems, enabling superior resolvability in the angular domain. The number of antenna elements is expected to be scaled up by a further order-of-magnitude in the future systems. The improved delay and angular resolvability make it possible to resolve the MPC associated with environment geometric features, and observe the dynamic behavior of MPC parameters in non-static environments. Signals in the mm-wave frequency bands experience high free-space pathloss. Thus, a large number of small cells have to be densely placed (i.e., network densification) to guarantee the coverage. For localization purposes, this means anchors, i.e., base stations, are more likely to be accessible from the mobile user side with line-of-sight (LoS) connection and shorter distances.

IoT networks [7] are aimed at providing communications to a massive number of devices and smart sensors with range from a few meters (RFID, UWB, BLE) up to a few kilo-meters (LoRa, Sigfox, NB-IoT), and location-awareness is crucial for various IoT related applications. The low-cost, low-power and low-data rate features of IoT devices have strong impact on the dedicated localization solutions, which should have low complexities to achieve low power

consumption without asking for extra infrastructures. The included publications [T3] and [T4] focus on IoT localization solutions based on RSS measurements.

1.2.2 Technical Challenges for Radio-based Localization

This section discusses a number of technical challenges that have been identified for radio-based localization:

- LoS path availability: LoS path information provides the most location-relevant information of all MPCs, but it is often blocked in indoor and dense urban scenarios.
- Multipath propagation, which has long been considered as the main source of estimation errors for many range-based localization approaches. However, the position-related information that is conveyed in MPCs can be exploited for localization if they can be well resolved [2], [15].
- Time synchronization: timing-reference synchronization between nodes is crucial for time delay estimation, therefore it is an important prerequisite for range-based localization systems.
- Additional information and infrastructure are often needed, for instance, floor plan of the environment and phased arrays for extracting angular information from radio signals.
- Complexity considerations: some devices have limited computational capabilities and lower-power characteristic, therefore dedicated localization solutions should be developed with a good balance between complexity and accuracy.

1.2.3 Multipath-Assisted Localization

Radio signals arrive at receivers via a number of propagation paths, i.e., MPCs, including the LoS path, and paths due to reflections, scattering, and diffraction from surrounding objects, e.g., buildings surfaces, trees, vehicles, etc. Most of the standard localization methods either detect the existence of LoS path and avoid non-LoS (NLoS) measurements, or try to mitigate the influence on the estimation of the LoS path induced by multipath propagation. In contrast, many recent works [19]–[21] exploit the position-related information that is conveyed in the specular reflection MPCs for localization. More specifically, signals are considered from additional virtual sources which are time-synchronized to the physical transmitter, thus positioning become possible in cases of LoS blockage or insufficient number of transmitters. More information will be introduced in Chapter 2 and Chapter 3. Some works also consider distinct scatters [21] or

dense multipath component (DMC) [22] for positioning, where DMC incorporates MPCs that cannot be resolved due to finite observation aperture therefore cannot be modeled deterministically.

1.3 Research Questions of the Thesis

The research work of this thesis focuses on two aspects: (i) sequential detection of MPCs and estimation of their parameters, and the use of estimated MPC parameters for localization and mapping; (ii) target tracking for long-range IoT networks by exploiting both angular and range information. The detailed research questions considered in each aspect are given as follows.

For multipath-assisted localization and mapping, the achievable levels of accuracy and robustness highly depend on the quality of extracted position-related information of MPCs from radio measurements. Specular reflected MPCs can be modeled with the physical anchors (PAs) and virtual anchors (VAs) representing the mirrored positions of the PAs w.r.t. planar surfaces in the propagation environment, which are collectively referred to as environment features. In dynamic scenarios, these features are sometimes invisible at the target node's position due to a blockage by surrounding objects, leading to birth and death process of MPCs. Furthermore, the number of specular MPCs as well as their parameters, i.e., distances, angles, phases, and amplitudes are unknown and time-varying. The included publications [T1], [T2], [T5] and [T6] focus on the topic of MPC detection and the sequential estimation of MPC parameters from radio signals. The potential of using massive MIMO for multipath-assisted localization and mapping with standard cellular signal bandwidth is further demonstrated in [T1] and [T2].

For IoT networks, positioning is typically accomplished by using classical methods, such as fingerprinting or range-based methods. The achievable accuracy of fingerprinting is related to the density of fingerprints and degrades in dynamic scenarios. Extracting the range of LoS path from exchanged signals between nodes can be very inaccurate due to imperfect time synchronization, NLoS propagation, or the use of narrowband signals. Moreover, RSS-based ranging can be unreliable under the conditions of imperfect knowledge of path-loss exponent (PLE) and environmental influence. The publication [T3] and [T4] exploit AoA information from non-coherent RSS measurements, which is then fused with range information for target tracking for mid- to long-range outdoor scenarios.

1.4 Thesis Outline

This thesis consists of two main parts, an overview of research field in Part I and the main research contributions in the form of a collection of publications in Part II.

The structure of Part I of this thesis is as follows. Chapter 1 briefly introduces the existing radio-based technologies and main research questions of this thesis. Chapter 2 presents the geometry-based stochastic environment model and the general probabilistic formulations of the position estimation, tracking, and SLAM problems. Chapter 3 first introduces the geometry-based stochastic signal model, and then summarizes the existing and proposed parametric channel estimation methods as presented in [T1], [T2], [T5] and [T6]. Chapter 4 focuses on target tracking solutions for IoT networks, as presented in [T3], and [T4]. Finally, in Chapter 5 summarizes the main research contributions and my personal contributions in each of the included publications, and suggests a few interesting extensions of the presented work for future research.

Chapter 2

Multipath Channel Information for Localization

This chapter first introduces the geometry-based environment model which represents position-related information conveyed in specular MPCs with environment features, i.e., VAs. Based on this model, probabilistic geometric formulations of multipath-assisted positioning, tracking and SLAM problems are provided in the following sections.

2.1 Geometry-based Environment Model

For the sake of brevity, horizontal-only signal propagation in a two-dimensional (2D) scenario is assumed in this chapter, but it is straightforward to extend this to three-dimensional (3D) scenarios. At a discrete observation time n, radio signals exchange between J physical anchors (PAs) located at $\boldsymbol{a}_{1,n}^{(j)} \in \mathbb{R}^2$ with $j \in \{1, \cdots, J\}$ and a mobile target at $\boldsymbol{p}_n \in \mathbb{R}^2$. The signals propagate via different mechanisms, i.e., LoS propagation, specular reflection on smooth surfaces of interacting objects (IOs), diffuse scattering on rough surfaces of IOs, diffraction at the IO edges, and penetration [23]. The key concept for multipath-assisted localization is using VAs to model position-related information conveyed in the specular reflected paths or in the paths from distinct scatterers. As illustrated in Fig. 2.1a, VAs coordinates $\boldsymbol{a}_{l,n}^{(j)}$ of the jth PA with $l \in \{2, \cdots, L_n^{(j)}\}$ are computed with exact room geometry knowledge, i.e., 1st-order VAs are obtained by mirroring the PAs w.r.t. planar surfaces, and higher-order VAs are constructed by further mirroring lower-order VAs w.r.t. planar surfaces. It

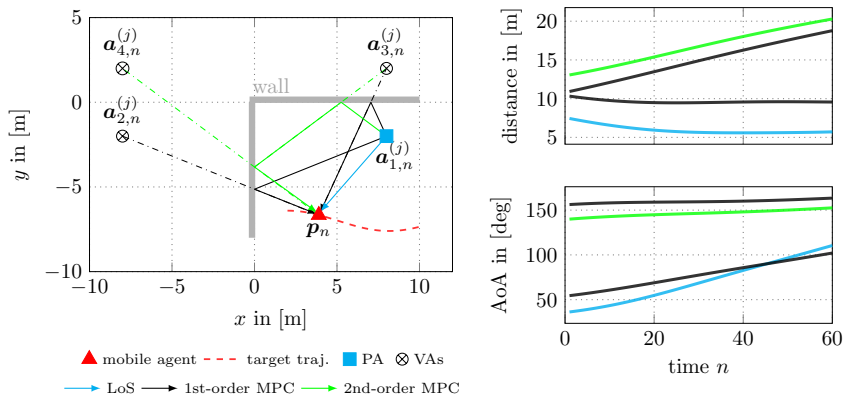

(a) **(b)**

Figure 2.1: (a) Example of a PA and the according VAs computed with known room geometry. (b) Time-varying distances and MPC AoAs that are associated with the four anchors.

may happen that the visibilities of VAs from the target position $\boldsymbol{p}_n$ are blocked by IOs at some time steps, i.e., the corresponding reflections are geometrically impossible. The time-varying visibility conditions in dynamic scenarios lead to death and birth process of MPCs. The number of visible VAs $L_n = \sum_{j=1}^{J} L_n^{(j)}$ equals the number of existing MPCs (i.e., model-order), and model-order is typically unknown and time-varying in dynamic scenarios. More details about the VA calculations and visibility region of VAs can be found in [2], [24].

Each specular MPC is characterized by its angle-of-departure (AoD) $\varphi_{l,n}^{\mathrm{Tx}(j)}$, angle-of-arrival (AoA) $\varphi_{l,n}^{\mathrm{Rx}(j)}$, time delay $\tau_{l,n}^{(j)} \in \mathbb{R}$ and complex amplitude $\alpha_{l,n}^{(j)} \in \mathbb{C}$. The MPC parameters are time-varying under dynamic channel conditions with mobile target, as shown in Fig. 2.1b. At each time n, the time delay and AoA can be computed via non-linear transformation using the mobile agent position $\boldsymbol{p}_n$ and its respective VA position $\boldsymbol{a}_{l,n}^{(j)}$ as follows

$$\tau_{l,n}^{(j)} = \frac{\|\boldsymbol{a}_{l,n}^{(j)} - \boldsymbol{p}_n\|}{c}, \quad \varphi_{l,n}^{\mathrm{Rx}(j)} = \angle(\boldsymbol{a}_{l,n}^{(j)} - \boldsymbol{p}_n) - \psi \tag{2.1}$$

where $\|\cdot\|$ denotes the Euclidean norm and ψ denotes the agent orientation and c is the speed of light.

2.2 Multipath-assisted Localization

2.2.1 Technical Challenges

Multipath-assisted localization problems are often complicated by the following issues:

- Estimation of MPC parameters: MPC parameters are usually estimated from multidimensional measurements using antenna arrays and multiple frequencies (wideband or UWB) using super-resolution algorithms. Sequential estimation of time-varying MPC parameters in dynamic scenarios is one of the focus areas of the thesis work. This is discussed in detail in Chapter 3.
- Model-order estimation is a crucial issue, and it becomes more challenging given a limited resolution capability of measurement systems and under low SNR conditions. Related discussions are provided in Section 3.2.4.
- Data association (DA): To find the association between estimated MPCs and PAs/VAs is another critical issue, and it becomes more challenging in case of MPC overlapping or in the presence of clutter components.
- Knowledge of environment geometry: For simplicity, the environment geometry (floor plan) and VA positions are usually assumed as known prior. However, in practice it is either not available or noisy, thus the VAs positions $\boldsymbol{a}_n$ have to be estimated jointly with the location of mobile agent $\boldsymbol{p}_n$, leading to the SLAM problem which will be briefly introduced in Section 2.2.5.

For two-stage solutions, where the MPC estimates from a parametric channel estimator are used as measurements in a localization algorithm, the DA can be performed in two ways: (i) If a snapshot-based parametric channel estimator is used, the association between VAs and MPC estimates is evaluated at each time in the localization stage [20]; (ii) If a sequential parametric channel estimator is used (see for Section 3.3), the estimated MPCs originating from the same VA are already associated over time and then used jointly in the localization or mapping stage [19], [T1], [T2]. This thesis focuses on the second approach and DA methods are introduced in Section 3.3.2. It would be rather complex to consider all the above issues jointly in a single solution. Instead, simplifying assumptions are usually made to reduce the complexity in practice. For the general probabilistic formulations presented in this chapter, known model-order and known associations are assumed unless otherwise specified.

2.2.2 Probabilistic Geometric Model

At each time n, the target state refers to its position $\boldsymbol{p}_n$, the states of all VAs representing their positions are denoted with a stacked vector $\boldsymbol{a}_n$, $\boldsymbol{\omega}_n$ accounts for the MPC states and $\boldsymbol{z}_n$ represents the measurement vector.

Joint Posterior PDF

The Bayesian estimation of the target state $\boldsymbol{p}_n$ relies on the posterior PDF $f(\boldsymbol{p}_n|\boldsymbol{z}_{1:n})$, which is the marginal PDF of the joint posterior PDF $f(\boldsymbol{p}_n, \boldsymbol{a}_n|\boldsymbol{z}_{1:n})$. Assuming that $\boldsymbol{p}_n$ and $\boldsymbol{a}_n$ are random variables, the joint posterior PDF of the target state $\boldsymbol{p}_n$ and VA states $\boldsymbol{a}_n$ conditioned on the measurements for all times up to n $\boldsymbol{z}_{1:n} = [\boldsymbol{z}_1^{\mathrm{T}} \cdots \boldsymbol{z}_n^{\mathrm{T}}]^{\mathrm{T}}$ is given as

$$f(\boldsymbol{p}_n, \boldsymbol{a}_n|\boldsymbol{z}_{1:n}) = \frac{f(\boldsymbol{z}_{1:n}|\boldsymbol{p}_n, \boldsymbol{a}_n) f(\boldsymbol{p}_n, \boldsymbol{a}_n)}{f(\boldsymbol{z}_{1:n})} \tag{2.2}$$

using Bayes' theorem, where $f(\boldsymbol{p}_n, \boldsymbol{a}_n)$ represents the joint prior PDF of the target state and VA states and $f(\boldsymbol{z}_{1:n}|\boldsymbol{p}_n, \boldsymbol{a}_n)$ is the likelihood function for the measurements. The denominator $f(\boldsymbol{z}_{1:n})$ is a constant after the measurements $\boldsymbol{z}_{1:n}$ are observed. According to (2.2), the marginal posterior PDF $f(\boldsymbol{p}_n|\boldsymbol{z}_{1:n})$ can then be obtained as

$$\begin{aligned} f(\boldsymbol{p}_n|\boldsymbol{z}_{1:n}) &= \int f(\boldsymbol{p}_n, \boldsymbol{a}_n|\boldsymbol{z}_{1:n}) \mathrm{d}\boldsymbol{a}_n \\ &\propto \int f(\boldsymbol{z}_{1:n}|\boldsymbol{p}_n, \boldsymbol{a}_n) f(\boldsymbol{p}_n, \boldsymbol{a}_n) \mathrm{d}\boldsymbol{a}_n. \end{aligned} \tag{2.3}$$

Since the measurements $\boldsymbol{z}_n$ are directly related to MPC states $\boldsymbol{\omega}_n$ via the measurement model and not to the states of the target and VAs, the posterior PDF (2.3) can be expressed as

$$\begin{aligned} f(\boldsymbol{p}_n|\boldsymbol{z}_{1:n}) &\propto \int f(\boldsymbol{z}_{1:n}|\boldsymbol{p}_n, \boldsymbol{a}_n; \boldsymbol{\omega}_n) f(\boldsymbol{p}_n, \boldsymbol{a}_n) \mathrm{d}\boldsymbol{a}_n \\ &= \int f(\boldsymbol{z}_{1:n}|\boldsymbol{\omega}_n) f(\boldsymbol{\omega}_n|\boldsymbol{p}_n, \boldsymbol{a}_n) f(\boldsymbol{p}_n, \boldsymbol{a}_n) \mathrm{d}\boldsymbol{a}_n. \end{aligned} \tag{2.4}$$

If the knowledge of the floor plan and VA positions are known, the joint posterior PDF (2.4) reduces to

$$\begin{aligned} f(\boldsymbol{p}_n|\boldsymbol{z}_{1:n}) &\propto f(\boldsymbol{z}_{1:n}|\boldsymbol{p}_n; \boldsymbol{a}_n; \boldsymbol{\omega}_n) f(\boldsymbol{p}_n) \\ &= f(\boldsymbol{z}_{1:n}|\boldsymbol{\omega}_n) f(\boldsymbol{\omega}_n|\boldsymbol{p}_n; \boldsymbol{a}_n) f(\boldsymbol{p}_n). \end{aligned} \tag{2.5}$$

By following the common assumption that the measurements $\boldsymbol{z}_{1:n}^{(j)}$, the MPC

states $\boldsymbol{\omega}_n^{(j)}$ and the VA states $\boldsymbol{a}_n^{(j)}$ are statistically independent over different anchors, the likelihood functions in (2.4) and (2.5) further factorize as

$$f(\boldsymbol{z}_{1:n}|\boldsymbol{p}_n, \boldsymbol{a}_n; \boldsymbol{\omega}_n) = \prod_{j=1}^{J} f(\boldsymbol{z}_{1:n}^{(j)}|\boldsymbol{p}_n, \boldsymbol{a}_n^{(j)}; \boldsymbol{\omega}_n^{(j)}) \tag{2.6}$$

$$f(\boldsymbol{z}_{1:n}|\boldsymbol{\omega}_n) = \prod_{j=1}^{J} f(\boldsymbol{z}_{1:n}^{(j)}|\boldsymbol{\omega}_n^{(j)}), \tag{2.7}$$

and the conditional PDF factorizes as

$$f(\boldsymbol{\omega}_n|\boldsymbol{p}_n; \boldsymbol{a}_n) = \prod_{j=1}^{J} f(\boldsymbol{\omega}_n^{(j)}|\boldsymbol{p}_n; \boldsymbol{a}_n^{(j)}). \tag{2.8}$$

The individual conditional PDF $f(\boldsymbol{\omega}_n^{(j)}|\boldsymbol{p}_n; \boldsymbol{a}_n^{(j)})$ of the MPC parameters $\boldsymbol{\omega}_n^{(j)}$ given the agent state $\boldsymbol{p}_n$ and VA states $\boldsymbol{a}_n^{(j)}$ is described by the non-linear transformation given in (2.1).

Measurement Model

The likelihood function $f(\boldsymbol{z}_n|\boldsymbol{\omega}_n)$ in (2.4) and (2.5) is a probabilistic representation of the measurement models introduced below. Note that $\boldsymbol{z}_n$ and $\boldsymbol{\omega}_n$ are general notations representing measurements and MPC states, the content of the two vectors may vary in different problem formulations with different system setups.

For direct localization algorithms where $\boldsymbol{z}_n$ represents the received channel impulse responses or transfer functions, the linearized measurement model is given by

$$\boldsymbol{z}_n = \boldsymbol{s}(\boldsymbol{\omega}_n) + \boldsymbol{\epsilon}_n \tag{2.9}$$

as further detailed later in (3.3), where $\boldsymbol{\epsilon}_n$ denotes the measurement noise and $\boldsymbol{s}(\boldsymbol{\omega}_n)$ represents the non-linear mapping from the MPC parameters to the specular observation vector described in Section 3.1.1.

For two-stage algorithms [19], [20], the measurements are the MPC parameter estimates $\boldsymbol{z}_n = \hat{\boldsymbol{\omega}}_n$ obtained from a parametric channel estimator, and the measurement model is given as

$$\boldsymbol{z}_n = \boldsymbol{\omega}_n + \boldsymbol{n}_n \tag{2.10}$$

where $\boldsymbol{n}_n$ denotes the Gaussian noise process, which is independent and identically distributed (iid) across anchors, MPCs and time n. The approximation

of iid Gaussian measurement noise is of course a simplification. A detailed characterization of estimation errors of different linear or non-linear multivariate estimators is a research area in it self and here we resort to a Gaussian approximation to get a tractable solution.

The vector $\boldsymbol{z}_n$ may also refer to RSS measurements for RSS-based localization algorithms [25], [26] [T3], [T4], where only the LoS propagation path is considered. The measurement model representing the non-linear mapping from the LoS path parameters, like range and angle, to the RSS observations is derived from the RSS and RSS difference (RSSD) models, as introduced in Section 4.2.

Bayesian Estimation

Given the marginal posterior PDF $f(\boldsymbol{p}_n|\boldsymbol{z}_{1:n})$, the estimation of the target state $\boldsymbol{p}_n$ can be performed either by means of the maximum a-posteriori (MAP) estimator

$$\hat{\boldsymbol{p}}_n^{\mathrm{MAP}} = \arg\max_{\boldsymbol{p}_n} f(\boldsymbol{p}_n|\boldsymbol{z}_{1:n}) \tag{2.11}$$

or by means of the minimum mean-square error (MMSE) estimator

$$\hat{\boldsymbol{p}}_n^{\mathrm{MMSE}} = \int \boldsymbol{p}_n f(\boldsymbol{p}_n|\boldsymbol{z}_{1:n}) \mathrm{d}\boldsymbol{p}_n. \tag{2.12}$$

2.2.3 Positioning of Static Targets

If the target is static, i.e., $\boldsymbol{p}_n = \boldsymbol{p}$, the MAP estimation of the target state can be formulated with the posterior PDF (2.5) as

$$\begin{aligned} \hat{\boldsymbol{p}}^{\mathrm{MAP}} &= \arg\max_{\boldsymbol{p}} f(\boldsymbol{p}|\boldsymbol{z}) \\ &= \arg\max_{\boldsymbol{p}} \prod_{j=1}^{J} f(\boldsymbol{z}^{(j)}|\boldsymbol{p}; \boldsymbol{a}^{(j)}; \boldsymbol{\omega}^{(j)}) f(\boldsymbol{p}) \end{aligned} \tag{2.13}$$

given deterministic known VA positions. Assuming uniform prior PDF $f(\boldsymbol{p})$ in the considered area, the MAP estimator reduces to a maximum-likelihood (ML) estimator, which is given by

$$\hat{\boldsymbol{p}}^{\mathrm{ML}} = \arg\max_{\boldsymbol{p}} \prod_{j=1}^{J} f(\boldsymbol{z}^{(j)}|\boldsymbol{p}; \boldsymbol{a}^{(j)}; \boldsymbol{\omega}^{(j)}). \tag{2.14}$$

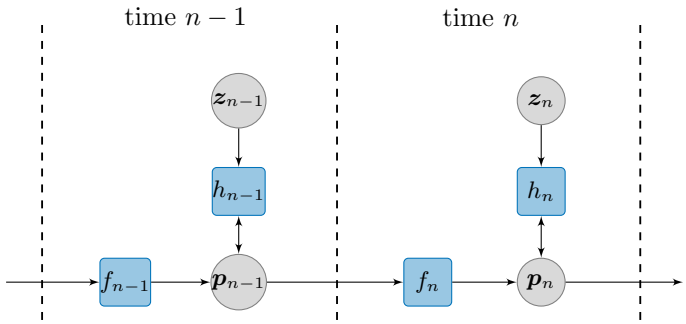

Figure 2.2: Illustration of the sequential Bayesian estimation process for time steps $n-1$ and n, assuming first-order Markov process. f_n denotes the state-transition PDF $f(\boldsymbol{p}_n|\boldsymbol{p}_{n-1})$ and h_n denotes the likelihood function $f(\boldsymbol{z}_n|\boldsymbol{p}_n)$.

2.2.4 Tracking of Mobile Targets

If the target is non-static, the state is further defined as $\boldsymbol{x}_n = [\boldsymbol{p}_n^{\mathrm{T}}, \Delta\boldsymbol{p}_n^{\mathrm{T}}]^{\mathrm{T}}$ with $\Delta\boldsymbol{p}_n$ denoting the velocity. The tracking of the time-varying target state $\boldsymbol{x}_n$ relies on sequential estimation methods as illustrated in Fig. 2.2, where the posterior PDF $f(\boldsymbol{p}_n|\boldsymbol{z}_{1:n})$ is obtained by following a recursive version of (2.5) with two steps: prediction and update. Given the posterior PDF $f(\boldsymbol{x}_{n-1}|\boldsymbol{z}_{1:n-1})$ at time $n-1$, the prior PDF $f(\boldsymbol{x}_n|\boldsymbol{z}_{1:n-1})$ is obtained at the prediction step using the Chapman–Kolmogorov equation [27] as

$$f(\boldsymbol{x}_n|\boldsymbol{z}_{1:n-1}) = \int f(\boldsymbol{x}_n|\boldsymbol{x}_{n-1}) f(\boldsymbol{x}_{n-1}|\boldsymbol{z}_{1:n-1}) \mathrm{d}\boldsymbol{x}_{n-1} \tag{2.15}$$

where $f(\boldsymbol{x}_n|\boldsymbol{x}_{n-1})$ is the state-transition PDF describing the statistical evolution of the target state over time [28], [29]. At time $n = 1$ the initial PDF is assumed to be $f(\boldsymbol{x}_1|\boldsymbol{x}_0) \triangleq f(\boldsymbol{x}_1)$. At the update step, the prior PDF is updated via Bayes' rule and the posterior PDF at time n is calculated as

$$f(\boldsymbol{x}_n|\boldsymbol{z}_{1:n}) = \frac{f(\boldsymbol{z}_n|\boldsymbol{x}_n) f(\boldsymbol{x}_n|\boldsymbol{z}_{1:n-1})}{f(\boldsymbol{z}_n|\boldsymbol{z}_{1:n-1})}. \tag{2.16}$$

State-Space Model

The state-transition PDF $f(\boldsymbol{x}_n|\boldsymbol{x}_{n-1})$ describes the statistical evolution of the target state over time, and it is typically defined by the motion models [28], [29] introduced as follows. To account for smooth uniform motions of the target, the nearly-constant velocity (NCV) model defined in Cartesian coordinate system

is typically used, given as

$$\boldsymbol{x}_n = \boldsymbol{F}_{\mathrm{NCV}}\boldsymbol{x}_{n-1} + \boldsymbol{\Gamma}\boldsymbol{\nu}_n \tag{2.17}$$

where the state-transition matrix $\boldsymbol{F}_{\mathrm{NCV}}$ and the matrix $\boldsymbol{\Gamma}$ are given by

$$\boldsymbol{F}_{\mathrm{NCV}} = \begin{bmatrix} 1 & 0 & \Delta T & 0 \\ 0 & 1 & 0 & \Delta T \\ 0 & 0 & 1 & 0 \\ 0 & 0 & 0 & 1 \end{bmatrix}, \quad \boldsymbol{\Gamma} = \begin{bmatrix} \frac{\Delta T^2}{2} & 0 \\ 0 & \frac{\Delta T^2}{2} \\ \Delta T & 0 \\ 0 & \Delta T \end{bmatrix}. \tag{2.18}$$

The driving process $\boldsymbol{\nu}_n$ is iid across n, zero-mean and Gaussian with covariance matrix $\sigma_\nu^2\boldsymbol{I}_2$. For the NCV model, σ_ν represents the average speed increment along the x or y axis during the sampling period ΔT.

If the agent is moving with a constant velocity and performing a turn with a constant angular rate Ω, the motion can be modeled with the coordinated turn (CT) model

$$\boldsymbol{x}_n = \boldsymbol{F}_{\mathrm{CT}}\boldsymbol{x}_{n-1} + \boldsymbol{\Gamma}\boldsymbol{\nu}_n \tag{2.19}$$

with the state-transition matrix given by

$$\boldsymbol{F}_{\mathrm{CT}} = \begin{bmatrix} 1 & 0 & \frac{\sin(\Omega\Delta T)}{\Omega} & -\frac{1-\cos(\Omega\Delta T)}{\Omega} \\ 0 & 1 & \frac{1-\cos(\Omega\Delta T)}{\Omega} & \frac{\sin(\Omega\Delta T)}{\Omega} \\ 0 & 0 & \cos(\Omega\Delta T) & -\sin(\Omega\Delta T) \\ 0 & 0 & \sin(\Omega\Delta T) & \cos(\Omega\Delta T) \end{bmatrix}. \tag{2.20}$$

For the CT model, σ_ν represents the average angular speed increment over a sampling period ΔT.

Knowing the correct noise variances σ_ν^2 for motion models is crucial for optimal sequential Bayesian estimation. However, determining the variances in advance is not straightforward, especially when the target is highly maneuverable. Using a constant predefined value of variance that deviates largely from the true one can potentially lead to a poor convergence behavior. Moreover, it is usually hard to describe the complex movement pattern with a single motion model. To resolve motion uncertainty of the target, localization algorithms [30], [T4] often incorporate the interacting multiple model (IMM) method [31] which fuses multiple motion models and switches between them according to their updated weights. Therefore, the requirement on presetting and tuning noise variances for the state-transition PDFs can be relaxed.

2.2.5 SLAM

Until now, we have assumed that the floor plan and VA positions are perfectly known. However, they are either unknown or only partially available in practice, leading to the simultaneous localization and mapping (SLAM) problem [32] where the VA states $\boldsymbol{a}_n$ are jointly estimated with the target state using measurements from the present and past $\boldsymbol{z}_{1:n}$. The joint posterior PDF $f(\boldsymbol{x}_n, \boldsymbol{a}_n|\boldsymbol{z}_{1:n})$ can be obtained by following a recursive version of (2.4). Specifically, given the posterior PDF $f(\boldsymbol{x}_{n-1}, \boldsymbol{a}_{n-1}|\boldsymbol{z}_{1:n-1})$ at time $n-1$, the prior PDF $f(\boldsymbol{x}_n, \boldsymbol{a}_n|\boldsymbol{z}_{1:n-1})$ is obtained at the prediction step as

$$\begin{aligned} &f(\boldsymbol{x}_n, \boldsymbol{a}_n|\boldsymbol{z}_{1:n-1}) \\ &\propto \iint f(\boldsymbol{x}_n|\boldsymbol{x}_{n-1}) f(\boldsymbol{a}_n|\boldsymbol{a}_{n-1}) f(\boldsymbol{x}_{n-1}, \boldsymbol{a}_{n-1}|\boldsymbol{z}_{1:n-1}) \mathrm{d}\boldsymbol{x}_{n-1} \mathrm{d}\boldsymbol{a}_{n-1}. \end{aligned} \tag{2.21}$$

In the update step, the posterior PDF at time n is obtained as

$$f(\boldsymbol{x}_n, \boldsymbol{a}_n|\boldsymbol{z}_{1:n}) = \frac{f(\boldsymbol{z}_n|\boldsymbol{x}_n, \boldsymbol{a}_n) f(\boldsymbol{x}_n, \boldsymbol{a}_n|\boldsymbol{z}_{1:n-1})}{f(\boldsymbol{z}_n|\boldsymbol{z}_{1:n-1})} \tag{2.22}$$

where the likelihood function factorizes as $f(\boldsymbol{z}_n|\boldsymbol{x}_n, \boldsymbol{a}_n) = \prod_{j=1}^{J} f(\boldsymbol{z}_n^{(j)}|\boldsymbol{p}_n, \boldsymbol{a}_n^{(j)}; \boldsymbol{\omega}_n^{(j)})$. For VAs representing specular reflected MPCs as illustrated in Fig. 2.1a, if the VAs are static their state-transition PDFs $f(\boldsymbol{a}_n|\boldsymbol{a}_{n-1})$ can be represented by the identity function, i.e., $f(\boldsymbol{a}_n|\boldsymbol{a}_{n-1}) = \delta(\boldsymbol{a}_n - \boldsymbol{a}_{n-1})$, where $\delta(\cdot)$ is the Dirac delta function. If a physical anchor (PA) and its associated VAs are non-static, the state-space models introduced in Section 2.2.4 can be used. For VAs representing scattered MPCs or DMC, the according state-transition PDFs are derived in [21] and [22].

RANSAC Method

The above probabilistic formulations introduce the states of the target and VAs as random variables. As an alternative, the states of the target and VAs can also be assumed as deterministic unknown, and the SLAM problem is formulated as follows: Using the estimates of MPC parameters as measurements $\hat{\boldsymbol{\omega}}_{m,n}^{(j)} \forall\, (j,m,n) \in \mathcal{I}$, find the inlier set $\mathcal{I}_{\mathrm{inl}} \subset \mathcal{I}$, the estimated target position $\hat{\boldsymbol{p}}_n \;\forall\; n \in \{1, \ldots, N\}$ and the estimated VA states $\hat{\boldsymbol{a}}_{m,n}^{(j)} \forall\, (j,m,n) \in \mathcal{I}_{\mathrm{inl}}$ that solves the joint optimization problem

$$\min_{\substack{\mathcal{I}_{\mathrm{inl}}, \boldsymbol{p}_n, \boldsymbol{a}_{m,n}^{(j)} \\ \forall j, \forall n, \forall m}} \sum_{(j,m,n) \in \mathcal{I}_{\mathrm{inl}}} \left(\hat{\boldsymbol{\omega}}_{m,n}^{(j)} - h(\boldsymbol{p}_n, \boldsymbol{a}_{m,n}^{(j)}) \right)^2 + \sum_{(j,m,n) \in \mathcal{I}_{\mathrm{outl}}} C \tag{2.23}$$

where $\boldsymbol{\omega}_{m,n}^{(j)} = h(\boldsymbol{p}_n, \boldsymbol{a}_{m,n}^{(j)})$ denotes the non-linear transformation from the target state $\boldsymbol{p}_n$ and VA states $\boldsymbol{a}_{m,n}^{(j)}$ to the MPC states $\boldsymbol{\omega}_{m,n}^{(j)}$ as shown in (2.1), $\mathcal{I}_{\text{outl}} = \mathcal{I} \setminus \mathcal{I}_{\text{inl}}$ denotes the outlier set, and C is the constant penalty for each outlier. The optimization problem (2.23) is highly non-linear and non-convex. Its character changes if both $\hat{\boldsymbol{p}}_n$ and $\boldsymbol{a}_{m,n}^{(j)}$ span 3D, or at least one of them are restricted to a 2D plane or a line as shown in [6]. Furthermore, the problem is ill-defined if there are too few measurements [33], [34]. The problem can be solved using minimal solvers and the random sample consensus (RANSAC) [6], [35] method, which provides an initial estimates of the target position, the VA positions, as well as an estimate of the inlier set. The estimates are then refined by other methods, e.g., the Newton method.

In the included publications [T1] and [T2], a RANSAC-based SLAM framework using MPCs parameter estimates of a massive MIMO system as measurements is discussed.

2.3 Algorithm Implementation

For the above probabilistic formulations, if the system models are non-linear or the posterior PDF is non-Gaussian and multimodal, the straightforward ML estimation or the sequential Bayesian estimation cannot be solved analytically. In this case, approximate sub-optimal Bayesian methods such as the extended Kalman filter (EKF) [36] or particle filters (PFs) [37] are needed.

2.3.1 Particle Filter

For the sake of simplicity, we introduce the filtering process with PF for a single anchor, therefore the index j is omitted. Sampling importance resampling (SIR) PF is a sub-optimal sequential Monte Carlo (MC) method which can be used to realize the recursive Bayesian filtering process, where the prediction and update steps are formulated in an approximate manner [37]. The key idea of the PF is to approximate the PDFs involved in (2.15) and (2.16) with a finite set of random samples (particles) and corresponding weights, i.e., $\{\boldsymbol{x}_n^k, w_n^k\}_{k=1}^K$, where K is the number of particles and the weights are normalized such that $\sum_{k=1}^K w_n^k = 1$. Specifically, at time n, the particles are sampled from an importance density $q(\boldsymbol{x}_n|\boldsymbol{x}_{n-1}, \boldsymbol{z}_n)$, and the weights are updated according to

$$w_n^k \propto w_{n-1}^k \frac{f(\boldsymbol{z}_n|\boldsymbol{x}_n^k) f(\boldsymbol{x}_n^k|\boldsymbol{x}_{n-1}^k)}{q(\boldsymbol{x}_n|\boldsymbol{x}_{n-1}, \boldsymbol{z}_n)}. \tag{2.24}$$

The most common choice of the importance density is the state-transition PDF, i.e., $q(\boldsymbol{x}_n|\boldsymbol{x}_{n-1}, \boldsymbol{z}_n) = f(\boldsymbol{x}_n^k|\boldsymbol{x}_{n-1}^k)$, since it is intuitive and simple to implement. This means that each particle $\boldsymbol{x}_n^k$ at time n can be obtained by simply passing

the particle $\boldsymbol{x}_{n-1}^k$ at time $n-1$ through the system dynamics as shown in Section 2.2.4. With this choice, the weights update (2.24) can be simplified as

$$w_n^k \propto w_{n-1}^k f(\boldsymbol{z}_n|\boldsymbol{x}_n^k), \tag{2.25}$$

and the posterior PDF $f(\boldsymbol{x}_n|\boldsymbol{z}_{1:n})$ is approximated as

$$f(\boldsymbol{x}_n|\boldsymbol{z}_{1:n}) \approx \sum_{k=1}^{K} w_n^k \delta(\boldsymbol{x}_n - \boldsymbol{x}_n^k). \tag{2.26}$$

In practice, filtering with PF may experience the following issues. It may happen that after a few iterations/time steps, all but one particle have negligible weights, i.e., particle degeneracy. The effects of degeneracy can be reduced by using resampling, which replaces the particles with negligible weights by new particles in the proximity of the particles with large weights. The particle weights after the resampling step are set to $w_n^k = 1/K$. Systematic resampling [37] is one of the popular schemes given its simple implementation. The resampling process may introduce another problem—particle collapse, i.e., particles with high weights are statistically selected many times during resampling leading to a loss of diversity among the particles in state space, therefore all particles will collapse to a single point within a few iterations. Particle collapse becomes more severe if small process noises are used for state-transition PDFs. One commonly used method to counteract this effect is performing Markov Chain Monte Carlo sampling [38], which is conceptually similar to the resampling step dealing with particle degeneracy. Regularization using Kernels with broader distribution is another common remedy. Specifically, the posterior PDF is smoothed by approximating it as $f(\boldsymbol{x}_n|\boldsymbol{z}_{1:n}) \approx \sum_{k=1}^{K} w_n^k R(\boldsymbol{x}_n - \boldsymbol{x}_n^k)$ where $R(\cdot)$ denotes the regularization Kernel, e.g., Gaussian Kernel.

Finally, using the approximated posterior PDF, an approximation of the MMSE estimate (2.12) can be obtained according to

$$\boldsymbol{x}_n^{\mathrm{MMSE}} \approx \sum_{m=1}^{K} w_n^k \boldsymbol{x}_n^k. \tag{2.27}$$

It is straightforward to extend the above particle-based implementations to solve the recursive steps (2.21) and (2.22) of the SLAM problem, as discussed in [20].

2.4 Performance Evaluation Metrics

For time-invariant statistical models, the Cramér–Rao lower bound (CRLB) [36] is commonly used as a theoretical lower bound on the variance of an un-

biased estimator. The CRLB for the agent position $\boldsymbol{p}$ is defined as

$$\mathrm{var}(\hat{\boldsymbol{p}}) = \mathbb{E}\left\{(\hat{\boldsymbol{p}} - \boldsymbol{p})(\hat{\boldsymbol{p}} - \boldsymbol{p})^{\mathrm{H}}\right\} \geq \boldsymbol{J}_{\boldsymbol{p}}^{-1} \tag{2.28}$$

where $\mathbb{E}\{\cdot\}$ denotes the expectation, and $\boldsymbol{J}_{\boldsymbol{p}}$ is the Fisher information matrix (FIM) of the vector $\boldsymbol{p}$, which can be obtained by applying the chain rule [36],

$$\boldsymbol{J}_{\boldsymbol{p}} = \boldsymbol{T}\boldsymbol{J}_{\boldsymbol{\omega}}\boldsymbol{T}^{\mathrm{H}}. \tag{2.29}$$

The Jacobian matrix $\boldsymbol{T} = \frac{\partial \boldsymbol{\omega}}{\partial \boldsymbol{p}}$ contains the first-order partial derivatives of the MPC parameter vector $\boldsymbol{\omega}$ w.r.t. the target state $\boldsymbol{p}$. The FIM $\boldsymbol{J}_{\boldsymbol{\omega}}$ of the MPC state vector $\boldsymbol{\omega}$ is introduced in Section 3.4. The influence of multipath propagation on the position estimate in terms of the CRLBs has been illustrated in many works, e.g., [15], [39]–[42]. In particular, [15, Section 3.3] and [41] present the CRLBs considering overlapping MPCs and non-overlapping MPCs, respectively, in a dense multipath channel, [40] considers the uncertainty of the geometric information of individual anchors, and [42] illustrate the CRLBs for position estimation using massive MIMO.

The posterior-CRLB [43] denoting a theoretical performance bound for discrete-time filtering problem is introduced in [43] and in Section 3.4.

Chapter 3

Estimation of Multipath Channel Parameters

In this chapter, a geometry-based stochastic signal model (GSSM) is introduced, which provides the basis for the subsequent sections presenting parametric channel estimation methods for both static and time-varying scenarios. After that, performance evaluation metrics and multidimensional channel sounding are briefly introduced.

3.1 Signal Model

In general, the radio propagation channels are observed with finite apertures, which are mainly related to the frequency bandwidth of the measurement system, temporal observation window and the antenna array geometry. Narrowband systems are considered flat over frequency spectrum and the inverse of the bandwidth (i.e., delay resolution) is typically larger than the maximum excess delay [23]. In this case, many MPCs may fall into the same delay bin therefore cannot be resolved. Wideband and UWB systems [44], on the other hand, deliver high delay resolution, but the profile of their frequency spectra varies significantly i.e., frequency-selective. Fig. 3.1 illustrates the resolvability of MPCs in the delay domain given different system bandwidths, using synthetic radio signals generated with the four MPCs shown in Fig. 2.1. It shows that at time $n = 1$, the MPCs especially the two closely-located MPCs around 10 m become separable as the bandwidth increases. Furthermore, their time-varying distances can only be resolved in the delay-power spectrum given wideband or UWB signals. As shown in Fig. 3.2, the resolvability of MPCs in the angular domain improves when the number of Rx array elements increases. Considering that the resolvability of MPCs is crucial for multipath-assisted loc-

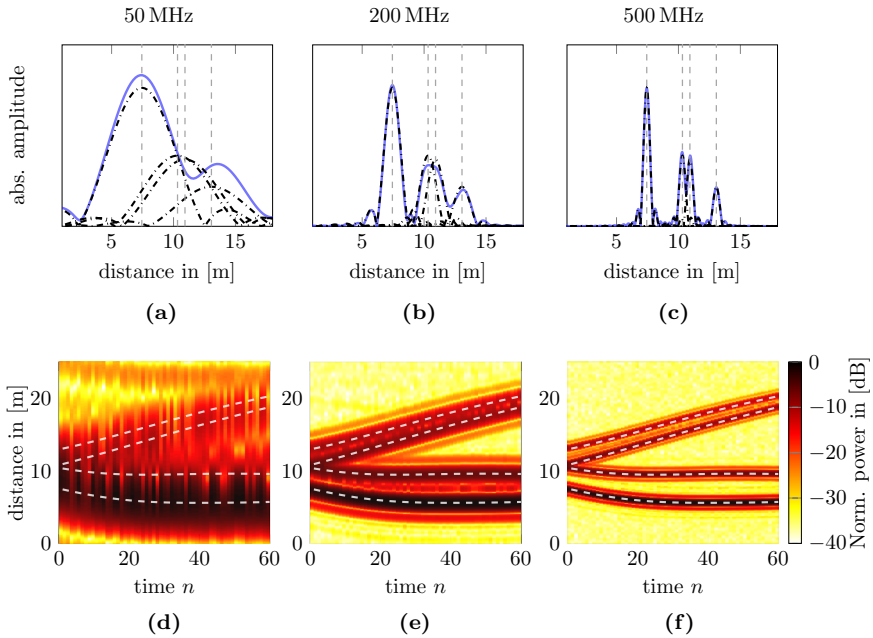

Figure 3.1: Synthetic radio signals generated using the MPC parameters shown in Fig. 2.1 and three different bandwidths, 50 MHz, 200 MHz and 500 MHz. A root-raised-cosine (RRC) signal pulse with normalized energy and roll-off factor 0.6 was used. (a)-(c) At time $n = 1$, the individual MPC contributions $\boldsymbol{b}(\boldsymbol{\theta}_{l,1})\alpha_{l,1}$ are denoted with black dash-dotted line, and the blue solid line represents the sum $\sum_{l=1}^{L_1} \boldsymbol{b}(\boldsymbol{\theta}_{l,1})\alpha_{l,1}$ (see for Eq. 3.3). The vertical dashed lines denote the true MPC propagation distances. (d)-(f) Delay-power spectra versus time given 50 dB output SNR. The dashed lines denote the true time-varying MPC propagation distances.

alization, wideband or UWB systems and large antenna arrays are preferred in that sense.

Suitable signal models are needed for the estimation of multipath channel information conveyed in radio measurements and for the derivation of analytical performance bound, i.e., CRLB [15], [39], [41] and posterior-CRLB [43]. In this thesis, a geometry-based stochastic signal model (GSSM) is used which comprises geometry dependent specular MPCs, stochastically modeled dense multipath and measurement noise. It is straightforward to account for the temporal behavior of MPCs using the GSSM, thus it is well suited for non-static environments. Note that the signal model is presented in the frequency domain considering that radio systems are all band-limited and the channel properties become frequency dependent as the signal bandwidth increases. Furthermore, the signal model is introduced for a single anchor for simplicity, therefore the

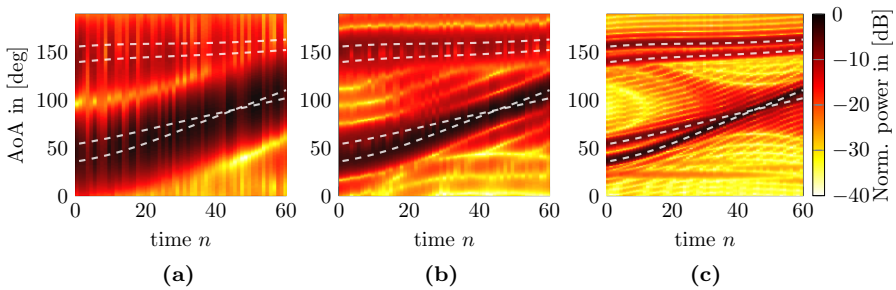

Figure 3.2: Angular-power spectra versus time of synthetic radio measurements, which are generated using the four deterministic MPC shown in Fig. 2.1 given 50 dB SNR and 50 MHz signal bandwidth. The number of Rx array elements is set: (a) 3×3-array (b) 8×8-array (c) 25×25-array. The dashed lines denote the true time-varying MPC AoAs.

index j is omitted in this chapter.

3.1.1 Geometry-Based Stochastic Signal Model

Let us consider a MIMO system in a two-dimensional scenario with horizontal-only propagation as depicted in Fig. 2.1a. The signals are exchanged between a mobile agent at position $\boldsymbol{p}_n \in \mathbb{R}^{2\times1}$ and the physical anchor at position $\boldsymbol{a}_{1,n} \in \mathbb{R}^{2\times1}$, which act as transmitter (Tx) or receiver (Rx) based on the technology used. The Tx and the Rx are assumed to be time-synchronized and equipped with an N_{Tx}-element array and an N_{Rx}-element array, respectively. The reflected paths are modeled with VAs at positions $\boldsymbol{a}_{l,n} \in \mathbb{R}^{2\times1}$ with $l \in \{2,\ldots,L_n\}$. For simplicity, we assume (i) single-polarized antennas at both sides.[1]; (ii) the Tx is moving with a sufficiently low speed, therefore Doppler frequency shifts are neglected. Under a far-field plane-wave assumption, the general baseband representation of the sampled received signal $\boldsymbol{r}_n \in \mathbb{C}^{N_{\mathrm{Tx}}N_{\mathrm{Rx}}N_{\mathrm{f}}\times1}$ at a discrete observation time n is given by [45], [47]

$$\boldsymbol{r}_n = \underbrace{\sum_{l=1}^{L_n} \alpha_{l,n}\boldsymbol{b}_{\mathrm{Tx}}(\varphi_{l,n}^{\mathrm{Tx}}) \otimes \boldsymbol{b}_{\mathrm{Rx}}(\varphi_{l,n}^{\mathrm{Rx}}) \otimes \boldsymbol{b}_{\mathrm{f}}(\tau_{l,n})}_{\text{Deterministic MPCs}} + \underbrace{\boldsymbol{w}_n}_{\text{DMC+AWGN}} \tag{3.1}$$

where N_{f} denotes the number of frequency samples, and $\otimes$ denotes the Kronecker product. The first summand on the right side comprises the contributions of L_n deterministic MPCs, each being characterized by its complex

[1] For signal models considering dual-polarized transceivers, the readers are referred to [45], [46] and the included publications [T1] and [T2].

amplitude $\alpha_{l,n} \in \mathbb{C}$, AoD $\varphi_{l,n}^{\mathrm{Tx}}$, AoA $\varphi_{l,n}^{\mathrm{Rx}}$ with respect to the orientation of the Rx array ψ, and the time delay $\tau_{l,n}$ to the array's center of gravity. The propagation distance $d_{l,n} = c\tau_{l,n}$ is related to the time delay via the speed of light c. The array orientations are assumed to be known. $\boldsymbol{b}_{\mathrm{Tx}}(\varphi_{l,n}^{\mathrm{Tx}}) \in \mathbb{C}^{N_{\mathrm{f}} \times 1}$ and $\boldsymbol{b}_{\mathrm{Rx}}(\varphi_{l,n}^{\mathrm{Rx}}) \in \mathbb{C}^{N_{\mathrm{f}} \times 1}$ represent the far-field complex array responses of the Tx and Rx at center frequency f_{c} w.r.t. the AoD and AoA. Note that we drop the frequency dependency of array responses, i.e., $\boldsymbol{b}_{\mathrm{Tx}}(\varphi_{l,n}^{\mathrm{Tx}}) = \boldsymbol{b}_{\mathrm{Tx}}(\varphi_{l,n}^{\mathrm{Tx}}, f)$ and $\boldsymbol{b}_{\mathrm{Rx}}(\varphi_{l,n}^{\mathrm{Rx}}) = \boldsymbol{b}_{\mathrm{Rx}}(\varphi_{l,n}^{\mathrm{Rx}}, f)$, by assuming that the signal bandwidth is equal to or smaller than the antenna bandwidth[2]. The vector $\boldsymbol{b}_{\mathrm{f}}(\tau_{l,n}) \in \mathbb{C}^{N_{\mathrm{f}} \times 1}$ accounts for the system response and baseband signal spectrum [23], [45], yields

$$\boldsymbol{b}_{\mathrm{f}}(\tau_{l,n}) = \boldsymbol{g}_{\mathrm{Tx}} \circ \boldsymbol{g}_{\mathrm{Rx}} \circ \boldsymbol{a}(\tau_{l,n}) \circ \boldsymbol{s}_{\mathrm{f}} \tag{3.2}$$

where $\circ$ denotes the Hadamard product. The frequency responses $\boldsymbol{g}_{\mathrm{Tx}}$ and $\boldsymbol{g}_{\mathrm{Rx}}$ of the Tx and Rx are usually measured by a back-to-back calibration procedure (see for Section 3.5). The third term $\boldsymbol{a}(\tau)$ represents the complex shifting vector defined as $\boldsymbol{a}(\tau) = [\mathrm{e}^{-j2\pi(-\frac{N_{\mathrm{f}}-1}{2})f_{\mathrm{s}}\tau} \cdots \mathrm{e}^{-j2\pi(+\frac{N_{\mathrm{f}}-1}{2})f_{\mathrm{s}}\tau}]^{\mathrm{T}}$ with f_{s} denoting the sampling interval in the frequency domain. The last term $\boldsymbol{s}_{\mathrm{f}} = \boldsymbol{s}_{\mathrm{sig}} \circ \boldsymbol{s}_{\mathrm{sig}}^{*}$ represents the spectrum of the transmitted complex baseband signal, and $\boldsymbol{s}_{\mathrm{sig}}$ denotes the transfer function of the signal pulse. The sinc pulse and the root-raised-cosine (RRC) pulse are commonly used in radio systems.

For brevity, we define $\boldsymbol{b}(\boldsymbol{\theta}_{l,n}) = \boldsymbol{b}_{\mathrm{Tx}}(\varphi_{l,n}^{\mathrm{Tx}}) \otimes \boldsymbol{b}_{\mathrm{Rx}}(\varphi_{l,n}^{\mathrm{Rx}}) \otimes \boldsymbol{b}_{\mathrm{f}}(\tau_{l,n})$, and the dispersion parameters of each MPC is given by $\boldsymbol{\theta}_{l,n} = [\tau_{l,n}, \varphi_{l,n}^{\mathrm{Tx}}, \varphi_{l,n}^{\mathrm{Rx}}]^{\mathrm{T}}$. Accordingly, the signal model (3.1) is simplified as

$$\begin{aligned} \boldsymbol{r}_n &= \sum_{l=1}^{L_n} \boldsymbol{b}(\boldsymbol{\theta}_{l,n})\alpha_{l,n} + \boldsymbol{w}_n \\ &= \boldsymbol{B}(\boldsymbol{\theta}_n)\boldsymbol{\alpha}_n + \boldsymbol{w}_n \end{aligned} \tag{3.3}$$

where $\boldsymbol{B}(\boldsymbol{\theta}_n) = [\boldsymbol{b}(\boldsymbol{\theta}_{1,n}) \cdots \boldsymbol{b}(\boldsymbol{\theta}_{L_n,n})] \in \mathbb{C}^{N_{\mathrm{Tx}}N_{\mathrm{Rx}}N_{\mathrm{f}} \times L_n}$, $\boldsymbol{\theta}_n = [\boldsymbol{\theta}_{1,n}^{\mathrm{T}} \cdots \boldsymbol{\theta}_{L_n,n}^{\mathrm{T}}]^{\mathrm{T}}$ and $\boldsymbol{\alpha}_n = [\alpha_{1,n} \cdots \alpha_{L_n,n}]^{\mathrm{T}}$. To have a more compact notation, we can further define $\boldsymbol{s}(\boldsymbol{\omega}_n) = \boldsymbol{B}_n(\boldsymbol{\theta}_n)\boldsymbol{\alpha}_n$, yields

$$\boldsymbol{r}_n = \boldsymbol{s}(\boldsymbol{\omega}_n) + \boldsymbol{w}_n \tag{3.4}$$

where $\boldsymbol{\omega}_n = [\boldsymbol{\omega}_{1,n}^{\mathrm{T}} \cdots \boldsymbol{\omega}_{L_n,n}^{\mathrm{T}}]^{\mathrm{T}}$ with $\boldsymbol{\omega}_{l,n} = [\boldsymbol{\theta}_{l,n}^{\mathrm{T}}, \alpha_{l,n}]^{\mathrm{T}}$ denoting the state of each MPC.

[2]Here, the antenna bandwidth denotes the frequency range over which (i) the antenna can properly send and receive signals; (ii) the antenna response is considered to be invariant.

Noise Process

The second term $\boldsymbol{w}_n$ in (3.1) represents the aggregate noise process which accounts for the dense multipath component (DMC) incorporating MPCs that cannot be resolved due to finite observation aperture and the measurement noise. The measurement noise process is independent additive white Gaussian noise (AWGN) with double-sided power spectral density $N_0/2$. For DMC, we assume uncorrelated scattering along the delay and angular dispersion domains, and represent it by a circularly symmetric complex Gaussian process with angular-delay power spectrum $\boldsymbol{p}(\boldsymbol{\theta}) = \boldsymbol{p}(\varphi^{\mathrm{Tx}}, \varphi^{\mathrm{Rx}}, \tau)$, where $\varphi^{\mathrm{Tx}} \in [-\pi, \pi)$, $\varphi^{\mathrm{Rx}} \in [-\pi, \pi)$ and the time delay τ is bounded by the maximum delay spread of the physical channel $\tau_{\max}$ [47], [48]. Assume that the DMC and measurement noise are independent and $\boldsymbol{w}_n$ is circularly symmetric complex Gaussian with the auto-covariance matrix $\boldsymbol{C}_n$ given as

$$\begin{aligned} \boldsymbol{C}_n &= \boldsymbol{C}_{\mathrm{dmc},n} + \boldsymbol{C}_{\mathrm{awgn}} \\ &= \int_{\boldsymbol{\theta}} \boldsymbol{b}(\boldsymbol{\theta}) \boldsymbol{b}^{\mathrm{H}}(\boldsymbol{\theta}) \boldsymbol{p}(\boldsymbol{\theta}) \mathrm{d}\boldsymbol{\theta} + \sigma^2 \boldsymbol{I}_{N_{\mathrm{Tx}} N_{\mathrm{Rx}} N_{\mathrm{f}}} \end{aligned} \tag{3.5}$$

where $\sigma^2 = N_0/T_{\mathrm{s}}$ is the noise variance and $\boldsymbol{I}_{[\cdot]}$ represents identity matrix with dimension given in the subscript $_{[\cdot]}$. Direct calculation of the first term in (3.5) is computationally demanding. With narrowband assumption, a computationally attractive solution can be applied which factorizes the full covariance matrix of DMC into Kronecker products [23], [49],[3] yields,

$$\boldsymbol{C}_{\mathrm{dmc},n} = \boldsymbol{C}_{\mathrm{Rx},n} \otimes \boldsymbol{C}_{\mathrm{Tx},n} \otimes \boldsymbol{C}_{\mathrm{f},n} \tag{3.6}$$

where $\boldsymbol{C}_{\mathrm{Tx},n}$ and $\boldsymbol{C}_{\mathrm{Rx},n}$ describe the angular distribution of the DMC at the transmitter and receiver sides, respectively. For simplicity, it is commonly assumed that the angular-power spectrum of DMC is uniform over φ^{Tx} and φ^{Rx} and the DMC is spatially uncorrelated across antenna elements, therefore the covariance matrices in the angular domain become identity matrix, i.e., $\boldsymbol{C}_{\mathrm{Tx},n} = \boldsymbol{I}_{N_{\mathrm{Tx}}}$ and $\boldsymbol{C}_{\mathrm{Rx},n} = \boldsymbol{I}_{N_{\mathrm{Rx}}}$. The third term $\boldsymbol{C}_{\mathrm{f},n} = \boldsymbol{C}_{\mathrm{f}}(\boldsymbol{\omega}_{\mathrm{dmc},n})$ represents the covariance matrix of DMC in frequency domain, which is characterized by using a parametrized power delay profile (PDP). In [45], [50], an single-exponentially decaying PDP is used. Other candidates that have been proposed are the double-exponential decaying model [50] and gamma function [47]. The noise parameters at time n are collectively given by $\boldsymbol{\omega}_{\mathrm{n},n} = [\boldsymbol{\omega}_{\mathrm{dmc},n}^{\mathrm{T}}, \sigma]^{\mathrm{T}}$.

[3]The Kronecker model is based on the assumption of uncorrelated scattering between angle, time-delay domains of the DMC. Moreover, the spatial correlation at the Tx is independent of correlation at the Rx.

Component SNR

The output component signal-to-noise ratio (SNR) of the l th MPC including array gain and frequency sample gain is defined as

$$\mathrm{SNR}_{l,n} = 10\log_{10}\left(\frac{\|\alpha_{l,n}\boldsymbol{b}_n(\boldsymbol{\theta}_{l,n})\|^2 T_\mathrm{s}}{N_0 + P_{\mathrm{dmc},n}}\right). \tag{3.7}$$

where $P_{\mathrm{dmc},n}$ denotes the DMC power. The SNRs is directly related to the detectability of each estimated MPC [51]–[53], and the variances of estimated MPC parameters [41].

3.1.2 Likelihood Function

The likelihood function of the received signal vector $\boldsymbol{r}_n$ according to the baseband representation of the sampled signal (3.3), reads

$$f(\boldsymbol{r}_n|\boldsymbol{\omega}_n, \boldsymbol{\omega}_{\mathrm{n},n}) = \frac{\mathrm{e}^{-(\boldsymbol{r}_n - \boldsymbol{s}(\boldsymbol{\omega}_n))^\mathrm{H}\boldsymbol{C}_n^{-1}(\boldsymbol{r}_n - \boldsymbol{s}(\boldsymbol{\omega}_n))}}{\pi^{N_\mathrm{Tx}N_\mathrm{Rx}N_\mathrm{f}}\det(\boldsymbol{C}_n)} \tag{3.8}$$

where $\det(\cdot)$ represents the determinant of a matrix. The discrete-time signal model (3.3) and its likelihood function (3.8) serve as the basis for the parametric channel estimation methods introduced in the subsequent sections.

3.2 Snapshot-based Parametric Channel Estimation

For static radio propagation channels, subspace methods e.g., multiple signal classification (MUSIC) [54] and estimation of signal parameter via rotational invariance techniques (ESPRIT) [55], [56] or ML methods as for example [57] are standard super-resolution methods for estimating time-invariant MPC parameters. Note that we drop the time index n for the introduction of following snapshot-based parametric channel estimators for brevity.

3.2.1 ML Estimation

If the noise process in the signal model (3.1) only accounts for the measurements noise, i.e., $\boldsymbol{C} = \sigma^2\boldsymbol{I}_{N_\mathrm{Tx}N_\mathrm{Rx}N_\mathrm{f}}$, and the noise variance σ^2 is known, the estimation of MPC state $\boldsymbol{\omega}$ can be performed by means of the the ML estimator

$$\hat{\boldsymbol{\omega}}^\mathrm{ML} = \arg\max_{\boldsymbol{\omega}} \log\, f(\boldsymbol{z}|\boldsymbol{\omega}) \tag{3.9}$$

and the prior PDF of MPC state is assumed to be non-informative (uniform). The log-likelihood function $\log\, f(\boldsymbol{z}|\boldsymbol{\omega})$ is obtained according to the joint likelihood (3.8), reads

$$\log\, f(\boldsymbol{z}|\boldsymbol{\omega}) \propto -(\boldsymbol{r}-\boldsymbol{s}(\boldsymbol{\omega}))^{\mathrm{H}}\boldsymbol{C}^{-1}(\boldsymbol{r}-\boldsymbol{s}(\boldsymbol{\omega})). \tag{3.10}$$

The maximization problem (3.9) can be solved for MPC complex amplitudes $\boldsymbol{\alpha}$ given the estimates of MPC dispersion parameters $\hat{\boldsymbol{\theta}}$ by using the least square estimator

$$\hat{\boldsymbol{\alpha}} = \left(\boldsymbol{B}(\hat{\boldsymbol{\theta}})^{\mathrm{H}}\boldsymbol{B}(\hat{\boldsymbol{\theta}})\right)^{-1}\boldsymbol{B}(\hat{\boldsymbol{\theta}})^{\mathrm{H}}\boldsymbol{z}. \tag{3.11}$$

3.2.2 EM Estimation

The ML estimation (3.9) is a multi-dimensional nonlinear optimization procedure. The calculation of $\hat{\boldsymbol{\omega}}^{\mathrm{ML}}$ is typically computationally prohibitive due to the large dimension of the signal vector and the highly non-linear signal model, and no closed form exists as the global maxima of (3.9). The expectation-maximization (EM)-based methods have been proven viable approximations of the ML methods, which decompose a joint maximization problems into a number of independent maximization processes. Specifically, the likelihood function (3.10) is maximized w.r.t. the state of each MPC while keeping the states of other MPCs as known constant, and the maximization process is repeated until convergence is reached. The space-alternating generalised expectation-maximization (SAGE) [58], [59] algorithm is a widely used EM-based method.

3.2.3 Joint ML Estimation

In recent years, parametric channel estimation methods have been introduced that also consider the estimation of DMC state $\boldsymbol{\omega}_{\mathrm{dmc}}$, for instance the RIMAX algorithm [45] and the super-resolution sparse Bayesian parametric channel estimation algorithm [60]. The estimation of DMC helps to improve the detection and estimation accuracy of the deterministic MPCs. Assuming uniform prior PDFs for the MPC state $\boldsymbol{\omega}$ and the noise state $\boldsymbol{\omega}_{\mathrm{n}}$, the joint ML estimation problem is formulated as

$$\{\hat{\boldsymbol{\omega}}^{\mathrm{ML}}, \hat{\boldsymbol{\omega}}_{\mathrm{n}}^{\mathrm{ML}}\} = \arg\max_{\boldsymbol{\omega},\boldsymbol{\omega}_{\mathrm{n}}} \log\, f(\boldsymbol{z}|\boldsymbol{\omega},\boldsymbol{\omega}_{\mathrm{n}}). \tag{3.12}$$

In general, the maximization cannot be solved analytically. Instead, it is usually solved by maximizing the log-likelihood function (3.8) alternately w.r.t. $\boldsymbol{\omega}$ and $\boldsymbol{\omega}_{\mathrm{n}}$. To be more specific, given the noise state estimate $\hat{\boldsymbol{\omega}}_{\mathrm{n}}$, an estimate of the

MPC state is obtained by maximizing the likelihood (3.8) w.r.t. $\boldsymbol{\omega}$ as

$$\hat{\boldsymbol{\omega}} = \arg\max_{\boldsymbol{\omega}} -(\boldsymbol{r} - \boldsymbol{s}(\boldsymbol{\omega}))^{\mathrm{H}} \boldsymbol{C}(\hat{\boldsymbol{\omega}}_{\mathrm{n}})^{-1} (\boldsymbol{r} - \boldsymbol{s}(\boldsymbol{\omega})) \tag{3.13}$$

where the maximization for MPC complex amplitudes $\boldsymbol{\alpha}$ is solved using a weighted least square form as

$$\hat{\boldsymbol{\alpha}} = \left(\boldsymbol{B}(\hat{\boldsymbol{\theta}})^{\mathrm{H}} \boldsymbol{C}(\hat{\boldsymbol{\omega}}_{\mathrm{n}})^{-1} \boldsymbol{B}(\hat{\boldsymbol{\theta}}) \right)^{-1} \boldsymbol{B}(\hat{\boldsymbol{\theta}})^{\mathrm{H}} \boldsymbol{C}(\hat{\boldsymbol{\omega}}_{\mathrm{n}})^{-1} \boldsymbol{z}. \tag{3.14}$$

With $\hat{\boldsymbol{\omega}}$, the likelihood (3.8) is further maximized w.r.t. $\boldsymbol{\omega}_{\mathrm{n}}$

$$\hat{\boldsymbol{\omega}}_{\mathrm{n}} = \arg\max_{\boldsymbol{\omega}_{\mathrm{n}}} \left(-\log\left(\det(\boldsymbol{C})\right) - (\boldsymbol{r} - \boldsymbol{s}(\hat{\boldsymbol{\omega}}))^{\mathrm{H}} \boldsymbol{C}(\boldsymbol{\omega}_{\mathrm{n}})^{-1} (\boldsymbol{r} - \boldsymbol{s}(\hat{\boldsymbol{\omega}})) \right), \tag{3.15}$$

leading to an estimate of the noise state $\hat{\boldsymbol{\omega}}_{\mathrm{n}}$. The number of iterations between (3.13) and (3.15) needed for achieving convergence mainly depends on the number of estimated MPCs, their separability and individual component SNRs.

3.2.4 Model-Order Estimation

If the number of MPCs L (model-order) is known, the above conventional methods generally deliver accurate estimation results. However, it is typically unknown in practice, and these methods have in common that they do not incorporate the model-order estimation into the estimation problem. Instead, it is either set to a constant number which is large enough to capture all the dominant multipath components, or estimated within an extended outer stage using for example eigenvalue-based methods, or the generic information theoretic criteria, e.g., the Akaike/Bayesian criterion and the minimum description length (MDL) principle [61]. The outer stage schemes mostly tend to overestimate the model-order, especially when the DMC is ignored in the estimation process. Inspired by the ideas of sparse estimation and compressed sensing, some super-resolution sparse Bayesian parametric channel estimation methods [60], [62]–[64] have recently appeared which aim to reconstruct sparse signals from a reduced set of measurements specified by a sparse weight vector. By introducing a sparsity-promoting prior model for the weights, the estimation of model-order and MPC parameters can be jointly formulated in a Bayesian framework. In Section 3.3.3, a probabilistic method [20], [65], [T5], [T6] is discussed which models the model-order estimation problem by introducing a random variable representing the existence of each potential MPC and estimates its associated existence probability.

3.2.5 EADF

The far-field complex array responses $\boldsymbol{b}_{\mathrm{Tx}}(\varphi_{l,n}^{\mathrm{Tx}})$ and $\boldsymbol{b}_{\mathrm{Rx}}(\varphi_{l,n}^{\mathrm{Rx}})$ in (3.1) are traditionally obtained by measuring and storing the radiation pattern of the antenna arrays on sampling grids in a spherical coordinate system in an anechoic chamber. However. the stored complex data file is typically significant in size, and cannot be used to calculate the derivatives w.r.t. the angular parameters that are needed for the parametric estimators and CRLB calculations. To address this problem, the effective aperture distribution function (EADF) [66] has been proposed, which performs efficient interpolation on any off-grid angles, and it achieves a high data compression and reduces the number of samples needed to fully describe the array beam pattern.

3.3 Sequential Parametric Channel Estimation

In dynamic scenarios, the true number of MPCs L_n as well as their parameters $\boldsymbol{\omega}_n$ are unknown and time-varying. To capture the temporal behavior of MPC parameters, many sequential estimation methods have been proposed, which can be grouped into two broad categories. Methods of the first-category sequentially estimate the MPC parameters directly based on the radio channel measurements [46], [67], [68], [T1], [T2]. Methods of the second-category adopt a two-stage structure, where the MPC estimates from a snapshot-based parametric channel estimator are used as noisy measurements in a tracking filter, for instance the Kalman filter (KF)-based method [69] and the message-passing algorithm in [T5] and [T6].

The second-category methods are often complicated by the data association (DA) uncertainty, i.e., it is unknown which measurement should be used for the state update of which MPC. Methods for solving DA problems are introduced in Section 3.3.2. Selecting proper state-transition models for MPC states and model-order estimation are essentially considered in all sequential parametric channel estimators. Radio channels are normally densely sampled over space and time in measurement campaigns leading to smoothly varying MPC dispersion parameters $\boldsymbol{\theta}_n$ over time steps, but their detailed motion patterns in each subspace cannot be known in advance. In this case, the nearly-constant velocity model introduced in Section 2.2.4 can be used to capture the smooth and uniform motions of $\boldsymbol{\theta}_n$ and it has proved viable using real radio measurements in many works, for instance [46], [69], [T2] and [T6]. The MPC amplitudes $|\boldsymbol{\alpha}_n|$ typically experience rapid fluctuations when moving within a small distance comparable to a wavelength due to small scale fading. In general, the amplitudes of deterministic MPCs are modeled statistically using Rician PDFs, and the amplitudes of weak MPCs are modeled with Rayleigh PDFs. For simplicity, these PDFs can be approximated as Gaussian, leading to

Gaussian state-transition PDFs for amplitudes [46], [T2] and [T6]. In terms of the model-order estimation, most of the existing sequential estimation methods consider it in an outer stage using the methods discussed in Section 3.2.4.

3.3.1 EKF-based Algorithm

The EKF [36] is widely used in the first-category sequential estimation methods, despite the fact that it is a suboptimal filter due to the inherent linearization of the nonlinear system models using first-order Taylor series. If the models are highly nonlinear, the first-order approximation may introduce large errors into the mean and covariance. More specifically, the covariances are tend to be underestimated and the bias of the estimated mean may be accumulated over time leading to divergence from the true values. Furthermore, an accurate initialization and sufficiently high spatial sampling rate of the radio channel are crucial for the EKF to achieve optimal performance. The EKF-based methods sequentially estimate the mean and covariances of MPC parameters by alternating between the following prediction and update steps [36].

Prediction Step

The MPC state vector at time n is defined as $\boldsymbol{x}_n = [\boldsymbol{\omega}_n^{\mathrm{T}}, \Delta\boldsymbol{\omega}_n^{\mathrm{T}}]^{\mathrm{T}}$, with $\Delta\boldsymbol{\omega}_n$ comprising the velocities of MPCs parameters. Given the posterior state vector $\boldsymbol{x}_{n-1}$ and posterior error covariance matrix $\boldsymbol{P}_{n-1}$ at time $n-1$, the prior state vector $\boldsymbol{x}_n^-$ and the prior covariance matrix $\boldsymbol{P}_n^-$ are obtained at the prediction step as

$$\boldsymbol{x}_n^- = \boldsymbol{F}\boldsymbol{x}_{n-1}, \tag{3.16}$$

$$\boldsymbol{P}_n^- = \boldsymbol{F}\boldsymbol{P}_{n-1}\boldsymbol{F}^{\mathrm{T}} + \boldsymbol{Q} \tag{3.17}$$

where $\boldsymbol{F}$ is the state-transition matrix (see for Section. 2.2.4) and $\boldsymbol{Q}$ is the covariance matrix.

Measurement Update Step

The measurement at time n is used to update the predicted state vector $\boldsymbol{x}_n^-$ and the error covariance matrix $\boldsymbol{P}_n^-$, yielding the posterior covariance matrix $\boldsymbol{P}_n$ and posterior state vector $\boldsymbol{x}_n$ as

$$\boldsymbol{P}_n = (\boldsymbol{I} + \boldsymbol{K}_n\boldsymbol{D}_n)\boldsymbol{P}_n^-, \tag{3.18}$$

$$\Delta\boldsymbol{x}_n = \boldsymbol{P}_n\boldsymbol{q}_n, \tag{3.19}$$

$$\boldsymbol{x}_n = \boldsymbol{x}_n^- + \Delta\boldsymbol{x}_n \tag{3.20}$$

where the Kalman gain matrix $\boldsymbol{K}_n$ is formulated as

$$\boldsymbol{K}_n = \boldsymbol{P}_n^- \boldsymbol{D}_n^{\mathrm{H}} (\boldsymbol{D}_n \boldsymbol{P}_n^- \boldsymbol{D}_n^{\mathrm{H}} + \boldsymbol{R}_n)^{-1}. \tag{3.21}$$

The score function $\boldsymbol{q}_n$ and the Fisher information matrix $\boldsymbol{D}_n$ comprising the first-order and the second-order partial derivatives of the log-likelihood function (3.10) w.r.t. the predicted state $\boldsymbol{x}_n^-$ respectively are given by [36], [46], [T2]

$$\boldsymbol{q}_n = 2\Re\left\{\boldsymbol{J}_n^{\mathrm{H}} \boldsymbol{R}_n^{-1} (\boldsymbol{r}_n - \boldsymbol{s}(\boldsymbol{\omega}_n^-))\right\}, \tag{3.22}$$

$$\boldsymbol{D}_n = 2\Re\left\{\boldsymbol{J}_n^{\mathrm{H}} \boldsymbol{R}_n^{-1} \boldsymbol{J}_n\right\}. \tag{3.23}$$

The Jacobian matrix $\boldsymbol{J}_n$ represents the the first-order partial derivatives of the signal vector $\boldsymbol{s}(\boldsymbol{\omega}_n^-)$ (3.3) w.r.t. the predicted state $\boldsymbol{x}_n^-$, which essentially linearizes the nonlinear models around the current estimates, i.e.,

$$\boldsymbol{J}_n = \frac{\partial \boldsymbol{s}(\boldsymbol{\omega}_n^-)}{\partial (\boldsymbol{x}_n^-)^{\mathrm{T}}}. \tag{3.24}$$

At time $n = 1$, the MPC estimates from a ML or EM-based snapshot-based channel estimator (e.g., SAGE and RIMAX) mentioned in Section 3.2 can be used as the initial prior state $\boldsymbol{x}_1^-$ for the EKF.

3.3.2 Belief Propagation-based Algorithm

It is noted that most of the existing methods solve the data association (DA), model-order estimation and sequential estimation of MPC parameters in separate blocks. In this section, a second-category method based on the work in [T5] and [T6] is introduced, which uses belief propagation (BP) (also known as message-passing or sum–product algorithm) [70], [71] and formulates the above problems in a joint Bayesian framework. In the following, some discussions on DA and false alarm measurements that are generally concerned for sequential Bayesian detection and estimation are given first, followed by a brief overview on the BP-based sequential channel estimation method.

Data Association

When the MPC estimates of a snapshot-based parametric channel estimator are used as measurements, it may happen that a measurement does not originate from a true MPC (false alarm), or a measurement originating from a true MPC is not detected (missed detection). In such cases, to decide which measurement should be used for the state update of which potential MPC is not straightforward. Furthermore, due to finite apertures of measurement systems and limited resolution capabilities of snapshot-based parametric channel

estimators, some measurements might not be well resolved and incorporate contributions from more than one MPCs, which makes the DA problem even more complicated. Existing sequential channel estimation methods mostly adopt "hard" association by assuming that measurements are fine resolved and each of them originates from single MPC that is specified by metrics such as the global nearest neighbor [29, Chapter 2.4], and the optimal subpattern assignment (OSPA) metric (see for Section 3.4). Probabilistic DA [29], [71], on the other hand, solves the origin uncertainty problem in a "soft" manner, in which the association probabilities for all current measurements are computed and used to form a mixture PDF for the update of each MPC state. Following [71], the associations between measurements and legacy MPCs (the MPCs that are already detected in the previous time) can be described by the MPC-oriented association random vector $\boldsymbol{a}_n$ indicating if each of the legacy MPCs generates any measurement, or equivalently described by the measurement-oriented association random vector $\boldsymbol{b}_n$ indicating if each of the measurements is generated by a legacy MPCs. To make the DA scalable to varying numbers of MPCs and measurements, the BP-based method [T5] and [T6] uses both association vectors $\boldsymbol{a}_n$ and $\boldsymbol{b}_n$, by following [20], [71], [72].

False Alarm Measurements

False alarms measurements originate mainly from the snapshot-based parametric channel estimator, and system model mismatch as for example DMC or the violation of the plane-wave assumption. The former part depends on the model-order estimation scheme used in the snapshot-based estimator and the measurement setup for instance the number of antennas, radio-frequency bandwidth, and the latter is related to the propagation environment. Knowing the correct mean number of false alarms (MNFA) $\mu_{\mathrm{fa},n}$ is crucial for optimal performance of Bayesian detection and estimation algorithms. However, determining the MNFA in advance is not straightforward, especially when the MNFA is time-varying. Using a fixed predefined value of MNFA that deviates largely from the true one, can potentially lead to decreased detection performance of MPCs and an increased number of detected false alarms.

3.3.3 MPC Detection and State Estimation

To incorporate model-order estimation into the joint estimation framework, a probabilistic model for MPC existence can be used, where each potential MPC state is augmented by a binary random existence variable $r_{k,n}$ with $k \in \{1, \ldots, K_n\}$ and associated with an existence probability. Accordingly, the MPC state vector at time n is further given by $\boldsymbol{y}_{k,n} = [\boldsymbol{x}_{k,n}^{\mathrm{T}}, r_{k,n}]^{\mathrm{T}}$. The existence probabilities are jointly estimated with other unknown variables and used for the detection of potential MPCs modeling the birth and death process

of these components in dynamic scenarios [20], [65], [T5], [T6]. The number of detected potential MPC represents an estimate of the model-order $\hat{L}_n$ at time n. Furthermore, as shown in Section 3.1.1, the complex amplitudes of MPCs are an integral part of the multipath channel model and must be estimated alongside with the dispersion parameters. The amplitude information can be exploited to improve detection and estimation accuracy of MPCs. To be more specific, the statistics of MPC amplitudes can be used to determine the variances of MPCs dispersion parameters [41] and the unknown and time-varying detection probabilities [51]–[53], which improves the detectability and maintenance of low SNR MPCs and enables a better discrimination against false alarms.

The above mentioned problems, i.e., model-order estimation, probabilistic DA and sequential estimation of MPC parameters and MNFA, can be jointly formulated in a Bayesian framework, where the joint posterior PDF is given by $f(\boldsymbol{y}_{1:n}, \boldsymbol{a}_{1:n}, \boldsymbol{b}_{1:n}, \boldsymbol{\mu}_{\mathrm{fa},1:n}, \boldsymbol{m}_{1:n} | \boldsymbol{z}_{1:n})$. The detection of individual potential MPC relies on the marginal posterior existence probabilities $p(r_{k,n} = 1 | \boldsymbol{z}_{1:n})$, obtained as

$$p(r_{k,n} = 1 | \boldsymbol{z}_{1:n}) = \int f(\boldsymbol{x}_{k,n}, r_{k,n} = 1 | \boldsymbol{z}_{1:n}) \mathrm{d}\boldsymbol{x}_{k,n}, \tag{3.25}$$

and a potential MPC is detected as an actual specular MPC which generates measurement if $p(r_{k,n} = 1 | \boldsymbol{z}_{1:n})$ exceeds a predefined existence probability threshold [73].

The sequential estimation of the MPC states $\boldsymbol{x}_{k,n}$ and the MNFA $\mu_{\mathrm{fa}n}$ relies on the posterior PDFs $f(\boldsymbol{x}_{k,n} | r_{k,n} = 1, \boldsymbol{z}_{1:n})$ and $f(\mu_{\mathrm{fa}n} | \boldsymbol{z}_{1:n})$. More specifically, the estimates can be obtained by means of the MMSE estimator [36], i.e.,

$$\boldsymbol{x}_{k,n}^{\mathrm{MMSE}} \triangleq \int \boldsymbol{x}_{k,n} f(\boldsymbol{x}_{k,n} | r_{k,n} = 1, \boldsymbol{z}_{1:n}) \mathrm{d}\boldsymbol{x}_{k,n} \tag{3.26}$$

$$\mu_{\mathrm{fa},n}^{\mathrm{MMSE}} \triangleq \int \mu_{\mathrm{fa},n} f(\mu_{\mathrm{fa},n} | \boldsymbol{z}_{1:n}) \mathrm{d}\mu_{\mathrm{fa},n} \tag{3.27}$$

The posterior PDFs involved in (3.25), (16) and (17) are the marginal PDFs of $f(\boldsymbol{y}_{1:n}, \boldsymbol{a}_{1:n}, \boldsymbol{b}_{1:n}, \boldsymbol{\mu}_{\mathrm{fa},1:n}, \boldsymbol{m}_{1:n} | \boldsymbol{z}_{1:n})$. Due to nonlinear and non-Gaussian system models, the joint posterior PDF is complex and direct marginalization is infeasible. By following common assumptions as for example statistically independent measurements and MPC states, the joint posterior PDF can be factorized as a product of lower-dimensional local functions and represented with a factor graph, and BP by means of sum-product algorithm can be performed on the factor graph [70], [71] for efficient calculation of marginal posterior PDFs with reduced complexity.

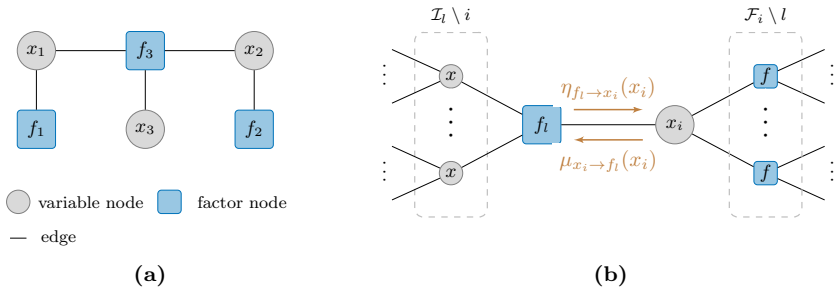

Figure 3.3: (a) Factor graph representation of the factorization $f(\boldsymbol{x}) = f_1(x_1)f_2(x_2) \times f_3(x_1, x_2, x_3)$.(b) Messages propagate between the factor node f_l and the adjacent variable node x_i [70], [71].

Sum-Product Algorithm

In the following, the basic principle of sum-product algorithm is introduced, and the detailed information can be found in [70], [71]. To obtain the approximate marginal PDFs from a global function $f(\boldsymbol{x}_\mathcal{I})$ using sum-product algorithm, the prerequisite is that $f(\boldsymbol{x}_\mathcal{I})$ can be factorized as a product of lower-dimensional local functions (factors), i.e., $f(\boldsymbol{x}_\mathcal{I}) = \prod_{l=1}^{F} f_l(\boldsymbol{x}_{\mathcal{I}_l})$, and the factorization can be further represented with a factor graph. The vector $\boldsymbol{x}_{\mathcal{I}_l} = \{x_i\}$ with $i \in \mathcal{I}_l$ accounts for the variables related to the local function f_l where the set $\mathcal{I}_l$ contains the related variable indexes. The set $\mathcal{F}_i$ contains the indexes of local functions related to the variable x_i. A factor graph is a bipartite graphical representation consisting of variables nodes representing variables x_i, factor nodes representing local functions f_l, and edges connecting the related nodes [70]. An example of factor graph is given in Fig. 3.3a. The messages propagate between a factor node $f_l(\boldsymbol{x}_{\mathcal{I}_l})$ and an adjacent variable node x_i shown in Fig. 3.3b are given by

$$\eta_{f_l \to x_i}(x_i) = \int f_l(\boldsymbol{x}_{\mathcal{I}_l}) \prod_{i' \in \mathcal{I}_l \setminus i} \mu_{x_{i'} \to f_l}(x_{i'}) \mathrm{d}x_{\sim i} \tag{3.28}$$

$$\mu_{x_i \to f_l}(x_i) = \prod_{l' \in \mathcal{F}_i \setminus l} \eta_{f_{l'} \to x_i}(x_i). \tag{3.29}$$

With the messages above, the belief for each variable x_i is calculated according to

$$q(x_i) = \frac{1}{C_i} \prod_{l \in \mathcal{F}_i} \eta_{f_l \to x_i}(x_i) \tag{3.30}$$

where C_i is the normalization constant ensuring $\int q(x_i)\mathrm{d}x_i = 1$. The belief $q(x_i)$ equals to the marginal PDF of x_i for tree-structured factor graphs, such as the one shown in Fig. 3.3a. For factor graph with loops, the beliefs have been proved to be accurate approximations of the marginal PDFs in many works such as [20], [72]. In general, the integrations involved in the calculations of the messages and beliefs cannot be obtained analytically, a computationally efficient sequential particle-based message passing implementation [65], [74] can be used to provides approximate computations.

3.4 Performance Evaluation Metrics

OSPA Metric

The OSPA metric [75] provides a mathematical consistent measure of the miss-distance between a reference multi-target state and its estimate. It has been widely adopted for various applications like clustering, data association, and performance evaluation of multi-target estimation or filtering algorithms [20], [65], [76]. In [60], [68], [T5], [T6], the OSPA metric is applied to evaluate the performance of parametric channel estimation methods, and it can efficiently capture the model-order estimation error and MPC parameter estimation error. Given the true MPC state vector $\boldsymbol{x}_n$ (stacking L_n MPCs) and its estimate $\hat{\boldsymbol{x}}_n$ (stacking $\hat{L}_n$ estimated MPCs), if $\hat{L}_n > L_n$, the OSPA metric evaluated for distance parameters at time n is defined as

$$\begin{aligned} &d_{\mathrm{ospa}}(\hat{\boldsymbol{x}}_n, \boldsymbol{x}_n) \\ &= \left[\frac{1}{\hat{L}_n}\left(\min_{\pi\in\prod_k}\sum_{l=1}^{L_n}\left[d^{(d_\mathrm{c})}\left(d_{l,n}, \hat{d}_{\pi_l,n}\right)\right]^{p_\mathrm{o}} + \quad d_\mathrm{c}^{p_\mathrm{o}}\left(\hat{L}_n - L_n\right)\right)\right]^{\frac{1}{p_\mathrm{o}}} \end{aligned} \tag{3.31}$$

where $\prod_k$ denotes the set of permutations on $\{1, \cdots, k\}$ with $k \leq \hat{L}_n$, π_l denotes the lth integer number inside the permutation vector, and $d^{(d_\mathrm{c})}(\cdot,\cdot) = \min(d_\mathrm{c}, d(\cdot,\cdot))$ where $d(\cdot,\cdot)$ denotes a distance metric (e.g., Euclidean metric), that is cut off at d_c. The cutoff parameter d_c denotes the weighting of how the metric penalizes the model-order estimation errors as opposed to MPC state estimation errors. The metric order is denoted as p_o.

To evaluate sequential estimation performance over time durations, modified OSPA metrics [77] are proposed to account for the dissimilarity between continuously estimated variables and the associated true tracks.

CRLB and Posterior-CRLB

As mentioned in Section 2.4, the CRLB and posterior-CRLB [36] are commonly used as performance benchmarks denoting the theoretical lower bounds

on the estimation variances of an unbiased estimator and an unbiased sequential Bayesian estimator, respectively. For time-invariant MPC dispersion parameters $\boldsymbol{\omega}$ in static scenarios, the CRLB is defined as

$$\mathrm{var}(\hat{\boldsymbol{\omega}}) = \mathbb{E}\left\{(\hat{\boldsymbol{\omega}} - \boldsymbol{\omega})(\hat{\boldsymbol{\omega}} - \boldsymbol{\omega})^{\mathrm{H}}\right\} \geq \boldsymbol{J}_{\boldsymbol{\omega}}^{-1} \tag{3.32}$$

where the FIM $\boldsymbol{J}_{\boldsymbol{\omega}}$ of the MPC parameter vector $\boldsymbol{\omega}$ is given by

$$\boldsymbol{J}_{\boldsymbol{\omega}} = \mathbb{E}\left\{\left(\frac{\partial}{\partial \boldsymbol{\omega}} f(\boldsymbol{z}|\boldsymbol{\omega})\right)\left(\frac{\partial}{\partial \boldsymbol{\omega}} f(\boldsymbol{z}|\boldsymbol{\omega})\right)^{\mathrm{H}}\right\}. \tag{3.33}$$

The likelihood function of the received signal vector $f(\boldsymbol{z}|\boldsymbol{\omega})$ given the MPC state is introduced in Section 3.1.1.

For discrete-time filtering problem, the posterior-CRLB for the MPC state at each time $\boldsymbol{x}_n = [\boldsymbol{\omega}_n^{\mathrm{T}}, \Delta\boldsymbol{\omega}_n^{\mathrm{T}}]^{\mathrm{T}}$ is given by the inverse of the posterior FIM $\boldsymbol{J}_{\mathrm{x}n}$, which is obtained by following the recursive process [43]

$$\boldsymbol{J}_{\mathrm{x}n} = \boldsymbol{D}_{\mathrm{x}n-1}^{22} - \boldsymbol{D}_{\mathrm{x}n-1}^{21}(\boldsymbol{J}_{\mathrm{x}n-1} + \boldsymbol{D}_{\mathrm{x}n-1}^{11})^{-1}\boldsymbol{D}_{\mathrm{x}n-1}^{12}. \tag{3.34}$$

The recursive sub-matrices $\boldsymbol{D}_{\mathrm{x}n-1}^{11}$, $\boldsymbol{D}_{\mathrm{x}n-1}^{12}$, $\boldsymbol{D}_{\mathrm{x}n-1}^{21}$ and $\boldsymbol{D}_{\mathrm{x}n-1}^{22}$ are computed with the partial derivatives of the state-transition PDFs $f(\boldsymbol{x}_n|\boldsymbol{x}_{n-1})$ and likelihood functions $f(\boldsymbol{z}_n|\boldsymbol{x}_n)$ w.r.t. the state vector $\boldsymbol{x}_n$ and $\boldsymbol{x}_{n-1}$ [43]. The information matrix $\boldsymbol{J}_{\mathrm{x}1}$ can be initialized with the FIM $\boldsymbol{J}_{\boldsymbol{\omega}}$ at time $n = 1$ as given in (3.33).

Note that the posterior-CRLB is in general tighter than the CRLB. If the coherence between the measurements of consecutive time steps reduces, i.e., the state-space model becomes less informative, the posterior-CRLB will converge to CRLB.

3.5 Multidimensional Channel Sounding

To validate the proposed algorithms, measurement campaigns using RUSK-LUND channel sounder shown in Fig. 3.4a were performed during the thesis work. The basic principles of wireless channel sounding are introduced as follows. The Tx emits periodical sounding signals to excite the channel, the output of the channel is then recorded by the Rx. To measure time-varying channels, the repetition period of the sounding signals should be larger than the pulse duration and the maximum excess delay of the channel, but smaller than the channel coherence time, i.e., the time duration over which the channel is considered static. According to the Nyquist sampling theorem, the temporal sampling frequency should be at least twice the maximum Doppler frequency.

The RUSK-LUND channel sounder is designed for measuring the frequency transfer functions, and it is capable to measure in the 300 MHz, 2 GHz, and

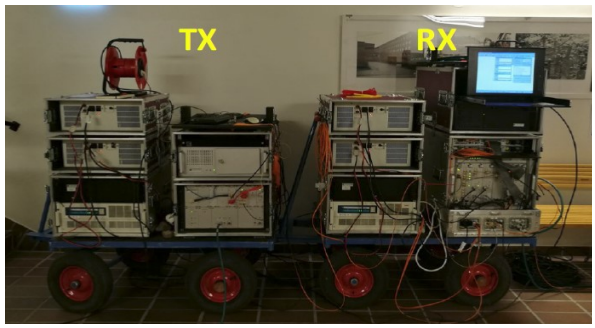

(a)

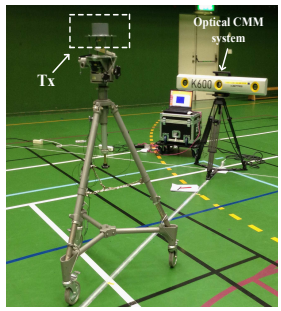

(b)

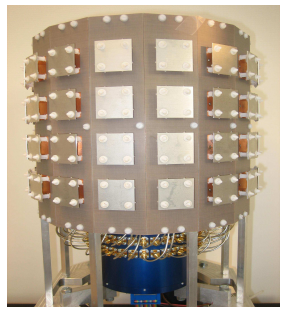

(c)

Figure 3.4: Pictures of the RUSK-Lund channel Sounder (a), a conical monopole omni-directional antenna used as the Tx and the optical CMM system which captures its groundtruth positions (b), and the cylindrical array (c).

5 GHz bands with a bandwidth up to 240 MHz. The channel sounder does not measure the channels between all Tx and Rx antenna pairs simultaneously, instead, it uses the switched array principle to perform MIMO measurements, which sequentially swipe through all the antenna pairs. For frequency domain measurements, it uses a multi-tone, OFDM-like signal to ensure a constant power spectral density over the whole bandwidth. Averaging over several transfer functions (or impulse responses) that are consecutively recorded within the channel coherent time is commonly used to enhance the signal SNR.

To remove the impact of the measurement equipment itself, i.e., the frequency responses $\boldsymbol{g}_{\mathrm{Tx}}$ and $\boldsymbol{g}_{\mathrm{Rx}}$ in (3.2), a back-to-back calibration has to be performed. More specifically, the frequency response of the measurement system is measured and then used for compensation so that only the transfer functions of the wireless channels are measured. Note that the Tx and Rx antennas are not included in the calibration process since they are considered as

a part of the channel during measurements and are often calibrated separately.

For wireless channel sounding, it is important to synchronize the Tx and Rx in frequency and time. For our measurements campaigns, the synchronization was performed by using common time reference signals for instance pulse-per-second signals, or using Rubidium clocks or GPS clocks. If the measurements are further used for evaluating radio-based localization algorithms, time synchronization between the channel sounder and a system capturing ground truth position information should be further established by using reference signals or GPS/Rubidium clocks.

Chapter 4

RSS-based Localization for IoT Networks

Internet-of-Things (IoT) networks dedicated for machine-type communications are considered as an important complement or feature of current and 5G-and-beyond radio systems. Location-awareness is a key enabler for various IoT related applications. In this chapter, we focus on the localization solutions for IoT networks, with particular interest in the received signal strength (RSS)-based methods.

4.1 Localization Methods for IoT Networks

Conventional IoT networks are typically implemented by using technologies like the radio frequency identification, Bluetooth Low Energy, Wi-Fi, with coverage from a few meters up to around a hundred meters depending on the surrounding environment. In recent years, IoT networks based on cellular systems or low-power wide area networks (LPWANs), e.g., SIGFOX and LoRa, further extend the coverage to urban size or even larger in rural areas. Most of the IoT networks serve low-rate applications with low-power requirements, which have a strong impact on the design of dedicated localization solutions. To maintain sufficient accuracy and robustness without asking for frequently updated measurements and keep low-complexity is the main concern in most of the research works. Existing localization solutions typically use features like ToA, TDoA, AoA, or RSS. Among these, RSS is especially appealing since it is readily available in most of wireless systems. In this thesis, we focus on RSS-based localization solutions for the mid- to long-range outdoor scenarios.

In general, RSS-based localization is performed using proximity, fingerprinting [10], [11] or ranging-based [12], [13] methods. Fingerprinting exploits the

RSS spatial distribution by matching RSS measurements with the pre-acquired measurements (fingerprints) at the positions of interest. The achievable accuracy is related to the density of fingerprints and degrades in dynamic scenarios. RSS-based ranging for localization is also commonly used, which exploits a path-loss model (PLM) [13] to map RSS measurements to range estimates, and then uses them to infer the target position w.r.t. the anchor coordinates. The ranging accuracy is mainly limited by the precision of path-loss exponent (PLE) information, and it is strongly influenced by multipath propagation phenomena. Some recent works [78] also explore the potential of using angular information extracted from non-coherent RSS measurements for localization. Angular information is mostly obtained by using phase coherent antennas, however this is not ideal for IoT networks in order to maintain a low system cost.

In the following, the RSS model and RSSD model needed for extracting range and angle information are introduced first, followed by the general formulations of RSS-based target tracking problems.

4.2 RSS Model and RSSD Model

At time n, the RSS (in dBm) obtained at the ath antenna ($a \in \mathcal{A}_s \triangleq \{1, \cdots, A_j\}$) of jth anchor ($j \in \mathcal{J} \triangleq \{1, \cdots, J\}$) is given as

$$P^a_{j,n} \triangleq P_{0,j} + G_{\mathrm{Rx}}(\varphi^a_{j,n}) - 10\eta_{j,n} \log_{10}\left(\frac{d^a_{j,n}}{d_0}\right) + S^a_{\mathrm{S},j,n} + S^a_{\mathrm{L},j,n} + n^a_{j,n}\,, \quad (4.1)$$

according to the PLM [13], where the AoA $\varphi^a_{j,n}$ and propagation distance $d^a_{j,n}$ can be computed as shown in (2.1). The first term on the right side, $P_{0,j}$, accounts for the transmit power P_{Tx} (in dBm), the transmit antenna gain G_{Tx} and the path loss

$$L_{\mathrm{ref},j}(d_0) = 20\log_{10}(\frac{\lambda}{4\pi}) - 10\eta_{n,j}\log_{10}(d_0) \quad (4.2)$$

at the reference distance d_0, i.e.,

$$P_{0,j} = P_{\mathrm{Tx}} + G_{\mathrm{Tx}} + L_{\mathrm{ref},j}(d_0) \quad (4.3)$$

and λ is the wavelength. Furthermore, $G_{\mathrm{Rx}}(\varphi^a_{j,n})$ denotes the receive antenna gain at angle $\varphi^a_{j,n}$, $\eta_{j,n}$ is the PLE, $S^a_{\mathrm{L},j,n} \sim \mathcal{N}(0, \sigma^2_{\mathrm{S}})$ models the log-normal shadow fading which is position-dependent and slow-varying over time, $S^a_{\mathrm{S},j,n}$ represents the small scale fading modeling the random and fast variations of RSS in time or space. The last term $n^a_{j,n}$ accounts for the measurement noise which is modeled using a zero-mean Gaussian distribution with variance σ^2_{n}. The impact of small scale fading is usually reduced by averaging over samples

that are consecutively received within a certain time duration.

RSS-based ranging based on (4.1) can be problematic. P_{Tx} is typically unknown to receivers and slow-varying with battery draining over time. Unknown device orientation leads to the variation of G_{Tx}. The PLE $\eta_{j,n}$ of each anchor is also unknown, time-varying, and strongly depends on the surrounding environment. Joint estimation of these unknown parameters at each time n is challenging especially for long-range IoT systems. These systems typically use very high receive sensitivity to increase coverage, but at the expense of very low signal bandwidth and data rate. This means that the estimates can be unreliable especially in dynamic scenarios given limited number of measurements. For simplicity, those parameters are normally assumed to be known constant. Under a far-field propagation condition, the parameters P_{Tx}, G_{Tx} and $\eta_{j,n}$ are approximately the same for all the antennas at each anchor. Moreover, the shadow fading process $S^i_{\mathrm{L},k,j}$ is highly correlated over adjacent antennas.

Inspired by the above arguments, the difference between RSS measurements obtained from adjacent antennas with indexes $\{r_1, r_2\} \in \mathcal{A}_j$ at each anchor can be described by the RSSD model [T3], [T4], i.e.,

$$P^{(r_1,r_2)}_{\Delta,j,n} \triangleq P^{r_1}_{j,n} - P^{r_2}_{j,n} = G^{(r_1,r_2)}_{\Delta,j,n}(\varphi_{j,n}) + \omega^{(r_1,r_2)}_{j,n}, \tag{4.4}$$

which excludes those unknown but common parameters in (4.1). The first term representing the receive antenna gain difference is given by

$$G^{(r_1,r_2)}_{\Delta,n,s}(\varphi_{j,n}) = G_{\mathrm{Rx}}(\varphi^{r_1}_{n,s}) - G_{\mathrm{Rx}}(\varphi^{r_2}_{j,n}). \tag{4.5}$$

The noise term $\omega^{(r_1,r_2)}_{j,n}$ is approximated as the difference between two iid noise processes $n^{r_1}_{n,s}$ and $n^{r_2}_{j,n}$, thus $\omega^{(r_1,r_2)}_{j,n} \sim \mathcal{N}(0,\, 2\sigma^2_{\mathrm{n}})$.

The likelihood functions of the RSS measurements $z^k_{j,n}$ with $k \in^{\triangle} \{1, \cdots, K_j\}$ and the likelihood functions of the RSSD measurements $z^l_{\mathrm{D},j,n}$ with $l \in^{\triangle} \{1, \cdots, D_j\}$ are derived from (4.1) and (4.4), given by

$$f(z^k_{j,n}|\boldsymbol{p}_n, \eta_{j,n}) = \frac{1}{\sqrt{2\pi(\sigma^2_{\mathrm{S}} + \sigma^2_{\mathrm{n}})}} \exp\Big\{-\frac{(z^k_{j,n} - s^k_{j,n})^2}{2(\sigma^2_{\mathrm{S}} + \sigma^2_{\mathrm{n}})}\Big\}, \tag{4.6}$$

$$f(z^l_{\mathrm{D},j,n}|\boldsymbol{p}_n) = \frac{1}{\sqrt{4\pi\sigma^2_{\mathrm{n}}}} \exp\Big\{-\frac{(z^l_{\mathrm{D},j,n} - G^{(r^l_1,r^l_2)}_{\Delta,n,s}(\varphi_{j,n}))^2}{4\sigma^2_{\mathrm{n}}}\Big\} \tag{4.7}$$

where $s^k_{j,n} = P_{0,j} + G_{\mathrm{Rx}}(\varphi^k_{j,n}) - 10\eta_{j,n}\log_{10}(d^k_{j,n}/d_0)$.

The RSS model (4.1), the RSSD model (4.4) and their likelihood functions (4.6) and (4.7) are needed for the inference of range and angular information from RSS observations, and for the related localization problems introduced in

the following.

4.3 RSS-based Target Tracking

The RSS-based positioning problems solved for static agent have been well studied in many works, e.g., [26], [79], where methods based on the least square and ML estimators [36] are mostly utilized. In this thesis, we focus on the tracking problem of target state $\boldsymbol{x}_n = [\boldsymbol{p}_n^{\mathrm{T}}, \Delta\boldsymbol{p}_n^{\mathrm{T}}]^{\mathrm{T}}$ where the anchor positions are always assumed to be known.

The tracking of agent state $\boldsymbol{x}_n$ can be solved with a sequential Bayesian estimation process introduced in Section 2.2.4, by exploiting the range information extracted from RSS measurements $\boldsymbol{z}_n$ (given known PLEs), or the AoA information extracted from RSSD measurements $\boldsymbol{z}_{\mathrm{D},n}$ [T3]. Assuming that the measurements are statistically independent to each other, the likelihood function of $\boldsymbol{z}_n$ at each time factorizes as

$$f(\boldsymbol{z}_n|\boldsymbol{x}_n) = \prod_{j=1}^{J}\prod_{k=1}^{K_j} f(z_{j,n}^k|\boldsymbol{p}_n;\eta_{j,n}), \tag{4.8}$$

and the individual likelihood $f(z_{j,n}^k|\boldsymbol{p}_n;\eta_{j,n})$ is calculated according to (4.6). Similarly, the likelihood of RSSD measurements $\boldsymbol{z}_{\mathrm{D},n}$ factorizes as

$$f(\boldsymbol{z}_{\mathrm{D},n}|\boldsymbol{x}_n) = \prod_{j=1}^{J}\prod_{l=1}^{D_j} f(z_{\mathrm{D},j,n}^l|\boldsymbol{p}_n), \tag{4.9}$$

and the individual likelihood $f(z_{\mathrm{D},j,n}^l|\boldsymbol{p}_n)$ is given in (4.7).

4.3.1 Unknown PLEs

As mentioned above, the PLEs are typically unknown and time-varying in practice. The joint sequential estimation of the target state $\boldsymbol{x}_n$ and PLEs $\boldsymbol{\eta}_n = [\eta_{1,n}\cdots\eta_{J,n}]^{\mathrm{T}}$ can be formulated in the similar way as the SLAM problem described in Section 2.2.5, where the joint posterior PDF $f(\boldsymbol{x}_n, \boldsymbol{\eta}_n|\boldsymbol{z}_{1:n})$ is obtained by following a recursive process, consisting of a prediction step

$$\begin{aligned} &f(\boldsymbol{x}_n, \boldsymbol{\eta}_n|\boldsymbol{z}_{1:n-1}) \\ &\propto \iint f(\boldsymbol{x}_n|\boldsymbol{x}_{n-1}) f(\boldsymbol{\eta}_n|\boldsymbol{\eta}_{n-1}) f(\boldsymbol{x}_{n-1}, \boldsymbol{\eta}_{n-1}|\boldsymbol{z}_{1:n-1}) \mathrm{d}\boldsymbol{x}_{n-1}\mathrm{d}\boldsymbol{\eta}_{n-1}. \end{aligned} \tag{4.10}$$

and an update step

$$f(\boldsymbol{x}_n, \boldsymbol{\eta}_n|\boldsymbol{z}_{1:n}) = \frac{f(\boldsymbol{z}_n|\boldsymbol{x}_n, \boldsymbol{\eta}_n) f(\boldsymbol{x}_n, \boldsymbol{\eta}_n|\boldsymbol{z}_{1:n-1})}{f(\boldsymbol{z}_n|\boldsymbol{z}_{1:n-1})}. \tag{4.11}$$

Assuming that PLE states evolve independently across anchors and time, the corresponding state-transition PDF of the joint states $\boldsymbol{\eta}_n$ can be factorized as $f(\boldsymbol{\eta}_n|\boldsymbol{\eta}_{n-1}) = \prod_{j=1}^{J} f(\eta_{j,n}|\eta_{j,n-1})$. If the propagation conditions from the target to anchors are static, the individual state-transition PDF can be represented by an identity function, i.e., $f(\eta_{j,n}|\eta_{j,n-1}) = \delta(\eta_{j,n} - \eta_{j,n-1})$. Otherwise, it can be modeled with the motion models introduced in Section 2.2.4 and [29]. The likelihood function factorizes as

$$f(\boldsymbol{z}_n|\boldsymbol{x}_n, \boldsymbol{\eta}_n) = \prod_{j=1}^{J} \prod_{k=1}^{K_j} f(z_{j,n}^k|\boldsymbol{x}_n, \eta_{j,n}) \tag{4.12}$$

and the individual likelihood $f(z_{j,n}^k|\boldsymbol{x}_n, \eta_{j,n})$ is given in (4.6).

4.3.2 Information Fusion

Most of the existing RSS-based localization methods exploit a single geometric feature, i.e., either range or AoA, however, these information can be fused efficiently to improve estimation accuracy and robustness [T5]. Moreover, the methods should be adaptive to dynamic channel conditions (i.e., unknown and time-varying PLEs) and target motion uncertainty, while the later one can be solved by using interacting multiple model (IMM) method as mentioned in Section 2.2.4. The above considerations lead to a joint sequential Bayesian estimation framework which estimates the target state $\boldsymbol{x}_n$, the PLEs $\boldsymbol{\eta}_n$ and the vector $\boldsymbol{m}_n$ stacking the indexes of different motion models, using the past and present measurement vectors $\boldsymbol{z}_{1:n} \triangleq [\boldsymbol{z}_1^{\mathrm{T}}, \ldots, \boldsymbol{z}_n^{\mathrm{T}}]^{\mathrm{T}}$ and $\boldsymbol{z}_{\mathrm{D},1:n} \triangleq [\boldsymbol{z}_{\mathrm{D},1}^{\mathrm{T}}, \ldots, \boldsymbol{z}_{\mathrm{D},n}^{\mathrm{T}}]^{\mathrm{T}}$. The estimation of unknown variables rely on the marginal posterior PDFs $f(\boldsymbol{x}_n|\boldsymbol{z}_{1:n}, \boldsymbol{z}_{\mathrm{D},1:n})$, $f(\eta_{n,s}|\boldsymbol{z}_{1:n})$ and $f(m_n|\boldsymbol{z}_{1:n}, \boldsymbol{z}_{\mathrm{D},1:n})$, which can be efficiently obtained by running message-passing algorithm on the factor graph representation of the factorization of the joint posterior PDF $f(\boldsymbol{x}_{1:n}, \boldsymbol{m}_{1:n}, \boldsymbol{\eta}_{1:n}|\boldsymbol{z}_{1:n}, \boldsymbol{z}_{\mathrm{D},1:n})$. The adaptive target tracking algorithm exploiting both range and angular information is the key contribution of [T3] and [T4].

Chapter 5

Conclusions and Outlook

This chapter briefly summarizes the work performed in each of the research papers included in this thesis. For each paper, the research contributions and my personal contributions as a co-author are highlighted.

5.1 Research Contributions

[T1] Robust Phase-based Positioning using Massive MIMO with Limited Bandwidth

Research Contributions: This paper proposes an EKF-based algorithm which performs detection of specular MPCs and sequential estimation of their parameters. By tightly coupling the change of MPC distances to the phase shifts over consecutive snapshots, the MPC distances can be estimated far beyond the signal bandwidth dependent accuracy. This algorithm further incorporates the estimation of DMC comprising all the non-resolvable MPCs to improve the detection and estimation accuracy of the specular MPCs. The estimated MPC distances are subsequently used as the input of a distance-based localization and mapping algorithm. The performance is evaluated using real radio measurements with an antenna array of 64 duel-polarized elements at the base station side and standard cellular signal bandwidth of 40 MHz. The results show that high accuracy radio-based localization in harsh multipath environments is possible even with limited signal bandwidth by exploiting a massive MIMO system.

Personal Contributions: This paper results from a collaboration project between the Communications Engineering group and the Center for Mathematical Sciences at Lund University. I am the main contributor of this paper. I was responsible for the development and implementation of the parametric

channel estimation algorithm. I designed the measurement campaign and performed it together with colleagues, and also processed the measurement data and analyzed the results. I took the lead in writing the paper except for the localization section.

[T2] Massive MIMO-Based Localization and Mapping Exploiting Phase Information of Multipath Components

Research Contributions: This paper is a follow up to [T1]. We provide detailed formulations of the proposed EKF-based parametric channel estimation algorithm. Besides, in-depth analysis on the estimation results, including the dynamic behavior and statistical distributions of the estimated MPC parameters and their influence on the localization performance, are presented using both synthetic and real measurements in a challenging scenario.

Personal Contributions: I performed simulations using the measurement data and theoretical analysis on the results. I took the lead in writing the paper except for the localization section.

[T3] Target Tracking using Signal Strength Differences for Long-Range IoT Networks

Research Contributions: This paper provides an RSS-based solution for target tracking or AoA estimation in outdoor IoT scenarios. Assuming that the radiation patterns of antennas and array geometries are known, we propose an RSSD model based on the classic path-loss model, which provides direct mapping between AoAs and non-coherent RSSD observations without requiring information on the transmit power and path-loss exponent (PLE). The RSSDs model is exploited in a recursive Bayesian filtering method for target tracking where a particle filter-based implementation is used. We evaluate the performance using real outdoor measurements from a low-power wide area network (LoRaWAN) based IoT system. The results show the capability of the proposed framework for real-time target/AoA tracking. Furthermore, reasonable accuracy is achieved even with non-averaged measurements and under NLoS conditions.

Personal Contributions: I am the main contributor of this paper. I was responsible for the development and implementation of the algorithm. I designed the measurement campaign and performed it together with the second and the third authors. Moreover, I processed the measurement data and performed the result analysis. I took the lead in writing the paper.

[T4] RSS-based localization of Low-Power IoT Devices Exploiting AoA and Range Information

Research Contributions: We propose a message-passing algorithm exploiting both the range and angle information from non-coherent RSS measurements for target tracking. Considering that the PLEs are typically unknown and time-varying in dynamic scenarios, we develop a Bayesian model for the estimation of the target position and PLEs to different anchors, where the likelihood functions are derived from the path-loss model and the RSSD model proposed in [T3]. This Bayesian model is further represented with a factor graph which enables the use of message-passing algorithm for efficient computation of the marginal posterior PDFs of unknown variables. Moreover, this algorithm incorporates the interacting multiple model (IMM) method to resolve the motion uncertainty of the target. The performance is validated using real outdoor measurements from an IoT network based on LoRa system. Results show that the proposed algorithm well adapt to time-varying PLEs due to dynamic propagation conditions and delivers higher the localization accuracy and robustness compared to the method exploiting a single geometric feature. Furthermore, the algorithm scales well in different antenna array configurations, and is compatible with various existing IoT standards.

Personal Contributions: I conceived and planned this work. I am the main contributor of this paper, and responsible for the development and implementation of the algorithm, as well as the analysis on the result using both synthetic and measurement data. I took the lead in writing the paper.

[T5] Detection and Tracking of Multipath Channel Parameters Using Belief Propagation

Research Contributions: We propose a belief propagation (BP)-based algorithm for sequential detection and estimation of MPC parameters based on radio signals. Under dynamic channel conditions with moving transmitter/receiver, the number of MPCs, the MPC dispersion parameters, and the number of false alarm contributions are unknown and time-varying. We develop a Bayesian model for sequential detection and estimation of MPC dispersion parameters, and represent it by a factor graph enabling the use of BP for efficient computation of the marginal posterior distributions. At each time instance, a snapshot-based parametric channel estimator provides parameter estimates of a set of MPCs which are used as noisy measurements by the proposed BP-based algorithm. It performs joint probabilistic data association, estimation of the time-varying MPC parameters, and the mean number of false alarm measurements by means of the sum-product algorithm rules. The algorithm also exploits amplitude measurements enabling the reliable detection of "weak" MPCs with very low SNRs. Simulation results using synthetic radio

measurements show that the proposed algorithm has excellent performance regarding the scalability to the time-varying model order, estimation accuracy, and association property over time in a realistic and very challenging scenario.

Personal Contributions: This paper results from a collaboration project between the Communications Engineering group at Lund University and the Laboratory of Signal Processing and Speech Communication at Graz University of Technology, Austria. Dr. Erik Leitinger and I are the main contributors. We equally contributed to the algorithm development and implementation, performance evaluation using synthetic data and paper writing.

[T6] Sequential Detection and Estimation of Multipath Channel Parameters Using Belief Propagation

Research Contributions: This paper is a follow up to [T5]. In this paper, we present detailed mathematical derivations and more insights into the proposed algorithm. The results are demonstrated with both synthetic and real measurements. Moreover, the performance of the proposed algorithm are compared with the Kalman enhanced super-resolution tracking (KEST) [69] algorithm (a state-of-the-art sequential channel parameter estimation method), and posterior-CRLB. The results show that our algorithm compares well to state-of-the-art algorithms for high SNR MPCs, but it significantly outperforms them for medium or low SNR MPCs. Results using real radio measurements demonstrate the excellent performance of the proposed algorithm in realistic and challenging scenarios.

Personal Contributions: This paper is a follow up to [T5]. Dr. Erik Leitinger and I equally contributed to the derivation and implementation of the proposed algorithm and the reference state-of-the-art algorithm, measurement data processing, result analysis as well as paper writing.

5.2 General Conclusions

As mentioned above, this thesis explores some interesting topics in the field of radio-based localization both theoretically and experimentally. The following are a few general conclusions and observations drawn from the research work.

- High accurate radio-based localization in harsh multipath environments with limited signal bandwidth can be made possible by the following two factors. First, utilizing large-scale antenna arrays enables superior resolvability of MPCs in angular domain. Second, if the spatial sampling rate of the radio channel is sufficiently high, i.e., recording a few snapshots within one wavelength movement, it is possible to estimate the MPC dis-

tances far beyond the signal bandwidth dependent accuracy by measuring the phase shifts of MPCs over consecutive snapshots.

- The data association (DA), model-order detection and estimation of the time-varying MPC parameters are essentially considered in all sequential channel estimation methods, but they are mostly solved in separate blocks. With the proposed belief propagation (BP)-based algorithm, we show that the above issues, together with the estimation of mean number of false alarm measurements, can be probabilistically formulated in a joint Bayesian framework. Its factor graph representation enables the use of BP for efficient computation of the marginal posterior distributions needed for Bayesian detection and estimation. Furthermore, exploiting the amplitude information of MPCs to determine the unknown and time varying detection probabilities can significantly improves the detectability of "weak" MPCs with very low component SNRs.

- The dominant trends of the successive generations of mobile communication systems have been the search for more signal bandwidth (and thereby higher carrier frequencies as the lower bands are very congested) and the exploitation of larger scale antenna arrays. Correspondingly, their signal data is also getting larger in size. We noted that the computational complexity of many existing parametric channel estimation methods is already very high when processing signals of existing radio systems, not to mention the enormous amount of data associated with emerging systems. Estimation methods that are with reasonable complexity and highly scalable to varying number of MPCs are of great importance.

- IoT devices are typically limited in cost and have low power consumption. To improve the accuracy and robustness of RSS-based localization given the limited resources, the angular information can be estimated from non-coherent RSS measurements by exploiting the proposed RSSD model and then fused with the range information estimated using the classic path-loss model. Moreover, the path-loss exponents associated to different anchors can be jointly estimated with the target position in a localization solution to improve its adaptivity in dynamic scenarios.

5.3 Future Research

There are many aspects within or beyond the studied topics could be investigated further. The following is a selection of the most interesting and promising extensions of the work presented in the thesis for future research:

- To reduce the computational complexity of parametric channel estimation for large signal data, it can be possible that the estimation is performed in a decentralized manner using a BP-based algorithm, if the measured signals can be decomposed into individual parts.

- The estimation of DMC can improve the accuracy of the MPC parameter estimation. In most of the existing works, the DMC is assumed to be homogeneous over the angular domain. A promising direction is to extend these algorithms with a more general inhomogeneous spatially distributed DMC.

- The BP-based sequential detection and estimation algorithm can be extended to a more general inhomogeneous false alarm intensity coping with false alarms resulting from model mismatches in the radio signal such as DMC, or further incorporates correlations between measurements.

- As the number of accessible devices in IoT networks grows tremendously nowadays, information selection schemes which can efficiently select useful measurements from large amount of data are important for the design of low-complexity and robust localization solutions.

References

[1] D. Dardari, E. Falletti and M. Luise, Eds., *Satellite and Terrestrial Radio Positioning Techniques*. Oxford: Academic Press, 2012.

[2] P. Meissner, "Multipath-assisted indoor positioning", PhD thesis, Graz University of Technology, 2014.

[3] H. Wymeersch, G. Seco-Granados, G. Destino, D. Dardari and F. Tufvesson, "5G mmWave positioning for vehicular networks", *IEEE Wireless Commun.*, vol. 24, no. 6, pp. 80–86, 2017.

[4] K. Witrisal, P. Meissner, E. Leitinger, Y. Shen, C. Gustafson, F. Tufvesson, K. Haneda, D. Dardari, A. F. Molisch, A. Conti and M. Z. Win, "High-accuracy localization for assisted living: 5G systems will turn multipath channels from foe to friend", *IEEE Signal Process. Mag.*, vol. 33, no. 2, pp. 59–70, 2016.

[5] K. Witrisal, C. Antón-Haro, J. del Peral-Rosado, R. R. G.S. Granados, E. Leitinger, S. Grebien, T. Wilding, D. Dardari, E. Lohan, H. Wymeersch, J. Floch and et al., "Whitepaper on new localization methods for 5G wireless systems and the internet-of-things", *Technical report, COST Action IC15104 (IRACON)*, 2018.

[6] S. Burgess, Y. Kuang and K. Åström, "ToA sensor network self-calibration for receiver and transmitter spaces with difference in dimension", *Signal Process.*, vol. 107, pp. 33–42, 2015.

[7] M. Z. Win, F. Meyer, Z. Liu, W. Dai, S. Bartoletti and A. Conti, "Efficient multisensor localization for the internet of things: Exploring a new class of scalable localization algorithms", *IEEE Signal Process. Mag.*, vol. 35, no. 5, pp. 153–167, 2018.

[8] K. Witrisal, C. Anton-Haro, S. Grebien, W. Joseph, E. Leitinger, X. Li, J. A. Del Peral-Rosado, D. Plets, J. Vilà-Valls and T. Wilding, "Chapter 9 - localization and tracking", in *Inclusive Radio Communications for 5G and Beyond*, C. Oestges and F. Quitin, Eds., Academic Press, 2021, pp. 253–293.

[9] R. Mautz, "Indoor positioning technologies", Habilitation Thesis, ETH Zürich, 2012.

[10] B. Mager, P. Lundrigan and N. Patwari, "Fingerprint-based device-free localization performance in changing environments", *IEEE J. Sel. Areas Commun.*, vol. 33, no. 11, pp. 2429–2438, 2015.

[11] S. Yiu, M. Dashti, H. Claussen and F. Perez-Cruz, "Wireless RSSI fingerprinting localization", *Signal Process.*, vol. 131, pp. 235 –244, 2017.

[12] S. Tomic, M. Beko and R. Dinis, "RSS-based localization in wireless sensor networks using convex relaxation: Noncooperative and cooperative schemes", *IEEE Trans. Veh. Technol.*, vol. 64, no. 5, pp. 2037–2050, 2015.

[13] A. Zanella, "Best practice in RSS measurements and ranging", *IEEE Commun. Surveys Tuts.*, vol. 18, no. 4, pp. 2662–2686, Fourthquarter 2016.

[14] S. Gezici, Z. Tian, G. Giannakis, H. Kobayashi, A. Molisch, H. Poor and Z. Sahinoglu, "Localization via ultra-wideband radios: A look at positioning aspects for future sensor networks", *IEEE Signal Process. Mag.*, vol. 22, no. 4, pp. 70–84, 2005.

[15] E. Leitinger, "Cognitive indoor positioning and tracking using multipath channel information", PhD thesis, Graz University of Technology, 2015.

[16] R. Di Taranto, S. Muppirisetty, R. Raulefs, D. Slock, T. Svensson and H. Wymeersch, "Location-aware communications for 5G networks: How location information can improve scalability, latency, and robustness of 5G", *IEEE Signal Process. Mag.*, vol. 31, no. 6, pp. 102–112, 2014.

[17] M. Koivisto, A. Hakkarainen, M. Costa, P. Kela, K. Leppanen and M. Valkama, "High-efficiency device positioning and location-aware communications in dense 5G networks", *IEEE Commun. Mag.*, vol. 55, no. 8, pp. 188–195, 2017.

[18] H. Tataria, M. Shafi, A. F. Molisch, M. Dohler, H. Sjöland and F. Tufvesson, *6G wireless systems: Vision, requirements, challenges, insights, and opportunities*, 2021. arXiv: `2008.03213 [eess.SP]`.

[19] C. Gentner, T. Jost, W. Wang, S. Zhang, A. Dammann and U. C. Fiebig, "Multipath assisted positioning with simultaneous localization and mapping", *IEEE Trans. Wireless Commun.*, vol. 15, no. 9, pp. 6104–6117, 2016.

[20] E. Leitinger, F. Meyer, F. Hlawatsch, K. Witrisal, F. Tufvesson and M. Z. Win, "A belief propagation algorithm for multipath-based SLAM", *IEEE Trans. Wireless Commun.*, vol. 18, no. 12, pp. 5613–5629, 2019.

[21] R. Karásek and C. Gentner, "Stochastic data association for multipath assisted positioning using a single transmitter", *IEEE Access*, vol. 8, pp. 46 735–46 752, 2020.

[22] Y. Ge, H. Kim, F. Wen, L. Svensson, S. Kim and H. Wymeersch, "Exploiting diffuse multipath in 5G SLAM", in *IEEE Global Telecommun. Conf. (GLOBECOM)*, 2020, pp. 1–6.

[23] A. F. Molisch, *Wireless Communications*, 2nd. New York, USA: Wiley Publishing, 2011.

[24] E. Leitinger, P. Meissner, C. Rudisser, G. Dumphart and K. Witrisal, "Evaluation of position-related information in multipath components for indoor positioning", *IEEE J. Sel. Areas Commun.*, vol. 33, no. 11, pp. 2313–2328, 2015.

[25] M. Vari and D. Cassioli, "MmWaves RSSI indoor network localization", in *IEEE Int. Conf. on Commun. Workshops (ICC)*, 2014, pp. 127–132.

[26] X. Li, "RSS-based location estimation with unknown pathloss model", *IEEE Trans. Wireless Commun.*, vol. 5, no. 12, pp. 3626–3633, 2006.

[27] S. Thomas, "Estimation of nonlinear dynamic systems: Theory and applications", PhD thesis, Linköpings Universitet, 2006.

[28] Y. Bar-Shalom, T. Kirubarajan and X.-R. Li, *Estimation with Applications to Tracking and Navigation*. New York, NY, USA: Wiley, 2002.

[29] Y. Bar-Shalom, P. K. Willett and X. Tian, *Tracking and data fusion: a handbook of algorithms*. Storrs, CT, USA: Yaakov Bar-Shalom, 2011.

[30] G. Soldi, F. Meyer, P. Braca and F. Hlawatsch, "Self-tuning algorithms for multisensor-multitarget tracking using belief propagation", *IEEE Trans. Signal Process.*, vol. 67, no. 15, pp. 3922–3937, 2019.

[31] E. Mazor, A. Averbuch, Y. Bar-Shalom and J. Dayan, "Interacting multiple model methods in target tracking: A survey", *IEEE Trans. Aerosp. Electron. Syst.*, vol. 34, no. 1, pp. 103–123, 1998.

[32] S. Thrun, W. Burgard and D. Fox, *Probabilistic Robotics*. MIT, 2006.

[33] H. Stewénius, "Gröbner basis methods for minimal problems in computer vision", PhD thesis, Lund University, 2005.

[34] Y. Kuang, S. Burgess, A. Torstensson and K. Åström, "A complete characterization and solution to the microphone position self-calibration problem", in *IEEE Int. Conf. on Acoust., Speech and Signal Process.*, 2013, pp. 3875–3879.

[35] M. A. Fischler and R. C. Bolles, "Random sample consensus: A paradigm for model fitting with applications to image analysis and automated cartography", *Commun. ACM*, vol. 24, no. 6, 381–395, 1981.

[36] S. M. Kay, *Fundamentals of Statistical Signal Processing: Estimation Theory*. Upper Saddle River, NJ, USA: Prentice-H, 1993.

[37] M. Arulampalam, S. Maskell, N. Gordon and T. Clapp, "A tutorial on particle filters for online nonlinear/non-Gaussian Bayesian tracking", *IEEE Trans. on Signal Process.*, vol. 50, no. 2, pp. 174–188, 2002.

[38] B. P. Carlin, N. G. Polson and D. S. Stoffer, "A Monte Carlo approach to nonnormal and nonlinear state-space modeling", *J. Amer. Statist. Assoc.*, vol. 87, 493–500, 1992.

[39] Y. Shen and M. Z. Win, "Fundamental limits of wideband Localization—Part I: A general framework", *IEEE Trans. Inf. Theory*, vol. 56, no. 10, pp. 4956–4980, 2010.

[40] Y. Han, Y. Shen, X.-P. Zhang, M. Z. Win and H. Meng, "Performance limits and geometric properties of array localization", *IEEE Trans. Inf. Theory*, vol. 62, no. 2, pp. 1054–1075, 2016.

[41] T. Wilding, S. Grebien, E. Leitinger, U. Mühlmann and K. Witrisal, "Single-anchor, multipath-assisted indoor positioning with aliased antenna arrays", in *Asilomar-18*, Pacifc Grove, CA, USA, 2018, pp. 525–531.

[42] A. Shahmansoori, G. E. Garcia, G. Destino, G. Seco-Granados and H. Wymeersch, "Position and orientation estimation through millimeter-wave MIMO in 5G systems", *IEEE Trans. Wireless Commun.*, vol. 17, no. 3, pp. 1822–1835, 2018.

[43] P. Tichavsky, C. Muravchik and A. Nehorai, "Posterior Cramer-Rao bounds for discrete-time nonlinear filtering", *IEEE Trans. Signal Process.*, vol. 46, no. 5, pp. 1386–1396, 1998.

[44] D. Cassioli, M. Win and A. Molisch, "The ultra-wide bandwidth indoor channel: From statistical model to simulations", *IEEE J. Sel. Areas Commun.*, vol. 20, no. 6, pp. 1247–1257, 2002.

[45] A. Richter, "Estimation of radio channel parameters: Models and algorithms", PhD thesis, Ilmenau University of Technology, 2005.

[46] J. Salmi, A. Richter and V. Koivunen, "Detection and tracking of MIMO propagation path parameters using state-space approach", *IEEE Trans. Signal Process.*, vol. 57, no. 4, pp. 1538–1550, 2009.

[47] E. Leitinger, S. Grebien, B. H. Fleury and K. Witrisal, "Detection and estimation of a spectral line in MIMO systems", in *Proc. Asilomar-20*, Pacifc Grove, CA, USA, 2020, pp. 1090–1095.

[48] B. H. Fleury, "First- and second-order characterization of direction dispersion and space selectivity in the radio channel", *IEEE Trans. Inf. Theory*, vol. 46, no. 6, pp. 2027–2044, 2000.

[49] A. Paulraj, R. Nabar and D. Gore, *Introduction to Space-Time Wireless Communications*. Cambridge, UK: Cambridge University Press, 2003.

[50] J. Karedal, S. Wyne, P. Almers, F. Tufvesson and A. F. Molisch, "A measurement-based statistical model for industrial Ultra-Wideband channels", *IEEE Trans. Wireless Commun.*, vol. 6, no. 8, pp. 3028–3037, 2007.

[51] E. Leitinger, S. Grebien, X. Li, F. Tufvesson and K. Witrisal, "On the use of MPC amplitude information in radio signal based SLAM", in *Proc. IEEE SSP-18*, Freiburg, Germany, 2018, pp. 633–637.

[52] E. Leitinger, S. Grebien and K. Witrisal, "Multipath-based SLAM exploiting AoA and amplitude information", in *Proc. IEEE ICCW-19*, Shanghai, China, 2019, pp. 1–7.

[53] G. Soldi, F. Meyer, P. Braca and F. Hlawatsch, "Self-tuning algorithms for multisensor-multitarget tracking using belief propagation", *IEEE Trans. Signal Process.*, vol. 67, no. 15, pp. 3922–3937, 2019.

[54] R. Schmidt, "Multiple emitter location and signal parameter estimation", *IEEE Trans. Antennas Propag.*, vol. 34, no. 3, pp. 276–280, 1986.

[55] R. Roy and T. Kailath, "ESPRIT-estimation of signal parameters via rotational invariance techniques", *IEEE Trans. Acoust., Speech, Signal Process.*, vol. 37, no. 7, pp. 984–995, 1989.

[56] M. Haardt, F. Roemer and G. Del Galdo, "Higher-order SVD-based subspace estimation to improve the parameter estimation accuracy in multidimensional harmonic retrieval problems", *IEEE Trans. Signal Process.*, vol. 56, no. 7, pp. 3198–3213, 2008.

[57] B. Ottersten, M. Viberg, P. Stoica and A. Nehorai, "Exact and large sample maximum likelihood techniques for parameter estimation and detection in array processing", in *Radar Array Processing*, Springer, 1993, pp. 99–151.

[58] J. A. Fessler and A. O. Hero, "Space-alternating generalized expectation-maximization algorithm", *IEEE Trans. Signal Process.*, vol. 42, no. 10, pp. 2664–2677, 1994.

[59] B. H. Fleury, M. Tschudin, R. Heddergott, D. Dahlhaus and K. Ingeman Pedersen, "Channel parameter estimation in mobile radio environments using the SAGE algorithm", *IEEE J. Sel. Areas Commun.*, vol. 17, no. 3, pp. 434–450, 1999.

[60] S. Grebien, E. Leitinger, K. Witrisal and B. H. Fleury, "Super-resolution channel estimation including the dense multipath component — A sparse Bayesian approach", 2021, in preperation.

[61] P. Stoica and Y. Selen, "Model-order selection: A review of information criterion rules", *IEEE Signal Process. Mag.*, vol. 21, no. 4, pp. 36–47, 2004.

[62] D. Shutin and B. H. Fleury, "Sparse variational Bayesian SAGE algorithm with application to the estimation of multipath wireless channels", *IEEE Trans. Signal Proces.*, vol. 59, no. 8, pp. 3609–3623, 2011.

[63] M. A. Badiu, T. L. Hansen and B. H. Fleury, "Variational Bayesian inference of line spectra", *IEEE Trans. Signal Process.*, vol. 65, no. 9, pp. 2247–2261, 2017.

[64] T. L. Hansen, B. H. Fleury and B. D. Rao, "Superfast line spectral estimation", *IEEE Trans. Signal Process.*, vol. PP, no. 99, pp. 1–1, 2018.

[65] F. Meyer, P. Braca, P. Willett and F. Hlawatsch, "A scalable algorithm for tracking an unknown number of targets using multiple sensors", *IEEE Trans. Signal Process.*, vol. 65, no. 13, pp. 3478–3493, 2017.

[66] M. Landmann and G. D. Galdo, "Efficient antenna description for MIMO channel modelling and estimation", in *7th European Conf. on Wireless Technol., 2004.*, 2004, pp. 217–220.

[67] D. Shutin and B. Vexler, "Sparse Bayesian learning with dictionary refinement for super-resolution through time", in *Proc. IEEE CAMSAP-17*, 2017, pp. 1–5.

[68] F. Meyer, Y. Park and P. Gerstoft, "Variational Bayesian estimation of time-varying DOAs", in *Proc. IEEE Fusion-20*, Rustenburg, South Africa, 2020, pp. 1–6.

[69] T. Jost, W. Wang, U. Fiebig and F. Perez-Fontan, "Detection and tracking of mobile propagation channel paths", *IEEE Trans. Antennas Propag.*, vol. 60, no. 10, pp. 4875–4883, 2012.

[70] F. Kschischang, B. Frey and H.-A Loeliger, "Factor graphs and the sum-product algorithm", *IEEE Trans. Inf. Theory*, vol. 47, no. 2, pp. 498–519, 2001.

[71] F. Meyer, T. Kropfreiter, J. L. Williams, R. Lau, F. Hlawatsch, P. Braca and M. Z. Win, "Message passing algorithms for scalable multitarget tracking", *Proc. IEEE*, vol. 106, no. 2, pp. 221–259, 2018.

[72] J. Williams and R. Lau, "Approximate evaluation of marginal association probabilities with belief propagation", *IEEE Trans. Aerosp. Electron. Syst.*, vol. 50, no. 4, pp. 2942–2959, 2014.

[73] S. M. Kay, *Fundamentals of Statistical Signal Processing: Detection Theory.* Upper Saddle River, NJ, USA: Prentice Hall, 1998.

[74] F. Meyer, O. Hlinka, H. Wymeersch, E. Riegler and F. Hlawatsch, "Distributed localization and tracking of mobile networks including noncooperative objects", *IEEE Trans. Signal Inf. Process. Net.*, vol. 2, no. 1, pp. 57–71, 2016.

[75] D. Schuhmacher, B.-T. Vo and B.-N. Vo, "A consistent metric for performance evaluation of multi-object filters", *IEEE Trans. Signal Process.*, vol. 56, no. 8, pp. 3447–3457, 2008.

[76] E. Leitinger and F. Meyer, "Data fusion for multipath-based SLAM", in *Proc. Asilomar-20*, Pacifc Grove, CA, USA, 2020, pp. 934–939.

[77] M. Beard, B.-T. Vo and B.-N. Vo, "OSPA$^{(2)}$: Using the OSPA metric to evaluate multi-target tracking performance", in *IEEE Int. Conf. on Control, Automation and Inf. Sciences (ICCAIS)*, 2017, pp. 86–91.

[78] J. Jiang, C. Lin, F. Lin and S. Huang, "ALRD: AoA localization with RSSI differences of directional antennas for wireless sensor networks", in *Int. Conf. on Inform. Soc. (i-Society 2012)*, 2012, pp. 304–309.

[79] Y. Zhao, "Gaussian processes for positioning using radio signal strength measurements", PhD thesis, Linköping University, 2019.

Part II

Included Papers

Paper I

Robust Phase-Based Positioning Using Massive MIMO with Limited Bandwidth

This paper presents a robust phase-based positioning framework using a massive MIMO system. The phase-based distance estimates of MPCs together with other parameters are tracked with an EKF, the state dimension of which varies with the birth-death processes of paths. The RIMAX and the modeling of dense multipath component in the framework further enhance the quality of parameter tracking by providing an accurate initial state and the underlying noise covariance. The tracked MPCs are fed into a time-of-arrival self-calibration positioning algorithm for simultaneous trajectory and environment estimation. Throughout the positioning process, no prior knowledge of the surrounding environment and base station position is needed. The performance is evaluated with the measurement of a 2D complex movement, which was performed in a sports hall with an antenna array with 128 ports as base station using a standard cellular bandwidth of 40 MHz. The positioning result shows that the mean deviation of the estimated user equipment trajectory from the ground truth is 13 cm. In summary, the proposed framework is a promising high-resolution radio-based positioning solution for current and next generation cellular systems.

X. Li, K. Batstone, K. Åström, M. Oskarsson, C. Gustafson, F. Tufvesson,
"Robust Phase-Based Positioning Using Massive MIMO with Limited Bandwidth,"
in *Proc. IEEE 28th Annu. Int. Symp. Pers., Indoor, Mobile Radio Commun. (PIMRC)*, Montreal, Canada, pp. 1-7, Oct. 2017.

1 Introduction

High precision positioning information is a fundamental component of autonomous systems and location-aware applications in mobile devices. To pursue better user experience, these new services and systems keep bringing new challenges to the positioning systems regarding the accuracy, reliability, etc. The Global Positioning System (GPS) works well outdoors, but the accuracy and robustness degrade severely in scenarios like urban canyons and indoor environments due to poor propagation conditions between satellites and user equipment (UE). In contrast, cellular and wireless networks generally have good coverage in those GPS harsh environments. As a substitute or supplement to GPS, much effort has been put into the research of radio-based positioning techniques.

Accurate radio-based positioning commonly relies on geometrical information (distance, delay and angle) of multipath components (MPCs) from the radio channel. The estimation quality of these channel parameters in turn determines the positioning performance. In recent years, positioning with ultra-wideband (UWB) signal has drawn special interest because of the excellent accuracy[1]. The fine delay resolution due to the large bandwidth used makes it possible to resolve MPCs and track the distance changes in centimeter level. However, UWB positioning can only be applied in limited scenarios considering it is a low-power and short-range technique. These shortcomings naturally lead us to the question: is it possible to deliver comparable positioning accuracy by utilizing limited bandwidth in both indoor and outdoor scenarios? We try to solve the puzzle from a channel modelling perspective. The wireless propagation channel is commonly characterized as a sum of specular-like paths and non-resolvable components. Considering that cellular systems are typically operating with a carrier frequency at a few GHz with a bandwidth of 20-40 MHz, the delay resolution is in a scale of 7.5-15 m. However, we notice that the corresponding wavelengths are in the order of centimeters and one wavelength corresponds to a 2π phase shift. For each MPC, the delay and phase are two parameters which vary simultaneously with the wave propagating. If the spatial sampling rate of the radio channel is sufficiently high, i.e., taking a few snapshots within one wavelength movement, it is possible to track the distance change in centimeter level by measuring the phase shift between two consecutive snapshots. With limited bandwidth, the coherence in the delay domain is a challenge for successfully detecting and tracking many MPCs simultaneously. However, the large-scale antenna array could provide additional distinction between MPCs in the spatial domain. The feasibility of the phase-based positioning has been preliminarily proved in [2]. In that work, the phase and delay are assumed to be independent parameters, which are estimated separately and only the phase is used for the movement tracking. Because phase and delay affect each other with wave propagating, and phase estimates

are usually discontinuous in complex environments, there are risks of causing errors or losing tracks.

Motivated by the above analysis, we present a robust phase-based positioning framework in this paper. As a proof-of-concept study, the focus of this work is on demonstrating the possibility of high-resolution radio-based positioning given limited bandwidth and with no prior environment knowledge, rather than on reducing system complexity to implement real-time positioning. Based on some well-established algorithms, e.g,. the Extended Kalman Filter (EKF) [3] and the iterative maximum-likelihood estimation algorithm (RIMAX) [4], the MPC parameters are extracted from the channel measurement data. A time-of-arrival (TOA) self-calibration positioning algorithm, which is a structure-of-motion approach and widely used in image processing, is finally applied for simultaneous UE trajectory and environment estimation. The main contributions are

- The unique mapping between the phase shift and the distance change in our dynamic model leads to a simpler kinematic model by involving less parameters, and the robustness of the system is also improved.
- The performance is evaluated with real measurements of a complex movement. The results prove that the proposed framework provides outstanding MPC tracking and positioning performance even with limited bandwidth.

The paper is structured as follows. In Section II, dynamic propagation channel modeling is discussed. Section III introduces the estimation of path parameters with the EKF. Section IV describes details of the measurement campaign. The MPC tracking results are presented in Section V. Section VI introduces the TOA positioning algorithm and positioning result is presented. Finally, Section VII concludes the paper.

2 Dynamic Propagation Channel Modeling

An observation of the propagation channel, the impulse response $\mathbf{h}_k$ could be decomposed into three non-overlapping components: specular components $\mathbf{h}_{sp}$, dense multipath component (DMC) $\mathbf{h}_{dmc}$ and measurement noise $\mathbf{h}_n$, yielding

$$\mathbf{h}_k = \mathbf{h}_{sp} + \mathbf{h}_{dmc} + \mathbf{h}_n. \tag{1}$$

Positioning relies on the geometrical information from $\mathbf{h}_{sp}$, which is characterized as a superposition of MPCs. The other two components constitute measurement impairments for our purpose.

2.1 Channel Model

In the proposed framework, the double-directional radio channel model [5] is employed to extract the spatial and temporal information of the MPCs from the measured channel transfer function $\mathbf{H} \in \mathbb{C}^{N_s \times N_f \times N_{\mathrm{Tx}} \times N_{\mathrm{Rx}}}$, given as

$$\mathbf{H}(f) = \sum_{l=1}^{L} \boldsymbol{\gamma}_l e^{-j2\pi f \frac{d_l}{c}} \mathbf{G}_{\mathrm{Rx}}(\varphi_{\mathrm{Rx},l}, \theta_{\mathrm{Rx},l}) \mathbf{G}_{\mathrm{Tx}}(\varphi_{\mathrm{Tx},l}, \theta_{\mathrm{Tx},l})^{\mathrm{T}} \tag{2}$$

where N_s, N_f, N_{Tx} and N_{Rx} refer to the number of channel snapshots, frequency sample points, transmit and receive antenna elements. $\mathbf{G}_{\mathrm{Tx}} \in \mathbb{C}^{N_{\mathrm{Tx}} \times N_a N_e}$ and $\mathbf{G}_{\mathrm{Rx}} \in \mathbb{C}^{N_{\mathrm{Rx}} \times N_a N_e}$ describe the far-field antenna response of all antenna array ports at the transmit and receive sides, with respect to the azimuth and elevation angles of departure (AODs) $(\varphi_{\mathrm{Tx},l}, \theta_{\mathrm{Tx},l})$ and angles of arrival (AOAs) $(\varphi_{\mathrm{Rx},l}, \theta_{\mathrm{Rx},l})$ of the lth path. N_a and N_e represent the number of azimuth and elevation angular samples. L is the number of propagation paths. The complex path weight is parametrized as $\boldsymbol{\gamma}_l = \boldsymbol{\alpha}_l e^{j\boldsymbol{\phi}_l}$ where $\boldsymbol{\alpha}_l$ and $\boldsymbol{\phi}_l$ represent the vectors of magnitude and phase, respectively. Instead of using delay, we directly interpret the phase shift as a distance measure, i.e., phase-based distance d_l. The time-variant structural vectors associated with the propagation environment geometry and the path weights are defined as

$$\boldsymbol{\mu} = [\boldsymbol{d}^{\mathrm{T}} \quad \boldsymbol{\varphi}_{\mathrm{Tx}}^{\mathrm{T}} \quad \boldsymbol{\theta}_{\mathrm{Tx}}^{\mathrm{T}} \quad \boldsymbol{\varphi}_{\mathrm{Rx}}^{\mathrm{T}} \quad \boldsymbol{\theta}_{\mathrm{Rx}}^{\mathrm{T}}], \tag{3}$$

$$\boldsymbol{\alpha} = [\boldsymbol{\alpha}_{\mathrm{HH}}^{\mathrm{T}} \quad \boldsymbol{\alpha}_{\mathrm{HV}}^{\mathrm{T}} \quad \boldsymbol{\alpha}_{\mathrm{VH}}^{\mathrm{T}} \quad \boldsymbol{\alpha}_{\mathrm{VV}}^{\mathrm{T}}], \tag{4}$$

$$\boldsymbol{\phi} = [\boldsymbol{\phi}_{\mathrm{HH}}^{\mathrm{T}} \quad \boldsymbol{\phi}_{\mathrm{HV}}^{\mathrm{T}} \quad \boldsymbol{\phi}_{\mathrm{VH}}^{\mathrm{T}} \quad \boldsymbol{\phi}_{\mathrm{VV}}^{\mathrm{T}}] \tag{5}$$

where $\{\mathrm{HH}, \mathrm{HV}, \mathrm{VH}, \mathrm{VV}\}$ represent four polarimetric transmissions, e.g., HV means horizontal-to-vertical transmission.

2.2 Dynamic Model

A discrete white noise acceleration model is used to describe the changes of propagation parameters [6], with the assumption that the motion and underlying noise process of different parameters are uncorrelated. The discrete-time state transition equation is expressed as

$$\mathbf{x}_k = \mathbf{F}\mathbf{x}_{k-1} + \boldsymbol{v}_k \tag{6}$$

where $\boldsymbol{v}_k$ is state noise following zero mean normal distribution with the variance matrix $\mathbf{Q}$. The state transition matrix $\mathbf{F}$ is formulated as

$$\mathbf{F} = \begin{bmatrix} \mathbf{I}_5 & \mathbf{I}_5 & \mathbf{0} & \mathbf{0} \\ \mathbf{0} & \mathbf{I}_5 & \mathbf{0} & \mathbf{0} \\ \mathbf{0} & \mathbf{0} & \mathbf{I}_4 & \mathbf{0} \\ \mathbf{0} & \mathbf{0} & \mathbf{0} & \mathbf{I}_4 \end{bmatrix}. \tag{7}$$

The state vector at snapshot k is

$$\boldsymbol{x}_k = [\boldsymbol{\mu}^{\mathrm{T}} \quad \Delta\overline{\boldsymbol{\mu}}^{\mathrm{T}} \quad \boldsymbol{\alpha}^{\mathrm{T}} \quad \boldsymbol{\phi}^{\mathrm{T}}] \tag{8}$$

where the vector $\Delta\overline{\boldsymbol{\mu}}$ contains the velocities of the structural parameters in $\boldsymbol{\mu}$. Here, we intentionally decouple the phase evolution from the MPC tracking to preserve the unique mapping between the phase shift and the distance d_l. The evolution of the state vector from one snapshot to the next is modelled as

$$\begin{aligned} \boldsymbol{\mu}_k &= \boldsymbol{\mu}_{k-1} + \Delta\overline{\boldsymbol{\mu}}_{k-1} + \boldsymbol{v}_{\boldsymbol{\mu}_k} \\ \Delta\boldsymbol{\mu}_k &= \Delta\overline{\boldsymbol{\mu}}_{k-1} + \boldsymbol{v}_{\Delta\overline{\boldsymbol{\mu}}_k} \\ \boldsymbol{\alpha}_{i,k} &= \boldsymbol{\alpha}_{i,k-1} + \boldsymbol{v}_{\boldsymbol{\alpha}_k} \\ \boldsymbol{\phi}_{i,k} &= \boldsymbol{\phi}_{i,k-1} + \boldsymbol{v}_{\boldsymbol{\phi}_k} \end{aligned} \tag{9}$$

where $\boldsymbol{v}_{[\,.\,]}$ denotes the state noise vector. The selection and tuning of process noise variance are very important especially for the narrowband case, because the orthogonality is not tightly held between close-by MPCs. Small variance may lead to smooth but slow tracking, and some small movements might be missed. Large variance enables quick response to non-smooth movements like sharp turns, but with high risk of phase slip. Hence, a trade-off is needed. Here, we follow the guideline that the value of $\boldsymbol{v}_{\Delta\overline{\boldsymbol{\mu}}_k}$ should be in the same order as the maximum acceleration magnitude [6]. The complex path weight is assumed to be slowly varying and to account for larger changes in the propagation processes, e.g., reflection, scattering, etc. Reinitializations of $\boldsymbol{\gamma}_l$ are sometimes needed in the tracking process [3].

3 Propagation Path Parameters Estimation

As shown in the proposed framework (Fig. 1), the MPC parameters are estimated with an EKF. We realize that an accurate initial state estimation is a prerequisite for the fast convergence and accurate tracking in the EKF. In this work, the RIMAX algorithm is applied to the first snapshot for the initial estimates of MPC parameters and noise covariance [4]. Besides, the state dimension adjustment is performed alongside the EKF iteration.

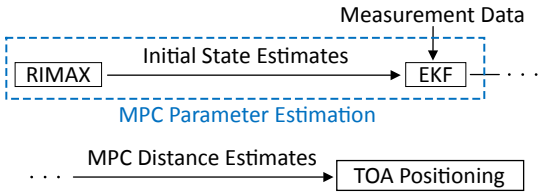

Figure 1: Proposed positioning framework.

3.1 Initialization with RIMAX

Firstly, MPC detection is performed with a successive path cancellation framework, where the maximum-likelihood (ML)-based 3D-grid approach is used. Each detected path is further optimized locally. This detection framework uses oversampling to enhance delay and angle resolution, therefore closely located MPCs could be detected.

After subtracting the specular-like components, the residual is considered as the colored noise process with a covariance matrix $\mathbf{R}$, which consists of the measurement noise following a Gaussian distribution $\mathcal{N}(0,\, \sigma^2\mathbf{I})$, and the DMC. The DMC is modelled stochastically and the covariance matrix has a shifted Kronecker structure, which is computationally efficient especially when a large antenna array is used [7]. The full noise covariance matrix is given by

$$\mathbf{R} = \mathbf{R}_{\mathrm{R}} \otimes \mathbf{R}_{\mathrm{T}} \otimes \mathbf{R}_f + \sigma^2\mathbf{I} \tag{10}$$

where $\mathbf{R}_f \in \mathbb{C}^{N_f \times N_f}$ is the covariance matrix in the frequency domain with Toeplitz structure. We observed that the power delay profile of the residual shows a spatially white characteristic at the base station (BS) side, therefore the covariance matrices $\mathbf{R}_{\mathrm{T}} \in \mathbb{C}^{N_{\mathrm{Tx}} \times N_{\mathrm{Tx}}}$ and $\mathbf{R}_{\mathrm{R}} \in \mathbb{C}^{N_{\mathrm{Rx}} \times N_{\mathrm{Rx}}}$, which describe the angular distributions at the transmit and receive sides respectively, are assumed as identity matrices in this implementation.

The structural vectors of MPCs and the parameter set of DMC are optimized alternatingly with the Levenberg-Marquardt algorithm and the ML-Gauss-Newton algorithm, respectively. The details can be found in [4].

3.2 Extended Kalman Filter

The path parameters are tracked with an EKF [3]. Due to the non-linear channel model used, we firstly linearize the data model $\mathbf{h}_{sp}(\mathbf{x})$ by taking the first-order partial derivatives over the state vector, which gives the Jacobian matrix as

$$\mathbf{D}(\mathbf{x}) = \frac{\partial \mathbf{h}_{sp}(\mathbf{x})}{\partial \mathbf{x}^{\mathrm{T}}}. \tag{11}$$

The first-order and the second-order partial derivative of the log-likelihood function, i.e., the score function $\mathbf{q}$ and the Fisher information matrix $\mathbf{J}$, are also needed in the iteration. These are computed as

$$\mathbf{q}(\mathbf{h}|\mathbf{x},\mathbf{R}) = 2 \cdot \Re\left\{\mathbf{D}^{\mathrm{H}}(\mathbf{x})\mathbf{R}^{-1}(\mathbf{h}-\mathbf{h}_{sp}(\mathbf{x}))\right\}, \tag{12}$$

$$\mathbf{J}(\mathbf{x},\mathbf{R}) = 2 \cdot \Re\left\{\mathbf{D}^{\mathrm{H}}(\mathbf{x})\mathbf{R}^{-1}\mathbf{D}(\mathbf{x})\right\}. \tag{13}$$

The procedure of the EKF is summarized as

$$\hat{\mathbf{x}}_{(k|k-1)} = \mathbf{F}\hat{\mathbf{x}}_{(k-1|k-1)}, \tag{14}$$

$$\mathbf{P}_{(k|k-1)} = \mathbf{F}\mathbf{P}_{(k-1|k-1)}\mathbf{F}^{\mathrm{T}} + \mathbf{Q}, \tag{15}$$

$$\mathbf{P}_{(k|k)} = (\mathbf{P}^{-1}_{(k|k-1)} + \mathbf{J})^{-1}, \tag{16}$$

$$\Delta\hat{\mathbf{x}}_{(k)} = \mathbf{P}_{(k|k)}\mathbf{q}, \tag{17}$$

$$\hat{\mathbf{x}}_{(k|k)} = \hat{\mathbf{x}}_{(k|k-1)} + \Delta\hat{\mathbf{x}}_{(k)} \tag{18}$$

where $\mathbf{P}_{(k|k-1)}$ and $\mathbf{P}_{(k|k)}$ are the filter error covariances denoting the prediction and update uncertainties of the state vector, respectively.

3.3 State Dimension Adjustment

In channel sounding, the number of co-existing propagation paths varies over time. The detection and elimination (death-birth) of paths are assumed to be statistically independent and performed alongside the EKF iteration with two separate steps. The first step is to remove unreliable paths by evaluating the relative variance of each path [4], defined as

$$\mathrm{var}_r = \sum_{p=1}^{N_p} \frac{\mathrm{var}_{\gamma_p}}{\mid \gamma_p \mid^2} < \varepsilon_r \tag{19}$$

where γ_p is the magnitude of the estimated path weight of polarization $p \in \{\mathrm{HH}, \mathrm{HV}, \mathrm{VH}, \mathrm{VV}\}$ and var_{γ_p} is the estimation error variance extracted from the filtering error covariance matrix. Intuitively, var_r should be smaller than 0 dB, which indicates that the certainty of the magnitude estimation should be larger than its uncertainty. A reliability check is performed every 30 snapshots and only paths with var_r smaller than the threshold ε_r are preserved in the state for further tracking. Hence, the MPC lifetime is here defined as the time duration that the relative variance of a MPC is below a given threshold, which is geometry-independent in this sense. The next step is to detect new paths. We limit the number of newly initialized MPCs in each snapshot to control the model complexity and reduce the interference between coherent paths [4].

Figure 2: Overview of the measurement area in the sports hall, Medicon Village, Lund, Sweden. Room dimension is around 20 m × 36 m × 7.5 m.

4 Measurement Campaign

This framework is designed for the multiple-input multiple-output (MIMO) case where angular information is available from both sides. However, UEs with single or few antennas are more common in practice and the lack of AODs makes the path estimation and tracking a harder problem. To test the performance of the proposed framework in a real but controlled environment, a measurement campaign was performed in a large sports hall with the RUSK LUND channel sounder. Fig. 2 shows an overview of the measurement area. A cylindrical antenna array with 128 ports (Fig. 3a) is used as BS at the Rx side, the center of which is 1.42 m above the ground. A conical monopole omnidirectional antenna (Fig. 3b) is used to represent a UE at the Tx side. The distance between UE and BS is around 17 m and line-of-sight (LOS) conditions apply. The transfer functions were recorded at a center frequency around 2.7 GHz and with a signal bandwidth of 40 MHz. To avoid large variation of path parameters, especially the phase slip between two consecutive snapshots, the spatial sampling rate of the wireless channel was sufficiently high. In total, 6000 channel snapshots were collected in 19.7 s. The Tx was placed on a tripod and manually moved to write the "**Lund**" letters in a $2\,\mathrm{m}^3$ space. Meanwhile, an optical coordinate measuring machine (CMM) system (Fig. 3b) was used to capture the UE motion with accuracy down to millimeter, which acts as the ground truth for performance analysis.

5 MPC Tracking Results and Analysis

This section focuses on the performance of MPC tracking results. Fig. 4 shows the tracked propagation distances of MPCs from the EKF implementation. It could be observed that the LOS component with the distance around 17 m is tracked steadily since the beginning. About 2 m apart from the LOS is the ground reflection path which is tracked shortly in the end. Besides, many

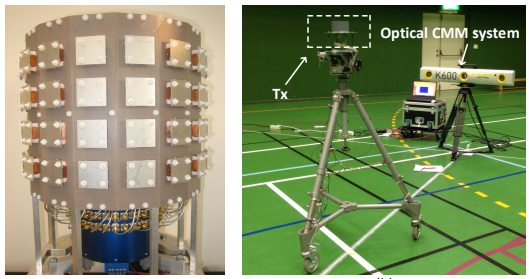

Figure 3: (a) The cylindrical antenna array at the Rx side; (b) The conical monopole omnidirectional antenna at the Tx side and the optical CMM system.

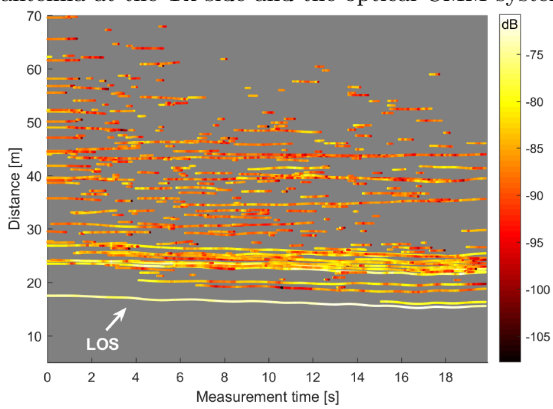

Figure 4: The tracked absolute propagation distances of MPCs. The color indicates the power in dB scale.

other MPCs with long lifetimes could also be observed in the range of 20-70 m propagation distance. For better evaluation of the tracking performance, we zoom into the LOS component and compare the distance estimates with the ground truth. The black dashed line denotes the distance estimates from EKF. The red solid line in Fig. 5 is the true propagation distance of the LOS component which is calculated based on the 3D coordinates from the optical system and the coordinates of the BS. The two curves are manually time synchronized for better comparison. As shown from the comparison, the EKF could catch all the movements of the UE, even some fine ones and sharp turns. The estimates have a good match with the ground truth most of the time, besides some deviations observed after 16 s. The biggest deviation from the ground truth is about 8 cm. The MPCs located in the same delay bin as the LOS component are correlated and they show degraded quality of tracking.

We further analyzed the angular-power distribution of the tracked MPCs.

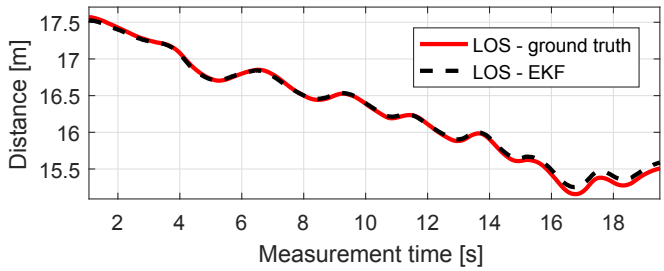

Figure 5: Performance evaluation of the tracked LOS component.

The MPCs are plotted in a 3D coordinate system based on the estimates of distances and azimuth/elevation AOAs without considering the interaction order. The top view (Fig. 6a) shows that the tracked MPCs are distributed over the entire azimuth domain and paths are intensively detected in the similar direction as the LOS component. From the vertical distribution (Fig. 6b), a few paths are observed from the ground or at similar height as the BS, but most of the paths are from the complex ceiling structure of the room, e.g., the metal beams of the ceiling in Fig. 2. Those complex room structures would bring additional uncertainties to the distance estimates. Moreover, the similar behaviour of the long-tracked MPCs in the angular domain may become a challenge for 3D positioning, for which the MPCs with sparse angles are preferred. However, it is interesting to see the performance in the real but non-ideal case.

Ghost components around some high-power MPCs are observed during the tracking. They usually have similar angles and propagation distances as the dominant MPCs close by and experience very short lifetimes. These components are mainly generated due to power compensation in the estimation procedure and do not have actual physical meaning, therefore they are not considered in the following positioning step.

6 Positioning Algorithm and Results

As seen in Fig. 4 and Fig. 5, most of the MPCs can only be observed during fractions of the measurement duration and the estimation quality is not consistent during the whole tracking process for an individual MPC, i.e., there are outliers in the data for which the errors are substantial. Therefore, the question here is how to optimize the positioning performance in the presence of missing data and outliers, which is a highly non-convex problem.

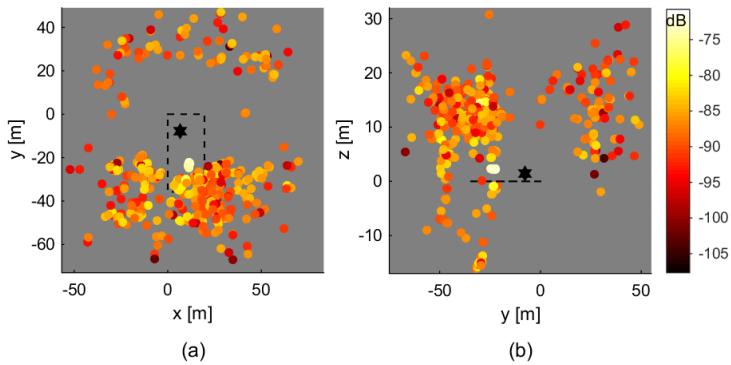

Figure 6: 3D plot of the tracked MPCs. Black dashed line denotes the room geometry and the hexagram represents the location of BS. The top-view plot (a) shows how tracked MPCs distributed in the azimuth plane. The side-view plot (b) shows the vertical distribution.

6.1 Mathematical Formulation of Geometrical Problem

A few assumptions are firstly given for modeling the geometrical problem. The tracked MPCs from EKF are numbered with $i = 1, 2, \ldots, m$, where $i = 1$ represents the LOS component. These paths are assumed to originate from n UE positions $\mathbf{Tx}_j \in \mathbb{R}^3$, $j = 1, \ldots, n$. The BS is stationary at position $\mathbf{Rx}_1 \in \mathbb{R}^3$. To formulate the measured distances, we assume that the tracked MPCs are reflected from planar surfaces and mirror the BS, i.e., each MPC can be considered as being received at a mirrored BS position $\mathbf{Rx}_i$. The distance estimates are only given for a set I of (i, j) combinations due to missing data. As it will be shown, the errors of outliers in the distance estimates are substantial. However, for a large amount of distance estimates the errors are fairly small (in the order of a few centimeters). The measured distances are then

$$d_{ij} = \|\mathbf{Rx}_i - \mathbf{Tx}_j\|_2 + \epsilon_{ij}, \forall (i, j) \in I \tag{20}$$

where $\epsilon_{ij} \in N(0, \sigma_{inl}^2)$ for $(i, j) \in I_{inl}$ and ϵ_{ij} are drawn from an unknown distribution for $(i, j) \in I_{outl}$. This distribution has a significantly larger variance. One useful approach is to minimize the negative log likelihood. To simplify the problem, we assume that the negative log likelihood for the outliers is a constant, i.e., each outlier gives the same penalty. In this way the problem becomes an optimization problem.

Problem 1 *(Time-of-Arrival Self-Calibration) Given absolute distance estimates $d_{ij} \forall (i, j) \in I$, find the inlier set $I_{inl} \subset I$, the UE positions $\mathbf{Tx}_j \in \mathbb{R}^3$ and the mirrored BS positions $\mathbf{Rx}_i \in \mathbb{R}^3$ that solves the following optimization*

problem

$$\min_{I_{inl},\mathbf{Rx}_i,\mathbf{Tx}_j} \sum_{(i,j)\in I_{inl}} (d_{ij} - \|\mathbf{Rx}_i - \mathbf{Tx}_j\|_2)^2 + \sum_{(i,j)\in I_{outl}} C \tag{21}$$

where $I_{outl} = I \setminus I_{inl}$. This is a highly non-linear, non-convex optimization problem. The problem changes character if both $\mathbf{Tx}_j$ and $\mathbf{Rx}_j$ span 3D, or either one of them or both are restricted to a plane or a line as shown in [8]. The problem is ill-defined if there is too little data. For planar problems we require $m \geq 3, n \geq 3$, [9]. For 3D problems more data is needed, typically $m \geq 4, n \geq 6$, [10]. Algorithms for solving Problem 1 using hypothesize and test paradigm are presented in [11].

6.2 Estimation of the Distance Estimates Error Distribution and Mirrored BS Positions

The modified version of Problem 1 where say the transmitter positions $\mathbf{Tx}_j$ are known, is a substantially better conditioned problem. In this case, we can solve for

$$\min_{I_{inl},\mathbf{Rx}_i} \sum_{i|(i,j)\in I_{inl}} (d_{ij} - \|\mathbf{Rx}_i - \mathbf{Tx}_j\|_2)^2 + \sum_{i|(i,j)\in I_{outl}} C \tag{22}$$

independently for each mirrored BS position $\mathbf{Rx}_i$. This can be done by using Random Sample Consensus (RANSAC) [12].

The resulting residuals $d_{ij} - \|\mathbf{Rx}_i - \mathbf{Tx}_j\|_2$ can be used to empirically assess properties of the error distribution. We selected those paths that were longer than 500 snapshots from the tracked $m = 282$ MPCs, which gave a set of 50 MPCs. For each of them, we estimated the mirrored BS position using RANSAC (to obtain I_{inl}) followed by the non-linear optimization of (22) (to obtain $\mathbf{Rx}_i$). In total these 50 tracked MPCs gave us 103 480 distance samples, i.e., approximately 2000 each. Of these 77 490 were considered to be inliers. This gives us an estimated inlier ratio of 75%. The standard deviation of the inlier residuals is 4.6 cm.

Using the ground truth UE positions $\mathbf{Tx}_j$, we robustly initialized the LOS component receiver position, i.e., $\mathbf{Rx}_1$ as well as all the mirrored BS positions of MPCs. This was followed by non-linear refinement. The reconstructed BS position $\mathbf{Rx}_1$ along with some examples of the mirrored BS positions are shown in Fig. 7. It could be observed that the estimated BS position is located close to the true position, and the mirrored BS positions look plausible.

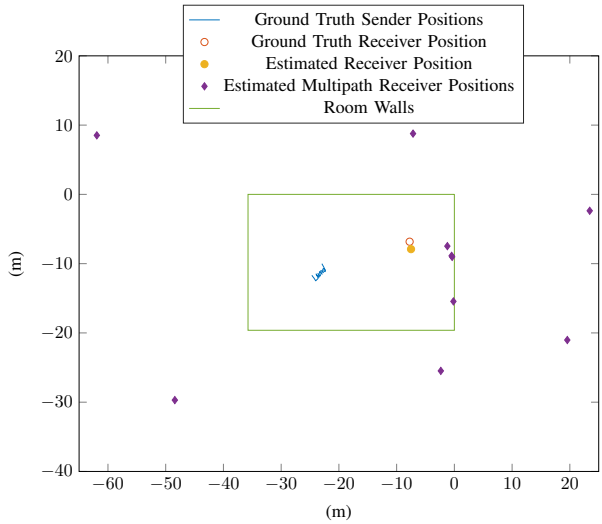

Figure 7: Robust estimation of BS position and mirrored BS positions using the ground truth UE positions.

6.3 Estimation of UE Positions

We now target the full version of Problem 1, where the UE positions, the BS position and all the mirrored BS positions are unknown. To make this highly complex estimation problem tractable, two assumptions are made here. Firstly, $\mathbf{Tx}_j$ are assumed to be constrained in a plane, because the UE was moved approximately in a plane in the measurement. Secondly, we assume that we know which distance estimates are inliers. This problem is then proceeded by splitting the whole dataset in a number of smaller segments in time, which results in 117 segments of length 100 snapshots with 50 snapshots overlap between adjacent segments. For each segment, we robustly initialized both $\mathbf{Rx}_j$ and $\mathbf{Tx}_j$ using minimal solvers and RANSAC [8] based only on the distance estimates from the EKF. This is followed by non-linear optimization. The different solutions from the 117 segments were then registered into a common coordinate system using the overlap between segments. The estimated UE positions (in red) is shown in Fig. 8. Also shown (in dashed grey) is the ground truth. The two trajectories have been rigidly registered to each other. It could be observed that the estimated trajectory shows a clear "**Lund**"-word pattern, with all the fine movements details caught. However, the overall shape is stretched along the diagonal direction, which results in a larger deviation from the ground truth especially in the beginning and the end. The largest deviation of the estimated UE position from the ground truth happens at the sharp turn of "**L**", which is 26 cm, and the overall mean deviation is 13 cm. The main

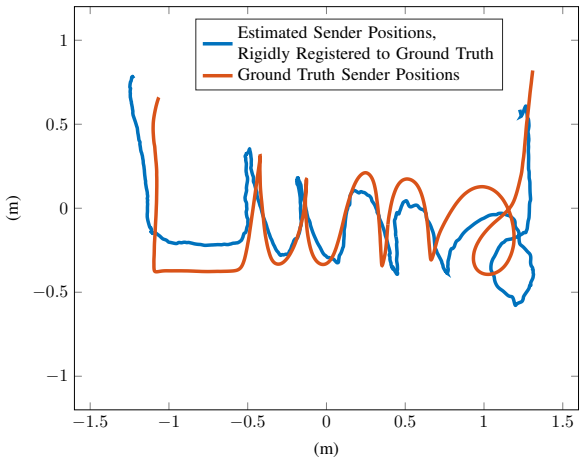

Figure 8: The ground truth (dashed-grey) and the estimated UE positions (red). Note that this estimation is only based on the distance estimates and no ground truth UE positions are used.

reason of the stretch problem is that many MPCs are tracked in a similar direction as the LOS component, as shown in Fig. 6. The similar behaviour of MPCs in the angular domain will cause the estimated UE positions to be scaled or projected.

7 Summary and Conclusion

In this paper, we introduced and showed a proof-of-concept for a robust phase-based positioning framework using massive MIMO. MPC parameters, e.g., phase-based distance and angle, are estimated and tracked with an EKF. A TOA self-calibration positioning algorithm is then used for trajectory estimation. The positioning results of a 2D complex movement measurement show that the proposed positioning framework could achieve outstanding positioning performance even with standard cellular bandwidths. Besides, no prior knowledge of the surroundings is needed, so the framework could be easily applied in different environments given that there are enough many scatterers present. To sum up, phase-based positioning using massive MIMO is a promising high-resolution positioning solution for current and next generation cellular systems.

8 Acknowledgements

The authors would like to thank Erik Leitinger, Jose Flordelis, Joao Vieira and Christian Nelson for helping with the measurements. We would also like to acknowledge the support from Björn Olofsson with the motion capture system. This work was supported by the Swedish Research Council VR and the strategic research area ELLIIT.

References

[1] E. Leitinger, P. Meissner, M. Lafer and K. Witrisal, "Simultaneous localization and mapping using multipath channel information", in *IEEE Int. Conf. on Commun. Workshop (ICCW)*, 2015, pp. 754–760.

[2] M. Zhu, J. Vieira, Y. Kuang, K. Åström, A. F. Molisch and F. Tufvesson, "Tracking and positioning using phase information from estimated multipath components", in *IEEE Int. Conf. on Commun. Workshop (ICCW)*, 2015, pp. 712–717.

[3] J. Salmi, A. Richter and V. Koivunen, "Detection and tracking of MIMO propagation path parameters using state-space approach", *IEEE Trans. Signal Process.*, vol. 57, no. 4, pp. 1538–1550, 2009.

[4] A. Richter, "Estimation of radio channel parameters: Models and algorithms", PhD thesis, Technischen Universität Ilmenau, Fakultät für Elektrotechnik und Informationstechnik, 2005.

[5] A. F. Molisch, *Wireless Communications*, 2nd. New York, USA: Wiley Publishing, 2011.

[6] Y. Bar-Shalom and X.-R. Li, *Estimation with Applications to Tracking and Navigation*. New York, NY, USA: John Wiley & Sons, Inc., 2001.

[7] J. Salmi, "Contributions to measurement-based dynamic MIMO channel modeling and propagation parameter estimation", PhD thesis, Helsinki University of Technology, Finland, 2009.

[8] S. Burgess, Y. Kuang and K. Åström, "ToA sensor network self-calibration for receiver and transmitter spaces with difference in dimension", *Signal Process.*, vol. 107, pp. 33–42, 2015.

[9] H. Stewénius, "Gröbner basis methods for minimal problems in computer vision", PhD thesis, Lund University, 2005.

[10] Y. Kuang, S. Burgess, A. Torstensson and K. Åström, "A complete characterization and solution to the microphone position self-calibration problem", in *IEEE Int. Conf. on Acoust., Speech and Signal Process.*, 2013, pp. 3875–3879.

[11] K. Batstone, M. Oskarsson and K. Åström, "Robust time-of-arrival self calibration with missing data and outliers", in *24th European Signal Process. Conf. (EUSIPCO)*, 2016, pp. 2370–2374.

[12] M. A. Fischler and R. C. Bolles, "Random sample consensus: A paradigm for model fitting with applications to image analysis and automated cartography", *Commun. ACM*, vol. 24, no. 6, pp. 381–395, 1981.

Paper II

Massive MIMO-based Localization and Mapping Exploiting Phase Information of Multipath Components

In this paper, we present a robust multipath-based localization and mapping framework that exploits the phases of specular multipath components (MPCs) using a massive multiple-input multiple-output (MIMO) array at the base station. Utilizing the phase information related to the propagation distances of the MPCs enables the possibility of localization with extraordinary accuracy even with limited bandwidth. The specular MPC parameters along with the parameters of the noise and the dense multipath component (DMC) are tracked using an extended Kalman filter (EKF), which enables to preserve the distance-related phase changes of the MPC complex amplitudes. The DMC comprises all non-resolvable MPCs, which occur due to finite measurement aperture. The estimation of the DMC parameters enhances the estimation quality of the specular MPCs and therefore also the quality of localization and mapping. The estimated MPC propagation distances are subsequently used as input to a distance-based localization and mapping algorithm. This algorithm does not need prior knowledge about the surrounding environment and base station position. The performance is demonstrated with real radio-channel measurements using an antenna array with 128 ports at the base station side and a standard cellular signal bandwidth of 40 MHz. The results show that high accuracy localization is possible even with such a low bandwidth.

X. Li, E. Leitinger, M. Oskarsson, K. Åström and F. Tufvesson,
"Massive MIMO-based Localization and Mapping Exploiting Phase Information of Multipath Components,"
IEEE Trans. Wireless Commun., vol. 18, no. 9, pp. 4254–4267, Sept. 2019.

1 Introduction

High precision localization is a key enabler for future location-aware applications expected in future 5G communication networks [1]. Therefore, localization techniques that can offer the necessary accuracy in complex environments, e.g., dense urban environments or indoors, are strongly needed. Massive multiple-input-multiple-output (MIMO) transmission schemes [2], [3] are one possibility to counteract localization degradation due to harsh multipath propagation in dense urban environments and indoors, even though only small signal bandwidth is used.

1.1 State of the Art

Achieving the required level of accuracy robustly is still elusive in environments that are characterized by harsh multipath channel conditions. Therefore, most existing localization approaches supporting multipath channels either use sensing technologies that mitigate multipath effects [4]–[6] or fuse information from multiple information sources [7]–[10]. Fingerprint-based approaches actually exploit the diversity of multipath channels by matching position-labeled channel measurements with the acquired measurements at the positions of interest [11], [12]. Similarly, this can be achieved by using machine learning methods with the additional capability of interpolation between the position-labeled channel training measurements [13], [14]. However, site-specific training phases require a lot of accurate position-labeled channel measurements and may lead to performance degradation in dynamic environments.

Multipath-assisted localization algorithms [15]–[18] exploit position-related information contained in the specular multipath propagation components (MPCs) that can be associated to the local geometry, which actually turns the multipath effect into an advantage. MPCs due to specular reflections at flat surfaces are modeled by virtual anchors (VAs), which are mirror images of the physical anchors (PAs), i.e., base station [19]. By associating the estimated MPC parameters to VAs, these VAs can be used as additional PAs for location estimation. In recent years, many works that use wideband/ultra-wideband (UWB) signals have shown the potential of multipath-based positioning [20], tracking [21], [22] and simultaneous localization and mapping (SLAM) [23]–[26] with accuracy on a centimeter level. The works [27]–[29] use cooperation amongst agents to enhance multipath-assisted localization performance in infrastructure-limited scenarios.

However, all these multipath-assisted algorithms have in common that they require accurate extraction of location-related parameters of MPCs (i.e., distances/delays and angles). The estimation quality of MPC parameters in turn determines the localization performance, while, good resolvability between MPCs is a prerequisite for accurate estimation. However, using only limited

bandwidth systems leads to low resolvability of MPCs in the delay domain, especially in dense multipath environments. Utilizing large-scale antenna arrays extends signal processing alternatives from the time-frequency domain to also include the spatial domain, and therefore helps to resolve closely spaced MPCs by exploiting the spatially sparse structure of the multipath channel [30]. In [17], [18], the theoretically achievable localization performance given as the Cramér-Rao lower bound (CRLB) on the position and orientation estimation error for millimeter-wave massive MIMO systems is presented. The results in there show the large localization performance improvement when position-related information of MPCs is estimated with a massive MIMO system. Considering that cellular systems are typically operating at a few GHz with a bandwidth of 20-40 MHz, the corresponding resolution of one time sample is only 7.5-15 m. However, since the phase of MPCs is connected to the carrier frequency and this lies in the GHz region for typical radio systems, centimeter accuracy can be achieved if the phase is properly exploited as for example in global navigation satellite systems [31] or terrestrial radio systems [32]. If the spatial sampling rate of the radio channel is sufficiently high, i.e., recording a few snapshots within one wavelength movement, it is possible to track the distance change on centimeter level by measuring the phase shift between measurements at two consecutive time instances.

1.2 Contributions and Organization of the Paper

In this work, a multipath-assisted localization and mapping framework is presented that exploits the phase information of individual MPCs by using a massive single-input multiple-output (SIMO)[1] radio system. As shown in Fig. 2, the framework is composed of two consecutive steps: (i) Using an extended Kalman filter (EKF) [33], which is initialized with the iterative maximum-likelihood estimation algorithm (RIMAX) [34], the dispersion parameters, i.e., the delays/ distances and angle-of-arrivals (AoAs) of the specular MPCs, the noise and dense multipath component (DMC) parameters are estimated from channel measurements; (ii) The MPC distances estimates are subsequently used as input in the localization step[2]. A distance-based algorithm is applied that simultaneously estimates the mobile agent positions and VA/PA positions[3]. Both synthetic and real channel measurements are used when demonstrating the performance of MPC parameter estimation, followed by an in-depth statistical

[1] We consider a simpler scenario here, where the mobile agent is equipped with a single omnidirectional antenna. However, the framework can be easily extended to MIMO setup.

[2] In the SIMO setup, the angular information is available at PA side. The angular information is exploited by the channel estimator for better resolvability of individual MPCs, however, in this work the AoAs are not used for localization.

[3] Since these estimates are only relative w.r.t. a global coordinate system, we register them to the coordinate system of the measured geometric groundtruth of the mobile agents' movement trajectory.

analysis of MPC parameters in terms of lifetime, signal-to-interference-plus-noise ratio (SINR)[4], etc. The performance of the localization algorithm is evaluated with the same real channel measurements.

The main contributions are summarized as:

- We present a novel MIMO channel estimation and tracking algorithm that tightly couples the tracked MPC distances to the phase change of the MPC complex amplitudes from one measurement snapshot to the next. With this, it is possible to estimate the MPC distances far beyond the signal bandwidth dependent accuracy.
- We analyze the dynamic behaviour and statistical distributions of the estimated MPC parameters and connect them to the localization potential.
- We use the estimated MPC distances from real channel measurements to show that radio-based localization in harsh multipath environments is possible even using only low signal bandwidth by exploiting a massive MIMO system.

Parts of this paper were published in [35], where the feasibility of the phase-based localization using standard cellular bandwidths was demonstrated. This paper presents more insights into the framework as well as more in-depth analysis of the channel estimation results with both synthetic and real measurements.

The rest of the paper is structured as follows: Section 2 introduces the radio signal model and the multipath-based localization and mapping problem. Section 3 and 4 present EKF-based channel estimation and tracking algorithm and distance-based localization and mapping algorithm. The numerical results and analysis are reported in Section 5. Finally, Section 6 concludes the paper.

Mathematical notations: Boldface upper case letters represent matrices. Boldface lower case letters denote column vectors. Superscripts $^{\mathrm{T}}$, * and $^{\mathrm{H}}$ denote matrix transpose, complex conjugation and Hermitian transpose, respectively. The Kronecker product and Khatri-Rao product operators are denoted with $\otimes$ and $\lozenge$, respectively. $\|\cdot\|$ is the Euclidean norm. $|\cdot|$ represents the absolute value. $\mathrm{card}(\cdot)$ denotes the cardinality of a set. $\hat{\mathbf{A}}$ denotes an estimate of $\mathbf{A}$. $\boldsymbol{I}_{[\cdot]}$ represents identity matrix with dimension denoted in the subscript $[\cdot]$. $\mathrm{diag}(\boldsymbol{a})$ denotes a diagonal matrix with the vector $\boldsymbol{a}$ being the diagonal entries. The operation $\mathrm{toep}(\boldsymbol{a}, \boldsymbol{a}^{\mathrm{H}})$ constructs a Hermitian Toeplitz matrix with vectors $\boldsymbol{a}$ and $\boldsymbol{a}^{\mathrm{H}}$ being the first column and the first row.

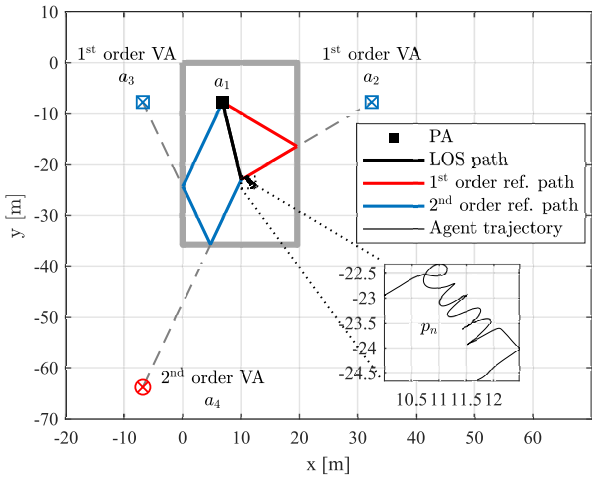

Figure 1: Floor plan of the sports hall in Medicon village, Lund, Sweden. The bold grey line represents the surrounding walls. Besides, three examples of the 1st order and 2nd order geometrically expected VAs, as well as the corresponding reflection paths from the mobile agent to the physical anchor (PA) are given. The groundtruth trajectory of the mobile agent is given by the letters "**Lund**" in a $2\,\mathrm{m}^2$ area, as shown in the zoom-in sub-plot.

2 Problem Formulation

Multipath-based localization utilizes geometrical information contained in specular MPCs—delays/distances, angles of departure (AoDs) and angles of arrival (AoAs)—estimated from received radio signals [15]. Each estimated specular MPC, which originates from a reflection on planar surfaces, can be either associated with a PA or with one of the VAs, which represent the mirrored positions of the PA w.r.t. the planar surfaces. These VAs can be used as additional PAs for localization. From now on a PA or VAs are collectively referred to as features. Fig. 1 shows the floor plan of the indoor environment in which the measurement campaign was performed, together with the positions of the PA and of three exemplary VAs with their corresponding reflection paths. We consider the case that the mobile agent acts as a transmitter with unknown time-varying positions $\boldsymbol{p}_n \in \mathbb{R}^{3\times 1}$, $n = 2, \ldots, N$. The feature positions are denoted with $\boldsymbol{a}_m \in \mathbb{R}^{3\times 1}$, $m \in \mathcal{M} = \{1, \ldots, M\}$, where the PA represents a receiver at a static but unknown position $\boldsymbol{a}_1$, and the positions[5] of the geomet-

[4]The SINR can be interpreted as a reliability measure of estimated MPC parameters and is directly tied to the CRLB of multipath-based localization [15].

[5]The coordinate of the position is given in the 3D Cartesian coordinate system. For a feature position, $\boldsymbol{a}_m = [x_m \quad y_m \quad z_m]^{\mathrm{T}}$, and for the mobile agent position $\boldsymbol{p}_n = [x_n \quad y_n \quad z_n]^{\mathrm{T}}$.

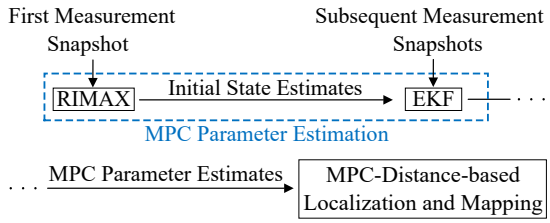

Figure 2: Block diagram of the proposed multipath-based localization and mapping framework.

rically expected VAs are denoted as $\boldsymbol{a}_m$, $m = 2, \ldots, M$. The feature positions are fixed over time since the PA is static. A specular MPC is consistently associated with a feature for the duration that this feature is visible at the agent position. Those visible features at each agent position $\boldsymbol{p}_n$ are called expected features, with the positions given as $\boldsymbol{a}_l \in \mathbb{R}^{3\times 1}$, $l \in \mathcal{L}_n$, and $\mathcal{L}_n$ is a subset of $\mathcal{M}$, i.e., $\mathcal{L}_n \subseteq \mathcal{M}$. The number of expected features $L_n = \mathrm{card}(\mathcal{L}_n)$ is unknown and time-varying, and it depends on the visibility at each agent position. Besides, the floor plan of the surrounding environment is assumed as unknown, which means feature positions $\boldsymbol{a}_l$ are unknown.

Fig. 2 shows the block diagram of the proposed multipath-based localization and mapping framework. First, the MPC parameters are estimated using an EKF-based channel estimator and tracking algorithm. Considering that an accurate initial state estimate is a prerequisite for the fast convergence and accurate tracking in the EKF, and the initialization step should avoid bringing too many artifacts into the initial state vector, the RIMAX algorithm is applied at time $n = 1$ for the initial estimates of MPC parameters and noise covariance [34]. The estimated MPC distances are subsequently used in the localization and mapping algorithm.

2.1 Radio Signal Model

The baseband signal $\boldsymbol{y}_n$ in frequency domain received by the PA at time n is modeled as

$$\boldsymbol{y}_n = \boldsymbol{s}_n + \boldsymbol{w}_{\mathrm{dmc},n} + \boldsymbol{w}_n \quad \in \mathbb{C}^{N_\mathrm{f} N_\mathrm{Tx} N_\mathrm{Rx} \times 1}, \tag{1}$$

where the first term comprises specular MPCs and the second and third terms represent DMC and additive white Gaussian noise, respectively. We assume time-synchronization between the mobile agent and the PA, and time synchronization between VAs is automatically achieved as they arise due to reflections. The values N_f, N_Tx and N_Rx refer to the number of frequency sample points, transmit and receive antenna elements, respectively. Since $N_\mathrm{Tx} = 1$ for a SIMO setup, we ignore N_Tx in the dimension notations of matrices/vectors from now

on.

Specular MPCs

$\boldsymbol{s}_n = [\boldsymbol{s}_{f_1,n}^{\mathrm{T}} \cdots \boldsymbol{s}_{f_{N_\mathrm{f}},n}^{\mathrm{T}}]^{\mathrm{T}}$ is obtained by sampling the continuous response $\boldsymbol{s}_n(f)$ in the frequency domain at time n, where f_i with $i = 1, \ldots, N_\mathrm{f}$ is the frequency samples in the domain $\{-\frac{N_\mathrm{f}-1}{2N_\mathrm{f}}B_\mathrm{w}, \ldots, \frac{N_\mathrm{f}-1}{2N_\mathrm{f}}B_\mathrm{w}\}$ and B_w is the signal bandwidth. $\boldsymbol{s}_n(f) = \sum_{l\in\mathcal{L}_n} \boldsymbol{s}_{l,n}(f)$ comprises L_n specular MPCs. The contribution of each MPC is given by $\boldsymbol{s}_{l,n}(f) = s_{\mathrm{sig},n}(f)\boldsymbol{h}_{l,n}(f)$, where $s_{\mathrm{sig},n}(f)$ is the transmitted baseband signal response, and $\boldsymbol{h}_{l,n}(f) \in \mathbb{C}^{N_{\mathrm{Rx}}\times 1}$ is a frequency domain representation of the MPC's channel impulse response, given as [36]

$$\boldsymbol{h}_{l,n}(f) = \boldsymbol{B}_{\mathrm{Rx}}(\varphi_{l,n}, \theta_{l,n})\boldsymbol{\Gamma}_{l,n}\boldsymbol{B}_{\mathrm{Tx}}^{\mathrm{T}}\mathrm{e}^{-j2\pi(f+f_c)\tau_{l,n}}, \tag{2}$$

where f_c is the carrier frequency, $\tau_{l,n}$ represents the propagation delays of the lth MPC. The matrices $\boldsymbol{B}_{\mathrm{Tx}} \in \mathbb{C}^{1\times 2}$ and $\boldsymbol{B}_{\mathrm{Rx}}(\cdot,\cdot) \in \mathbb{C}^{N_{\mathrm{Rx}}\times 2}$ describe the far-field complex antenna responses of the omnidirectional antenna at the transmit side, and of the antenna array at the receive side w.r.t. the AoAs in elevation and azimuth domain, respectively. The delay of the specular MPC indexed by l is proportional to the distance between the agent and the PA or between the agent and the VAs. That is $\tau_{l,n} = \|\boldsymbol{p}_n - \boldsymbol{a}_l\|/c = d_{l,n}/c$, where $d_{l,n}$ is the propagation distance and c is the speed of light. We note that similar geometrical expressions can be extended to the azimuth and elevation AoAs $(\varphi_{l,n}, \theta_{l,n})$, respectively. The parameters of each specular MPC are comprised in the vector $\boldsymbol{\mu}_{l,n} = [d_{l,n} \quad \varphi_{l,n} \quad \theta_{l,n}] \in \mathbb{R}^{3\times 1}$. The complex path weight matrix $\boldsymbol{\Gamma}_{l,n} \in \mathbb{C}^{2\times 2}$ accounts for the frequency independent attenuation and phase change, given as

$$\boldsymbol{\Gamma}_{l,n} = \begin{bmatrix} \gamma_{\mathrm{HH},l,n} & \gamma_{\mathrm{VH},l,n} \\ \gamma_{\mathrm{HV},l,n} & \gamma_{\mathrm{VV},l,n} \end{bmatrix}. \tag{3}$$

The individual polarimetric complex path weights of the matrix are given by $\gamma_{\mathrm{p},l,n} = \alpha_{\mathrm{p},l,n}e^{j\phi_{\mathrm{p},l,n}}$, where $\alpha_{\mathrm{p},l,n}$ and $\phi_{\mathrm{p},l,n}$ represent the magnitude and phase, respectively. The subscript $\mathrm{p} \in \{\mathrm{HH}, \mathrm{HV}, \mathrm{VH}, \mathrm{VV}\}$ indicates the four polarimetric transmission coefficients (as for example HV indexes the horizontal-to-vertical transmission coefficient).

Noise process

The second term in (1), $\boldsymbol{w}_{\mathrm{dmc},n}$ denotes the multiplication of the signal spectrum with the DMC defined by the covariance matrix $\boldsymbol{R}_{\mathrm{dmc},n} \in \mathbb{C}^{N_\mathrm{f}N_{\mathrm{Rx}}\times N_\mathrm{f}N_{\mathrm{Rx}}}$, and the third term in (1), $\boldsymbol{w}_n$ denotes the measurement noise which is assumed circularly symmetric complex Gaussian noise with covariance matrix

$\boldsymbol{R}_{\mathrm{w},n} = \sigma^2_{\mathrm{w},n}\boldsymbol{I}_{N_\mathrm{f}N_\mathrm{Rx}} \in \mathbb{C}^{N_\mathrm{f}N_\mathrm{Rx}\times N_\mathrm{f}N_\mathrm{Rx}}$. The noise covariance matrix is given by $\boldsymbol{R}_n = \boldsymbol{R}_{\mathrm{w},n} + \boldsymbol{R}_{\mathrm{dmc},n}$.

The estimation of the noise parameters directly for the noise covariance matrix $\boldsymbol{R}_n$ is computationally very expensive, especially for the massive MIMO setup. Using the narrowband assumption, a Kronecker decomposition of the noise covariance matrix $\boldsymbol{R}_n$ can be applied [34], [37]. The noise covariance matrix then reduces to

$$\boldsymbol{R}_n = \boldsymbol{R}_{\mathrm{Rx},n} \otimes \boldsymbol{R}_{\mathrm{f},n}(\boldsymbol{x}_{\mathrm{dmc},n}) + \sigma^2_{\mathrm{w},n}\boldsymbol{I}_{N_\mathrm{f}N_\mathrm{Rx}}, \tag{4}$$

where $\boldsymbol{R}_{\mathrm{f},n} \in \mathbb{C}^{N_\mathrm{f}\times N_\mathrm{f}}$ denotes the covariance matrix of DMC in frequency domain, which has Toeplitz structure and is given as

$$\boldsymbol{R}_{\mathrm{f},n}(\boldsymbol{x}_{\mathrm{dmc},n}) = \mathrm{toep}\left(\boldsymbol{\kappa}(\boldsymbol{x}_{\mathrm{dmc},\boldsymbol{n}}), \boldsymbol{\kappa}(\boldsymbol{x}_{\mathrm{dmc},\boldsymbol{n}})^\mathrm{H}\right). \tag{5}$$

Here, $\boldsymbol{\kappa}(\boldsymbol{x}_{\mathrm{dmc},\boldsymbol{n}})$ is the sampled power delay spectrum (PDS) in frequency domain characterized by $\boldsymbol{x}_{\mathrm{dmc},n} = [\alpha_{\mathrm{dmc},n} \quad \beta_{\mathrm{dmc},n} \quad \tau_{\mathrm{on},n}]^\mathrm{T}$. The DMC is modeled with an exponentially decaying power profile in the delay domain, where $\alpha_{\mathrm{dmc},n}$ is the power at the onset delay $\tau_{\mathrm{on},n}$, and $\beta_{\mathrm{dmc},n}$ is the normalized coherence bandwidth of DMC (detailed parameters can be found in [34, Section 2.5]). Furthermore, it is assumed that the DMC is spatially uncorrelated at the receiver side, therefore the covariance matrix in the angular domain $\boldsymbol{R}_{\mathrm{Rx},n} = \boldsymbol{I}_{N_\mathrm{Rx}}$.

Signal Parameter Estimation

Given the radio signal observations $\boldsymbol{y} = [\boldsymbol{y}_1^\mathrm{T} \cdots \boldsymbol{y}_N^\mathrm{T}]^\mathrm{T}$, the EKF-based parametric channel estimation algorithm, described in Section 3, provides $\widetilde{K}$ continuously estimated MPCs and noise parameters. Those MPCs are indexed by $\tilde{k}$ with $\tilde{k} \in \widetilde{\mathcal{K}} = \{1, \ldots, \widetilde{K}\}$, and each of them is consistently associated with an estimated feature position $\boldsymbol{a}_{\tilde{k}}$ for the duration of its lifetime (described in Section 3.2). The estimated MPCs have different lifetimes, which means they are observed during different fractions of the measurement time. At time n, a subset of MPCs indexed by $k \in \mathcal{K}_n$, $\mathcal{K}_n \subseteq \widetilde{\mathcal{K}}$ are estimated, and the estimated parameters of each MPC and the noise parameters are given as

$$\hat{\boldsymbol{\mu}}_{k,n} = [\hat{d}_{k,n} \quad \hat{\varphi}_{k,n} \quad \hat{\theta}_{k,n}]^\mathrm{T} \in \mathbb{R}^{3\times 1} \tag{6}$$

$$\hat{\boldsymbol{x}}_{\mathrm{noise,n}} = [\hat{\boldsymbol{x}}^\mathrm{T}_{\mathrm{dmc},n} \quad \hat{\sigma}_{\mathrm{w},n}]^\mathrm{T} \in \mathbb{R}^{4\times 1}. \tag{7}$$

Ideally, the number of estimated MPCs at time n, i.e., $K_n = \mathrm{card}(\mathcal{K}_n)$, should be equal to L_n. However, during the estimation process, miss detection of specular MPCs and false alarm which leads to clutter components might happen. Hence, K_n is time-varying and it can be equal to, or larger/smaller than

L_n. In the next section, the estimated parameters are provided as input to the localization and mapping algorithm.

2.2 Localization and Mapping Problem

In this work, we only use the estimated distances $\hat{d}_{k,n}$ of the MPCs within the localization and mapping algorithm. The estimates are corrupted by noise and possible biases, so the measurement model of the localization algorithm is given as

$$\hat{d}_{k,n} = \|\boldsymbol{p}_n - \boldsymbol{a}_k\| + \epsilon_{k,n}, \forall (k,n) \in I, \tag{8}$$

where I of all (k,n) indexing combinations represents the set of all the estimated MPCs. Distance estimates which are considered to be inliers have a known distribution $\epsilon_{k,n} \sim \mathcal{N}(0, \sigma^2_{\text{inl}})$ for $(k,n) \in I_{\text{inl}}$. Outliers (comprise false alarms and specular MPCs with large errors) represent distance estimates $\hat{d}_{k,n}$ that follow an unknown distribution of $\epsilon_{k,n}$ for $(k,n) \in I_{\text{outl}}$ with typically much larger variance. One useful approach is to minimize the negative log-likelihood. To simplify the problem, we assume that the negative log-likelihood for the outliers is a constant C, i.e., each outlier has the same penalty. In this way the problem becomes an optimization problem.

Problem 2 *(Localization and Mapping) Given absolute distance estimates $\hat{d}_{k,n} \forall\ (k,n) \in I$, find the inlier set $I_{inl} \subset I$, the estimated mobile agent positions $\hat{\boldsymbol{p}}_n\ \forall\ n \in \{1,\ldots,N\}$ and the estimated feature positions $\hat{\boldsymbol{a}}_k \forall\ (k,n) \in I_{inl}$ that solves the following optimization problem*

$$\min_{\substack{I_{inl}, \boldsymbol{p}_n, \boldsymbol{a}_k \\ \forall n, \forall k}} \sum_{(k,n) \in I_{inl}} (\hat{d}_{k,n} - \|\boldsymbol{p}_n - \boldsymbol{a}_k\|)^2 + \sum_{(k,n) \in I_{outl}} C, \tag{9}$$

where $I_{\text{outl}} = I \backslash I_{\text{inl}}$. The estimated feature positions $\hat{\boldsymbol{a}}_k$ are also assumed to be fixed over time since the PA is static. This is a highly non-linear, non-convex optimization problem. The problem changes character if both $\hat{\boldsymbol{p}}_n$ and $\hat{\boldsymbol{a}}_k$ span 3D, or either one of them or both are restricted to a plane or a line as shown in [38]. The problem is ill-defined if there is too little data. For planar problems we require $K_n \geq 3, N \geq 3$, [39]. For 3D problems more data is needed, typically $K_n \geq 4, N \geq 6$ or $K_n \geq 5, N \geq 5$, [40].

In the following two sections, we introduce the framework as shown in Fig. 2. At first, the EKF channel estimation and tracking algorithm is presented, followed by the MPC-distances-based localization and mapping algorithm.

3 EKF-based Channel Estimation Algorithm

The MPC parameters are firstly initialized with the RIMAX algorithm, and then an EKF is adopted for continuous channel parameters tracking. It should be noted that instead of estimating the absolute phase of each MPC at each time instance, we track the continuous phase changes between consecutive snapshots. Given a few snapshots being taken within one wavelength movement of the mobile agent, a phase change from 0 to 2π is translated into a distance change $\Delta d_{l,n}$ from 0 to λ. The two parameters $\boldsymbol{\phi}_{\mathrm{p},l,n}$ and $d_{l,n}$ in (2) are both phase related, but the estimates $\hat{\boldsymbol{\phi}}_{\mathrm{p},l,n}$ are usually non-continuous in complex propagating environments, which leads to a high risk of phase slip, i.e., a jump of an integer number of phase cycles. Therefore, $\hat{\boldsymbol{\phi}}_{\mathrm{p},l,n}$ of each MPC is locked to the initial estimate provided by the RIMAX algorithm, the evolution $\Delta\hat{\boldsymbol{\phi}}_{\mathrm{p},l,n}$ however is not involved in the tracking process using the EKF. In detail, we exclude $\Delta\boldsymbol{\phi}_{\mathrm{p},l,n}$ from the state space model and the corresponding derivative $\frac{\partial \boldsymbol{s}(\hat{\boldsymbol{x}}_n)}{\partial(\Delta\hat{\boldsymbol{\phi}}_n)^{\mathrm{T}}}$ from the Jacobian matrix (Section 3.2). In this way, we ensure the unique mapping between the phase shift and the distance change $\Delta d_{l,n}$.

3.1 State Space and Measurement Model

The state space vector of L_n MPC parameters at time n is given by

$$\boldsymbol{x}_n = [\boldsymbol{\mu}_n^{\mathrm{T}} \quad \Delta\boldsymbol{\mu}_n^{\mathrm{T}} \quad \boldsymbol{\alpha}_n^{\mathrm{T}} \quad \boldsymbol{\phi}_n^{\mathrm{T}}]^{\mathrm{T}} \in \mathbb{R}^{14L_n\times 1}\,, \tag{10}$$

where the geometry-related parameter are stacked into

$$\boldsymbol{\mu}_n = [\boldsymbol{d}_n^{\mathrm{T}} \quad \boldsymbol{\varphi}_n^{\mathrm{T}} \quad \boldsymbol{\theta}_n^{\mathrm{T}}]^{\mathrm{T}} \in \mathbb{R}^{3L_n\times 1}, \tag{11}$$

and the vector $\Delta\boldsymbol{\mu}_n \in \mathbb{R}^{3L_n\times 1}$ contains the change rates of the MPC parameters contained in $\boldsymbol{\mu}_n$. The magnitudes and phases of the according complex MPC weights are stacked into

$$\boldsymbol{\alpha}_n = [\boldsymbol{\alpha}_{\mathrm{HH},n}^{\mathrm{T}} \quad \boldsymbol{\alpha}_{\mathrm{HV},n}^{\mathrm{T}} \quad \boldsymbol{\alpha}_{\mathrm{VH},n}^{\mathrm{T}} \quad \boldsymbol{\alpha}_{\mathrm{VV},n}^{\mathrm{T}}]^{\mathrm{T}} \in \mathbb{R}^{4L_n\times 1}, \tag{12}$$

$$\boldsymbol{\phi}_n = [\boldsymbol{\phi}_{\mathrm{HH},n}^{\mathrm{T}} \quad \boldsymbol{\phi}_{\mathrm{HV},n}^{\mathrm{T}} \quad \boldsymbol{\phi}_{\mathrm{VH},n}^{\mathrm{T}} \quad \boldsymbol{\phi}_{\mathrm{VV},n}^{\mathrm{T}}]^{\mathrm{T}} \in \mathbb{R}^{4L_n\times 1}. \tag{13}$$

Each sub-vector on the right side of (11), (12) and (13) has the dimension of $(L_n\times 1)$, as for example, $\boldsymbol{d}_n = [d_{1,n} \cdots d_{L_n,n}]^{\mathrm{T}}$, $\boldsymbol{\alpha}_{\mathrm{HH},n} = [\alpha_{\mathrm{HH},1,n} \cdots \alpha_{\mathrm{HH},L_n,n}]^{\mathrm{T}}$ and $\boldsymbol{\phi}_{\mathrm{HH},n} = [\phi_{\mathrm{HH},1,n} \cdots \phi_{\mathrm{HH},L_n,n}]^{\mathrm{T}}$.

The state transition model defined by a discrete white noise acceleration model [41, Section 6.3.2] describes the time evolution of the state vector. With the assumption that the motion and underlying noise process of different MPC parameters are uncorrelated, the discrete-time state transition model is given

as

$$\boldsymbol{x}_n = \boldsymbol{F}\boldsymbol{x}_{n-1} + \boldsymbol{v}_n, \tag{14}$$

where $\boldsymbol{v}_n$ is state noise vector following zero mean normal distribution with the variance matrix $\boldsymbol{Q}$. The state transition matrix $\boldsymbol{F}^1 \in \mathbb{R}^{14\times 14}$ of a single MPC is formulated as

$$\boldsymbol{F}^1 = \begin{bmatrix} \boldsymbol{I}_3 & \boldsymbol{I}_3\Delta T & \boldsymbol{0} & \boldsymbol{0} \\ \boldsymbol{0} & \boldsymbol{I}_3 & \boldsymbol{0} & \boldsymbol{0} \\ \boldsymbol{0} & \boldsymbol{0} & \boldsymbol{I}_4 & \boldsymbol{0} \\ \boldsymbol{0} & \boldsymbol{0} & \boldsymbol{0} & \boldsymbol{I}_4 \end{bmatrix}, \tag{15}$$

where ΔT is the channel sampling duration. The variance matrix $\boldsymbol{Q}^1 \in \mathbb{R}^{14\times 14}$ of a single MPC is defined as

$$\boldsymbol{Q}^1 = \begin{bmatrix} \boldsymbol{Q}^1_{\boldsymbol{\mu}} & \boldsymbol{0} & \boldsymbol{0} \\ \boldsymbol{0} & \boldsymbol{Q}^1_{\boldsymbol{\alpha}} & \boldsymbol{0} \\ \boldsymbol{0} & \boldsymbol{0} & \boldsymbol{Q}^1_{\boldsymbol{\phi}} \end{bmatrix}. \tag{16}$$

The sub-matrix $\boldsymbol{Q}^1_{\boldsymbol{\mu}} \in \mathbb{R}^{6\times 6}$ related to the structural vector $\hat{\boldsymbol{\mu}}$ is given as

$$\boldsymbol{Q}^1_{\boldsymbol{\mu}} = \mathrm{diag}(\boldsymbol{q}_{\Delta\boldsymbol{\mu}}) \otimes \begin{bmatrix} \frac{1}{4}\Delta T^4 & \frac{1}{2}\Delta T^3 \\ \frac{1}{2}\Delta T^3 & \Delta T^2 \end{bmatrix}, \tag{17}$$

where $\boldsymbol{q}_{\Delta\boldsymbol{\mu}} = [q_d \quad q_\varphi \quad q_\theta]^{\mathrm{T}} \in \mathbb{R}^{3\times 1}$ and the square root of each entry in the vector denotes the acceleration of corresponding structural parameter. The sub-matrices related to α and ϕ are given as $\boldsymbol{Q}^1_{\boldsymbol{\alpha}} = q_\alpha \boldsymbol{I}_4$ and $\boldsymbol{Q}^1_{\boldsymbol{\phi}} = q_\phi \boldsymbol{I}_4$. It should be noted that the evolutions $\Delta\alpha$ and $\Delta\phi$ are not involved in the state space model. However, we assign small values to the variances q_α and q_ϕ to account for slow variations of α and ϕ during the propagation processes in the free space. The same variances are assumed for different polarimetric transmission coefficients. The selection and tuning process of the noise variance are very important especially for the narrowband case, because the orthogonality is not tightly held between close-by MPCs [42]. Small variance may lead to smooth but slow tracking, and some small movements might be missed. Large variance enables quick response to non-smooth movements like sharp turns, but leads to high risk of phase slip. Hence, a trade-off is needed. Here, we follow the guideline that the value of $\sqrt{q_{[\cdot]}}$ should be in the same order as the maximum acceleration magnitude [41]. The extension of the matrices (15) and (16) to the multipath case is done with a Kronecker operation as $\boldsymbol{F} = \boldsymbol{F}^1 \otimes \boldsymbol{I}_{L_n}$ and $\boldsymbol{Q} = \boldsymbol{Q}^1 \otimes \boldsymbol{I}_{L_n}$ [33].

The corresponding linearized measurement model, which describes the non-

linear mapping from MPC parameters to channel measurement, is defined as

$$\boldsymbol{y}_n = \boldsymbol{s}(\boldsymbol{x}_n) + \boldsymbol{r}_n, \tag{18}$$

where $\boldsymbol{r}_n$ contains the measurement noise with covariance matrix $\boldsymbol{R}_n$ defined in Section 2.1 and $\boldsymbol{s}(\boldsymbol{x}_n)$ represents the non-linear mapping from the MPC parameters to the specular observation vector described in (39). The first-order Taylor series approximation can be used for linearizing the model $\boldsymbol{s}(\boldsymbol{x}_n)$, and the linearized measurement matrix is represented with the Jacobian matrix $\boldsymbol{J}_n$ described in (31).

3.2 MPC Parameters Tracking Using an EKF

The MPC parameters are tracked using an EKF similar to [33] starting from time $n = 2$, where the state vector at time $n = 1$ and the estimated noise covariance matrix $\hat{\boldsymbol{R}}_n$ are provided by the RIMAX algorithm (see Section 3.3). The filtered posterior state vector $\hat{\boldsymbol{x}}_n$ is given by

$$\hat{\boldsymbol{x}}_n = [\hat{\boldsymbol{\mu}}_n^{\mathrm{T}} \quad \Delta\hat{\boldsymbol{\mu}}_n^{\mathrm{T}} \quad \hat{\boldsymbol{\alpha}}_n^{\mathrm{T}} \quad \hat{\boldsymbol{\phi}}_n^{\mathrm{T}}]^{\mathrm{T}} \in \mathbb{R}^{14K_n \times 1}, \tag{19}$$

where the sub-vectors are given as

$$\hat{\boldsymbol{\mu}}_n = [\hat{\boldsymbol{d}}_n \quad \hat{\boldsymbol{\varphi}}_n \quad \hat{\boldsymbol{\theta}}_n]^{\mathrm{T}} \in \mathbb{R}^{3K_n \times 1}, \tag{20}$$

$$\hat{\boldsymbol{\alpha}}_n = [\hat{\boldsymbol{\alpha}}_{\mathrm{HH},n} \quad \hat{\boldsymbol{\alpha}}_{\mathrm{HV},n} \quad \hat{\boldsymbol{\alpha}}_{\mathrm{VH},n} \quad \hat{\boldsymbol{\alpha}}_{\mathrm{VV},n}]^{\mathrm{T}} \in \mathbb{R}^{4K_n \times 1}, \tag{21}$$

$$\hat{\boldsymbol{\phi}}_n = [\hat{\boldsymbol{\phi}}_{\mathrm{HH},n} \quad \hat{\boldsymbol{\phi}}_{\mathrm{HV},n} \quad \hat{\boldsymbol{\phi}}_{\mathrm{VH},n} \quad \hat{\boldsymbol{\phi}}_{\mathrm{VV},n}]^{\mathrm{T}} \in \mathbb{R}^{4K_n \times 1}. \tag{22}$$

Prediction Step

The prior state vector $\hat{\boldsymbol{x}}_n^-$ and the prior filter error covariances matrix $\mathcal{P}_n^-$ given measurements up until time $n-1$, are respectively given by

$$\hat{\boldsymbol{x}}_n^- = \boldsymbol{F}\hat{\boldsymbol{x}}_{n-1}, \tag{23}$$

$$\mathcal{P}_n^- = \boldsymbol{F}\mathcal{P}_{n-1}\boldsymbol{F}^{\mathrm{T}} + \boldsymbol{Q}. \tag{24}$$

Measurement Update Step

The measurement at time n is used to update the predicted state vector $\hat{\boldsymbol{x}}_n^-$ and the corresponding matrix $\mathcal{P}_n^-$, resulting into the posterior covariance matrix $\mathcal{P}_n$

and posterior state vector $\hat{\boldsymbol{x}}_n$, obtained by

$$\mathcal{P}_n = (\boldsymbol{I}_{14K_n} + \boldsymbol{K}_n \boldsymbol{D}_n)\mathcal{P}_n^-, \tag{25}$$

$$\Delta\hat{\boldsymbol{x}}_n = \mathcal{P}_n \boldsymbol{q}_n, \tag{26}$$

$$\hat{\boldsymbol{x}}_n = \hat{\boldsymbol{x}}_n^- + \Delta\hat{\boldsymbol{x}}_n\,, \tag{27}$$

where the Kalman gain matrix $\boldsymbol{K}_n$ is formulated as

$$\boldsymbol{K}_n = \mathcal{P}_n^- \boldsymbol{D}_n^{\mathrm{H}} (\boldsymbol{D}_n \mathcal{P}_n^- \boldsymbol{D}_n^{\mathrm{H}} + \hat{\boldsymbol{R}}_n)^{-1}, \tag{28}$$

and $\boldsymbol{q}_n \in \mathbb{R}^{14K_n \times 1}$ is the score function and $\boldsymbol{D}_n \in \mathbb{R}^{14K_n \times 14K_n}$ represents the Fisher information matrix, which are the first-order and the second-order partial derivatives of the negative log-likelihood function, respectively. The score function $\boldsymbol{q}_n$ and the Fisher information matrix $\boldsymbol{D}_n$ are given by

$$\boldsymbol{q}_n = 2\Re\left\{\boldsymbol{J}_n^{\mathrm{H}} \hat{\boldsymbol{R}}_n^{-1} (\boldsymbol{y}_n - \boldsymbol{s}(\hat{\boldsymbol{x}}_n^-))\right\}, \tag{29}$$

$$\boldsymbol{D}_n = 2\Re\left\{\boldsymbol{J}_n^{\mathrm{H}} \hat{\boldsymbol{R}}_n^{-1} \boldsymbol{J}_n\right\}\,, \tag{30}$$

where the Jacobian matrix $\boldsymbol{J}_n \in \mathbb{C}^{N_{\mathrm{f}} N_{\mathrm{Rx}} \times 14K_n}$ represents the the first-order partial derivatives of the linearized signal vector $\boldsymbol{s}(\hat{\boldsymbol{x}}_n^-)$, i.e.,

$$\boldsymbol{J}_n = \frac{\partial \boldsymbol{s}(\hat{\boldsymbol{x}}_n^-)}{\partial (\hat{\boldsymbol{x}}_n^-)^{\mathrm{T}}}. \tag{31}$$

State Dimension Adjustment

During the channel measurements, the number of tracked MPCs may vary over time. The birth and death processes of MPCs are assumed to be statistically independent and therefore the state dimension adjustment is performed alongside with the EKF.

Birth of MPC Potentially new MPCs are detected in the initialization process using the SAGE algorithm as described in Section 3.3, and the estimated covariance matrix $\hat{\boldsymbol{R}}_n$ at time n is used to estimate the complex weight with (37) given below.

Death of MPC The posterior covariance matrix $\mathcal{P}_n$ comprises the uncertainties of the state vector after update with measurement. Using the contained variances of the complex MPC weights, a reliability measure of a MPC is calculated and used to adjust the dimension of the state space vector $\hat{\boldsymbol{x}}_n$, i.e., to control the death of MPCs. At first, the SINR of each MPC [34] is calculated,

i.e.,

$$\mathrm{SINR}_{k,n} = \sum_{\mathrm{p}} \frac{|\,\hat{\gamma}^{\mathrm{p}}_{k,n}\,|^2}{v^{\mathrm{p}}_{k,n}}\,, \tag{32}$$

where $|\hat{\gamma}^{\mathrm{p}}_{k,n}|$ is the magnitude of the estimated MPC weight for polarization $\mathrm{p} \in \{\mathrm{HH}, \mathrm{HV}, \mathrm{VH}, \mathrm{VV}\}$ and $v^{\mathrm{p}}_{k,n}$ is the estimated variance of MPC weight. A MPC is considered as unreliable if the SINR is below a predefined detection threshold ε_{r}, i.e., $\mathrm{SINR}_{k,n} < \varepsilon_{\mathrm{r}}$, and therefore it is removed from the state vector. Hence, the MPC lifetime is here defined as the time duration that the SINR of a MPC is above a given threshold, which to some extended is geometry-independent. An intuitive choice for the detection threshold ε_{r} is 0 dB.

Reinitalization of complex weights

Even though the complex weights of the MPCs are assumed to vary only slowly in free space propagation, larger changes are expected due to small scale fading in the propagation processes, e.g., reflection, scattering, etc. Since the evolution of complex amplitudes $\boldsymbol{\gamma}_{k,n}$ is not included into the prediction model, a reinitialization of complex weights $\boldsymbol{\gamma}_{k,n}$ is performed to be able to follow these abrupt changes. Using the posterior MPC parameters and the estimated covariance matrix $\hat{\boldsymbol{R}}_n$ at time n, the reinitialization is performed by using (37) after the mobile agent being moved a distance of about one wavelength.

3.3 MPC Parameters and Noise Parameters Initialization with RIMAX

Given the baseband signal $\widetilde{\boldsymbol{y}}_n$ at time n, depending on the time instance, the parameters of new MPCs, i.e., $\hat{\boldsymbol{\mu}}_{k',n}$ with $k' \in \mathcal{K}'_n = \{1, \ldots, K'_n\}$, are either estimated for the first time using $\widetilde{\boldsymbol{y}}_n = \boldsymbol{y}_1$ at time $n = 1$, or using the residual $\widetilde{\boldsymbol{y}}_n = \boldsymbol{y}_n - \sum_{k \in \mathcal{K}_{n-1}} \boldsymbol{s}(\hat{\boldsymbol{\mu}}_{k,n}, \hat{\boldsymbol{\gamma}}_{k,n})$, at time $n = 2, \ldots, N$, where $\boldsymbol{s}(\hat{\boldsymbol{\mu}}_{k,n}, \hat{\boldsymbol{\gamma}}_{k,n})$ represents the specular contribution of each MPC which is already inside the state vector defined in (39). After the parameters of K'_n MPCs are estimated, the state vector will contain finally the parameters of $K_n = K'_n + K_{n-1}$ MPCs, and $K_{-1} = 0$. The estimation of each new MPC is discussed in the following section.

Successive cancellation of MPCs

The estimation starts by using the space-alternating generalized expectation-maximization (SAGE) algorithm that is based on successive cancellation of MPCs [43]. At first, an initial estimate of the k'th new MPC's parameters

$\hat{\boldsymbol{\mu}}_{k',n}$ is found by searching for the maximum of the power spectrum of $\widetilde{\boldsymbol{y}}_n^-$, with $\widetilde{\boldsymbol{y}}_n^- = \widetilde{\boldsymbol{y}}_n$ when $k' = 1$, i.e.,[6]

$$\{\hat{n}'_a, \hat{n}'_e, \hat{i}\} = \arg \max_{n'_a, n'_e, i} |\boldsymbol{b}^{\mathrm{Rx}}(\varphi_{\mathrm{s},n'_a}, \theta_{\mathrm{s},n'_e}) \widetilde{\boldsymbol{y}}_n^- \boldsymbol{a}^*_{\mathrm{f},i}|, \tag{33}$$

where $\hat{\boldsymbol{\mu}}_{k',n} = [d'_{\hat{i}}, \varphi_{\mathrm{s},\hat{n}'_a} \theta_{\mathrm{s},\hat{n}'_e}]^{\mathrm{T}}$, and $\boldsymbol{a}_{\mathrm{f},i}$ is the ith column of $\mathbf{A}_{\mathrm{f}}$ in (35). $\varphi_{\mathrm{s},n'_{\mathrm{a}}}$ and $\theta_{\mathrm{s},n'_{\mathrm{e}}}$ are the azimuth and elevation angles after interpolation, with $n'_{\mathrm{a}} = 1, \cdots, N'_{\mathrm{a}}$ and $n'_{\mathrm{e}} = 1, \cdots, N'_{\mathrm{e}}$. N'_{a} and N'_{e} denote the number of azimuth, elevation angular samples after interpolation. The sub-vectors are given as

$$\boldsymbol{b}^{(\mathrm{Rx})}(\varphi_{\mathrm{s},n'_{\mathrm{a}}}, \theta_{\mathrm{s},n'_{\mathrm{e}}}) = \boldsymbol{b}^{(\mathrm{Rx})}_{\mathrm{H}}(\varphi_{\mathrm{s},n'_{\mathrm{a}}}, \theta_{\mathrm{s},n'_{\mathrm{e}}}) + \boldsymbol{b}^{(\mathrm{Rx})}_{\mathrm{V}}(\varphi_{\mathrm{s},n'_{\mathrm{a}}}, \theta_{\mathrm{s},n'_{\mathrm{e}}}). \tag{34}$$

The vector $\boldsymbol{b}^{\mathrm{Rx}}_{(\mathrm{H/V})} \in \mathbb{C}^{N_{\mathrm{Rx}} \times 1}$ represents the projection from $(\varphi_{\mathrm{s},n'_{\mathrm{a}}}, \theta_{\mathrm{s},n'_{\mathrm{e}}})$ to the array response by using the effective aperture distribution function (EADF). At the transmit side, the antenna response is denoted by a scalar $b^{\mathrm{Tx}}_{(\mathrm{H/V})}$ due to a single antenna being used. The EADF performs efficient interpolation of the measured beam pattern via a two-dimensional discrete Fourier transform to obtain antenna responses of arbitrary azimuth and elevation angles that are off the sampling grid. The reader is referred to [44] for more details regarding the EADF formulation. For interpolation in the delay/distance domain, the complex shifting matrix

$$\boldsymbol{A}_{\mathrm{f}} = \begin{bmatrix} \mathrm{e}^{-j2\pi(-\frac{N_{\mathrm{f}}-1}{2})f'_1} & \cdots & \mathrm{e}^{-j2\pi(-\frac{N_{\mathrm{f}}-1}{2})f'_{N'_{\mathrm{f}}}} \\ \vdots & & \vdots \\ \mathrm{e}^{-j2\pi(+\frac{N_{\mathrm{f}}-1}{2})f'_1} & \cdots & \mathrm{e}^{-j2\pi(+\frac{N_{\mathrm{f}}-1}{2})f'_{N'_{\mathrm{f}}}} \end{bmatrix} \in \mathbb{C}^{N_{\mathrm{f}} \times N'_{\mathrm{f}}} \tag{35}$$

is applied for an increased number of frequency points $f'_i = \frac{i}{N'_{\mathrm{f}}}$ with $i = 1, \ldots, N'_{\mathrm{f}}$, where N'_{f} denotes the number of frequency samples after interpolation. The corresponding distance samples are given as $d'_i = \frac{cN_{\mathrm{f}}}{B_{\mathrm{w}}} f'_i$. The estimate of the corresponding complex weight $\hat{\boldsymbol{\gamma}}_{k',n}$ is given in two forms. If there is no estimate of noise covariance matrix, $\hat{\boldsymbol{R}}_n = \boldsymbol{I}_{N_{\mathrm{f}} N_{\mathrm{Rx}}}$ is then assumed and $\hat{\boldsymbol{\gamma}}_{k',n}$ is given in a least square form, i.e.,

$$\hat{\boldsymbol{\gamma}}_{k',n} = (\boldsymbol{B}^{\mathrm{H}}(\hat{\boldsymbol{\mu}}_{k',n}) \boldsymbol{B}(\hat{\boldsymbol{\mu}}_{k',n}))^{-1} \boldsymbol{B}^{\mathrm{H}}(\hat{\boldsymbol{\mu}}_{k',n}) \widetilde{\boldsymbol{y}}_n^-. \tag{36}$$

Otherwise, with the estimated $\hat{\boldsymbol{R}}_n$, $\hat{\boldsymbol{\gamma}}_{k',n}$ is given in a weighted least square form, i.e.,

$$\hat{\boldsymbol{\gamma}}_{k',n} = (\boldsymbol{B}^{\mathrm{H}}(\hat{\boldsymbol{\mu}}_{k',n}) \hat{\boldsymbol{R}}_n^{-1} \boldsymbol{B}(\hat{\boldsymbol{\mu}}_{k',n}))^{-1} \boldsymbol{B}^{\mathrm{H}}(\hat{\boldsymbol{\mu}}_{k',n}) \hat{\boldsymbol{R}}_n^{-1} \widetilde{\boldsymbol{y}}_n^- \tag{37}$$

[6] $\widetilde{\boldsymbol{y}}_n$ is reshaped to a matrix with dimension $N_{\mathrm{Rx}} \times N_{\mathrm{f}}$ before used in (33).

where the matrix valued function $\boldsymbol{B}(\hat{\boldsymbol{\mu}}_{k',n}) \in \mathbb{C}^{N_\mathrm{f}N_\mathrm{Rx}\times 4}$ accounts for the structure of the radio channel of four polarimetric transmissions and is defined as

$$\boldsymbol{B}(\hat{\boldsymbol{\mu}}_{k',n}) = [\boldsymbol{b}_\mathrm{H}^\mathrm{Rx} \lozenge b_\mathrm{H}^\mathrm{Tx} \lozenge \boldsymbol{b}_\mathrm{f} \quad \boldsymbol{b}_\mathrm{V}^\mathrm{Rx} \lozenge b_\mathrm{H}^\mathrm{Tx} \lozenge \boldsymbol{b}_\mathrm{f} \quad \boldsymbol{b}_\mathrm{H}^\mathrm{Rx} \lozenge b_\mathrm{V}^\mathrm{Tx} \lozenge \boldsymbol{b}_\mathrm{f} \quad \boldsymbol{b}_\mathrm{V}^\mathrm{Rx} \lozenge b_\mathrm{V}^\mathrm{Tx} \lozenge \boldsymbol{b}_\mathrm{f}]. \quad (38)$$

The vector $\boldsymbol{b}_\mathrm{f} \in \mathbb{C}^{N_\mathrm{f}\times 1}$ accounts for the system frequency response by using the complex shifting matrix defined in (35). The detailed formulation of the matrix valued function (38) can be found in [34]. The non-linear mapping from the estimated parameters of k'th MPC to the specular observation vector[7] is given as

$$\boldsymbol{s}(\hat{\boldsymbol{\mu}}_{k',n}, \hat{\boldsymbol{\gamma}}_{k',n}) = \boldsymbol{B}(\hat{\boldsymbol{\mu}}_{k',n})\hat{\boldsymbol{\gamma}}_{k',n}. \quad (39)$$

The estimated specular component of the k'th MPC, together with the components of $k'-1$ previously initialized new MPCs indexed with j are then subtracted from the channel observation, i.e., the residual is updated to

$$\widetilde{\boldsymbol{y}}_n^- = \widetilde{\boldsymbol{y}}_n - \boldsymbol{s}(\hat{\boldsymbol{\mu}}_{k',n}, \hat{\boldsymbol{\gamma}}_{k',n}) - \sum_{j=1}^{k'-1} \boldsymbol{s}(\hat{\boldsymbol{\mu}}_{j,n}, \hat{\boldsymbol{\gamma}}_{j,n}). \quad (40)$$

A new MPC is further initialized from the updated residual $\widetilde{\boldsymbol{y}}_n^-$ only if two constraints are both met: (i) The maximum allowed number of MPCs that are estimated/tracked simultaneously K_max is limited, so $K_{n-1} + k' < K_\mathrm{max}$; (ii) The ratio between the energy sum of the estimated MPCs, with each denoted as $p_{\mathrm{sp},k/j,n}$, over the full signal energy p_n at time n, i.e., $\beta_n = \sum_{k\in\mathcal{K}_{n-1}} \frac{p_{\mathrm{sp},k,n}}{p_n} + \sum_{j=1}^{k'} \frac{p_{\mathrm{sp},j,n}}{p_n}$, should be smaller than the maximum allowed ratio denoted as β_max, i.e., $\beta_n < \beta_\mathrm{max}$. This is to control the model complexity and reduce the interference between coherent MPCs. The same procedure from (33) to (40) is repeated until the parameters of K_n' MPCs are estimated and added to the state vector and $K_n = K_n' + K_{n-1}$.

After subtracting the contribution of the K_n estimated MPCs, the residual $\widetilde{\boldsymbol{y}}_n^-$ is used to estimate the noise standard deviation and DMC parameters $\hat{\boldsymbol{x}}_\mathrm{noise,n} = [\hat{\boldsymbol{x}}_{\mathrm{dmc},n}^\mathrm{T} \quad \hat{\sigma}_{\mathrm{w},n}]^\mathrm{T}$. The initial estimates of $\hat{\boldsymbol{x}}_{\mathrm{dmc},n}$ is computed from the averaged power delay profile over N_Rx antenna elements. The reader is referred to [34, Section 6.1.8]) for detailed processing. The estimated covariance matrix $\hat{\boldsymbol{R}}_n$ is then calculated using $\hat{\boldsymbol{x}}_\mathrm{noise,n}$ with (4) and (5).

Refinement with RIMAX

These initial estimated state vectors of MPC parameters, noise and DMC parameters are optimized by alternating maximization of the log-likelihood

[7] Given an estimated state vector $\hat{\boldsymbol{x}}_n$ of K_n MPCs, the specular observation vector is given as $\boldsymbol{s}(\hat{\boldsymbol{x}}_n) = \sum_{k\in\mathcal{K}_n} \boldsymbol{s}(\hat{\boldsymbol{\mu}}_{k,n}, \hat{\boldsymbol{\gamma}}_{k,n})$

function by the RIMAX algorithm, which uses Levenberg-Marquardt and ML-Gauss-Newton algorithms for optimization [34]. It is worth mentioning that K_n influences how much one can actually benefit from the joint optimization of all parameters in RIMAX initialization. If a nonsensical solution with a very large K_n is given in (3.3), the estimated parameters of specular MPCs tend to converge to local minima which are biased from the true values due to noise over-fitting after optimization iterations. In practice, the maximum K_n allowed in the RIMAX initialization should be chosen to capture all the significant specular MPCs in the propagation environment. Considering the alternating maximization to jointly estimate the MPC parameters $\hat{\boldsymbol{x}}_n$ and the noise parameters $\hat{\boldsymbol{x}}_{\mathrm{noise,n}} = [\hat{\boldsymbol{x}}_{\mathrm{dmc},n}^{\mathrm{T}} \quad \hat{\sigma}_{\mathrm{w},n}]^{\mathrm{T}}$ is very computationally demanding and therefore it's only applied at time $n = 1$, but not during the subsequent tracking of the channel parameters.

4 Localization and Mapping

Given the distance estimates $\hat{d}_{k,n}$ from EKF, the localization problem is formulated as the joint estimation and optimization process of the inlier set I_{inl}, mobile agent positions $\boldsymbol{p}_n$ and features (PA and VAs) positions $\boldsymbol{a}_k$ in Problem 2 in (9), which is a highly non-convex problem. To make it a better conditioned problem with reasonable complexity, we introduce two modified versions of (9) with given assumptions and prior information.

4.1 Experiment I

In this experiment, we assume that all mobile agent positions $\boldsymbol{p}_n$ are known, then the optimization problem of Problem 2 in (9) is reduced to

$$\min_{\substack{I_{\mathrm{inl},k},\boldsymbol{a}_k \\ \forall n}} \sum_{k|(k,n)\in I_{\mathrm{inl}}} (\hat{d}_{k,n} - \|\boldsymbol{p}_n - \boldsymbol{a}_k\|)^2 + \sum_{k|(k,n)\in I_{\mathrm{outl}}} C \tag{41}$$

independently for each feature position $\boldsymbol{a}_k$ with $k \in \mathcal{K}_n$ and $n = 1, \ldots N$, by using random sample consensus (RANSAC) [45]. $I_{\mathrm{inl},k}$ is the inlier subset for each k and it is possible to have no inliers at some estimated feature positions, i.e., $I_{\mathrm{inl},k} = \emptyset$. We assume the association between an estimated MPC and a feature is consistent during the tracking process, and the corresponding feature position is fixed over time. Given a vector containing all the distance estimates of one MPC, we randomly choose a minimal set, i.e., estimates at three time instances and corresponding (known) mobile agent positions, to give an initial estimate of the feature position. Then, we extend to the full vector and determine how many of the remaining estimates agree with the estimated feature position, i.e., number of inliers. Different minimal sets give different solutions,

we choose the one with the largest number of inliers. The same procedure is repeated for all the tracked MPCs. The RANSAC gives initial estimates of feature positions and inlier set, which is then followed by non-linear optimization of (41). Moreover, the resulting residuals $\hat{d}_{k,n} - \|\boldsymbol{p}_n - \hat{\boldsymbol{a}}_k\|$ can be used to empirically assess properties of the error distribution.

4.2 Experiment II

In this experiment, we assume that both the mobile agent positions and feature positions are unknown. To make this estimation problem tractable, an estimate of the inlier set $\hat{I}_{\text{inl}}$ is firstly obtained by using the groundtruth mobile agent positions in (41), then the estimates $\hat{d}_{k,n} \forall\ (k,n) \in \hat{I}_{\text{inl}}$ are subsequently used as inputs in (9) and Problem 2 is reduced to

$$\min_{\substack{\boldsymbol{p}_n, \boldsymbol{a}_k \\ \forall n, \forall k}} \sum_{(k,n) \in \hat{I}_{\text{inl}}} (\hat{d}_{k,n} - \|\boldsymbol{p}_n - \boldsymbol{a}_k\|)^2. \tag{42}$$

Two assumptions are further made here. First, $\boldsymbol{p}_n$ are assumed to be constrained to a plane (e.g., $z_n = 0$). This is a natural assumption for many problems where the mobile agent is moved approximately in a plane during the measurement. Note that it does however introduce an ambiguity in the feature positions, since we can never determine the sign of the $z-$component. Second, we assume that the mobile agent has been moved in a continuous path. Algorithms for solving Problem 2 using hypothetical and test paradigm are also presented in [46]. In order to minimize drift and accumulation of initialization errors, we divide the whole dataset into a number of smaller segments in time (typically containing 100 time instances each). Fig. 3 shows two consecutive segments and the overlap in-between, each segment is then initialized independently.

For each segment, we initialize both $\hat{\boldsymbol{a}}_k$ with $k \in \mathcal{K}_n$ and $\hat{\boldsymbol{p}}_n$ using minimal solvers and RANSAC [38] based only on the distance estimates from the EKF. In detail, we start from a minimal set which is sampled from the distance estimates to estimate the corresponding mobile agent and feature positions. Since the LOS component is visible at all time instances, we always include the PA position in the minimal sample. Using the initial positions we can minimally trilaterate mobile agent and feature positions at other time instances, and count how many inliers we get for this initial estimate. The steps above are repeated and we choose the solution with the highest number of inliers. In minimal trilateration, two possible solutions are provided for each estimated position due to the ambiguity of the z-component. For the mobile agent position, with the assumption of the trajectory in the plane $z_n = 0$, we always choose the solution with the smallest $|\hat{z}_n|$. For the feature positions, the two solutions correspond to the two different signs of $|\hat{z}_k|$. Since this ambiguity can never

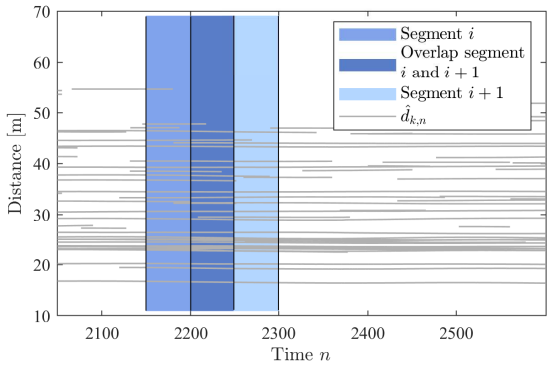

Figure 3: Depiction of how the estimated dataset from EKF being segmented before used in the localization and mapping algorithm. Each segment contains distance estimates from 100 consecutive time instances, and the overlap in-between is 50 time instances long.

be resolved, we consistently choose the solution with e.g., positive $\hat{z}_k$, without any loss of generality. To sum up, the RANSAC procedure provides an initial estimate of the mobile agent positions in the segment, as well as the feature positions and an estimate of the inlier set. The solution of (9) is then refined by using a Newton method.

The estimates for each segment are given in its own coordinate system. However, we need the whole solution to be in the same coordinate system. If we choose the segments so that the reconstructed mobile agent's MPC has an overlap in-between segments, we can use the overlapping mobile agent positions to register the different reconstructions. This is simply done in a least squares way by applying rotation and translation operations. After registration of all segments into one coordinate system, the mean values over all individual estimates are calculated for overlapping mobile agent positions and feature positions. We can then also do a final non-linear optimization of all estimated positions over all inlier data.

5 Evaluations and Results

To analyze the performance, the proposed framework is applied to both real and synthetic channel measurements, and the mobile agent is equipped with one single antenna in both cases. Besides, the results are presented in two aspects: (i) the MPC parameter estimation and tracking results, and comprehensive statistical analysis of the MPC dynamic behaviors, (ii) the evaluation of two localization and mapping experiments presented in Section 4 with real channel measurements.

Figure 4: Overview of the measurement area in the sports hall, Medicon Village, Lund, Sweden. Room dimension is around 20 m × 36 m × 7.5 m.

5.1 Experimental Setup

The real measurement campaign was performed in a large sports hall with the RUSK LUND channel sounder. Fig. 4 shows an overview of the measurement area. A cylindrical array with 64 dual-polarized antennas (Fig. 5a), i.e., 128 ports in total, is used as a static PA. The center of the array is 1.42 m above ground. A conical monopole omnidirectional antenna (Fig. 5b) is used to represent a mobile agent. The distance between the PA and the mobile agent is around 17 m and line-of-sight (LOS) conditions apply. The transfer functions (snapshots) were recorded at a center frequency around 2.7 GHz and with 129 frequency samples equispaced over a 40 MHz bandwidth. To avoid large variation of path parameters, especially a possible 2π phase slip between two consecutive snapshots, the spatial sampling rate of the wireless channel was sufficiently high. In total, there were 6000 channel snapshots collected in 19.7 s. The mobile agent was placed on a tripod and manually moved to write the "**Lund**" letters in an approximately 2 m^2 area. Meanwhile, an optical CMM system (Fig. 5b), which uses the camera technology to triangulate the positions with accuracy down to millimeter, was used to capture the mobile agent movement. The movement positions are further used as the groundtruth $\boldsymbol{p}_{\mathrm{true},n}$ for performance analysis. The floor plan and the zoom-in plot of the groundtruth are shown in Fig. 1

A synthetic measurement dataset was generated for validating the performance of the MPC parameters' initialization. The floor plan based on the Medicon Village in Fig. 1 (excluding the ceiling) and a ray tracer (RT) are used to generate dispersion parameters of MPCs. During the RT simulations, the real calibration file of the cylindrical antenna array (Fig. 5a) was used at the PA side and the mobile agent with a single omnidirectional antenna was assumed. DMC was also included and independently generated for each realization. The PA was kept static at the location which is the same as the real measurement setting. Meanwhile, the groundtruth coordinates of mobile agent

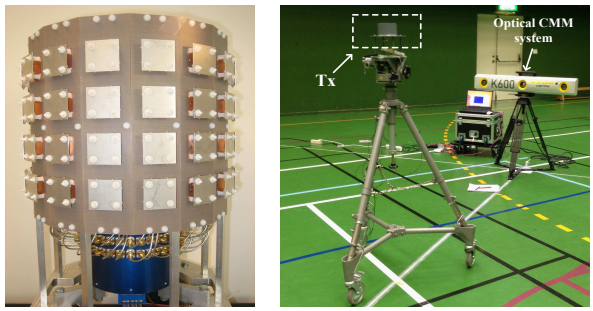

(a) (b)

Figure 5: (a) Photo of the cylindrical antenna array. (b) The conical monopole omnidirectional antenna and the optical CMM system.

at the first 100 time instances n from the optical system were used to synthetically generate 100 independent channel realizations. The energy ratio β_n is around 50% for each realization. The number of MPCs was restricted to $L_n = 6$ for each realization, including the LOS and the first order reflection paths from surrounding walls and ground.

5.2 Evaluation of the Channel Estimation Algorithm

MPC Initialization Performance

The RIMAX was applied to each synthetic channel realization independently. For consistent evaluation of the estimation errors between the reference state vector $\boldsymbol{x}_n$ from RT and the estimated state vectors $\hat{\boldsymbol{x}}_n$, the optimal sub-pattern assignment (OSPA) metric [47] was applied here. For the case $K_n \geq L_n$, it is defined as

$$d_{\text{ospa}}(\hat{\boldsymbol{x}}_n, \boldsymbol{x}_n) = \left[\frac{1}{K_n} \left(\min_{\pi \in \prod_{K_n}} \sum_{l=1}^{L_n} \left[d^{(d_c)} \left(d_{l,n}, \hat{d}_{\pi_l,n} \right) \right]^{p_o} + d_c^{p_o} \left(K_n - L_n \right) \right) \right]^{\frac{1}{p_o}}, \tag{43}$$

where $\prod_k$ denotes the set of permutations on $\{1, \cdots, k\}$ and $k \leq K_n$. $d(\cdot,\cdot)$ represents the Euclidean metric and the function $d^{(d_c)}(\cdot,\cdot) = \min(d_c, d(\cdot,\cdot))$. Besides, we have the cut-off parameter of distance $d_c = 1\,\text{m}$ and order parameter $p_o = 1$.

With the maximum allowed power ratio $\beta_{\max}$ set to 55 %, overestimation happened as expected after the SAGE step, around 20 MPCs are detected at each time n. After RIMAX iterations and state dimension adjustment, clutter components are enormously suppressed from the initial state vector,

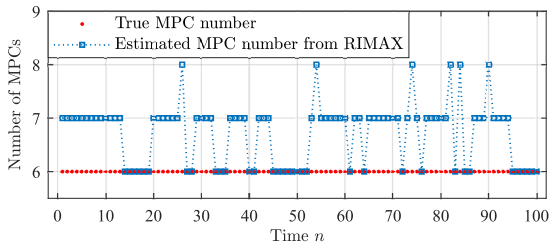

(a)

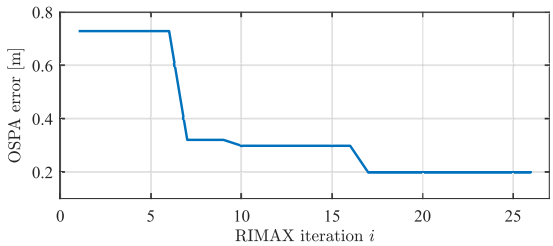

(b)

Figure 6: (a) The number of MPCs estimated using RIMAX K_n, compared with true number of MPC L_n for each channel simulation. (b) The convergence of the OSPA error versus the number of iterations of the joint optimization in RIMAX algorithm for the the synthetic channel realization at time $n = 1$.

only one or two clutter components remain for some time instances, as shown in Fig. 6a. For the synthetic realization at time $n = 1$ as shown in Fig. 6b, the estimated state order K_n is reduced from 20 to 7 with the RIMAX iterations and dimension adjustment, meanwhile the OSPA error decreases from around 0.73 m to 0.19 m. The RIMAX was applied independently to the 100 synthetic channel realizations, and the mean OSPA error over 100 simulations is 0.172 m.

MPC Tracking Results

Table 1 summarizes the parameters initialized in the EKF estimation for the "**Lund**" measurement, where the noise and DMC parameters are estimated at every 5th time instances and reinitialization of the complex amplitude $\boldsymbol{\gamma}_{k,n}$ is performed every 36th time instances. These values are adapted to movement of the mobile agent. Fig. 7 shows the tracked propagation distances of MPCs over measurement time from the EKF implementation. It is observed that the LOS component with the distance around 17 m is tracked steadily since the beginning. About 2 m apart from the LOS is the ground reflection path which is tracked shortly in the end. Besides, many other MPCs with long lifetimes are observed in the range of 20-50 m propagation distance. The spatial distribution

Table 1: The parameters used in the EKF estimation for the "**Lund**" measurement.

q_d	q_φ	q_θ	q_α	q_ϕ	ΔT
$8.81\,\mathrm{m}^2/\mathrm{s}^4$	$3\times10^{-3}\,\mathrm{rad}^2/\mathrm{s}^4$	$1.56\times10^{-4}\,\mathrm{rad}^2/\mathrm{s}^4$	0	$10^{-6}\,\mathrm{rad}^2/\mathrm{s}^4$	$3.3\times10^{-3}\,\mathrm{s}$

reinit. of $\boldsymbol{\gamma}_{k,n}$	estim. of noise/DMC	$K_{\max}$	$\beta_{\max}$
36th time instance	5th time instance	30	40%

of the tracked MPCs are further given in Fig. 8. The MPCs are plotted in a 3D Cartesian coordinate system based on the estimates of distances $\hat{d}_{k,n}$ and azimuth/elevation AoAs $(\hat{\varphi}_{k,n}^{(\mathrm{Rx})}, \hat{\theta}_{k,n}^{(\mathrm{Rx})})$ without considering the path interaction order. The top view (Fig. 8a) shows that the tracked MPCs are distributed over the entire azimuth domain and paths are intensively detected in the similar direction as the LOS component. From the vertical distribution (Fig. 8b), a few paths are observed from the ground or at similar height as the PA, while the most of the estimated paths are from the complex ceiling structure of the room, e.g., the metal beams of the ceiling in Fig. 4. Those complex room structures brought additional uncertainties to the distance estimates. Moreover, the similar behaviour of the long-tracked MPCs in the angular domain may become a challenge for 3D localization, for which the MPCs with sparse angles are preferred. However, it is interesting to see the performance in the real but non-ideal case.

Clutter components around some high-power MPCs are observed during the tracking. They usually have similar angles and propagation distances as the dominant MPCs close by and experience very short lifetime. These components are mainly generated due to power compensation in the estimation procedure and do not have actual physical meaning, therefore they are not considered in the localization step.

For a better evaluation of the tracking performance, we zoom into the LOS component and compare the distance estimates with the groundtruth. The red solid line in Fig. 9a represents the true propagation distance of the LOS path, which is calculated based on the 3D coordinates from the optical system and the groundtruth coordinates of the PA. As shown from the comparison, the EKF performed a smooth tracking of the movements, with all the non-linear and quick motions being captured. The distance estimates have a good match with the groundtruth most of the time, besides some deviations observed after 16 s. The maximum deviation from the groundtruth is about 8 cm, while the predicted errors of the LOS distance estimates from the posterior covariance matrix (Fig. 9b) are in the scale of sub-centimeters, which are clearly underestimated. Also, it is shown that the errors are accumulated during the tracking and reach the maximum at the sharp turns of "**L**".

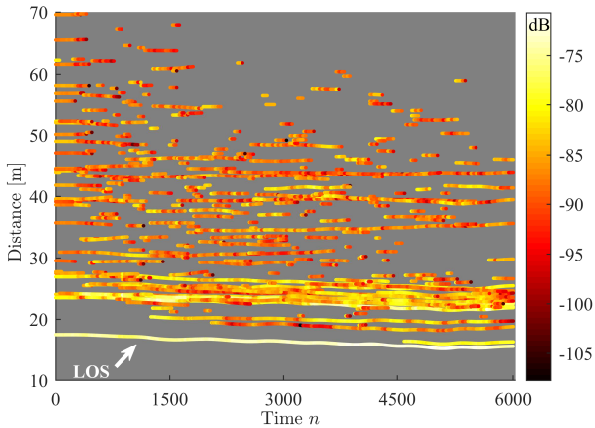

Figure 7: The tracked propagation distances of MPCs $\hat{d}_{k,n}$ over measurement time, with the color indicating the power in dB scale.

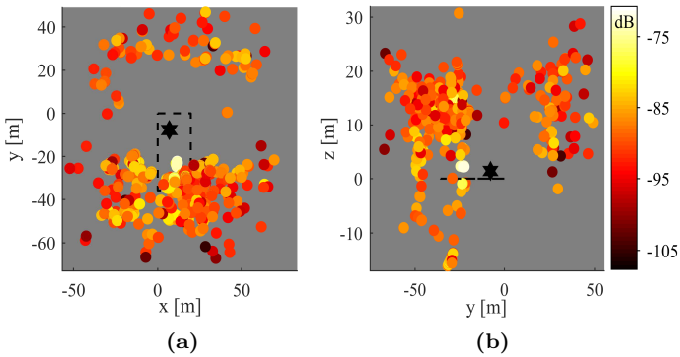

Figure 8: 3D plot of the tracked MPCs based on the estimated distances $\hat{d}_{k,n}$ and azimuth/elevation AoAs $(\hat{\varphi}_{k,n}, \hat{\theta}_{k,n})$. Black dashed line denotes the room geometry and the hexagram represents the location of BS. The top-view plot (a) shows how tracked MPCs are distributed in the azimuth plane. The side-view plot (b) shows the vertical distribution.

MPC Lifetime Analysis

In this section, we focus on the statistical characterization of MPC lifetimes in this path intense environment and the analysis is presented from two perspectives: (i) empirical distribution of tracked MPC lifetime and the comparison with statistical distributions, (ii) the relation between the lifetime and parameters like averaged SINR, averaged power of each MPC. The clutter components which do not contain any geometrical meanings are excluded from the stat-

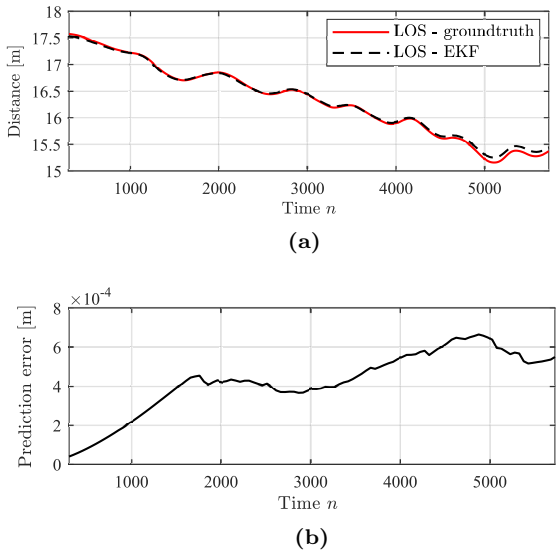

Figure 9: Performance evaluation of the tracked LOS component. In (a), the black dashed line denotes the distance estimates from EKF. The red solid line is the propagation distance computed with the groundtruth. The two curves are manually synchronized for better comparison. (b) shows the estimation errors of the propagation distances, which are subtracted from the posterior filter covariance matrix.

istical analysis. From the phase evolution perspective, we have the minimum resolvability of one wavelength movement, therefore any MPCs with lifetime (converted into distance) less than one wavelength are considered as clutters.

The empirical lifetime cumulative distribution function (CDF) of the tracked MPCs (Fig. 10) shows that over 90 % of the tracked MPCs are with lifetime smaller than 4 s, and insufficient samples leads to a non-smooth curve from 4 s to 19.7 s. The lack of long and robustly tracked MPCs clearly make Problem 2 in (9) a tougher problem. Further, we considered the lognormal, exponential, and the Birnbaum-Saunders (B-S) [48] distributions as the potential fitting statistical distributions for the empirical lifetime CDF, and conducted the goodness-of-fit χ^2-test. The lognormal distribution yields a better fit with the empirical CDF especially in the small lifetime region, while the B-S and exponential distributions deviate significantly from the empirical curve. The χ^2-tests yield a rejection rate of 100 % for all the three distributions. Besides, the mean square error (MSE) of the B-S and exponential distribution compared with the measurement are 0.0192 and 0.0378, respectively, lognormal distribution has the MSE of 0.0038. The significance level is set to 5 %.

As shown in (Fig. 11a), the Pearson's rank correlation between the averaged MPC lifetimes and the averaged powers is 0.167, showing a weak dependency

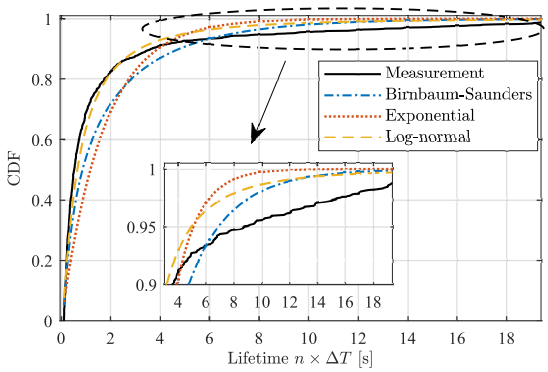

Figure 10: Empirical distribution of tracked MPC lifetime from the "**Lund**" measurement and the comparison with statistical distributions.

between the two variables, which means high power of MPCs does not guarantee continuously stable tracking. The Pearson's rank correlation between the averaged MPC lifetimes and the averaged SINRs is 0.731 (Fig. 11b), indicating a high dependency between the two variables.

5.3 Multipath-Assisted Localization

As seen in Fig. 7 and Fig. 9a, most of the specular MPCs can only be observed during fractions of the measurement time (i.e., missing data) and the estimation quality of MPC dispersion parameters is not consistent during the whole tracking process for an individual MPC, i.e., outliers exist in the data, of which the errors are substantial. In this section, we present the performance evaluation of the two experiments described above, with the presence of missing data and outliers.

5.4 Evaluation of Experiment I

We start by looking at experiment I (4.1), i.e., all the mobile agent positions are assumed to be known, but the inlier set, the feature positions are all unknown.

Those tracked MPCs that were longer than 500 time instances are selected from the tracked 282 MPCs, which gave a set of 50 MPCs. For each of them, we estimated the feature (both PA and VA) positions using RANSAC (to obtain $\hat{I}_{\text{inl}}$) followed by the non-linear optimization of (41) (to obtain $\hat{\boldsymbol{a}}_k$). In total these 50 tracked MPCs gave us 103 480 distance samples, i.e., approximately 2000 each. Of these 77 490 were considered to be inliers. This gives us an estimated inlier ratio of 75%. The standard deviation of the inlier residuals is 4.6 cm. Some examples of the estimated VA positions which corresponds to some long tracked MPCs are shown in Fig. 12, where the reconstructed PA position $\hat{\boldsymbol{a}}_1$ is

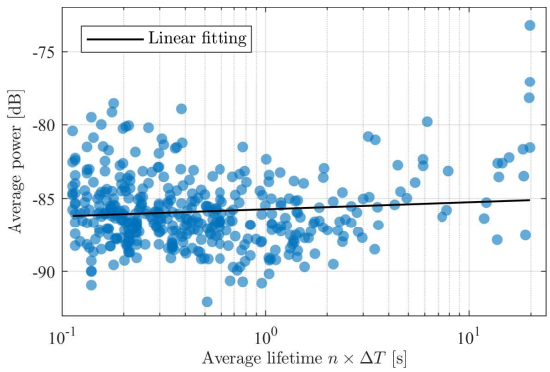

(a)

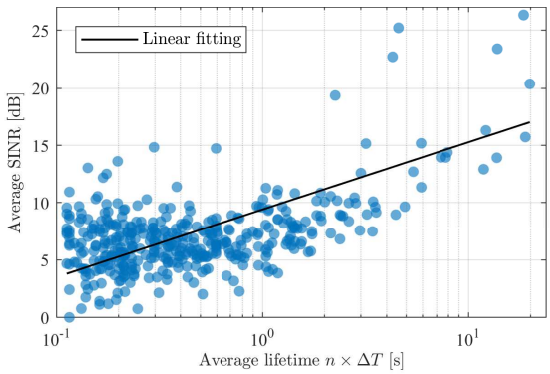

(b)

Figure 11: Relation between the averaged lifetimes [s] and (a) averaged powers [dB] and (b) averaged SINRs [dB] of the tracked MPCs.

registered to the groundtruth PA position, meanwhile the same transformation is applied to all the estimated VA positions. It could be observed that the estimated and transformed VA positions reasonably reconstructed the geometrical features, even for the 2$^{\text{nd}}$ and 3$^{\text{rd}}$ order VAs.

5.5 Evaluation of Experiment II

We now turn our attention to the experiment II (4.2), where only the distance estimates $\hat{d}_{k,n}$ are given as input and no prior knowledge about the mobile agent positions and feature positions. In order to use the calibration procedure described in the previous section, for the "**Lund**" dataset, we proceeded by splitting the whole dataset in a number of smaller segments in time. This resulted in 117 segments of length 100 time instances with 50 time-instances

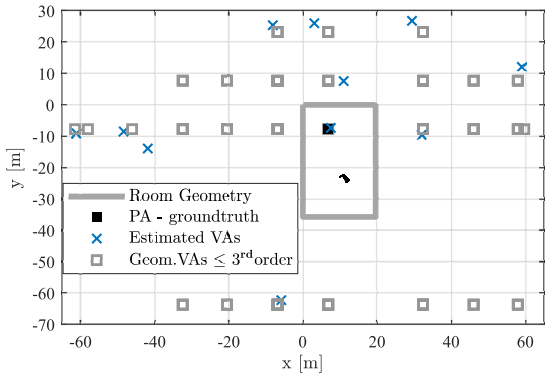

Figure 12: Evaluation of experiment I (4.1). Estimation of feature positions with the prior knowledge of the groundtruth mobile agent positions, meanwhile the inlier set was estimated. Some examples of the estimated and transformed VAs are denoted with blue cross, and the gray squares indicate geometrically expected VAs.

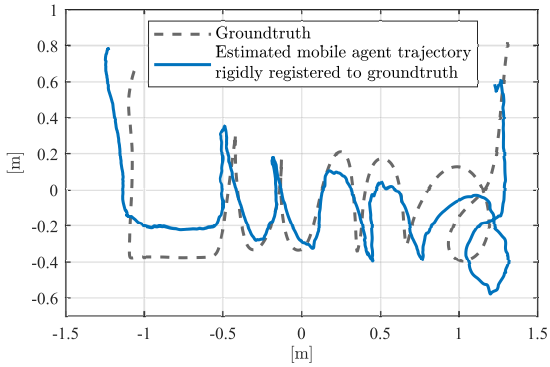

Figure 13: Evaluation of experiment II (4.2). The groundtruth (deshed gray), and the estimated mobile agent trajectory (solid blue) which is registered to the groundtruth coordinate system.

overlap between adjacent segments. For each segment, we initialized both $\hat{\boldsymbol{a}}_k$ and $\hat{\boldsymbol{p}}_n$ using the RANSAC in Section 4.2. The different solutions from the 117 segments were then registered into a common coordinate system using the overlap between the segments. The estimated mobile agent trajectory and the groundtruth are shown in Fig. 13.

Considering the estimated mobile agent trajectory and the groundtruth are in different coordinate systems, the alignment between the two systems is firstly needed for further performance evaluation. This is done by solving the

following least-squares problem

$$\min_{\boldsymbol{R},\boldsymbol{r}_0} \sum_i ||\boldsymbol{R}\hat{\boldsymbol{p}}_i + \boldsymbol{r}_0 - \boldsymbol{p}_{\mathrm{true},i}||^2, \tag{44}$$

where $\boldsymbol{R}$ is the rotation matrix, and $\boldsymbol{r}_0$ is the translational offset vector [49], [50]. It could be observed that the estimated trajectory shows a clear "**Lund**" pattern, with all the fine movements details caught. However, the overall shape is stretched along the diagonal direction, which results in a larger deviation from the groundtruth especially in the beginning and the end. The largest deviation of the estimated mobile agent position from the groundtruth happens at the sharp turn of "**L**", which is 26 cm. Furthermore, the root mean square error (RMSE) is defined as $d_{\mathrm{RMSE}} = \sqrt{(\sum_{n=1}^{N} |\hat{\boldsymbol{p}}_n - \boldsymbol{p}_{\mathrm{true},n}|^2)/N}$, and the RMSE of the estimated agent trajectory (after being registered) compared with the groundtruth is 14 cm.

6 Conclusion and Outlook

In this paper, we introduced a high-resolution phase-based localization and mapping framework using massive MIMO system. The proposed channel estimation and tracking algorithm uses an EKF and tightly couples the phase-based distance to the phase shift between consecutive channel measurements, which makes it possible to resolve the MPC distances accurately even when using only low signal bandwidth. A distance-based localization and mapping algorithm is then used for the mobile agent trajectory estimation with the presence of missing data and outliers. The performance evaluation with a real indoor measurement shows that the proposed localization framework can achieve outstanding accuracy even with standard cellular bandwidths. The largest agent position error is 26 cm and the RMSE position error is 14 cm. Besides, no prior knowledge of the surroundings and base station position is needed, hence the framework can be applied in different environments given that there are sufficiently many scatterers present. To sum up, the multipath-distance-based localization method that exploits the phases of MPCs using massive MIMO is a promising high-resolution localization solution for current and next generation cellular systems.

Regarding the future research, the current localization algorithm can be extended to further exploit MPC parameters like AoAs/AoDs, while the array orientation information is needed to calibrate angular estimates into the global coordinate system. Moreover, a soft-decision association between the estimated MPCs and environment features using probabilistic approach can be used to replace the hard-decision association now.

7 Acknowledgements

The authors would like to thank Jose Flordelis, Joao Vieira and Christian Nelson for helping with the measurements, as well as the support from Björn Olofsson with the motion capture system. We would also like to acknowledge the fruitful discussions within framework of the COST Action CA15104 (IRACON).

References

[1] R. Di Taranto, S. Muppirisetty, R. Raulefs, D. Slock, T. Svensson and H. Wymeersch, "Location-aware communications for 5G networks: How location information can improve scalability, latency, and robustness of 5G", *IEEE Signal Process. Mag.*, vol. 31, no. 6, pp. 102–112, 2014.

[2] F. Rusek, D. Persson, B. K. Lau, E. G. Larsson, T. L. Marzetta, O. Edfors and F. Tufvesson, "Scaling up MIMO: Opportunities and challenges with very large arrays", *IEEE Signal Process. Mag.*, vol. 30, no. 1, pp. 40–60, 2013.

[3] N. Garcia, H. Wymeersch, E. G. Larsson, A. M. Haimovich and M. Coulon, "Direct localization for massive MIMO", *IEEE Trans. Signal Process.*, vol. 65, no. 10, pp. 2475–2487, 2017.

[4] S. Marano, W. M. Gifford, H. Wymeersch and M. Z. Win, "NLOS identification and mitigation for localization based on UWB experimental data", *IEEE J. Sel. Areas Commun.*, vol. 28, no. 7, pp. 1026–1035, 2010.

[5] H. Wymeersch, S. Marano, W. Gifford and M. Win, "A machine learning approach to ranging error mitigation for UWB localization", *IEEE Trans. Commun.*, vol. 60, no. 6, pp. 1719–1728, 2012.

[6] Y. Wang, Y. Wu and Y. Shen, "Multipath effect mitigation by joint spatiotemporal separation in large-scale array localization", in *IEEE Global Telecommun. Conf. (GLOBECOM)*, 2017, pp. 1–6.

[7] Y. Shen, H. Wymeersch and M. Z. Win, "Fundamental limits of wideband localization— part II: Cooperative networks", *IEEE Trans. Inf. Theory*, vol. 56, no. 10, pp. 4981–5000, 2010.

[8] Y. Shen, S. Mazuelas and M. Win, "Network Navigation: Theory and Interpretation", *IEEE J. Sel. Areas Commun.*, vol. 30, no. 9, pp. 1823–1834, 2012.

[9] R. M. Buehrer, H. Wymeersch and R. M. Vaghefi, "Collaborative sensor network localization: Algorithms and practical issues", *Proc. IEEE*, vol. 106, no. 6, pp. 1089–1114, 2018.

[10] M. Z. Win, W. Dai, Y. Shen, G. Chrisikos and H. V. Poor, "Network operation strategies for efficient localization and navigation", *Proc. IEEE*, vol. 106, no. 7, pp. 1224–1254, 2018.

[11] M. Vari and D. Cassioli, "MmWaves RSSI indoor network localization", in *IEEE Int. Conf. on Commun. Workshops (ICC)*, 2014, pp. 127–132.

[12] C. Steiner and A. Wittneben, "Efficient training phase for ultrawideband-based location fingerprinting systems", *IEEE Trans. Signal Process.*, vol. 59, no. 12, pp. 6021–6032, 2011.

[13] V. Savic and E. G. Larsson, "Fingerprinting-based positioning in distributed massive MIMO systems", in *82nd Veh. Technol. Conf. (VTC2015-Fall)*, 2015, pp. 1–5.

[14] J. Vieira, E. Leitinger, M. Sarajlic, X. Li and F. Tufvesson, "Deep convolutional neural networks for massive MIMO fingerprint-based positioning", in *IEEE 28th Annu. Int. Symp. on Personal, Indoor, and Mobile Radio Commun. (PIMRC)*, 2017, pp. 1–6.

[15] E. Leitinger, P. Meissner, C. Rudisser, G. Dumphart and K. Witrisal, "Evaluation of position-related information in multipath components for indoor positioning", *IEEE J. Sel. Areas Commun.*, vol. 33, no. 11, pp. 2313–2328, 2015.

[16] K. Witrisal, P. Meissner, E. Leitinger, Y. Shen, C. Gustafson, F. Tufvesson, K. Haneda, D. Dardari, A. F. Molisch, A. Conti and M. Z. Win, "High-accuracy localization for assisted living: 5G systems will turn multipath channels from foe to friend", *IEEE Signal Process. Mag.*, vol. 33, no. 2, pp. 59–70, 2016.

[17] A. Shahmansoori, G. E. Garcia, G. Destino, G. Seco-Granados and H. Wymeersch, "Position and orientation estimation through millimeter-wave MIMO in 5G systems", *IEEE Trans. Wireless Commun.*, vol. 17, no. 3, pp. 1822–1835, 2018.

[18] Z. Abu-Shaban, X. Zhou, T. Abhayapala, G. Seco-Granados and H. Wymeersch, "Error bounds for uplink and downlink 3D localization in 5G mmwave systems", *IEEETrans. Wireless Commun.*, vol. 17, no. 8, pp. 4939–4954, 2018.

[19] J. Borish, "Extension of the image model to arbitrary polyhedra", *J. of the Acoustical Society of America*, 1984.

[20] E. Leitinger, M. Fröhle, P. Meissner and K. Witrisal, "Multipath-assisted maximum-likelihood indoor positioning using UWB signals", in *IEEE Int. Conf. on Commun. Workshops (ICC)*, 2014, pp. 170–175.

[21] E. Leitinger, F. Meyer, P. Meissner, K. Witrisal and F. Hlawatsch, "Belief propagation based joint probabilistic data association for multipath-assisted indoor navigation and tracking", in *Int. Conf. on Localization and GNSS (ICL-GNSS)*, 2016, pp. 1–6.

[22] P. Meissner, E. Leitinger and K. Witrisal, "UWB for robust indoor tracking: Weighting of multipath components for efficient estimation", *IEEE Wireless Comm. Lett.*, vol. 3, no. 5, pp. 501–504, 2014.

[23] C. Gentner, T. Jost, W. Wang, S. Zhang, A. Dammann and U. C. Fiebig, "Multipath assisted positioning with simultaneous localization and mapping", *IEEE Trans. Wireless Commun.*, vol. 15, no. 9, pp. 6104–6117, 2016.

[24] Y. Kuang, K. Åström and F. Tufvesson, "Single antenna anchor-free UWB positioning based on multipath propagation", in *IEEE Int. Conf. on Commun. (ICC)*, 2013, pp. 5814–5818.

[25] E. Leitinger, F. Meyer, F. Tufvesson and K. Witrisal, "Factor graph based simultaneous localization and mapping using multipath channel information", in *IEEE Int. Conf. on Commun. Workshops (ICCW)*, Paris, France, 2017, pp. 652–658.

[26] E. Leitinger, F. Meyer, F. Hlawatsch, K. Witrisal, F. Tufvesson and M. Z. Win, "A scalable belief propagation algorithm for radio signal based SLAM", *Corr*, vol. arXiv:1801.04463v2, 2018.

[27] M. Froehle, E. Leitinger, P. Meissner and K. Witrisal, "Cooperative multipath-assisted indoor navigation and tracking (Co-MINT) using UWB signals", in *IEEEInt. Conf. on Commun. Workshops (ICC)*, 2013, pp. 16–21.

[28] J. Kulmer, E. Leitinger, S. Grebien and K. Witrisal, "Anchorless cooperative tracking using multipath channel information", *IEEE Trans. Wireless Commun.*, vol. 17, no. 4, pp. 2262–2275, 2018.

[29] H. Naseri and V. Koivunen, "Cooperative simultaneous localization and mapping by exploiting multipath propagation", *IEEE Trans. Signal Process.*, vol. 65, no. 1, pp. 200–211, 2017.

[30] K. Witrisal, E. Leitinger, S. Hinteregger and P. Meissner, "Bandwidth scaling and diversity gain for ranging and positioning in dense multipath channels", *IEEE Wireless Commun. Lett.*, vol. PP, no. 99, 2016.

[31] K. M. Pesyna, Z. M. Kassas, R. W. Heath and T. E. Humphreys, "A phase-reconstruction technique for low-power centimeter-accurate mobile positioning", *IEEE Trans. on Signal Process.*, vol. 62, no. 10, pp. 2595–2610, 2014.

[32] M. Zhu, J. Vieira, Y. Kuang, K. Åström, A. F. Molisch and F. Tufvesson, "Tracking and positioning using phase information from estimated multi-path components", in *IEEE Int. Conf. on Commun. Workshop (ICCW)*, 2015, pp. 712–717.

[33] J. Salmi, A. Richter and V. Koivunen, "Detection and tracking of MIMO propagation path parameters using state-space approach", *IEEE Trans. Signal Process.*, vol. 57, no. 4, pp. 1538–1550, 2009.

[34] A. Richter, "Estimation of radio channel parameters: Models and algorithms", PhD thesis, Ilmenau University of Technology, 2005.

[35] X. Li, K. Batstone, K. Åström, M. Oskarsson, C. Gustafson and F. Tufvesson, "Robust phase-based positioning using massive MIMO with limited bandwidth", in *IEEE 28th Annu. Int. Symp. on Personal, Indoor, and Mobile Radio Commun. (PIMRC)*, 2017, pp. 1–7.

[36] A. F. Molisch, *Wireless Communications*, 2nd. New York, USA: Wiley Publishing, 2011.

[37] W. Weichselberger, "Spatial structure of multiple antenna radio channels; A signal processing viewpoint", PhD thesis, Technische Universität Wien, 2003.

[38] S. Burgess, Y. Kuang and K. Åström, "ToA sensor network self-calibration for receiver and transmitter spaces with difference in dimension", *Signal Process.*, vol. 107, pp. 33–42, 2015.

[39] H. Stewénius, "Gröbner basis methods for minimal problems in computer vision", PhD thesis, Lund University, 2005.

[40] Y. Kuang, S. Burgess, A. Torstensson and K. Åström, "A complete characterization and solution to the microphone position self-calibration problem", in *IEEE Int. Conf. on Acoust., Speech and Signal Process.*, 2013, pp. 3875–3879.

[41] Y. Bar-Shalom, T. Kirubarajan and X.-R. Li, *Estimation with Applications to Tracking and Navigation*. New York, NY, USA: Wiley, 2002.

[42] P. Paschalidis, J. Nuckelt, K. Mahler, M. Peter, A. Kortke, M. Wisotzki, W. Keusgen and T. Kürner, "Investigation of MPC correlation and angular characteristics in the vehicular urban intersection channel using channel sounding and ray tracing", *IEEE Trans. on Veh. Technol.*, vol. 65, no. 8, pp. 5874–5886, 2016.

[43] B. H. Fleury, M. Tschudin, R. Heddergott, D. Dahlhaus and K. I. Pedersen, "Channel parameter estimation in mobile radio environments using the SAGE algorithm", *IEEE J. Sel. Areas Commun.*, vol. 17, no. 3, pp. 434–450, 1999.

[44] M. Landmann and G. D. Galdo, "Efficient antenna description for MIMO channel modelling and estimation", in *7th European Conf. on Wireless Technol., 2004.*, 2004, pp. 217–220.

[45] M. A. Fischler and R. C. Bolles, "Random sample consensus: A paradigm for model fitting with applications to image analysis and automated cartography", *Commun. ACM*, vol. 24, no. 6, pp. 381–395, 1981.

[46] K. Batstone, M. Oskarsson and K. Åström, "Robust time-of-arrival self calibration with missing data and outliers", in *24th European Signal Process. Conf. (EUSIPCO)*, 2016, pp. 2370–2374.

[47] D. Schuhmacher, B. T. Vo and B. N. Vo, "A consistent metric for performance evaluation of multi-object filters", *IEEE Trans. on Signal Process.*, vol. 56, no. 8, pp. 3447–3457, 2008.

[48] K. Mahler, W. Keusgen, F. Tufvesson, T. Zemen and G. Caire, "Measurement-based wideband analysis of dynamic multipath propagation in vehicular communication scenarios", *IEEE Trans. Veh. Technol.*, vol. 66, no. 6, pp. 4657–4667, 2017.

[49] B. K. Horn, H. M. Hilden and S. Negahdaripour, "Closed-form solution of absolute orientation using orthonormal matrices", *Journal of the Optical Society of America A*, vol. 5, no. 7, pp. 1127–1135, 1988.

[50] W. Kabsch, "A discussion of the solution for the best rotation to relate two sets of vectors", *Acta Crystallographica Section A: Crystal Physics, Diffraction, Theoretical and General Crystallography*, vol. 34, no. 5, pp. 827–828, 1978.

Paper III

Target Tracking using Signal Strength Differences for Long-Range IoT Networks

Radio based positioning or tracking solutions typically require wideband signals or phase coherent antennas. In this paper, we present a target tracking method based on received non-coherent signal strength differences (RSSDs) between antennas for outdoor Internet-of-things (IoT) scenarios. We introduce an RSSD model based on classical path-loss models. With known antenna patterns and antenna array geometries, the RSSD model enables direct mapping between RSSD and angle of arrival, without involving parameters like transmit power, path-loss coefficient, etc. The RSSD model is then exploited in a recursive Bayesian filtering method for target tracking where a particle filter-based implementation is used. The performance is evaluated using outdoor measurements in a low-power wide area network (LoRaWAN) based IoT system. Besides, we also investigate the potential of the RSSD model for AoA estimation. The experimental results show the capability of the proposed framework for real-time target/AoA tracking; reasonable accuracy is achieved even when using non-averaged RSS measurements and under non line-of-sight (NLoS) conditions. Furthermore, the non-coherent approach has low computational complexity, scales well, and is flexible to allow for different antenna array configurations.

X. Li, M. Abou Nasa, F. Rezaei, F. Tufvesson,
"Target Tracking using Signal Strength Differences for Long-Range IoT Networks,"
in *Proc. IEEE Int.Conf. on Commun. Workshops (ICCW)*, Dublin, Ireland, pp. 1-6,
June 2020.

1 Introduction

Location-awareness is a key enabler for various emerging applications related to the Internet-of-things (IoT). Numerous existing commercial systems and research prototypes for localization in IoT scenarios build upon features like time-of-arrival (ToA), angle-of-arrival (AoA), received signal strength (RSS), etc. Among these, RSS-based localization is especially appealing due to its simplicity and broad support for many low-cost technologies, for instance radio frequency identification (RFID), Bluetooth Low Energy, and LoRa [1], with a working range from a few meters up to several kilometers. In this work, we focus on RSS-based localization methods, with particular interest in the middle to long-range outdoor IoT scenarios.

To formulate the localization problem, connected IoT devices are classified as anchor nodes with known locations, and a target node of which the location is to be determined. RSS-based localization and tracking solutions are typically based on proximity, fingerprinting [2], [3] and ranging [4] methods. Fingerprinting-based localization exploits the unique structure of RSS spatial distribution by matching position-labeled RSS measurements with the pre-acquired measurements (fingerprints) at the positions of interest. The performance is influenced by the density of fingerprints and degrades in dynamic scenarios. RSS-based ranging for localization is another common approach. By exploiting a path-loss model (PLM) [5], it is possible to map the RSS measurement to a range estimate, which is further used to infer the target location w.r.t. the anchor coordinates. RSS-based ranging can be unreliable under the conditions of imperfect knowledge about source transmit power, path-loss coefficient, environmental influence, etc. Moreover, it should be noted that long-range IoT systems normally use very high receiver sensitivity for extending the coverage range, but very low bandwidth and packet rate. This means that when tracking a moving target, sufficient RSS samples are often not available to average out small scale fading. Typically, RSS-based ranging for outdoor IoT localization solutions provide accuracies from one to a few hundred meters [6], [7]. Instead of directly using RSS, localization approaches are proposed to use differences between RSS measurements (RSSDs) obtained at, e.g., consecutive sampling steps [8], different anchors [9], [10], or adjacent antennas at each anchor[11]. However, most of them are dedicated to short-range and indoor scenarios.

In this work, each anchor node is assumed to be equipped with an antenna array of known geometry and antenna pattern. On the basis of the PLM, we introduce an RSSD model, which enables direct mapping between the AoAs and the RSSD measurements obtained from non-coherent antennas, without involving parameters like transmit power, path-loss coefficient, etc. The RSSD model is then exploited in a recursive Bayesian filter for target tracking or AoA estimation. Experimental results using outdoor LoRaWAN based measurements show that real-time outdoor target tracking using RSSD

measurements is possible even with non-averaged measurements under NLoS conditions. Besides, the proposed framework has good generality, scales well with different antenna array configurations, and is compatible with different IoT technologies.

The rest of the paper is structured as follows: Section II introduces the RSSD model and problem formulation. Section III presents the RSSD-based tracking algorithms. Experimental results are given in Section IV. Section V concludes the paper.

2 Problem Overview

We consider the case that a target node is equipped with a single antenna and has unknown time-varying positions $\boldsymbol{p}_k = [p_{\mathrm{x},k},\, p_{\mathrm{y},k}]^{\mathrm{T}} \in \mathbb{R}^{2\times 1}$, $k = 1, \cdots, K$. In the area of interest, J anchor nodes are distributed with known positions $\boldsymbol{c}_j \in \mathbb{R}^{2\times 1}$ and known array orientations ϕ_j, $j \in \mathcal{J} \triangleq \{1, \cdots, J\}$. Each anchor node has N_j directional antennas indexed with $i \in \mathcal{N}_j \triangleq \{1, \cdots, N_j\}$ and the angular separation between adjacent antennas is β, as depicted in Fig. 1. The anchor position $\boldsymbol{c}_j$ refers to the center of the array, or more precisely the intersection point of perpendicular lines to antennas' surfaces. The target node is assumed to be the transmitter, and anchor nodes to be the receivers, but with some straightforward modifications, it can work in the opposite direction as well. At time k, AoA $\varphi_{k,j}$ and the propagation distance[8] $d_{k,j}$ from the target to the jth anchor are defined as $\varphi_{k,j} = \angle(\boldsymbol{p}_k - \boldsymbol{c}_j) + \phi_j$ and $d_{k,j} = \|\boldsymbol{p}_k - \boldsymbol{c}_j\|$, $\|\cdot\|$ is the Euclidean norm. With known distance L_{c} from antenna phase center $\boldsymbol{c}_j^i$ to $\boldsymbol{c}_j$, and the orientation α_j^i of the ith antenna w.r.t. the local coordinate system of jth anchor, the propagation distance $d_{k,j}^i$ and AoA $\varphi_{k,j}^i$ w.r.t. ith antenna are easily calculated as $d_{k,j}^i = \sqrt{L_{\mathrm{c}}^2 + (d_{k,j})^2 - 2L_{\mathrm{c}} d_{k,j} \cos\beta_{k,j}^i}$ and $\varphi_{k,j}^i = \varphi_{k,j} + \dfrac{\pi}{2} - \alpha_j^i$, where the angle $\beta_{k,j}^i$ is given as $\beta_{k,j}^i = |\varphi_{k,j} - \alpha_j^i|$ and $|\cdot|$ is the absolute value, Here, we define the domain $\varphi_{k,j} \in [0^\circ \sim 180^\circ]$ as the positive array direction, $\varphi_{k,j} \in (180^\circ \sim 360^\circ)$ as the negative array direction.

[8] We assume that the propagation condition from the target to each anchor is either line-of-sight (LoS) or obstructed LOS (OLoS), hence the propagation distance could be approximately given as the norm product.

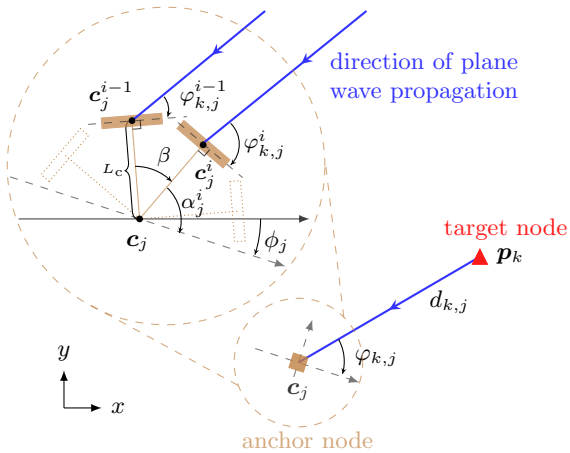

Figure 1: An exemplary antenna array structure equipped at an anchor node.

2.1 RSS model

At time k, the instantaneous received RSS (in dBm) at the ith antenna of jth anchor can be generally expressed as

$$P_{k,j}^{i} = P_0 + G_{\mathrm{Rx}}(\varphi_{k,j}^{i}) - 10\eta \log_{10}\left(\frac{d_{k,j}^{i}}{d_0}\right) + S_{\mathrm{L},k,j}^{i} + S_{\mathrm{S},k,j}^{i}, \tag{1}$$

according to the PLM [5]. The first term on the right side P_0 accounts for the transmit power P_{Tx} (in dBm), the transmit antenna gain G_{Tx} and the path loss $L_{\mathrm{ref}}(d_0)$ at the reference distance $d_0 = 1\,\mathrm{m}$, i.e., $P_0 = P_{\mathrm{Tx}} + G_{\mathrm{Tx}} + L_{\mathrm{ref}}(d_0)$. Furthermore, η is the path-loss coefficient, $G_{\mathrm{Rx}}(\varphi_{k,j}^{i})$ is the receive antenna gain, $S_{\mathrm{L},k,j}^{i}$ models the position-dependent shadowing term, which is slowly varying over time. The last term $S_{\mathrm{S},k,j}^{i}$ models the random and fast variations of RSS in time or space, of which the impact is normally reduced by averaging over multiple samples that are consecutively received within a certain time duration.

RSS-based ranging for localization based on (1) can be problematic. P_{Tx} is typically unknown to receivers, and may vary slowly with battery drain over time. Unknown device orientation leads to the variation of G_{Tx}. η is closely related to the specific characteristics of the environment. As common practice, those parameters are either simultaneously estimated at each time instance, or precomputed from measurements. Under far-field propagation conditions, the parameters P_{Tx}, G_{Tx} and η can be assumed as the same for the antennas at each anchor node. Besides, the position-dependent slow fading process $S_{\mathrm{L},k,j}^{i}$ are highly correlated over adjacent antennas. Inspired by the arguments above,

the difference between RSSs measured at adjacent antennas can be described by a much simpler model than (1), which excludes those unknown but common parameters.

2.2 RSSD model

Based on (1), the RSSD measurement between two antennas of the jth anchor node at time k is modeled as

$$\begin{aligned} P_{\Delta,k,j}^{(a,b)} &= P_{k,j}^{a} - P_{k,j}^{b} \\ &= G_{\Delta,k,j}^{(a,b)}(\varphi_{k,j}) + D_{k,j}^{(a,b)} + \omega_{k,j}^{(a,b)} \end{aligned} \tag{2}$$

where $\{a, b\} \in \mathcal{N}_j$, and $a < b$. The first term on the right side $G_{\Delta,k,j}^{(a,b)}(\varphi_{k,j})$ represents the antenna gain difference, given as

$$G_{\Delta,k,j}^{(a,b)}(\varphi_{k,j}) = G_{\mathrm{Rx}}(\varphi_{k,j}^{a}) - G_{\mathrm{Rx}}(\varphi_{k,j}^{b}). \tag{3}$$

The second term $D_{k,j}^{(a,b)} = 10\eta \log_{10} \frac{d_{k,j}^{b}}{d_{k,j}^{a}}$ in (2) involves the propagation distances and path-loss coefficient. The last term $\omega_{k,j}^{(a,b)}$ accounts for the difference between two independent fast fading processes, the difference between two highly correlated slow fading processes, as well as hardware-related impairments. Fig. 2 shows simulated values of $D_{k,j}^{(a,b)}$ by assuming $\eta = 3.5$ and $\beta = 45°$. It can be observed that given a constant AoA $\varphi_{k,j}$, the value of $D_{k,j}^{(a,b)}$ drops to under 1 dB after 5 m and continuously converges to 0 dB with distance $d_{k,j}$ increasing. Since we focus on scenarios where the distance $d_{k,j}$ is at least a few tens of meters, $D_{k,j}^{(a,b)}$ has a negligible impact on $P_{\Delta,k,j}^{(a,b)}$ compared to the other two terms in (2). Hence, the model (2) can be further simplified as

$$P_{\Delta,k,j}^{(a,b)} \triangleq G_{\Delta,k,j}^{(a,b)}(\varphi_{k,j}) + \omega_{k,j}^{(a,b)}. \tag{4}$$

An experimental measurement is performed to test how the simplified model works. Two directional antennas shown in Fig. 5b are placed in the middle of the open field (4.1) with the angular separation $\beta = 45°$ and one wavelength distance between phase centers. RSS samples are measured every 5° in the angular domain $\varphi_{k,j} \in [0° \sim 360°)$ while keeping $d_{k,j} = 20$ m. As shown in Fig. 3, the measured RSSDs with/without averaging match well with the predicted RSSD values $G_{\Delta,k,j}^{(a,b)}(\varphi_{k,j})$ in the positive array direction. In the negative array direction, the measured RSSDs show a similar but noisier pattern as $G_{\Delta,k,j}^{(a,b)}(\varphi_{k,j})$. We also noticed that one RSSD value is not uniquely mapped to one AoA, meaning that the posterior distribution of the AoA given one RSSD

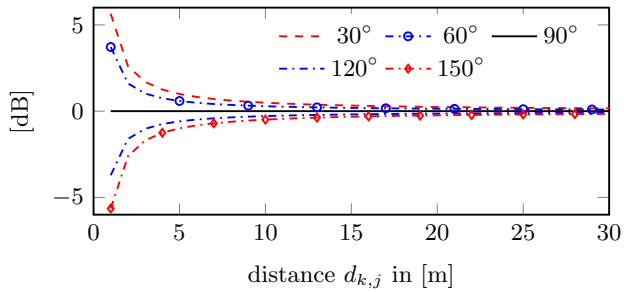

Figure 2: Experimental values of $D_{k,j}^{(a,b)}$ as a function of varying distance $d_{k,j}$ while keeping constant AoA $\varphi_{k,j}$.

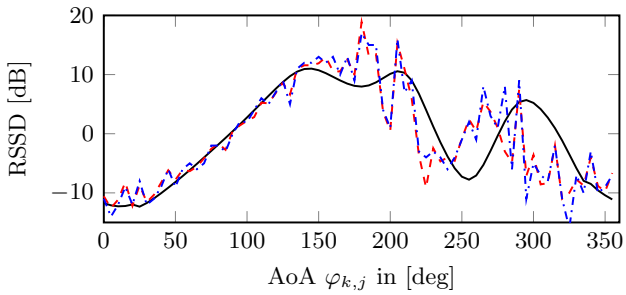

Figure 3: Comparison of ground truth RSSD $G_{\Delta,k,j}^{(a,b)}$ (——) and measured RSSDs $P_{\Delta,k,j}^{(a,b)}$: RSS samples are averaged at each AoA (- - -); one RSS sample is used at each AoA (-·-·-).

measurement can be multimodal. However, fusing RSSD measurements from more than one antenna pair and anchors would lead to a unimodal distribution. According to the empirical density of RSSD errors shown in Fig. 4, $\omega_{k,j}^{(a,b)}$ approximately follows a Gaussian process, i.e., $\omega_{k,j}^{(a,b)} \sim \mathcal{N}(\mu_{k,j}, \sigma_{k,j}^2)$, with the mean $\mu_{k,j}$ close to zero.

2.3 Target Tracking and AoA Estimation Problems

In reality, it is possible that at some time instances only a subset of antennas of each anchor, i.e., $\mathcal{N}'_{k,j}$ and $\mathcal{N}'_{k,j} \subseteq \mathcal{N}_j$, provide valid RSS measurements. At time k, we assume that at least two antennas at each anchor provide RSS measurements, i.e., $\text{card}\{\mathcal{N}'_{k,j}\} \geq 2$, $\text{card}\{\cdot\}$ represents the cardinality of a set. The RSSD measurements at the jth anchor are given as $\boldsymbol{z}_{k,j} = [z_{k,j}^1, \ldots, z_{k,j}^{l_{j,k}}, \ldots, z_{k,j}^{L_{j,k}}]^{\mathrm{T}}$, with $l_{j,k} \in \mathcal{L}_{j,k} \triangleq \{1, \cdots, L_{j,k}\}$. Each RSSD measurement $z_{k,j}^{l_{j,k}}$ is obtained by taking the differences between RSS measurements

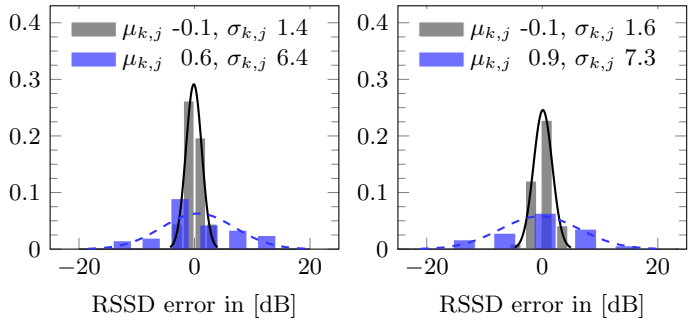

Figure 4: Empirical density of RSSD errors $|P^{(a,b)}_{\Delta,k,j} - G^{(a,b)}_{\Delta,k,j}|$. (a) samples are averaged at each AoA, (b) one sample is used at each AoA. Array positive direction: ▬, negative direction: ▬.

from antenna pairs with adjacent indexes, for instance $\{a_{l_{j,k}}, b_{l_{j,k}}\} \in \mathcal{N}'_{k,j}$, and $a_{l_{j,k}} < b_{l_{j,k}}$. Hence, the number of RSSD measurements $L_{j,k} = \text{card}\{\mathcal{N}'_{k,j}\} - 1$ is time variant. By stacking the vectors $\boldsymbol{z}_{k,j}$ from all anchors, we have the full measurement vector at time k, $\boldsymbol{z}_k = [\boldsymbol{z}^{\mathrm{T}}_{k,1}, \ldots, \boldsymbol{z}^{\mathrm{T}}_{k,j}, \ldots, \boldsymbol{z}^{\mathrm{T}}_{k,J}]^{\mathrm{T}}$.

As a proof-of-concept work, we investigate the potential of the proposed RSSD model in two aspects: i) tracking the target node $\boldsymbol{p}_k$ by fusing all the past and current measurements from all anchors $\boldsymbol{z}_{1:k} = [\boldsymbol{z}^{\mathrm{T}}_1, \ldots, \boldsymbol{z}^{\mathrm{T}}_k]^{\mathrm{T}}$; ii) recursively estimating the AoA $\varphi_{k,j}$ using RSSD measurements from a single anchor, $\boldsymbol{z}_{1:k,j} = [\boldsymbol{z}^{\mathrm{T}}_{1,j}, \ldots, \boldsymbol{z}^{\mathrm{T}}_{k,j}]^{\mathrm{T}}$. The reason to bring up the second aspect is that AoA estimates can potentially be fused with existing ranging features, such as the TDoA in LoRaWAN, to enhance outdoor IoT localization.

3 RSSD-based Tracking Algorithms

3.1 Target Tracking

State Space and Measurement Model

The state space vector of the target at time k is given by $\boldsymbol{x}_k = [\boldsymbol{p}^{\mathrm{T}}_k, \Delta\boldsymbol{p}^{\mathrm{T}}_k]^{\mathrm{T}} \in \mathbb{R}^{4\times 1}$, where the vector $\Delta\boldsymbol{p}_k = [\Delta p_{\mathrm{x},k}, \Delta p_{\mathrm{y},k}]^{\mathrm{T}} \in \mathbb{R}^{2\times 1}$ contains the change rates of the target position $\boldsymbol{p}_k$. The agent state evolves according to a first-order Markov process. The evolution of the state $\boldsymbol{x}_k$ is described by the state-transition probability density function (pdf) $f(\boldsymbol{x}_k|\boldsymbol{x}_{k-1})$, which is defined by a linear, near constant-velocity model [12, Section 6.3.2], i.e.,

$$\boldsymbol{x}_k = \boldsymbol{F}\boldsymbol{x}_{k-1} + \boldsymbol{\Gamma}\boldsymbol{n}_k, \tag{5}$$

where the state transition matrix $\boldsymbol{F} \in \mathbb{R}^{4\times4}$ and $\boldsymbol{\Gamma} \in \mathbb{R}^{4\times2}$ are given as

$$\boldsymbol{F} = \begin{bmatrix} 1 & 0 & \Delta T & 0 \\ 0 & 1 & 0 & \Delta T \\ 0 & 0 & \Delta T & 0 \\ 0 & 0 & 0 & \Delta T \end{bmatrix}, \quad \boldsymbol{\Gamma} = \begin{bmatrix} \frac{\Delta T^2}{2} & 0 \\ 0 & \frac{\Delta T^2}{2} \\ \Delta T & 0 \\ 0 & \Delta T \end{bmatrix}. \tag{6}$$

Here, ΔT is the update rate, $\boldsymbol{n}_k \in \mathbb{R}^{2\times1}$ is the driving process that is independent and identically distributed (iid) across k, zero-mean and Gaussian with covariance matrix $\sigma_{\mathrm{n}}^2 \boldsymbol{I}_2$. $\boldsymbol{I}_2$ represents the 2×2 identity matrix. The corresponding measurement model which describes the non-linear mapping from state vector to an RSSD measurement is defined as

$$z_{k,j}^{l_{j,k}} = G_{\Delta,k,j}^{(a_{l_{j,k}},b_{l_{j,k}})}(\boldsymbol{x}_k) + \omega_{l_{j,k}}, \tag{7}$$

where $G_{\Delta,k,j}^{(a_{l_{j,k}},b_{l_{j,k}})}(\boldsymbol{x}_k)$ represents the nonlinear mapping from the hidden state $\boldsymbol{x}_k$ to an RSSD observation described in (3), and $\omega_{l_{j,k}}$ is iid across $l_{j,k}$, j and k, zero-mean and Gaussian with variance σ_{g}^2.

Recursive Bayesian Filtering

The estimation of the target state $\boldsymbol{x}_k$ is formulated as a Bayesian filtering problem, where the posterior pdf $f(\boldsymbol{x}_k|\boldsymbol{z}_{1:k})$ is recursively obtained in two stages: prediction and update. The prediction step is based on the Chapman-Kolmogorov equation [13]

$$f(\boldsymbol{x}_k|\boldsymbol{z}_{1:k-1}) = \int f(\boldsymbol{x}_k|\boldsymbol{x}_{k-1}) f(\boldsymbol{x}_{k-1}|\boldsymbol{z}_{1:k-1}) \mathrm{d}\boldsymbol{x}_{k-1}, \tag{8}$$

and an update step is performed based on Bayes' rule

$$f(\boldsymbol{x}_k|\boldsymbol{z}_{1:k}) = \frac{f(\boldsymbol{z}_k|\boldsymbol{x}) f(\boldsymbol{x}_k|\boldsymbol{z}_{1:k-1})}{f(\boldsymbol{z}_k|\boldsymbol{z}_{1:k-1})} \tag{9}$$

given the measurement at time k. Assuming that the measurement $z_{k,j}^{l_{j,k}}$ is conditionally independent across $l_{j,k}$ and j given the target state $\boldsymbol{x}_k$, the likelihood function $f(\boldsymbol{z}_k|\boldsymbol{x}_k)$ is factorized as

$$f(\boldsymbol{z}_k|\boldsymbol{x}_k) = \prod_{j=1}^{J} \prod_{l_{j,k}=1}^{L_{j,k}} f(z_{k,j}^{l_{j,k}}|\boldsymbol{x}_k) \tag{10}$$

where

$$f(z_{k,j}^{l_{j,k}}|\boldsymbol{x}_k) = \frac{1}{\sqrt{2\pi\sigma_{\mathrm{g}}^2}} \exp\Big\{ - \frac{(z_{k,j}^{l_{j,k}} - G_{\Delta,k,j}^{(a_{l_{j,k}}, b_{l_{j,k}})}(\boldsymbol{x}_k))^2}{2\sigma_{\mathrm{g}}^2} \Big\}. \tag{11}$$

An estimate of the target state $\boldsymbol{x}_k$ is then provided by the minimum mean-square error (MMSE) estimator[14], given as

$$\hat{\boldsymbol{x}}_k^{\mathrm{MMSE}} \triangleq \int \boldsymbol{x}_k f(\boldsymbol{x}_k|\boldsymbol{z}_{1:k}) \mathrm{d}\boldsymbol{x}_k. \tag{12}$$

Particle-Based Implementation

A sequential Monte Carlo (particle-based) implementation [15] is used to realize the recursive Bayesian filtering process, where the prediction and update steps are formulated in an approximate manner. The posterior pdf $f(\boldsymbol{x}_k|\boldsymbol{z}_{1:k})$ is represented by a finite set of particles and corresponding weights, $\{(\bar{\boldsymbol{x}}_k^m, \bar{w}_k^m)\}_{m=1}^M$. Here, M is the number of particles and the weights sum to one, i.e., $\sum_{m=1}^M \bar{w}_k^m = 1$. At time k, the particles are predicted by simply passing the filtered particles at time $k-1$ through the system dynamics as shown in (6), yielding

$$\bar{\boldsymbol{x}}_k^m \sim f(\bar{\boldsymbol{x}}_k^m|\bar{\boldsymbol{x}}_{k-1}^m). \tag{13}$$

Then in the measurement update step, the weights $\bar{w}_k^m$ are computed according to (10), i.e., $\bar{w}_k^m = f(\boldsymbol{z}_k|\bar{\boldsymbol{x}}_k^m)$, and normalized as $\bar{w}_k^m = \bar{w}_k^m / \sum_{m=1}^M \bar{w}_k^m$. Two more steps are introduced after measurement update, i.e., resampling and regularization, to counteract particle degeneracy and impoverishment effects. The reader is referred to [13], [15] for more details. The posterior pdf can be approximated as $f(\boldsymbol{x}_k|\boldsymbol{z}_{1:k}) \approx \sum_{m=1}^M \bar{w}_k^m K(\boldsymbol{x}_k - \bar{\boldsymbol{x}}_k^m)$ where $K(\cdot)$ denotes the regularization Gaussian Kernel. An approximation of the MMSE state estimate (12) is calculated according to

$$\hat{\boldsymbol{x}}_k^{\mathrm{MMSE}} \approx \sum_{m=1}^{M} \bar{w}_k^m \bar{\boldsymbol{x}}_k^m. \tag{14}$$

The four steps are iterated after setting $k = k+1$.

At time $k = 1$, the particles are initialized by drawing samples $\bar{\boldsymbol{x}}_1^m$ from the prior pdf $f(\boldsymbol{x}_1|\boldsymbol{z}_1) \equiv f(\boldsymbol{x}_1)$. Two situations are considered here: i) *no-prior*: if no informative prior pdf $f(\boldsymbol{x}_1)$ is available, a 2-D uniform distribution with zero center and radius σ_p is used to initialize $\bar{\boldsymbol{p}}_1^m$, and for the position change rate, we use $\{\Delta\bar{p}_{\mathrm{x},1}^m, \Delta\bar{p}_{\mathrm{y},1}^m\} \sim \mathcal{U}(-\sigma_{\Delta p}, \sigma_{\Delta p})$; ii) *noisy-prior*: if noisy information of the ground truth start position $\boldsymbol{p}_1$ is given, $\bar{\boldsymbol{x}}_1^m$ follows a 2-D

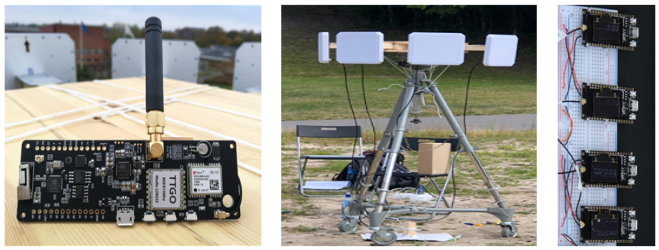

(a) **(b)** **(c)**

Figure 5: Experimental measurement setup: (a) target node: TTGO T-Beam ESP32 module. (b) anchor node 1: four 9 dBi circular antennas are used, and each antenna is connected to a TTGO-LORA32 gateway shown in (c).

uniform distribution with radius σ_p' and center $\boldsymbol{p}_1$.

3.2 AoA Estimation

The AoA estimation problem is solved by following the same steps given in 3.1. A few minor differences in the formulation are presented here. The AoA state vector is given as $\boldsymbol{x}_k = [\varphi_{k,j},\, \Delta\varphi_{k,j}]^{\mathrm{T}} \in \mathbb{R}^{2\times 1}$, where $\Delta\varphi_{k,j}$ is the change rate of $\varphi_{k,j}$. Accordingly, the sizes of the matrices in (5) should be adjusted, more details can be found in [12]. Only measurements from the jth anchor are involved in the likelihood function calculation in (10). We assume no prior pdf $f(\boldsymbol{x}_1)$ is available, hence the particles are initialized from a uniform distribution $\bar{\varphi}_{1,j}^m \sim \mathcal{U}(-\pi,\, \pi)$ and $\Delta\bar{\varphi}_{1,j}^m \sim \mathcal{U}(-\sigma_\varphi,\, \sigma_\varphi)$.

4 Experimental Results

4.1 Measurement Setup

A LoRaWAN network [1] is used in our experimental setup, where a single-hop link is established between the target node and the gateways. The gateways are connected to a network server via standard IP protocols, and act as bidirectional relays to convert between RF packets and IP packets. The data like GPS "ground truth" and RSS values are decoded in the network server. As shown in Fig. 5, the target node is equipped with an omnidirectional antenna and the transmit power is 14 dBm. Two anchor nodes are used, which are equipped with four and three directional antennas respectively, i.e., $N_1 = 4$ and $N_2 = 3$. The positive array directions are pointing to the target moving areas. The distance between the phase centers of two adjacent antennas is one wavelength, and the angular separation is $\beta = 45°$. One of the receive antenna

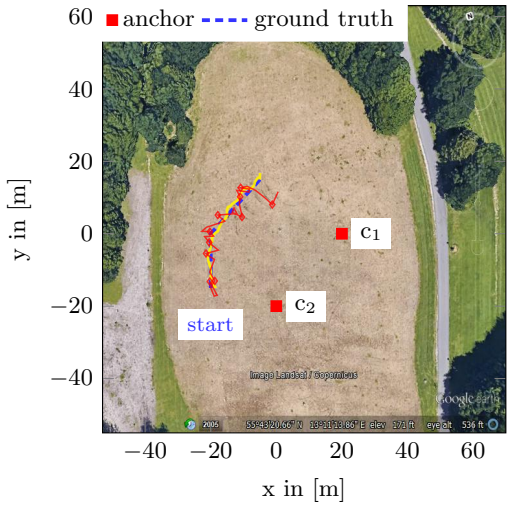

Figure 6: Target tracking results for open field datasets: *open field-ave* + *no-prior* (——); *open field-one* + *no-prior* (—⋄—). .Background map: © 2019 Google

beam patterns is measured and assumed to be the same for the rest of the antennas. The maximum spreading factor 12 is used to achieve the longest range, however at the cost of low data rate. The system is operating at the carrier frequency 868 MHz, with a bandwidth of 125 kHz. The gateways are listening to several different channels, every 6 seconds one packet is received at each antenna.

The measurement campaign was performed in two different outdoor scenarios, which are described as follows:

LoRa open field

The first scenario is an open field surrounded by rich vegetation in Sankt Hans backar, Lund, as shown in Fig. 6. The target node and two anchor nodes are placed at the same height about 1.5 m above the ground. LoS condition is satisfied and measurements are received at all antennas during the whole measurement time. In total, RSS measurements are collected at $K = 38$ sample positions, and the distance inbetween is 1 m. At each position, around five RSS samples are measured at each antenna. Parameters used in the tracking algorithms are: $M = 2000$, $\Delta T = 1\,\text{s}$, $\sigma_p = 40\,\text{m}$ and $\sigma_{\Delta p} = 1.5\,\text{m/s}$, $\sigma_\varphi = 3\,\text{degree/s}$, $\sigma_\text{g} = 2.5\,\text{dB}$.

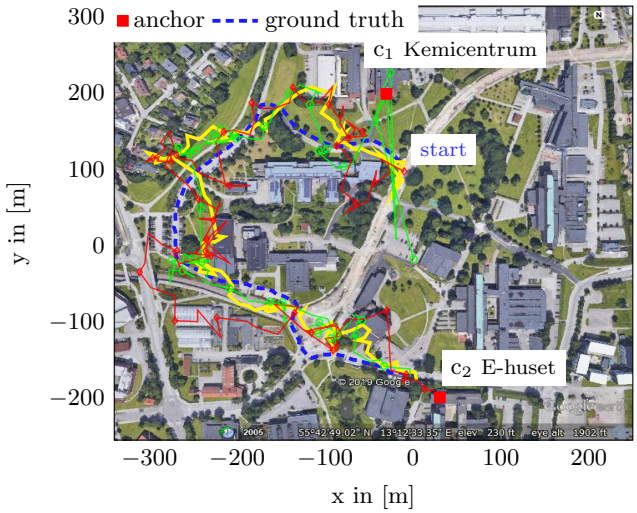

Figure 7: Target tracking results for urban datasets: *urban-ave* + *noisy-prior* (——); *urban-ave* + *no-prior* (—○—); *urban-one* + *noisy-prior* (—◇—). Background map: © 2019 Google

LoRa urban

The second scenario is the campus of Lund University, Sweden, as shown in Fig. 7. Two anchor nodes are placed on two building roofs, which are around 20 m above the ground. The target node is carried by a person walking along a predefined trajectory at a speed around 1 m/s. Every 6 seconds, the movement is paused and we collect around three samples at each antenna. At a few positions, only a subset of antennas provide valid RSS measurements. In total, we have $K = 120$ sample positions. The decoded GPS data from the network server is used as ground truth. Parameters used in the tracking algorithms are: $M = 2000$, $\Delta T = 1\,\text{s}$, $\sigma_p = 400\,\text{m}$, $\sigma_{\Delta p} = 7\,\text{m/s}$, $\sigma'_p = 50\,\text{m}$, $\sigma_\varphi = 5\,\text{degree/s}$, and $\sigma_\text{g} = 3.6\,\text{dB}$.

Using the measured RSS samples, we generate two type of datasets for performance evaluation: i) *open field-ave* and *urban-ave*: multiple RSS samples collected from the same antenna at each position are averaged; ii) *open field-one* and *urban-one*: only one RSS sample of each antenna is used.

4.2 Results

Target tracking

Fig. 8 and Fig. 9 present the target position estimation errors and corresponding empirical cumulative distribution functions (CDFs). For the open field

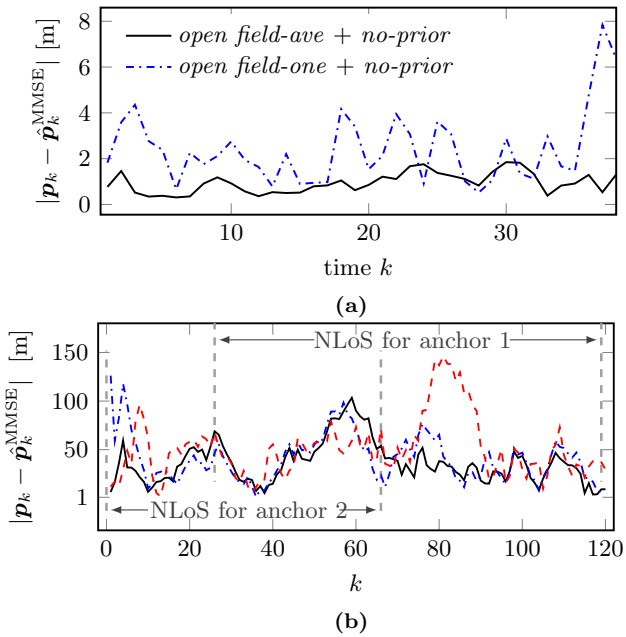

Figure 8: Target position estimation error: (a) open field datasets; (b) urban datasets: *urban-ave + noisy-prior* (——), *urban-ave + no-prior* (-·-·-), *urban-one + noisy-prior* (- - -). NLoS domains for anchors are denoted with gray dashed lines.

scenario, even without a prior information, the tracking algorithm gives a good initial estimate at $k = 1$ with/without measurement averaging. as shown in Fig. 6. The root mean square position error (RMSE) of the target is 1 m for *open field-ave* and 2.9 m for *open field-one*. The urban scenario is quite challenging, because during the whole measurement time, it is NLoS propagation from the target to one or both anchors. However, the anchors are placed on the high buildings, if the signal is received via roof diffraction, the information of target direction still remains. The target's RMSE is 42 m for *urban-ave + noisy-prior*, 47.5 m for *urban-ave + no-prior*. Given the most challenging scenario, i.e., *urban-one*, 59.5 m RMSE is achieved with a noisy prior, meaning that real-time outdoor target tracking is possible with RSSD measurements using the proposed framework.

AoA estimation

Empirical CDFs of AoA estimation errors are shown in Fig. 10. It can be observed that anchor 2 achieves similar performance as anchor 1 for all datasets, even with fewer RSSD measurements. Using *open field-ave* dataset, 90% of AoA estimation errors are smaller than 2°, and it increases to 5° when there

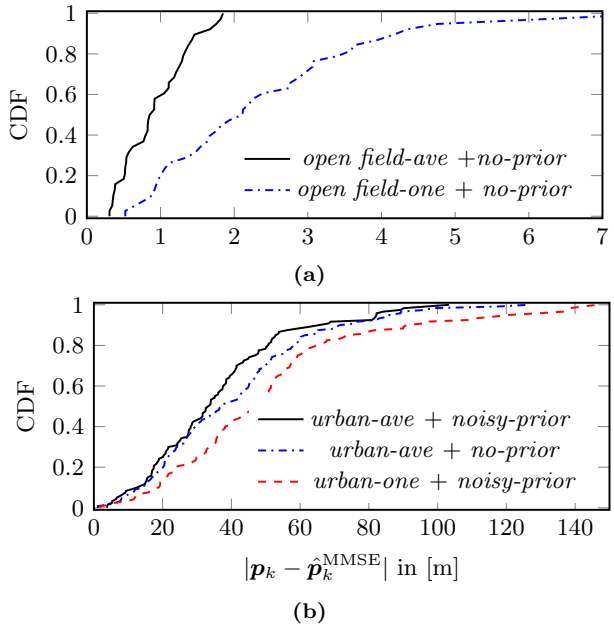

Figure 9: Empirical CDFs of the position estimation errors: (a) open field datasets; (b) urban datasets.

is no sample averaging (*open field-one*). As shown in Fig. 10b, 90% of errors are smaller than 11° when using *urban-ave*, and 19° when using *urban-one*. It means that for long-range and NLoS propagation conditions, AoA estimates with reasonable accuracy are feasible with the proposed framework. However, averaging over RSS samples did not show significant improvements of the estimates in our case.

5 Conclusion

We proposed an RSSD-based target-tracking/AoA-estimation algorithm for outdoor IoT scenarios. Given known antenna patterns and antenna array geometries, the RSSD model provides direct mapping between AoAs and RSSD measurements, without involving transmit power, path-loss coefficient, phase coherent arrays, etc. Experimental results using LoRaWAN based outdoor measurements show that the proposed framework is able to perform real-time target tracking with reasonable accuracy even without RSS measurements averaging and under NLoS propagation conditions. The AoA estimates can potentially be fused with range estimates to enhance localization. In summary, the proposed framework has very low computational complexity, and is com-

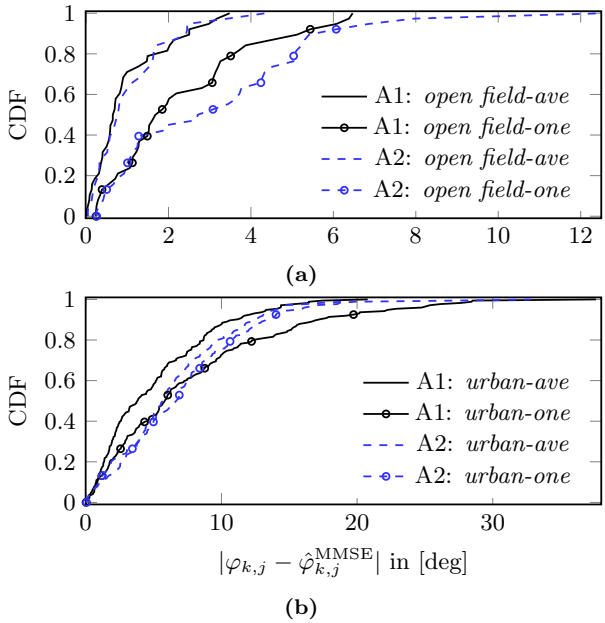

Figure 10: Empirical CDFs of the AoA estimation errors. (a) open field datasets; (b) urban datasets. Anchor 1 and 2 are abbreviated to A1 and A2.

patible with existing low cost IoT technologies and with different antenna array configurations.

6 Acknowledgment

This work was supported in part by the Swedish Research Council (VR), in part by the strategic research area ELLIIT.

References

[1] M. Centenaro, L. Vangelista, A. Zanella and M. Zorzi, "Long-range communications in unlicensed bands: The rising stars in the IoT and smart city scenarios", *IEEE Wirel. Commun.*, vol. 23, no. 5, pp. 60–67, 2016.

[2] S. Yiu, M. Dashti, H. Claussen and F. Perez-Cruz, "Wireless RSSI fingerprinting localization", *Signal Process.*, vol. 131, pp. 235 –244, 2017.

[3] H. Sallouha, A. Chiumento, S. Rajendran and S. Pollin, "Localization in ultra narrow band IoT networks: Design Guidelines and Trade-Offs", *CoRR*, vol. abs/1907.11205, 2019. arXiv: 1907.11205.

[4] S. Tomic, M. Beko and R. Dinis, "RSS-based localization in wireless sensor networks using convex relaxation: Noncooperative and cooperative schemes", *IEEE Trans. Veh. Technol.*, vol. 64, no. 5, pp. 2037–2050, 2015.

[5] A. Zanella, "Best practice in RSS measurements and ranging", *IEEE Commun. Surveys Tuts.*, vol. 18, no. 4, pp. 2662–2686, Fourthquarter 2016.

[6] N. Podevijn, D. Plets, J. Trogh, L. Martens, P. Suanet, K. Hendrikse and W. Joseph, "TDoA-based outdoor positioning with tracking algorithm in a public LoRa network", *Wirel. Commun. & Mobile Comput.*, p. 9, 2018.

[7] "LoRa alliance geolocation whitepaper", *LoRa Alliance*, 2018.

[8] Z. Jia and B. Guan, "Received signal strength difference–based tracking estimation method for arbitrarily moving target in wireless sensor networks", *Int. J. Distrib. Sens. Netw.*, vol. 14, no. 3, 2018.

[9] H. Lohrasbipeydeh, T. A. Gulliver and H. Amindavar, "Blind received signal strength difference based source localization with system parameter errors", *IEEE Trans. Signal Process.*, vol. 62, no. 17, pp. 4516–4531, 2014.

[10] A. K. M. M. Hossain and W. Soh, "Cramer-Rao bound analysis of localization using signal strength difference as location fingerprint", in *Proc. IEEE INFOCOM*, 2010, pp. 1–9.

[11] J. Jiang, C. Lin, F. Lin and S. Huang, "ALRD: AoA localization with RSSI differences of directional antennas for wireless sensor networks", in *Int. Conf. on Inform. Soc. (i-Society 2012)*, 2012, pp. 304–309.

[12] Y. Bar-Shalom, T. Kirubarajan and X.-R. Li, *Estimation with Applications to Tracking and Navigation*. New York, NY, USA: Wiley, 2002.

[13] S. Thomas, "Estimation of nonlinear dynamic systems: Theory and applications", PhD thesis, Linköpings Universitet, 2006.

[14] S. M. Kay, *Fundamentals of Statistical Signal Processing: Estimation Theory*. Upper Saddle River, NJ, USA: Prentice-H, 1993.

[15] M. S. Arulampalam, S. Maskell, N. Gordon and T. Clapp, "A tutorial on particle filters for online nonlinear/non-Gaussian Bayesian tracking", *IEEE Trans. Signal Process.*, vol. 50, no. 2, pp. 174–188, 2002.

Paper IV

RSS-Based Localization of Low-Power IoT Devices Exploiting AoA and Range Information

We present a localization algorithm for low-power long-range Internet-of-things (IoT) networks, which exploits angle of arrival (AoA) and range information from non-coherent received signal strength (RSS) measurements. In this work, each anchor node is equipped with array antennas of known geometry and radiation patterns. The position of the target node and the path-loss exponent to each anchor are unknown and possibly time-varying. The joint estimation problem is formulated with a Bayesian model, where the likelihood functions are derived from the classical path-loss model and an RSS difference model. A message passing method is then exploited for efficient computation of the marginal posterior distribution of each unknown variable. The proposed algorithm is validated using real outdoor measurements from a low-power wide area network based IoT system in a challenging scenario. Results show that the proposed algorithm can adapt to dynamic propagation conditions, and improve the localization accuracy compared to a method that exploits only single geometric feature. Furthermore, the algorithm scales well in different antenna array configurations, and is compatible with various existing IoT standards.

1 Introduction

Location-awareness is a key enabler for various emerging applications related to the Internet-of-things (IoT). Existing localization methods applied in IoT scenarios typically build upon features like time-of-arrival (ToA), angle-of-arrival (AoA), or received signal strength (RSS). Among these, RSS-based localization is especially appealing due to its broad support from low-cost technologies, such as the radio frequency identification, Bluetooth Low Energy, and low-power wide area network (LPWAN) [1] technologies like SIGFOX and LoRa. In this work, we focus on RSS-based localization methods, with particular interest in mid- to long-range outdoor scenarios.

To formulate the localization problem, connected IoT devices are classified as a target node of which the location is to be determined and anchor nodes with known locations. In general, target localization using RSS measurements are based on proximity, fingerprinting [2], [3] or ranging [4], [5] methods. Fingerprinting-based localization exploits the unique structure of the spatial distribution of RSS measurements by matching an RSS measurement with pre-acquired RSS measurements (fingerprints) at the positions of interest. The achievable accuracy is related to the density of fingerprints and degrades in dynamic scenarios. RSS-based ranging for localization is another common method. By exploiting the path-loss model (PLM) [5], it is possible to map an RSS measurement to a range estimate, which is further used to infer the target location w.r.t. the anchor coordinates. However, RSS-based ranging can be unreliable under the conditions of imperfect knowledge of path-loss exponent (PLE) and environmental influence. Typically, RSS-based ranging for outdoor IoT localization provide accuracies from one to a few hundred meters [6]. In recent years, the potential of AoA estimation using non-coherent RSS measurements for target localization is explored in some works [7], [8]. Angle information is mostly obtained by using phase coherent antennas, however this is not feasible for IoT networks when maintaining a low system cost. Most of the existing localization methods have in common that they exploit a single geometric feature, as for example range or angle, and are dedicated to short-range and indoor scenarios.

In this work, we propose a massage passing algorithm for target tracking, that exploits both range and angle information from RSS measurements obtained from anchors equipped with non-coherent antenna arrays. To be adaptive to dynamic propagation conditions, the PLE to each anchor is assumed to be unknown and time-varying. The joint estimation of the target location and PLEs is formulated in a Bayesian sense, where the likelihood functions are derived from the classical path-loss model [5] and an RSS difference (RSSD) model [8]. The statistical model is represented with a factor graph which enables the use of message passing for efficient computation of the marginal posterior distribution of each unknown variable. Furthermore, an interacting

multiple model (IMM) method is used to resolve the motion uncertainty of the target [9]. The results are validated using real outdoor measurements from an IoT network based on LoRa system.

2 Problem Formulation

We consider the case that a target node is equipped with an omnidirectional antenna and has unknown time-varying state $\boldsymbol{x}_n \triangleq [\boldsymbol{p}_n^{\mathrm{T}}, \boldsymbol{v}_n^{\mathrm{T}}]^{\mathrm{T}} \in \mathbb{R}^{4\times 1}$, $n = 1, \cdots, N$, where $\boldsymbol{p}_n \in \mathbb{R}^{2\times 1}$ is the position and $\boldsymbol{v}_n \in \mathbb{R}^{2\times 1}$ is the velocity. In the area of interest, anchor nodes indexed by $s \in \mathcal{S} \triangleq \{1, \cdots, S\}$ are distributed with known static positions $\boldsymbol{c}_s \in \mathbb{R}^{2\times 1}$ and array orientations ϕ_s. Each anchor node is equipped with A_s directional antennas indexed by $a \in \mathcal{A}_s \triangleq \{1, \cdots, A_s\}$, and the radiation patterns are assumed to be known. At time n, the AoA $\varphi_{n,s}$ (w.r.t. the sth anchor's coordinate system) and the propagation distance $d_{n,s}$ from the target to the center $\boldsymbol{c}_s$ of the sth anchor are defined as $\varphi_{n,s} = \angle(\boldsymbol{p}_n - \boldsymbol{c}_s) + \phi_s$ and $d_{n,s} = \|\boldsymbol{p}_n - \boldsymbol{c}_s\|$. The AoA $\varphi_{n,s}^a$ w.r.t. the ath antenna's local coordinate system and the distance $d_{n,s}^a$ to the ath antenna's phase center can be easily calculated from $d_{n,s}$ and $\varphi_{n,s}$ given known array geometry as shown in [8].

2.1 RSS Model and RSSD model

At time n, the RSS (in dBm) obtained at the ath antenna of sth anchor is given as

$$P_{n,s}^a \triangleq P_{0,s} + G_{\mathrm{Rx}}(\varphi_{n,s}^a) - 10\eta_{n,s}\log_{10}\left(\frac{d_{n,s}^a}{d_0}\right) + S_{n,s}^a + n_{n,s}^a\,, \tag{1}$$

according to the path-loss model [5]. The first term on the right side $P_{0,s}$ accounts for the transmit power P_{Tx} (in dBm), the transmit antenna gain G_{Tx} and the path loss $L_{\mathrm{ref},s}(d_0)$ at the reference distance $d_0 = 1\,\mathrm{m}$, i.e., $P_{0,s} = P_{\mathrm{Tx}} + G_{\mathrm{Tx}} + L_{\mathrm{ref},s}(d_0)$, $L_{\mathrm{ref},s}(d_0) = 20\log_{10}(\frac{\lambda}{4\pi}) - 10\eta_{n,s}\log_{10}(d_0)$, and λ is the wavelength. Furthermore, $G_{\mathrm{Rx}}(\varphi_{n,s}^a)$ is the receive antenna gain at angle $\varphi_{n,s}^a$, $\eta_{n,s}$ is the PLE, and $S_{n,s}^a \sim \mathcal{N}(0, \sigma_{\mathrm{S}}^2)$ models the log-normal shadow fading, which is independent and identically distributed (iid) across n and s. The shadow fading processes at adjacent antennas of each anchor are highly correlated and the correlation is denoted by C_{LSF}. We assume that P_{Tx} and G_{Tx} are known; $\eta_{n,s}$ is time-varying, unknown and independent across n and s. Here, the small scale fading and the measurement noise are jointly modeled using a zero-mean and Gaussian distribution that is iid across n, s and a, i.e., $n_{n,s}^a \sim \mathcal{N}(0, \sigma_{\mathrm{n}}^2)$, with variance σ_{n}^2.

Based on (1), the RSSD measurement between two adjacent antennas of the jth anchor node at time n is modeled as [8]

$$P_{\Delta,n,s}^{(r_1,r_2)} \triangleq G_{\Delta,n,s}^{(r_1,r_2)}(\varphi_{n,s}) + \omega_{n,s}^{(r_1,r_2)} \tag{2}$$

where the first term $G_{\Delta,n,s}^{(r_1,r_2)}(\varphi_{n,s})$ represents the antenna gain difference, given as $G_{\Delta,n,s}^{(r_1,r_2)}(\varphi_{n,s}) = G_{\mathrm{Rx}}(\varphi_{n,s}^{r_1}) - G_{\mathrm{Rx}}(\varphi_{n,s}^{r_2})$, with $\{r_1, r_2\} \in \mathcal{A}_s$, and $r_1 < r_2$. The noise term $\omega_{n,s}^{(r_1,r_2)}$ is approximated as the difference between two iid noise processes $n_{n,s}^{r_1}$ and $n_{n,s}^{r_2}$, thus $\omega_{n,s}^{(r_1,r_2)} \sim \mathcal{N}(0,\, 2\sigma_{\mathrm{n}}^2)$.

The models (1) and (2) provide nonlinear mappings from the hidden state $\boldsymbol{x}_n$ of the target to RSS and RSSD observations, which enables the proposed algorithm to infer and fuse the distance and AoA information for target localization.

2.2 Inference Problem

In reality, it happens that at some time instances only a subset of antennas of each anchor, i.e., $\mathcal{K}_{n,s} \subseteq \mathcal{A}_s$, provide valid RSS measurements. Hence, the number $K_{n,s} = |\mathcal{K}_{n,s}|$ of RSS measurements $z_{n,s}^k$, $k \in \mathcal{K}_{n,s} \triangleq \{1, \cdots, K_{n,s}\}$ is time-varying. Accordingly, the RSSD measurement $z_{\mathrm{D},n,s}^l$ with $l \in \mathcal{L}_{n,s} \triangleq \{1, \cdots, L_{n,s}\}$ and $L_{n,s} = K_{n,s} - 1$ is obtained by taking the difference between RSS measurements from antenna pairs with adjacent indices, i.e., $\{r_1^l, r_2^l\} \in \mathcal{K}_{n,s}$, $r_1^l < r_2^l$. At each time n, we assume that at least two antennas of each anchor provide RSS measurements. By stacking the measurement vectors $\boldsymbol{z}_{n,s} \triangleq [z_{n,s}^1, \ldots, z_{n,s}^{K_{n,s}}]^{\mathrm{T}}$ and $\boldsymbol{z}_{\mathrm{D},n,s} \triangleq [z_{\mathrm{D},n,s}^l, \ldots, z_{\mathrm{D},n,s}^{L_{n,s}}]^{\mathrm{T}}$ from all anchors, the full measurement vectors at time n are given as $\boldsymbol{z}_n \triangleq [\boldsymbol{z}_{n,1}^{\mathrm{T}}, \ldots, \boldsymbol{z}_{n,S}^{\mathrm{T}}]^{\mathrm{T}}$ and $\boldsymbol{z}_{\mathrm{D},n} \triangleq [\boldsymbol{z}_{\mathrm{D},n,1}^{\mathrm{T}}, \ldots, \boldsymbol{z}_{\mathrm{D},n,S}^{\mathrm{T}}]^{\mathrm{T}}$.

Our goal is to estimate of the target state $\boldsymbol{x}_n$, the path-loss exponents $\boldsymbol{\eta}_n = [\eta_{n,1}, \ldots, \eta_{n,S}]^{\mathrm{T}}$, using the past and present measurement vectors $\boldsymbol{z}_{1:n} \triangleq [\boldsymbol{z}_1^{\mathrm{T}}, \ldots, \boldsymbol{z}_n^{\mathrm{T}}]^{\mathrm{T}}$ and $\boldsymbol{z}_{\mathrm{D},1:n} \triangleq [\boldsymbol{z}_{\mathrm{D},1}^{\mathrm{T}}, \ldots, \boldsymbol{z}_{\mathrm{D},n}^{\mathrm{T}}]^{\mathrm{T}}$.

3 System Model and Statistical Formulation

3.1 Target Dynamics

For tracking a maneuvering target node, the IMM method [9]–[11] is used, which resolves the target motion uncertainty by using multiple dynamic models (i.e., modes) indexed by $m_n \in \mathcal{H} \triangleq \{1, \cdots, H\}$ at time n. The state-transition pdf of the target state $f_h(\boldsymbol{x}_n|\boldsymbol{x}_{n-1})$, $h \in \mathcal{H}$ when considering the hth mode is defined by the corresponding dynamic model. To account for the uniform

motion as well as the maneuver of the target such as left/right turn, the nearly-constant velocity (NCV) model and the coordinated turn (CT) model [9] are used respectively. The NCV model is defined as $\boldsymbol{x}_n = \boldsymbol{F}_{\mathrm{NCV}}\boldsymbol{x}_{n-1} + \boldsymbol{\Gamma}\boldsymbol{\nu}_{n,h}$, where the matri $\boldsymbol{F}_{\mathrm{NCV}} \in \mathbb{R}^{4\times 4}$ and $\boldsymbol{\Gamma} \in \mathbb{R}^{4\times 2}$ are chosen as in [9, Section 6.3.2] with the sampling period ΔT. The driving process $\boldsymbol{\nu}_{n,h} \in \mathbb{R}^{2\times 1}$ is iid across n and h, zero-mean and Gaussian with covariance matrix $\sigma_h^2\boldsymbol{I}_2$, $\boldsymbol{I}_2$ denotes a 2×2 diagonal matrix, and σ_h represents the average speed increment along x or y axis during the sampling period ΔT. Furthermore, the turn of a target is modeled with the CT model, characterized by a constant turn rate Ω_h and a (nearly) constant speed, i.e., $\boldsymbol{x}_n = \boldsymbol{F}_{\mathrm{CT}}(\Omega_h)\boldsymbol{x}_{n-1} + \boldsymbol{\Gamma}\boldsymbol{\nu}_{n,h}$, the matrices $\boldsymbol{F}_{\mathrm{CT}}(\Omega_h) \in \mathbb{R}^{4\times 4}$ are chosen as in [9, Section 11.7.1]. The dynamic mode (DM) index m_n is modeled as a random variable which evolve according to the first-order Markov chain with a constant transition matrix $\boldsymbol{P} \in [0,1]^{H\times H}$ over time, where $[0,1]^{H\times H}$ denotes a $H \times H$ matrix with entries between 0 and 1. The DM transition probability mass function (pmf) of m_n is given by $p(m_n = j|m_{n-1} = i) = [\boldsymbol{P}]_{i,j}$ for $i, j \in \mathcal{H}$. Note that $\sum_{j=1}^{H}[\boldsymbol{P}]_{i,j} = 1\ \forall\, i$. The target state $\boldsymbol{x}_n$ and the DM index m_n are assumed to jointly evolve according to a Markovian dynamic model. Furthermore, we assume that the state $\boldsymbol{x}_n$ is conditionally independent of m_{n-1} given $\boldsymbol{x}_{n-1}$ and m_n, and m_n is conditionally independent of $\boldsymbol{x}_{n-1}$ given m_{n-1}. Thus, the joint prior pdf $f(\boldsymbol{x}_{1:n}, \boldsymbol{m}_{1:n})$ of $\boldsymbol{x}_{1:n} \triangleq [\boldsymbol{x}_1^{\mathrm{T}}, \ldots, \boldsymbol{x}_n^{\mathrm{T}}]^{\mathrm{T}}$ and $\boldsymbol{m}_{1:n} \triangleq [m_1, \ldots, m_n]^{\mathrm{T}}$ can be factorized as

$$\begin{aligned} &f(\boldsymbol{x}_{1:n}, \boldsymbol{m}_{1:n}) \\ &= f(\boldsymbol{x}_0, m_0) \prod_{n'=1}^{n} f(\boldsymbol{x}_{n'}, m_{n'}|\boldsymbol{x}_{n'-1}, m_{n'-1}) \\ &= f(\boldsymbol{x}_0)f(m_0) \prod_{n'=1}^{n} f_{m_{n'}}(\boldsymbol{x}_{n'}|\boldsymbol{x}_{n'-1})f(m_{n'}|m_{n'-1}), \end{aligned} \tag{3}$$

where $f_{m_n}(\boldsymbol{x}_n|\boldsymbol{x}_{n-1}) = f(\boldsymbol{x}_n|m_n, \boldsymbol{x}_{n-1})$, $f(\boldsymbol{x}_0)$ and $f(m_0)$ are the initial prior pdf and pmf, which are assumed to be uniform on their respective regions of interest (RoIs).

3.2 Likelihood Functions

We assume that the individual measurements inside vectors $\boldsymbol{z}_{n,s}$ and $\boldsymbol{z}_{\mathrm{D},n,s}$ are conditionally independent given the states $\boldsymbol{x}_n$ and $\eta_{n,s}$, and $\eta_{n,s}$ is independent of RSSD measurements $\boldsymbol{z}_{\mathrm{D},n,s}$. The conditional pdfs $h(z_{n,s}^k|\boldsymbol{x}_n, \eta_{n,s})$ and

$h(z^l_{\mathrm{D},n,s}|\boldsymbol{x}_k)$ (i.e., likelihood functions) derived from (1) and (2) are given as

$$h(z^k_{n,s}|\boldsymbol{x}_n,\eta_{n,s}) = C_1 \exp\Big\{-\frac{(z^k_{n,s}-s^k_{n,s})^2}{2(\sigma^2_{\mathrm{S}}+\sigma^2_{\mathrm{n}})}\Big\}, \tag{4}$$

$$h(z^l_{\mathrm{D},n,s}|\boldsymbol{x}_n) = C_2 \exp\Big\{-\frac{(z^l_{\mathrm{D},n,s}-G^{(r^l_1,r^l_2)}_{\Delta,n,s}(\boldsymbol{x}_n))^2}{4\sigma^2_{\mathrm{n}}}\Big\}, \tag{5}$$

where $s^k_{n,s} = P_{0,s} + G_{\mathrm{Rx}}(\varphi^k_{n,s}) - 10\eta_{n,s}\log_{10}\left(\frac{d^k_{n,s}}{d_0}\right)$, and $G^{(r^l_1,r^l_2)}_{\Delta,n,s}(\boldsymbol{x}_n)$ represents the nonlinear mapping from the hidden state $\boldsymbol{x}_n$ to an RSSD observation described in (2), with $C_1 = \left(2\pi(\sigma^2_{\mathrm{S}}+\sigma^2_{\mathrm{n}})\right)^{-\frac{1}{2}}$, $C_2 = (4\pi\sigma^2_{\mathrm{n}})^{-\frac{1}{2}}$.

4 The Message Passing Localization Algorithm

4.1 State Estimation

The joint estimation of $\boldsymbol{x}_n$ and $\eta_{n,s}$ given the measurements $\boldsymbol{z}_{1:n}$ and $\boldsymbol{z}_{\mathrm{D},1:n}$ is formulated with a Bayesian model, where the joint posterior pdf $f(\boldsymbol{x}_{1:n}, m_{1:n}, \boldsymbol{\eta}_{1:n}|\boldsymbol{z}_{1:n}, \boldsymbol{z}_{\mathrm{D},1:n})$ can be factorized as

$$\begin{aligned}
&f(\boldsymbol{x}_{1:n}, m_{1:n}, \boldsymbol{\eta}_{1:n}|\boldsymbol{z}_{1:n}, \boldsymbol{z}_{\mathrm{D},1:n}) \\
&\quad\propto f(\boldsymbol{z}_{1:n}, \boldsymbol{z}_{\mathrm{D},1:n}|\boldsymbol{x}_{1:n}, m_{1:n}, \boldsymbol{\eta}_{1:n}) f(\boldsymbol{x}_{1:n}, m_{1:n}, \boldsymbol{\eta}_{1:n}) \\
&\quad= f(\boldsymbol{x}_0) f(m_0) \left(\prod_{s=1}^{S} f(\eta_{0,s})\right) \\
&\qquad\times \prod_{n'=1}^{n} f_{m_{n'}}(\boldsymbol{x}_{n'}|\boldsymbol{x}_{n'-1}) f(m_{n'}|m_{n'-1}) \prod_{s=1}^{S} f(\eta_{n',s}|\eta_{n'-1,s}) \\
&\qquad\times \prod_{k\in\mathcal{K}_{n',s}} h(z^k_{n',s}|\boldsymbol{x}_{n'},\eta_{n',s}) \prod_{l\in\mathcal{L}_{n',s}} h(z^l_{\mathrm{D},n',s}|\boldsymbol{x}_{n'}),
\end{aligned} \tag{6}$$

according to the Bayes' rule and independence assumptions over the prior pdfs, state-transition pdfs, and the likelihood functions.

Based on the marginal posterior pdfs $f(\boldsymbol{x}_n|\boldsymbol{z}_{1:n}, \boldsymbol{z}_{\mathrm{D},1:n})$ and $f(\eta_{n,s}|\boldsymbol{z}_{1:n})$, the Bayesian estimation of the target state $\boldsymbol{x}_n$, the PLEs $\eta_{n,s}$ can be approximately calculated by means of the minimum mean square error (MMSE) estimator [12],

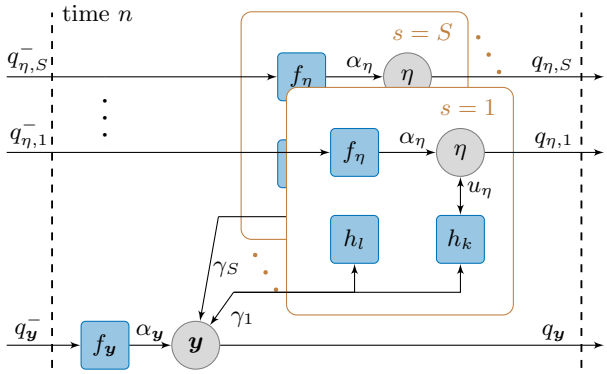

Figure 1: Factor graph representation of the factorized joint posterior pdf (6), shown for time n. For simplicity, the joint vector of $\boldsymbol{x}_n$ and m_n are denoted as $\boldsymbol{y}_n = [\boldsymbol{x}_n, m_n]^{\mathrm{T}}$, the time indices are omitted and the following short notations are used: the beliefs calculated at the previous time $n-1$, $q^-_{\eta,s} = q(\eta_{n-1,s})$ and $q^-_{\boldsymbol{y}} = q(\boldsymbol{y}_{n-1})$; the state-transition pdfs $f_{\boldsymbol{y}} = f(\boldsymbol{y}_n|\boldsymbol{y}_{n-1})$ and $f_\eta = f(\eta_{n,s}|\eta_{n-1,s})$; the predicted messages $\alpha_{\boldsymbol{y}} = \alpha(\boldsymbol{y}_n)$ and $\alpha_\eta = \alpha(\eta_{n,s})$; the measurement-update messages $u_\eta = u(\eta_{n,s})$ and $\gamma_s = \gamma^s(\boldsymbol{y}_n)$; the likelihood functions related to RSS/RSSD measurements $h_k = h(z^k_{n,s}|\boldsymbol{x}_n, \eta_{n,s})$ and $h_l = h(z^l_{\mathrm{D},n,s}|\boldsymbol{x}_n)$; the beliefs that approximately representing the marginal posterior pdfs $q_{\eta,s} = q(\eta_{n,s})$ and $q_{\boldsymbol{y}} = q(\boldsymbol{y}_n)$.

given as

$$\hat{\boldsymbol{x}}_n^{\mathrm{MMSE}} \triangleq \int \boldsymbol{x}_n f(\boldsymbol{x}_n|\boldsymbol{z}_{1:n}, \boldsymbol{z}_{\mathrm{D},1:n})\mathrm{d}\boldsymbol{x}_n, \tag{7}$$

$$\hat{\eta}_{n,s}^{\mathrm{MMSE}} \triangleq \int \eta_{n,s} f(\eta_{n,s}|\boldsymbol{z}_{1:n})\mathrm{d}\eta_{n,s}. \tag{8}$$

4.2 Message Passing Algorithm

The marginal posterior pdfs $f(\boldsymbol{x}_n|\boldsymbol{z}_{1:n}, \boldsymbol{z}_{\mathrm{D},1:n})$ and $f(\eta_{n,s}|\boldsymbol{z}_{1:n})$ are obtained by running massage passing on the factor graph (Fig. 1) representing the factorization of the joint posterior pdf $f(\boldsymbol{x}_{1:n}, m_{1:n}, \boldsymbol{\eta}_{1:n}|\boldsymbol{z}_{1:n}, \boldsymbol{z}_{\mathrm{D},1:n})$ (6). Following the generic rules for calculating messages and beliefs introduced in [13], the following operations are performed at each time n:

1. *Prediction*: First, a prediction step is performed, and the messages $\alpha(\eta_{n,s})$ and $\alpha(\boldsymbol{x}_n, m_n)$ are calculated as

$$\alpha(\eta_{n,s}) = \int q(\eta_{n-1,s}) f(\eta_{n,s}|\eta_{n-1,s})\mathrm{d}\eta_{n-1,s}, \tag{9}$$

$$\alpha(\boldsymbol{x}_n, m_n) = \sum_{m_{n-1}\in\mathcal{H}} \int q(\boldsymbol{x}_{n-1}, m_{n-1}) f_{m_n}(\boldsymbol{x}_n|\boldsymbol{x}_{n-1}) \times f(m_n|m_{n-1}) \mathrm{d}\boldsymbol{x}_{n-1}, \tag{10}$$

where $q(\eta_{n-1,s})$ and $q(\boldsymbol{x}_{n-1}, m_{n-1})$ are calculated at time $n-1$.

2. *Measurement update*: In the measurement update step, the messages $u(\eta_{n,s})$ are calculated as

$$u(\eta_{n,s}) = \sum_{m_n\in\mathcal{H}} \int \alpha(\boldsymbol{x}_n, m_n) \prod_{k\in\mathcal{K}_{n,s}} h(z_{n,s}^k|\boldsymbol{x}_n, \eta_{n,s}) \mathrm{d}\boldsymbol{x}_n, \tag{11}$$

and the message $\gamma^s(\boldsymbol{x}_n, m_n)$ from each anchor is given by

$$\gamma^s(\boldsymbol{x}_n, m_n) = \beta^s(\boldsymbol{x}_n, m_n)\beta_{\mathrm{D}}^s(\boldsymbol{x}_n, m_n), \tag{12}$$

where $\beta^s(\boldsymbol{x}_n, m_n)$ is the message passed form the factor node $h(z_{n,s}^l|\boldsymbol{x}_n, \eta_{n,s})$ to the variable node $\boldsymbol{x}_n$, given by

$$\beta^s(\boldsymbol{x}_n, m_n) = \int \alpha(\eta_{n,s}) \prod_{k\in\mathcal{K}_{n,s}} h(z_{n,s}^k|\boldsymbol{x}_n, \eta_{n,s}) \mathrm{d}\eta_{n,s}, \tag{13}$$

and $\beta_{\mathrm{D}}^s(\boldsymbol{x}_n, m_n)$ is the message passed form the factor node $h(z_{\mathrm{D},n,s}^l|\boldsymbol{x}_n)$ to the variable node $\boldsymbol{x}_n$, given by

$$\beta_{\mathrm{D}}^s(\boldsymbol{x}_n, m_n) = \prod_{l\in\mathcal{L}_{n,s}} h(z_{\mathrm{D},n,s}^l|\boldsymbol{x}_n). \tag{14}$$

3. *Belief calculation*: Finally, the beliefs $q(\eta_{n,s})$ approximating the marginal posterior pdfs $f(\eta_{n,s}|\boldsymbol{z}_{1:n})$ are calculated as

$$q(\eta_{n,s}) = \alpha(\eta_{n,s})u(\eta_{n,s}). \tag{15}$$

Furthermore, the belief $q(\boldsymbol{x}_n, m_n)$ approximating the the marginal posterior pdf $f(\boldsymbol{x}_n, m_n|\boldsymbol{z}_{1:n}, \boldsymbol{z}_{\mathrm{D},1:n})$ is calculated as

$$q(\boldsymbol{x}_n, m_n) = \alpha(\boldsymbol{x}_n, m_n) \prod_{s=1}^{S} \gamma^s(\boldsymbol{x}_n, m_n). \tag{16}$$

Finally, the belief $q(\boldsymbol{x}_n)$ and $q(m_n)$ approximating $p(\boldsymbol{x}_n|\boldsymbol{z}_{1:n}, \boldsymbol{z}_{\mathrm{D},1:n})$ and $p(m_n|\boldsymbol{z}_{1:n}, \boldsymbol{z}_{\mathrm{D},1:n})$ are calculated as $q(\boldsymbol{x}_n) = \int q(\boldsymbol{x}_n, m_n)\mathrm{d}m_n$ and $q(m_n) = \int q(\boldsymbol{x}_n, m_n)\mathrm{d}\boldsymbol{x}_n$.

4. *Particle-based implementation*: A sequential Monte Carlo (particle-based) implementation [11], [14] is used to represent the messages and beliefs presented above. Furthermore, a "stacked state" [15] which comprises the target state and the PLE state is used in the implementation. Hence, the resulting complexity scales linearly in the number of particles, in the number of measurements per anchor, and quadratically in the number of mode number H.

5 Performance Evaluation

We validate the proposed message passing based localization algorithm using both synthetic and real measured RSS datasets. The work in [8] which exploits AoA information from RSSD measurements for target tracking is used as a reference method. Note that in [8] a single dynamic model is used. To remove the influence of difference target dynamic models on the results in two methods and make a fair comparison, we extend the algorithm in [8] with the IMM method introduced in Section (3.1) and keep the same setup on the DM modes. For simplicity, the two methods above will be briefly referred to as "MP-tracking" and "AoA-tracking" in what follows.

5.1 Measurement and Simulation Setup

The synthetic datasets are generated according to the setup of real outdoor measurement, which is described as follows: A LoRa based network [1] is used in our experimental setup. As shown in Fig. 2, the target node is equipped with an omnidirectional antenna with known transmit power of 14 dBm. Two anchor nodes are used, which are equipped with four and three directional antennas respectively, i.e., $A_1 = 4$ and $A_2 = 3$, and each receive antenna is connected with a gateway as shown in Fig. 2c. The gateways act as bidirectional relays between the target node and a network server, in which the messages like GPS "ground truth" and RSS values are decoded. The distance between the phase centers and the orientation difference of two adjacent antennas are one wavelength and 45 degrees, respectively. One of the receive antenna beam patterns is measured and assumed to be the same for the rest of the antennas. The system is operating at the carrier frequency 868 MHz, with a bandwidth of 125 kHz. The maximum spreading factor 12 is used to achieve the longest working range, however at the cost of low data and package rate. The gateways are listening to several different channels, every 6 seconds one packet is received at each antenna.

The following parameters and simulation setup are used for both synthetic and real measurements. We assume that the initial target position is roughly known, and the particles for the initial target state are drawn from a 4-D

(a) (b) (c)

Figure 2: Experimental setup: (a) target node: TTGO T-Beam module, (b) anchor node: four 9 dBi circular antennas are used, and each antenna is connected to a TTGO gateway shown in (c).

uniform distribution with the center at $[\boldsymbol{p}_1\, 0\, 0]$, where $\boldsymbol{p}_1$ denotes the ground truth position of the target at time $n = 1$, and the supports for the position and velocity are given as $[-50, 50]$ m and $[-1, 1]$ m/s, respectively. The state-transition pdfs of the target state $f_h(\boldsymbol{x}_n|\boldsymbol{x}_{n-1})$ under three DM modes are defined by the following models respectively: 1) CT model for right turn with $\Omega_1 = -5\,\text{deg/s}$, $\sigma_1 = 0.001\,\text{m/s}^2$; 2) NCV model with $\sigma_2 = 0.001\,\text{m/s}^2$; 3) CT model for left turn with $\Omega_3 = 5\,\text{deg/s}$ and $\sigma_3 = 0.001\,\text{m/s}^2$. The sampling period $\Delta T = 6\,\text{s}$. The DM transition probabilities are chosen as $[\boldsymbol{P}]_{1,1} = [\boldsymbol{P}]_{3,3} = 0.95$, $[\boldsymbol{P}]_{2,2} = 0.96$, $[\boldsymbol{P}]_{2,1} = [\boldsymbol{P}]_{2,3} = 0.02$, $[\boldsymbol{P}]_{1,2} = [\boldsymbol{P}]_{3,2} = 0.04$, and $[\boldsymbol{P}]_{1,3} = [\boldsymbol{P}]_{3,1} = 0.01$. Besides, the state-transition pdfs of the path-loss exponents $f(\eta_{n,s}|\eta_{n-1,s})$ are given as Gaussian distributions with noise standard deviations $\sigma_\eta = 0.07$. The particles for the initial PLE state $\eta_{0,s}$ are drawn from a uniform distribution on $[1, 5]$. The pdf of each variable state is represented by 5000 particles.

5.2 Synthetic Measurements

Using the GPS positions of the anchors and the target at each time n, we calculate the ground truth distances and AoAs, and then apply them in model (1) to generate the synthetic RSS measurements. Furthermore, the ground truth PLEs are set according to the true propagation conditions and the estimates from the real meausrments as shown in Fig. 8. For each simulation run, the shadow fading and Gaussian noise processes are generated at each time n under one of the two setups: 1) *setup*-1: $\sigma_\text{S} = 2\,\text{dB}$, $\sigma_\text{n} = 0.8\,\text{dB}$, $c_\text{LSF} = 0.9$; 2) *setup*-2 (based on the statistics from real measurements): $\sigma_\text{S} = 4\,\text{dB}$, $\sigma_\text{n} = 1\,\text{dB}$, $C_\text{LSF} = 0.8$. The noise standard deviations σ_S are σ_n are assumed to be known in the simulations. In total, we performed 100 Monte-Carlo (MC) simulation runs for each setup.

Fig. 3a depicts the target position RMSEs of MP-tracking and AoA-tracking

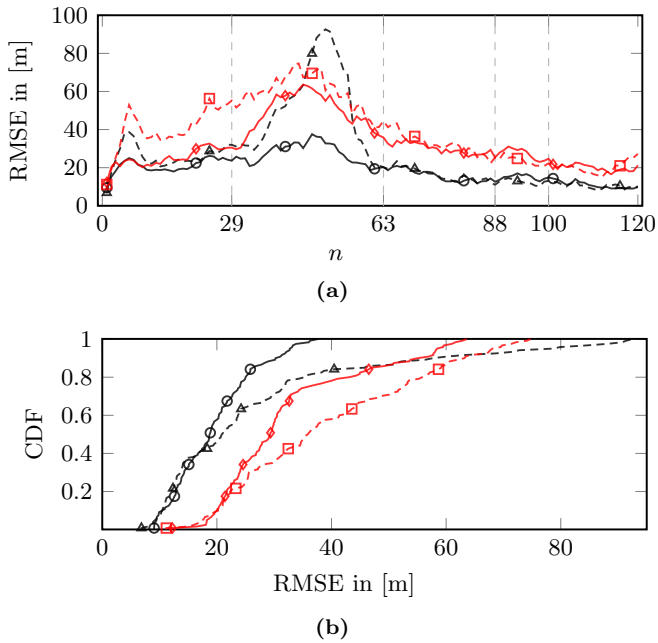

Figure 3: Results for synthetic data. (a) Target position RMSEs. (b) Empirical CDFs of the position RMSEs. *setup*-1: MP-tracking (—○—), AoA-tracking (- -△- -), *setup*-2: MP-tracking (—◇—), AoA-tracking (- -□- -). The vertical dashed lines highlight the times around which the target node performs sharp turns as shown in Fig. 6.

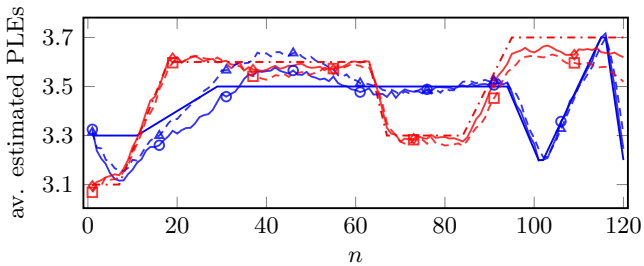

Figure 4: Results for synthetic data using MP-tracking. Averaged PLE estimates for (a) anchor 1: ground truth (——), *setup*-1 (—○—), *setup*-2 (- -△- -); (b) anchor 2: ground truth (-·-·-), *setup*-1 (—◇—), *setup*-2 (- -□- -).

methods, and the corresponding empirical cumulative distribution function (CDF) are given in Fig. 3b. By exploiting both range and angle information from RSS measurements, it shows that the MP-tracking method achieves lower RMSEs then the AoA-tracking method mostly. More specifically, the maximum RMSEs for MP-tracking are below 40 m and 65 m for *setup*-1 and *setup*-2, while

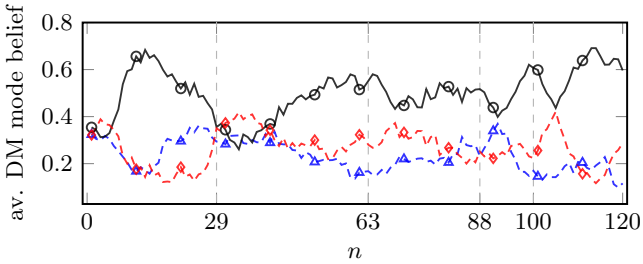

Figure 5: Results for synthetic data using MP-tracking. Averaged DM mode beliefs for *setup*-2. (a) CT model for right turn (- -△- -). (b) NCV (—○—). (C) CT model for left turn (- -◇- -).

the values are 95 m and 75 m for AoA-tracking. Fig. 4 shows the averaged PLE estimates over 100 MC runs. It can be seen that the PLE estimates of MP-tracking represent the ground truth well in both setups, which proves that MP-tracking can adapt to dynamic propagation conditions. Moreover, the averaged DM mode beliefs are given in Fig. 5. As can be observed, whenever the target performs a sharp turn, the belief of the corresponding DM mode increases and tends to be dominant, and the smooth movement in between those turns is captured by the NCV model, as expected.

5.3 Real Measurements

The real RSS measurements are collected at the campus of Lund University, Sweden, as shown in Fig. 6. Two anchor nodes are placed on two building roofs, which are around 20 m above the ground. The target node is carried by a person walking along a predefined trajectory at a speed around 1 m/s. Every 6 seconds, the movement is paused and we collect around three samples at each antenna. Still, at a few positions only a subset of antennas provide valid RSS measurements. In total, there are $N = 120$ sample time instances. In Fig. 6, we mark the time instances where the target performs sharp turns with brown circle. In the simulations, we assume the noise standard deviations for the shadow fading and Gaussian noise processes to be $\sigma_{\mathrm{S}} = 4\,\mathrm{dB}$, $\sigma_{\mathrm{n}} = 1\,\mathrm{dB}$. We evaluate the performance both for the averaged and non-averaged measurements. For the first case, the RSS measurements collected at each antenna are averaged. For the second case, we randomly pick one measurement from each antenna at each time, and in total 50 MC simulation runs are performed.

As shown in Fig. 7, the MP-tracking algorithm outperforms the AoA-tracking algorithm especially when non-averaged measurements are used. Furthermore, the true propagation conditions from the target to each anchor are denoted with line-of-sight (LoS), obstructed-LoS (OLoS) where the dir-

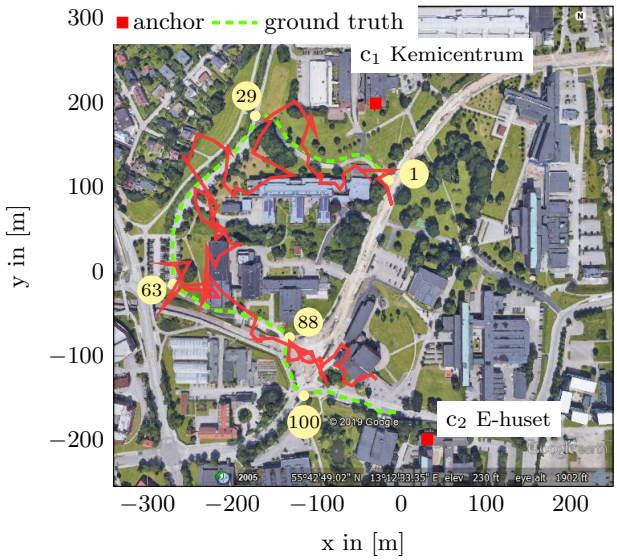

Figure 6: Picture of the outdoor measurement environment, Lund University, Sweden. Background map: © 2019 Google

ect propagation is blocked by trees, and non-LoS (NLoS) where the direct propagation is blocked by one or two buildings (abbreviated as bul.). As shown in Fig. 8, the PLE estimates well capture the dynamics of the true propagation conditions to each anchor.

6 Conclusion

We proposed a localization algorithm that exploits both range and angle information from non-coherent RSS measurements for IoT networks. Results using real outdoor measurements show that the proposed algorithm can adapt to dynamic propagation conditions, and improve the localization accuracy compared to the method which exploits single geometric feature. Moreover, the proposed algorithm is compatible with many existing low cost IoT technologies and different antenna array configurations.

7 Acknowledgment

This work was supported in part by the Swedish Research Council (VR), in part by the strategic research area ELLIIT and in part by the TU Graz.

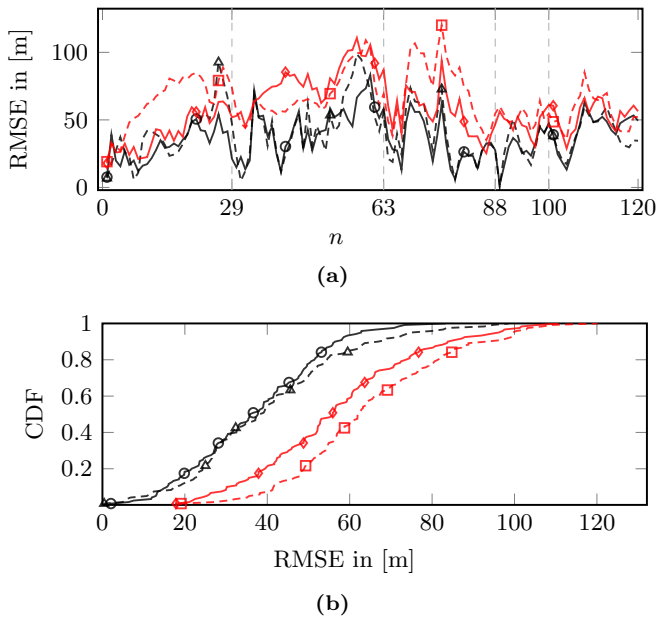

Figure 7: Results for real data. (a) Target position RMSEs. (b) Empirical CDFs of the position RMSEs. For averaged RSS measurements: MP-tracking (—o—), AoA-tracking (- -△- -), For single RSS measurement: MP-tracking (—◇—), AoA-tracking (- -□- -).

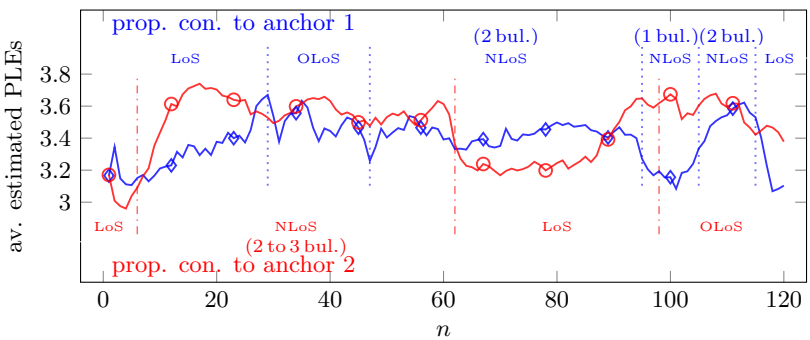

Figure 8: Results for real data. PLE estimation from anchor 1 (—◇—) and from anchor 2 (—o—). The propagation conditions from the target node to anchor 1 and anchor 2 are labeled in blue and red colors respectively. Furthermore, the vertical lines (·····) and (- · - · -) highlight the time instances around which the propagation conditions to anchor 1 and anchor 2 change respectively.

References

[1] M. Centenaro, L. Vangelista, A. Zanella and M. Zorzi, "Long-range communications in unlicensed bands: The rising stars in the IoT and smart city scenarios", *IEEE Wirel. Commun.*, vol. 23, no. 5, pp. 60–67, 2016.

[2] B. Mager, P. Lundrigan and N. Patwari, "Fingerprint-based device-free localization performance in changing environments", *IEEE J. Sel. Areas Commun.*, vol. 33, no. 11, pp. 2429–2438, 2015.

[3] S. Yiu, M. Dashti, H. Claussen and F. Perez-Cruz, "Wireless RSSI fingerprinting localization", *Signal Process.*, vol. 131, pp. 235 –244, 2017.

[4] S. Tomic, M. Beko and R. Dinis, "RSS-based localization in wireless sensor networks using convex relaxation: Noncooperative and cooperative schemes", *IEEE Trans. Veh. Technol.*, vol. 64, no. 5, pp. 2037–2050, 2015.

[5] A. Zanella, "Best practice in RSS measurements and ranging", *IEEE Commun. Surveys Tuts.*, vol. 18, no. 4, pp. 2662–2686, Fourthquarter 2016.

[6] "LoRa alliance geolocation whitepaper", *LoRa Alliance*, 2018.

[7] J. Jiang, C. Lin, F. Lin and S. Huang, "ALRD: AoA localization with RSSI differences of directional antennas for wireless sensor networks", in *Int. Conf. on Inform. Soc. (i-Society 2012)*, 2012, pp. 304–309.

[8] X. Li, M. A. Nasa, F. Rezaei and F. Tufvesson, "Target tracking using signal strength differences for long-range IoT networks", in *IEEE Int. Conf. on Commun. Workshops (ICCW)*, 2020.

[9] Y. Bar-Shalom, T. Kirubarajan and X.-R. Li, *Estimation with Applications to Tracking and Navigation*. New York, NY, USA: Wiley, 2002.

[10] E. Mazor, A. Averbuch, Y. Bar-Shalom and J. Dayan, "Interacting multiple model methods in target tracking: A survey", *IEEE Trans. Aerosp. Electron. Syst.*, vol. 34, no. 1, pp. 103–123, 1998.

[11] G. Soldi, F. Meyer, P. Braca and F. Hlawatsch, "Self-tuning algorithms for multisensor-multitarget tracking using belief propagation", *IEEE Trans. Signal Process.*, vol. 67, no. 15, pp. 3922–3937, 2019.

[12] S. M. Kay, *Fundamentals of Statistical Signal Processing: Estimation Theory*. Upper Saddle River, NJ, USA: Prentice-H, 1993.

[13] F. Kschischang, B. Frey and H.-A Loeliger, "Factor graphs and the sum-product algorithm", *IEEE Trans. Inf. Theory*, vol. 47, no. 2, pp. 498–519, 2001.

[14] M. S. Arulampalam, S. Maskell, N. Gordon and T. Clapp, "A tutorial on particle filters for online nonlinear/non-Gaussian Bayesian tracking", *IEEE Trans. Signal Process.*, vol. 50, no. 2, pp. 174–188, 2002.

[15] F. Meyer, O. Hlinka, H. Wymeersch, E. Riegler and F. Hlawatsch, "Distributed localization and tracking of mobile networks including noncooperative objects", *IEEE Trans. Signal Inf. Process. Net.*, vol. 2, no. 1, pp. 57–71, 2016.

Paper V

Detection and Tracking of Multipath Channel Parameters Using Belief Propagation

We present a belief propagation (BP) algorithm with probabilistic data association (DA) for detection and tracking of specular multipath components (MPCs). In real dynamic measurement scenarios, the number of MPCs reflected from visible geometric features, the MPC dispersion parameters, and the number of false alarm contributions are unknown and time-varying. We develop a Bayesian model for specular MPC detection and joint estimation problem, and represent it by a factor graph which enables the use of BP for efficient computation of the marginal posterior distributions. A parametric channel estimator is exploited to estimate at each time step a set of MPC parameters, which are further used as noisy measurements by the BP-based algorithm. The algorithm performs probabilistic DA, and joint estimation of the time-varying MPC parameters and mean false alarm rate. Preliminary results using synthetic channel measurements demonstrate the excellent performance of the proposed algorithm in a realistic and very challenging scenario. Furthermore, it is demonstrated that the algorithm is able to cope with a high number of false alarms originating from the prior estimation stage.

X. Li, E. Leitinger, F. Tufvesson,
"Detection and Tracking of Multipath Channel Parameters Using Belief Propagation,"
in *IEEE Proc. Asilomar-20*, Pacific Grove, CA, USA, pp. 1083-1089, Nov. 2020.

1 Introduction

The information of dispersive wireless radio channels in delay, angular, and frequency domain, and its temporal behavior in dynamic scenarios are of great importance for the design and development of radio-channel models [1], [2], 5G wireless communication technologies [3]–[5], and multipath-based localization and mapping [6]–[8]. The response of a wireless radio channel is typically represented by superimposed multipath components (MPCs) with parameters such as delay, angle-of-arrival (AoA), and angle-of-departure (AoD). These MPC parameters are usually estimated from multidimensional radio measurements using antenna arrays and multiple frequencies (wide-band or ultrawide-band signals) using super-resolution parametric channel tracking algorithms that perform sequential estimation of specular MPCs (SMCs).

1.1 State of the Art Methods

The existing MPC tracking algorithms can be grouped into two broad categories. Algorithms of the first category estimate and track the MPC parameters directly based on the radio signals using for example an extended Kalman filter (EKF) [9], [10]. Algorithms of the second category are based on a two-stage approach, where a snapshot-based parametric channel estimator such as [11]–[13] is incorporated into a tracking filter [14], or extended with a state-transition model that enables sequential Bayesian estimation [15]. In this work, we focus on the two-stage algorithms. In general, the correct model order (number of SMCs) is unknown, time-varying and need to be estimated, i.e., the model-order selection problem. One classical solution is to extend the tracking algorithm with an outer stage for model order detection using for example eigenvalue-based methods, or the generic information theoretic criteria, e.g., the Akaike/Bayesian information criterion. Another choice is to adopt sparsity-based algorithms, which aim to reconstruct sparse signals from a reduced set of measurements specified by a sparse weight vector. By introducing a sparsity-promoting prior model for the weights, the estimation of model order and MPC parameters can be jointly formulated inside a Bayesian framework. Most of the sparsity-based algorithms [16]–[18] are proposed for time-invariant measurement. Examples of sparsity-based sequential Bayesian algorithms are given in [15], [19]. In addition to the model-order selection, data association (DA) i.e., which measurement originates from which MPC, is potentially another problem for two-stage methods. In general, existing methods adopt single hypothesis, i.e., the state of each MPC is updated using a single measurement specified by the metrics such as the global nearest neighbor [20]. In comparison, probabilistic DA [20], [21] which evaluates all the current measurements for the update of each predicated MPC state would be more preferable in the presence of false alarm measurements.

1.2 Contributions

In this work, we propose a belief propagation (BP) -based algorithm for MPC detection and tracking (abbreviated as BP-MPCT) which uses the MPC estimates from a parametric super-resolution sparse Bayesian variational (abbreviated as SBL) channel estimator as measurements. This BP-MPCT algorithm jointly performs probabilistic DA and sequential estimation of potential specular MPC (PSMC) parameters and mean number of false alarms. Probabilistic DA and state estimation are performed by running BP on a factor graph [8], [21]. We use a probabilistic model for MPC existence where each PSMC state is augmented by a binary existence variable and associated with a probability of existence, which is also estimated and used for detection of the reliable MPCs modeling the birth and death. Inspired by [22]–[24], the algorithm also exploits the estimates of mean and variance of the complex amplitudes to calculate the detection probabilities of path components. It is therefore also suitable for unknown and time-varying detection probabilities [25].

2 Problem Formulation

2.1 Radio Signal Model

We consider a single-input–multiple-output (SIMO) channel model, where a baseband radio signal $s(t)$ is transmitted from a mobile user (UE) to a base station (BS) equipped with an antenna array of J elements. For the sake of simplicity we assume a two dimensional scenario with horizontal-only propagation.[9] The received signal at each antenna element indexed by $j \in \{1, \ldots, J\}$ is given as

$$r^{(j)}(t) = \sum_{l=1}^{L_t} \alpha_{l,t} s\big(t - f(\tau_{l,t}, \varphi_{l,t}, \boldsymbol{p}^{(j)})\big) + w(t) \tag{1}$$

where the first term comprises L_t SMCs, with each being characterized by the complex amplitude $\alpha_{l,t}$, the time delay $\tau_{l,t}$ to the array's center of gravity, and the AoA $\varphi_{l,t}$ with respect to the array orientation. The function $f(\tau_{l,t}, \varphi_{l,t}, \boldsymbol{p}^{(j)})$ maps the SMC parameters from the array's center to the position $\boldsymbol{p}^{(j)}$ of the jth array element [26]. We assume that the UE and BS are time synchronized and the array orientation is known. The second term $w(t)$ in (1) represents the measurement noise which is described by additive white Gaussian noise (AWGN) with double-sided power spectral density $N_0/2$.

[9] An extension to three dimensional scenarios with horizontal and vertical propagation is straightforward, but it would lead to a cumbersome notation and one would not gain any new insights.

The received signal $r^{(j)}(t)$ observed over a duration T is sampled with frequency $f_s = 1/T_s$, yielding a length $N_\mathrm{s} = T/T_\mathrm{s}$ sample vector $\boldsymbol{r}_n^{(j)} \in \mathbb{C}^{N_\mathrm{s}\times 1}$ from each array element, and n is the discrete time index. By stacking $\boldsymbol{r}_n^{(j)}$ from J array elements, the discrete time signal vector $\boldsymbol{r}_n \triangleq [(\boldsymbol{r}_n^{(1)})^\mathrm{T}, \ldots, (\boldsymbol{r}_n^{(J)})^\mathrm{T}]^\mathrm{T} \in \mathbb{C}^{N_\mathrm{s}J\times 1}$ is given as

$$\boldsymbol{r}_n = \boldsymbol{S}(\boldsymbol{\theta}_n)\boldsymbol{\alpha}_n + \boldsymbol{w}_n \tag{2}$$

where $\boldsymbol{S}(\boldsymbol{\theta}_n) \triangleq [\boldsymbol{s}(\boldsymbol{\theta}_{1,n}), \ldots, \boldsymbol{s}(\boldsymbol{\theta}_{L_n,n})] \in \mathbb{C}^{N_\mathrm{s}J\times L_n}$ with $\boldsymbol{s}(\boldsymbol{\theta}_{l,n}) \in \mathbb{C}^{N_\mathrm{s}J\times 1}$ accounting for signal samples of the lth SMC from all array elements, and $\boldsymbol{\alpha}_n \triangleq [\alpha_{1,n}, \ldots, \alpha_{L_n,n}]^\mathrm{T} \in \mathbb{C}^{L_n\times 1}$. The SMC parameter vector is $\boldsymbol{\theta}_n \triangleq [\boldsymbol{\theta}_{1,n}^\mathrm{T}, \ldots, \boldsymbol{\theta}_{L_n,n}^\mathrm{T}]^\mathrm{T}$, with $\boldsymbol{\theta}_{l,n} \triangleq [\tau_{l,n}, \varphi_{l,n}]^\mathrm{T}$. The vector $\boldsymbol{w}_n$ contains the sampled AWGN from all array elements. A SMC exists only during the time duration (i.e., lifetime) that the BS/associated environment features are visible at the UE position. We assume that the true model order L_n is unknown and time-varying in dynamic measurement scenarios.

2.2 Parametric Channel Estimation

At each time n, a SBL channel estimator [12], [16]–[18] is used to estimate the SMC parameters $\hat{\boldsymbol{\theta}}_n \triangleq [\hat{\boldsymbol{\theta}}_{1,n}^\mathrm{T}, \ldots, \hat{\boldsymbol{\theta}}_{M_n,n}^\mathrm{T}]^\mathrm{T}$ with $\hat{\boldsymbol{\theta}}_{m,n} = [\hat{\tau}_{m,n}, \hat{\varphi}_{m,n}]^\mathrm{T}$, the mean value vector $\boldsymbol{\mu}_{\alpha,n} \triangleq [\mu_{\alpha,1,n}, \ldots, \mu_{\alpha,M_n,n}]^\mathrm{T}$ and covariance matrix $\boldsymbol{\Sigma}_{\alpha,n} \in \mathbb{C}^{M_n\times M_n}$ of corresponding complex amplitudes and the model order M_n. During the estimation process, we assume that miss detection of SMCs and estimation of MPCs which did not originate from any distinct environment features might occur. Hence, M_n is time-varying and it can be equal to, or larger/smaller than the true model order L_n. We also introduce the normalized amplitude $\hat{u}_{m,n} = \sqrt{\mathrm{SNR}_{m,n}}$ with $\mathrm{SNR}_{m,n} = |\mu_{\alpha,m,n}|^2 / \left[\boldsymbol{\Sigma}_{\alpha,n}\right]_{m,m}$ as the square root of the estimated posterior signal-to-noise ratio (SNR) of the mth SMC [23], [24]. The normalized amplitudes $\hat{u}_{m,n}$ are directly related to the detection probabilities of the estimated SMCs as introduced in Sections 3.3 and 3.4.

The estimates are stacked into the vector $\boldsymbol{z}_n \triangleq [\boldsymbol{z}_{1,n}^\mathrm{T}, \ldots, \boldsymbol{z}_{M_n,n}^\mathrm{T}]^\mathrm{T}$, where $\boldsymbol{z}_{m,n} \triangleq [\hat{d}_{m,n}, \hat{\varphi}_{m,n}, \hat{u}_{m,n}]^\mathrm{T}$ with $\hat{d}_{m,n} = c\hat{\tau}_{m,n}$ and c denotes the speed of light. We also define the vectors $\boldsymbol{z} \triangleq [\boldsymbol{z}_1^\mathrm{T}, \ldots, \boldsymbol{z}_n^\mathrm{T}]^\mathrm{T}$ and $\boldsymbol{m} \triangleq [M_1, \ldots, M_n]^\mathrm{T}$. The vector $\boldsymbol{z}$ is further used as noisy measurements in the BP-MPCT algorithm.

2.3 Inference Problem

Given all the past and current measurements $\boldsymbol{z}$, our goal is to infer the time-varying states of the SMCs, as well as the model order. Besides, the unknown

and potentially time-varying false alarm measurement rate and detection probabilities are automatically adapted online, which avoids manually tunning of these measurement parameters for different datasets.

3 System model and Statistical Formulation

3.1 PSMC States and Dynamics

At each time n, the numbers of emerging SMCs and the SMCs that survived from the previous time are unknown. To account for this fact, the concept of potential SMC, i.e., PSMC, is introduced. At time n, a PSMC $\boldsymbol{y}_{k,n}$, $k \in \mathcal{K}_n \triangleq \{1, \ldots, K_n\}$ is either a legacy PSMC $\tilde{\boldsymbol{y}}_{k,n}$, which is already established in the previous time, or a new PSMC $\breve{\boldsymbol{y}}_{m,n}$ which is established for the first time. The existence/nonexistence of a PSMC as an actual SMC is modeled by a binary variable $r_{k,n} \in \{0, 1\}$, i.e., it exists (not exist) if $r_{k,n} = 1$ ($r_{k,n} = 0$). Thus, the number of PSMCs K_n represents the maximum possible number of SMCs that can be detected and estimated at time n.

The augmented state of a PSMC is defined as $\boldsymbol{y}_{k,n} \triangleq [\boldsymbol{\psi}_{k,n}, r_{k,n}]^{\mathrm{T}}$, where $\boldsymbol{\psi}_{k,n} = [\boldsymbol{x}_{k,n}^{\mathrm{T}}, u_{k,n}]^{\mathrm{T}}$ and $\boldsymbol{x}_{k,n} = [d_{k,n}, \varphi_{k,n}, v_{\mathrm{d},k,n}, v_{\varphi,k,n}]^{\mathrm{T}}$ with $v_{\mathrm{d},k,n}$ and $v_{\varphi,k,n}$ denoting the distance and angular velocities. The states of nonexisting PSMCs are obviously irrelevant, but will be convenient if formally considered. Therefore, all probability density functions (pdfs) defined for PSMC states $f(\boldsymbol{y}_{k,n}) = f(\boldsymbol{\psi}_{k,n}, r_{k,n})$ have the property that $f(\boldsymbol{\psi}_{k,n}, r_{k,n} = 0) = f_{k,n} f_{\mathrm{D}}(\boldsymbol{\psi}_{k,n})$, where $f_{k,n}$ is a constant representing the probability of nonexistence of $\boldsymbol{y}_{k,n}$, and $f_{\mathrm{D}}(\boldsymbol{\psi}_{k,n})$ is an arbitrary "dummy pdf" [21], [27]. Accordingly, the augmented states of legacy PSMCs and new PSMCs are denoted by $\tilde{\boldsymbol{y}}_{k,n} \triangleq [\tilde{\boldsymbol{\psi}}_{k,n}^{\mathrm{T}}, \tilde{r}_{k,n}]^{\mathrm{T}}$, $k \in \mathcal{K}_{n-1} \triangleq \{1, \ldots, K_{n-1}\}$ and $\breve{\boldsymbol{y}}_{m,n} \triangleq [\breve{\boldsymbol{\psi}}_{m,n}^{\mathrm{T}}, \breve{r}_{m,n}]^{\mathrm{T}}$, $m \in \mathcal{M}_n \triangleq \{1, \ldots, M_n\}$, respectively. At each time n, one new PSMC $\breve{\boldsymbol{y}}_{m,n}$ is introduced for each measurement $\boldsymbol{z}_{m,n}$, thus the number of new PSMCs equals to the number of measurements M_n. Before the current measurements $\boldsymbol{z}_n$ are observed, the number M_n is random. The new PSMCs become legacy PSMCs when the measurements at next time are observed, accordingly the set and number of legacy PSMCs are updated as $\mathcal{K}_n = \mathcal{K}_{n-1} \cup \mathcal{M}_n$ and $K_n = K_{n-1} + M_n$. We further define the stacked state vectors as follows: for legacy PSMCs $\tilde{\boldsymbol{y}} \triangleq [\tilde{\boldsymbol{y}}_1^{\mathrm{T}}, \ldots, \tilde{\boldsymbol{y}}_n^{\mathrm{T}}]^{\mathrm{T}}$, $\tilde{\boldsymbol{y}}_n \triangleq [\tilde{\boldsymbol{y}}_{1,n}^{\mathrm{T}}, \ldots, \tilde{\boldsymbol{y}}_{K_{n-1},n}^{\mathrm{T}}]^{\mathrm{T}}$, $\tilde{\boldsymbol{x}}_n \triangleq [\tilde{\boldsymbol{x}}_{1,n}^{\mathrm{T}}, \ldots, \tilde{\boldsymbol{x}}_{K_{n-1},n}^{\mathrm{T}}]^{\mathrm{T}}$, $\tilde{\boldsymbol{u}}_n \triangleq [\tilde{u}_{1,n}, \ldots, \tilde{u}_{K_{n-1},n}]^{\mathrm{T}}$, $\tilde{\boldsymbol{r}}_n \triangleq [\tilde{r}_{1,n}, \ldots, \tilde{r}_{K_{n-1},n}]^{\mathrm{T}}$; for new PSMCs $\breve{\boldsymbol{y}}_n \triangleq [\breve{\boldsymbol{y}}_{1,n}^{\mathrm{T}}, \ldots, \breve{\boldsymbol{y}}_{M_n,n}^{\mathrm{T}}]^{\mathrm{T}}$, $\breve{\boldsymbol{x}}_n \triangleq [\breve{\boldsymbol{x}}_{1,n}^{\mathrm{T}}, \ldots, \breve{\boldsymbol{x}}_{M_n,n}^{\mathrm{T}}]^{\mathrm{T}}$, $\breve{\boldsymbol{u}}_n \triangleq [\breve{u}_{1,n}, \ldots, \breve{u}_{M_n,n}]^{\mathrm{T}}$, $\breve{\boldsymbol{r}}_n \triangleq [\breve{r}_{1,n}, \ldots, \breve{r}_{M_n,n}]^{\mathrm{T}}$; for combination of the legacy and new PSMCs, $\boldsymbol{y}_n \triangleq [\tilde{\boldsymbol{y}}_n^{\mathrm{T}}, \breve{\boldsymbol{y}}_n^{\mathrm{T}}]^{\mathrm{T}}$, $\boldsymbol{y}_n \triangleq [\boldsymbol{y}_{1,n}^{\mathrm{T}}, \ldots, \boldsymbol{y}_{K_n,n}^{\mathrm{T}}]^{\mathrm{T}}$ with $k \in \mathcal{K}_n \triangleq \{1, \ldots, K_n\}$.

Assume that the states $\tilde{\boldsymbol{y}}_{k,n}$ with $k \in \mathcal{K}_n$ of the legacy PSMCs are distributed independently across k and n, and evolve independently according to

their respective Markovian state dynamics. The state-transition pdf for legacy PSMC state $\tilde{\boldsymbol{y}}_n$ factorizes as

$$f(\tilde{\boldsymbol{y}}_n|\boldsymbol{y}_{n-1}) = \prod_{k=1}^{K_{n-1}} f(\tilde{\boldsymbol{y}}_{k,n}|\boldsymbol{y}_{k,n-1}), \tag{3}$$

where $f(\tilde{\boldsymbol{y}}_{k,n}|\boldsymbol{y}_{k,n-1}) = f(\tilde{\boldsymbol{\psi}}_{k,n}, \tilde{r}_{k,n}|\boldsymbol{\psi}_{k,n-1}, r_{k,n-1})$ is the single PSMC state-transition pdf. If the PSMC did not exist at time $n-1$, i.e., $r_{k,n-1} = 0$, it cannot exist at time n as a legacy PSMC. This means that

$$f(\tilde{\boldsymbol{\psi}}_{k,n}, \tilde{r}_{k,n}|\boldsymbol{\psi}_{k,n-1}, 0) = \begin{cases} f_{\mathrm{D}}(\tilde{\boldsymbol{\psi}}_{k,n}), & \tilde{r}_{k,n} = 0 \\ 0, & \tilde{r}_{k,n} = 1\,. \end{cases} \tag{4}$$

If the PSMC existed at time $n-1$, i.e., $r_{k,n-1} = 1$, it either dies i.e., $\tilde{r}_{k,n} = 0$ or it still exist i.e., $\tilde{r}_{k,n} = 1$ with the survival probability denoted as P_{s}. If it does survive, the state $\tilde{\boldsymbol{\psi}}_{k,n}$ is distributed according to the state-transition pdf $f(\tilde{\boldsymbol{\psi}}_{k,n}|\boldsymbol{\psi}_{k,n-1})$. Thus we have

$$f(\tilde{\boldsymbol{\psi}}_{k,n}, \tilde{r}_{k,n}|\boldsymbol{\psi}_{k,n-1}, 1) = \begin{cases} (1-P_{\mathrm{s}}) f_{\mathrm{D}}(\tilde{\boldsymbol{\psi}}_{k,n}), & \tilde{r}_{k,n} = 0 \\ P_{\mathrm{s}} f(\tilde{\boldsymbol{\psi}}_{k,n}|\boldsymbol{\psi}_{k,n-1}), & \tilde{r}_{k,n} = 1\,. \end{cases} \tag{5}$$

We further factorize the state-transition pdfs as $f(\tilde{\boldsymbol{\psi}}_{k,n}|\boldsymbol{\psi}_{k,n-1}) = f(\tilde{\boldsymbol{x}}_{k,n}|\boldsymbol{x}_{k,n-1})$ $f(\tilde{u}_{k,n}|u_{k,n-1})$ given the independence assumptions between that the state vectors $\tilde{\boldsymbol{x}}_{k,n}$ and the normalized amplitudes $\tilde{u}_{k,n}$.

3.2 Associations of PSMCs with Measurements

The association of PSMCs and measurements is complicated by the DA uncertainty: at time n it is unknown which measurement $\boldsymbol{z}_{m,n}$ originates from which PSMC, or if a measurement did not originate from a PSMC (false alarm or clutter), or if a PSMC did not generate any measurement (missed detection). Any PSMC-to-measurement association is described by PSMC-oriented variables

$$a_{k,n} \triangleq \begin{cases} m \in \mathcal{M}_n, & \text{if the legacy PSMC } k \text{ generate} \\ & \text{the measurement } m \\ 0 & \text{if the legacy PSMC } k \text{ does not} \\ & \text{generate any measurement,} \end{cases}$$

stacked into the PSMC-oriented association vector $\boldsymbol{a}_n \triangleq [a_{1,n}, \ldots, a_{K_{n-1},n}]^{\mathrm{T}}$. To reduce computational complexity, following [8], [21], [27], we use a redundant description of PMSC-measurement associations, i.e., we introduce

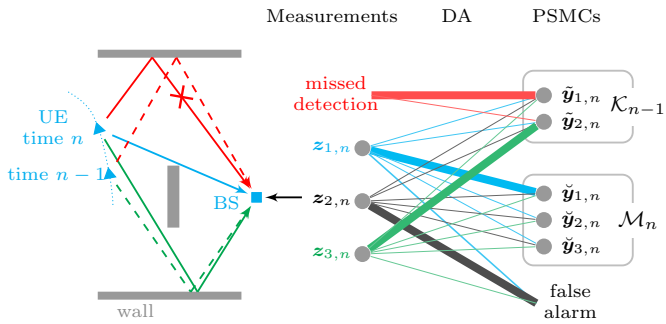

Figure 1: An example of probabilistic DA, where the association probability between a measurement and a PSMC is denoted with the line thickness. At time n, three measurements are generated from the SBL channel estimator. The probability that the measurement $\boldsymbol{z}_{1,n}$ is associated with the new PSMC $\breve{\boldsymbol{y}}_{1,n}$ is much higher than the probability that $\boldsymbol{z}_{1,n}$ is associated with a legacy PSMC. The measurement $\boldsymbol{z}_{3,n}$ is associated with the legacy PSMC $\tilde{\boldsymbol{y}}_{2,n}$ with high probability. Besides, it is highly possible that the measurement $\boldsymbol{z}_{2,n}$ is a false alarm and the legacy PSMC $\tilde{\boldsymbol{y}}_{1,n}$ did not generate any measurement (missed detection).

measurement-oriented association variables

$$b_{m,n} \triangleq \begin{cases} k \in \mathcal{K}_{n-1}, & \text{if the measurement } m \text{ is generated by the legacy PSMC } k \\ 0 & \text{if the measurement } m \text{ is not generated by any legacy PSMC,} \end{cases}$$

and define the measurement-oriented association vector $\boldsymbol{b}_n \triangleq [b_{1,n}, \ldots, b_{M_n,n}]^{\mathrm{T}}$. Note that the "redundant formulation" of using $\boldsymbol{a}_n$ together with $\boldsymbol{b}_n$ is the key to make the algorithm scalable to the varying numbers of PSMCs and measurements.

The example presented in Fig. 1 explains how the probabilistic DA is performed. The probabilities of all association hypotheses of PSMCs and measurements are evaluated, and a high probability indicates that the PSMC state explains a measurement well.

3.3 States of Unknown Parameters

The detection and estimation of PSMC states require the information of the spatial density of false alarm measurements, and the detection probabilities, i.e., the probability that a PSMC $\boldsymbol{y}_{k,n}$ generates a measurement $\boldsymbol{z}_{m,n}$. We assume that the false alarm measurements are independent and identically distributed (iid) according to the pdf $f_{\mathrm{c}}(\boldsymbol{z}_{m,n})$, which is uniform on the region

of interest (RoI), and the number of false alarm measurements at each time n, i.e., false alarm rate (FAR), is Poisson distributed with mean $\mu_{\mathrm{FA},n}$. The detection probability $P_{\mathrm{d}}(\boldsymbol{\psi}_{k,n}) \triangleq P_{\mathrm{d}}(u_{k,n})$ is characterized by its normalized amplitude [23], [24]. Both $\mu_{\mathrm{FA},n}$ and $P_{\mathrm{d}}(u_{k,n})$ are assumed to be unknown and potentially time-varying, and the algorithm is designed to automatically adapt these parameters online. More specifically, $\mu_{\mathrm{FA},n}$ is estimated continually along with the PSMC states, and $P_{\mathrm{d}}(u_{k,n})$ is given at each time by using the normalized amplitudes $u_{k,n}$, as explained in [23], [24] and Section 3.4. The mean FAR $\mu_{\mathrm{FA},n}$ is independent of the states of the legacy PSMCs, and evolve according to the state-transition pdf $f(\mu_{\mathrm{FA},n}|\mu_{\mathrm{FA},n-1})$.

3.4 Likelihood Functions

If the measurement $\boldsymbol{z}_{m,n}$ is originated from the PSMC k, i.e., $a_{k,n} = m$, then the conditional distribution given the state $\boldsymbol{\psi}_{k,n}$ is described by the pdf $f(\boldsymbol{z}_{m,n}|\boldsymbol{\psi}_{k,n})$. Assuming the individual measurements inside vector $\boldsymbol{z}_{m,n}$ are conditional independent given the state $\boldsymbol{\psi}_{k,n}$, the pdfs $f(\boldsymbol{z}_{m,n}|\boldsymbol{\psi}_{k,n})$ of PSMC-originated measurements factorizes as

$$f(\boldsymbol{z}_{m,n}|\boldsymbol{\psi}_{k,n}) = f(\hat{d}_{m,n}|d_{k,n})f(\hat{\varphi}_{m,n}|\varphi_{k,n})f(\hat{u}_{m,n}|u_{k,n}) \tag{6}$$

where the conditional pdfs $f(\hat{d}_{m,n}|d_{k,n})$ and $f(\hat{\varphi}_{m,n}|\varphi_{k,n})$ are defined by Gaussian measurement models, yields

$$f(\hat{d}_{m,n}|d_{k,n}) = \frac{1}{\sqrt{2\pi\sigma^2_{\mathrm{d},m,n}}} \exp\big(\frac{-(\hat{d}_{m,n} - d_{k,n})^2}{2\sigma^2_{\mathrm{d},m,n}}\big), \tag{7}$$

$$f(\hat{\varphi}_{m,n}|\varphi_{k,n}) = \frac{1}{\sqrt{2\pi\sigma^2_{\varphi,m,n}}} \exp\big(\frac{-(\hat{\varphi}_{m,n} - \varphi_{k,n})^2}{2\sigma^2_{\varphi,m,n}}\big). \tag{8}$$

The variances are computed using the norm amplitude measurements, i.e., $\sigma^2_{\mathrm{d},m,n} = c^2/(8\pi^2\beta_{\mathrm{bw}}\hat{u}^2_{m,n})$ and $\sigma^2_{\varphi,m,n} = c^2/(8\pi^2 f_{\mathrm{c}}^2\hat{u}^2_{m,n}D^2(\hat{\varphi}_{m,n}))$, where β_{bw} is the mean square bandwidth of the transmit signal pulse $s(t)$ and $D^2(\hat{\varphi}_{m,n})$ is the squared array aperture [24], [26]. The pdf $f(\hat{u}_{m,n}|u_{k,n})$ of the normalized amplitude $\hat{u}_{m,n}$ conditioned on the state $u_{k,n}$ is given by a unit-variance Rician distribution as in [23], [24].

If $\boldsymbol{z}_{m,n}$ is a false alarm measurement, it is distributed according to the pdf $f_{\mathrm{FA}}(\boldsymbol{z}_{m,n})$, which factorizes as

$$f_{\mathrm{FA}}(\boldsymbol{z}_{m,n}) = f_{\mathrm{FA}}(\hat{d}_{m,n})f_{\mathrm{FA}}(\hat{\varphi}_{m,n})f_{\mathrm{FA}}(\hat{u}_{m,n}) \tag{9}$$

where $f_{\mathrm{FA}}(\hat{d}_{m,n})$ and $f_{\mathrm{FA}}(\hat{\varphi}_{m,n})$ are assumed to be uniform in their respective

RoIs, i.e., $f_{\mathrm{FA}}(\hat{d}_{m,n}) = 1/d_{\max}$ and $f_{\mathrm{FA}}(\hat{\varphi}_{m,n}) = 1/2\pi$. The false alarm pdf $f_{\mathrm{FA}}(\hat{u}_{m,n})$ of the normalized amplitude is given by a unit-variance Rayleigh distribution [20, Ch. 1.6.7], i.e., $f_{\mathrm{FA}}(\hat{u}_{m,n}) = \hat{u}_{m,n}\exp(-\hat{u}_{m,n}^2/2)/P_{\mathrm{FA}}$. The false alarm probability is given as $P_{\mathrm{FA}} = \exp(-u_{\mathrm{th}}^2/2)$ with the normalized amplitude threshold u_{th}.

3.5 Joint Posterior pdf and Factor Graph

By using common assumptions [8], [21], and for fixed and thus observed measurements $\boldsymbol{z}$, it can be shown that the joint posterior pdf of $\tilde{\boldsymbol{y}}$, $\breve{\boldsymbol{y}}$, $\boldsymbol{a}$, $\boldsymbol{b}$, $\boldsymbol{\mu}_{\mathrm{FA}}$ and $\boldsymbol{m}$, conditioned on $\boldsymbol{z}$ is given by

$$
\begin{aligned}
&f(\tilde{\boldsymbol{y}}, \breve{\boldsymbol{y}}, \boldsymbol{a}, \boldsymbol{b}, \boldsymbol{\mu}_{\mathrm{FA}}, \boldsymbol{m}|\boldsymbol{z}) \\
&\propto f(\mu_{\mathrm{FA},1}) \prod_{m'=1}^{M_1} h(\breve{\boldsymbol{\psi}}_{m',1}, \breve{r}_{m',1}, b_{m',1}, \mu_{\mathrm{FA},1}; \boldsymbol{z}_1) \\
&\quad \times \prod_{n'=2}^{n} f(\mu_{\mathrm{FA},n'}|\mu_{\mathrm{FA},n'-1}) \left(\prod_{k=1}^{K_{n'-1}} f(\tilde{\boldsymbol{y}}_{k,n'}|\boldsymbol{y}_{k,n'-1}) \right) \\
&\quad \times \left(\prod_{k=1}^{K_{n'-1}} \prod_{m=1}^{M_{n'}} g(\tilde{\boldsymbol{y}}_{k,n'}, a_{k,n'}, \mu_{\mathrm{FA},n'}; \boldsymbol{z}_{n'}) \Psi(a_{k,n'}, b_{m,n'}) \right) \\
&\quad \times \left(\prod_{m=1}^{M_{n'}} f(\breve{\boldsymbol{y}}_{m,n'}) h(\breve{\boldsymbol{y}}_{m,n'}, b_{m,n'}, \mu_{\mathrm{FA},n'}; \boldsymbol{z}_{n'}) \right)
\end{aligned} \tag{10}
$$

where we introduced the functions $g(\tilde{\boldsymbol{y}}_{k,n}, a_{k,n}, \mu_{\mathrm{FA},n}; \boldsymbol{z}_n)$, $h(\breve{\boldsymbol{y}}_{m,n}, b_{m,n}, \mu_{\mathrm{FA},n}; \boldsymbol{z}_n)$, $f(\breve{\boldsymbol{y}}_{m,n})$, and $\Psi(a_{k,n}, b_{m,n})$ that will be discussed next.

The pseudo likelihood functions are given as $g(\tilde{\boldsymbol{y}}_{k,n}, a_{k,n}, \mu_{\mathrm{FA},n}; \boldsymbol{z}_n) = g(\tilde{\boldsymbol{\psi}}_{k,n}, \tilde{r}_{k,n}, a_{k,n}, \mu_{\mathrm{FA},n}; \boldsymbol{z}_n)$ and $h(\breve{\boldsymbol{y}}_{m,n}, b_{m,n}, \mu_{\mathrm{FA},n}; \boldsymbol{z}_n) = h(\breve{\boldsymbol{\psi}}_{m,n}, \breve{r}_{m,n}, b_{m,n}, \mu_{\mathrm{FA},n}; \boldsymbol{z}_n)$

$$
\begin{aligned}
&g(\tilde{\boldsymbol{\psi}}_{k,n}, 1, a_{k,n}, \mu_{\mathrm{FA},n}; \boldsymbol{z}_n) \\
&= \begin{cases} \dfrac{n(\mu_{\mathrm{FA},n}) f(\boldsymbol{z}_{m,n}|\tilde{\boldsymbol{\psi}}_{k,n}) P_{\mathrm{d}}(\tilde{u}_{k,n})}{\mu_{\mathrm{FA},n} f_{\mathrm{FA}}(\boldsymbol{z}_{m,n})}, & a_{k,n} = m \in \mathcal{M}_n \\ 1 - P_{\mathrm{d}}(\tilde{u}_{k,n}), & a_{k,n} = 0, \end{cases}
\end{aligned} \tag{11}
$$

and $g(\tilde{\boldsymbol{\psi}}_{k,n}, 0, a_{k,n}, \mu_{\mathrm{FA},n}; \boldsymbol{z}_n) = 1(a_{k,n}) n(\mu_{\mathrm{FA},n})$ with $n(\mu_{\mathrm{FA},n}) \triangleq (\mu_{\mathrm{FA},n}^{M_n} e^{-\mu_{\mathrm{FA},n}}$

$\times \frac{1}{M_n!})^{1/(K_{n-1}+M_n)}$ as well as

$$h(\breve{\boldsymbol{\psi}}_{m,n}, 1, b_{m,n}, \mu_{\mathrm{FA},n}; \boldsymbol{z}_n) = \begin{cases} 0, & b_{m,n} = k \in \mathcal{K}_{n-1} \\ \dfrac{n(\mu_{\mathrm{FA},n}) f(\boldsymbol{z}_{m,n}|\breve{\boldsymbol{\psi}}_{m,n})}{\mu_{\mathrm{FA},n} f_{\mathrm{FA}}(\boldsymbol{z}_{m,n})}, & b_{m,n} = 0, \end{cases} \tag{12}$$

and $h(\breve{\boldsymbol{\psi}}_{m,n}, 0, b_{m,n}, \mu_{\mathrm{FA},n}; \boldsymbol{z}_n) = n(\mu_{\mathrm{FA},n})$. The prior distributions $f(\breve{\boldsymbol{y}}_{m,n}) = f(\breve{\boldsymbol{\psi}}_{m,n}, \breve{r}_{m,n})$ for new PSMC states can be expressed as

$$f(\breve{\boldsymbol{\psi}}_{m,n}, \breve{r}_{m,n}) = \begin{cases} \mu_{\mathrm{n}} f_{\mathrm{n}}(\breve{\boldsymbol{\psi}}_{m,n}), & \breve{r}_{m,n} = 1 \\ f_{\mathrm{D}}(\breve{\boldsymbol{\psi}}_{m,n}), & \breve{r}_{m,n} = 0, \end{cases} \tag{13}$$

where μ_{n} and $f_{\mathrm{n}}(\breve{\boldsymbol{\psi}}_{m,n})$ are the mean and pdf of a Poisson point process, respectively. Finally, the binary indicator functions that check consistency for any pair $(a_{k,n}, b_{m,n})$ of PSMC-oriented and measurement-oriented association variable at time n, read [8], [21]

$$\Psi(a_{k,n}, b_{m,n}) = \begin{cases} 0, & a_{k,n} = m, b_{m,n} \neq k \\ & \text{or } \ b_{m,n} = k, a_{k,n} \neq m \\ 1, & \text{otherwise.} \end{cases} \tag{14}$$

In case the joint PSMC-oriented association vector $\boldsymbol{a}_n$ and the measurement-oriented association vector $\boldsymbol{b}_n$ do not describe the same association event, at least one indicator function in (10) is zero and thus $f(\tilde{\boldsymbol{y}}, \breve{\boldsymbol{y}}, \boldsymbol{a}, \boldsymbol{b}, \boldsymbol{\mu}_{\mathrm{FA}}, \boldsymbol{m}|\boldsymbol{z})$ is zero as well. The factor graph describing the factorization (10) of the joint posterior pdf is shown in Fig. 2.

4 The BP-based MPC Tracking algorithm

In the Bayesian setting, the detection of PSMCs $\boldsymbol{y}_{k,n}$ with $k \in \mathcal{K}_n$ relies on the marginal posterior existence probabilities $f(r_{k,n} = 1|\boldsymbol{z})$, and the estimation of the detected PSMC states $\boldsymbol{x}_{k,n}$, the amplitudes $u_{k,n}$ and the mean FAR $\mu_{\mathrm{FA},n}$ rely on the marginal posterior pdfs $f(\boldsymbol{\psi}_{k,n}|r_{k,n} = 1, \boldsymbol{z})$ and $f(\mu_{\mathrm{FA},n}|\boldsymbol{z})$. More specifically, a PSMC is detected if $p(r_{n,k} = 1|\boldsymbol{z}) > P_{\mathrm{det}}$ [28], where $p(r_{n,k} = 1|\boldsymbol{z})$ is obtained from the marginal posterior pdfs of the augmented PSMC state $f(\boldsymbol{y}_{k,n}|\boldsymbol{z}) = f(\boldsymbol{\psi}_{k,n}, r_{k,n}|\boldsymbol{z})$ as

$$p(r_{k,n} = 1|\boldsymbol{z}) = \int f(\boldsymbol{\psi}_{k,n}, r_{k,n} = 1|\boldsymbol{z}) \mathrm{d}\boldsymbol{\psi}_{k,n}. \tag{15}$$

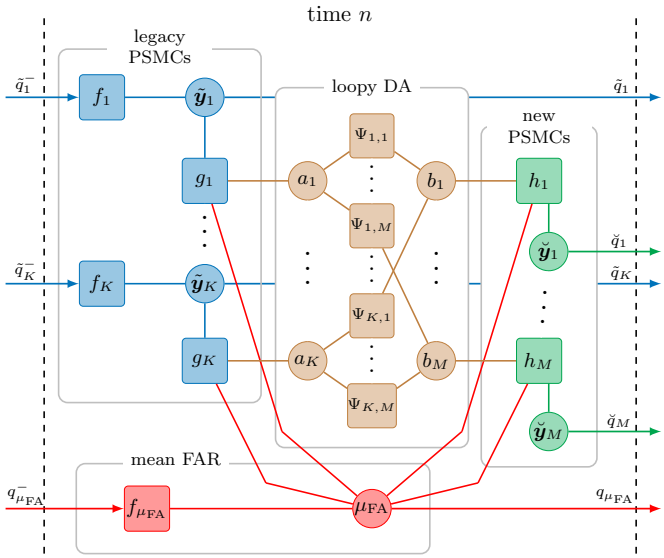

Figure 2: Factor graph representation of the factorized joint posterior pdf (10), shown for time n. For simplicity, the following short notations are used: $K \triangleq K_{n-1}$, $M \triangleq M_n$; *variable nodes*: $a_k \triangleq a_{k,n}$, $b_m \triangleq b_{m,n}$, $\mu_{\rm FA} \triangleq \mu_{{\rm FA},n}$, $\tilde{\boldsymbol{y}}_k \triangleq \tilde{\boldsymbol{y}}_{k,n}$, $\breve{\boldsymbol{y}}_m \triangleq \breve{\boldsymbol{y}}_{m,n}$; *factor nodes*: $f_k \triangleq f(\tilde{\boldsymbol{y}}_{k,n}|\boldsymbol{y}_{k,n-1})$, $f_{\mu_{\rm FA}} \triangleq f(\mu_{{\rm FA},n}|\mu_{{\rm FA},n-1})$, $g_k \triangleq g(\tilde{\boldsymbol{\psi}}_{k,n}, \tilde{r}_{k,n}, a_{k,n}, \mu_{{\rm FA},n}; \boldsymbol{z}_n)$, $h_m \triangleq h(\breve{\boldsymbol{\psi}}_{m,n}, \breve{r}_{m,n}, b_{m,n}, \mu_{{\rm FA},n}; \boldsymbol{z}_n)$, $\Psi_{k,m} \triangleq \Psi(a_{k,n}, b_{m,n})$; *beliefs*: $\tilde{q}_k^- \triangleq \tilde{q}(\tilde{\boldsymbol{\psi}}_{k,n-1}, \tilde{r}_{k,n-1})$, $\tilde{q}_k \triangleq \tilde{q}(\tilde{\boldsymbol{\psi}}_{k,n}, \tilde{r}_{k,n})$, $\breve{q}_m \triangleq \breve{q}(\breve{\boldsymbol{\psi}}_{m,n}, \breve{r}_{m,n})$, $q_{\mu_{\rm FA}}^- \triangleq q(\mu_{{\rm FA},n-1})$, $q_{\mu_{\rm FA}} \triangleq q(\mu_{{\rm FA},n})$.

The estimates of $\mu_{{\rm FA},n}$, and the states $\boldsymbol{\psi}_{k,n}$ and $u_{k,n}$ of detected PSMCs are calculated by means of the minimum mean-square error (MMSE) estimator [29]

$$\hat{\mu}_{{\rm FA},n}^{\rm MMSE} \triangleq \int \mu_{{\rm FA},n} f(\mu_{{\rm FA},n}|\boldsymbol{z}) {\rm d}\mu_{{\rm FA},n}, \tag{16}$$

$$\hat{\boldsymbol{x}}_{k,n}^{\rm MMSE} \triangleq \int \boldsymbol{x}_{k,n} f(\boldsymbol{\psi}_{k,n}|r_{k,n}=1,\boldsymbol{z}) {\rm d}\boldsymbol{\psi}_{k,n}, \tag{17}$$

$$\hat{u}_{k,n}^{\rm MMSE} \triangleq \int u_{k,n} f(\boldsymbol{\psi}_{k,n}|r_{k,n}=1,\boldsymbol{z}) {\rm d}\boldsymbol{\psi}_{k,n}, \tag{18}$$

where the marginal posterior pdf $f(\boldsymbol{\psi}_{k,n}|r_{k,n}=1,\boldsymbol{z})$ can be obtained from $f(\boldsymbol{\psi}_{k,n}, r_{k,n}|\boldsymbol{z})$ as

$$f(\boldsymbol{\psi}_{k,n}|r_{k,n}=1,\boldsymbol{z}) = \frac{f(\boldsymbol{\psi}_{k,n}, r_{k,n}=1|\boldsymbol{z})}{f(r_{k,n}=1|\boldsymbol{z})}. \tag{19}$$

Note that the posterior existence probabilities $f(r_{k,n} = 1|\boldsymbol{z})$ are also used in the pruning step removing PSMCs with $f(r_{k,n} = 1|\boldsymbol{z}_{1:n}) < P_{\text{prun}}$. As explained in Section 3.1, the number of legacy PSMCs are updated as $K_n = K_{n-1} + M_n$ at each time n, the pruning step would prevent K_n from growing indefinitely.

To obtain the marginal posterior pdfs $f(\tilde{\boldsymbol{\psi}}_{k,n}, \tilde{r}_{k,n}|\boldsymbol{z})$, $f(\breve{\boldsymbol{\psi}}_{m,n}, \breve{r}_{m,n}|\boldsymbol{z})$ and $f(\mu_{\text{FA},n}|\boldsymbol{z})$ of the join posterior pdf $f(\tilde{\boldsymbol{y}}, \breve{\boldsymbol{y}}, \boldsymbol{a}, \boldsymbol{b}, \boldsymbol{\mu}_{\text{FA}}, \boldsymbol{m}|\boldsymbol{z})$, direct marginalization is infeasible. However, their respective approximations $\tilde{q}(\tilde{\boldsymbol{y}}_{k,n}) = \tilde{q}(\tilde{\boldsymbol{\psi}}_{k,n}, \tilde{r}_{k,n})$, $\breve{q}(\breve{\boldsymbol{y}}_{m,n}) = \breve{q}(\breve{\boldsymbol{\psi}}_{m,n}, \breve{r}_{m,n})$ and $q(\mu_{\text{FA},n})$ can be obtained efficiently by running the iterative BP [30] on the factor graph in Fig. 2. Since this factor graph is loopy, we now specify the following order in which the message are computed: (i) messages are not sent backward in time; (ii) iterative message passing is only performed for probabilistic DA at each time step. In addition, the generic BP rules for calculating messages and beliefs introduced in [21, Ch. III] are also followed. A sequential particle-based message passing implementation [8], [21], [27] is used to approximate the messages and beliefs.

5 Experimental Results

The proposed BP-MPCT algorithm is validated using synthetic channel measurement data. Given the floor plan of a seminar room at Graz University of Technology [8], the true SMC parameters and model order are firstly obtained by using a ray tracing (RT) method, and then applied in the radio signal model (2) to synthetically generate the channel measurement data for each simulation run. We assume that the amplitude of each SMC follows free-space pathloss and is attenuated by 3 dB after each reflection. The transmit pulse $s(t)$ is a root-raised-cosine pulse with a symbol duration $T_{\text{p}} = 2$ ns and a roll-off factor of 0.6 at a center frequency of $f_{\text{c}} = 6$ GHz with bandwidth of 500 MHz. The number of samples $N_{\text{s}} = 94$. A 3×3 uniform rectangular array with an inter-element spacing of 1 cm is used at the BS. For each simulation run, the AWGN is generated with the noise variance $\sigma_{\text{w}}^2 = N_0/T_s$ specified with a given $\text{SNR}_{1\text{m}} = 10\log_{10}(\frac{|\alpha_{\text{LoS}}|^2}{N_0})$, where the amplitude α_{LoS} of the line-of-sight (LoS) component is fixed and computed at 1 m distance. The synthetic channel measurement data is used in the SBL channel estimator to obtain the noisy measurements $\boldsymbol{z}_{m,n}$ at each time n, and the true number of false alarm measurements is obtained by checking the optimal sub-pattern assignment (OSPA) matrix [31] between $\boldsymbol{z}_{m,n}$ and the true SMC parameters from RT. Note that we on purposely generated more false alarm measurements by setting the detection threshold (on individual MPC's SNR) to 8 dB in the SBL channel estimator, which is smaller than the threshold according to [18], therefore the performance of the BP-MPCT algorithm can be validated in more challenging situations. In total, we performed 50 simulation runs for each given $\text{SNR}_{1\text{m}} \in \{25\,\text{dB}, 30\,\text{dB},$

35 dB}.

The parameters used in the BP-MPCT algorithm are as follows: the number of particles is 10000, the survival probability $P_{\mathrm{s}} = 0.999$, the detection probability threshold $P_{\mathrm{det}} = 0.5$, the pruning threshold $P_{\mathrm{prun}} = 10^{-4}$, the mean number of newly detected SMCs $\mu_{\mathrm{n}} = 0.01$, the birth pdf $f_{\mathrm{n}}(\breve{\boldsymbol{\psi}}_{m,n})$ is uniform on the RoI, i.e., $f_{\mathrm{n}}(\breve{\boldsymbol{\psi}}_{m,n}) = 1/(2\pi d_{\max})$ with $d_{\max} = 30\,\mathrm{m}$. The P_{FA} is calculated for a threshold of $u_{\mathrm{th}} = 1$. The detection probabilities $P_{\mathrm{d}}(\hat{u}_{k,n}^{\mathrm{MMSE}})$ are calculated using the MMSE estimates of the normalized amplitudes $\hat{u}_{k,n}^{\mathrm{MMSE}}$ [23]. The particles for the initial mean FAR are drawn from a uniform distribution on [0.001, 15]. The particles for the initial states $\breve{\boldsymbol{\psi}}_{m,n}$ of a new PSMC are drawn from a 5-D uniform distribution with center at $[\hat{d}_{m,n}, \hat{\varphi}_{m,n}, 0, 0, \hat{u}_{m,n}]$ and the support of each component is given by: $[-0.3, 0.3]\,\mathrm{m}$, $[-0.7, 0.7]\,\mathrm{rad}$, $[-0.01, 0.01]\,\mathrm{m/s}$, $[-0.01, 0.01]\,\mathrm{rad/s}$, $[-1, 1]$. The state-transition pdf of $\boldsymbol{x}_{k,n}$ is defined by a nearly-constant velocity model [32, Section 6.3.2] with $\Delta T = 1\,\mathrm{s}$ and noise standard deviations $\sigma_{\mathrm{d}} = 0.01\,\mathrm{m/s^2}$ and $\sigma_{\varphi} = 0.02\,\mathrm{rad/s^2}$ for distance and AoA, respectively. Furthermore, the state-transition pdfs of the normalized amplitude $f(u_{k,n}|u_{k,n-1})$ and the mean FAR $f(\mu_{\mathrm{FA},n}|\mu_{\mathrm{FA},n-1})$ are given as Gaussian distributions with noise standard deviations $\sigma_u = 1$ and $\sigma_{\mathrm{FAR}} = 0.4$, respectively.

The results of the BP-MPCT algorithm after averaging over 50 simulation runs are presented in Fig. 3, and the estimates $\boldsymbol{z}_{m,n}$ from the SBL estimator (after excluding the false alarm measurements) are used for comparison. It can be seen that the mean OSPA (MOSPA) [31] errors on the distances, AoAs and amplitudes obtained with BP-MPCT are mostly lower than the errors with SBL, and the advantage gets more obvious at low $\mathrm{SNR}_{1\mathrm{m}}$. This can be explained that: given low $\mathrm{SNR}_{1\mathrm{m}}$, there exist more "weak" SMCs with low SNRs that are sometimes miss detected in SBL, and some of the miss detections can be reconstructed in BP-MPCT, which leads to the better estimation of the model order and therefore lower MOSPA errors. Given the $\mathrm{SNR}_{1\mathrm{m}} = 35\,\mathrm{dB}$, the MOSPA errors obtained with BP-MPCT are mostly below 2 cm for distances, 2 degrees for AoAs and -40 dB for amplitudes. Furthermore, raises of the MOSPA errors for BP-MPCT are observed at time instances where the true number of SMCs changes, which happen mainly due to model order mismatch instead of the increases on the root mean square errors of individual detected PSMCs. More specifically, it takes one or two steps until the existence probabilities of the legacy/new PSMCs reach the detection probability threshold P_{det}, so tracks are terminated or newly detected, and therefore the change on the model order can be followed. As shown in Fig. 3d, the BP-MPCT algorithm is able to follow the correct model order for the most of the time, even for $\mathrm{SNR}_{1\mathrm{m}} = 25\,\mathrm{dB}$. Moreover, the estimated mean FAR converges to the true value regardless of the $\mathrm{SNR}_{1\mathrm{m}}$ condition as depicted in Fig. 3e.

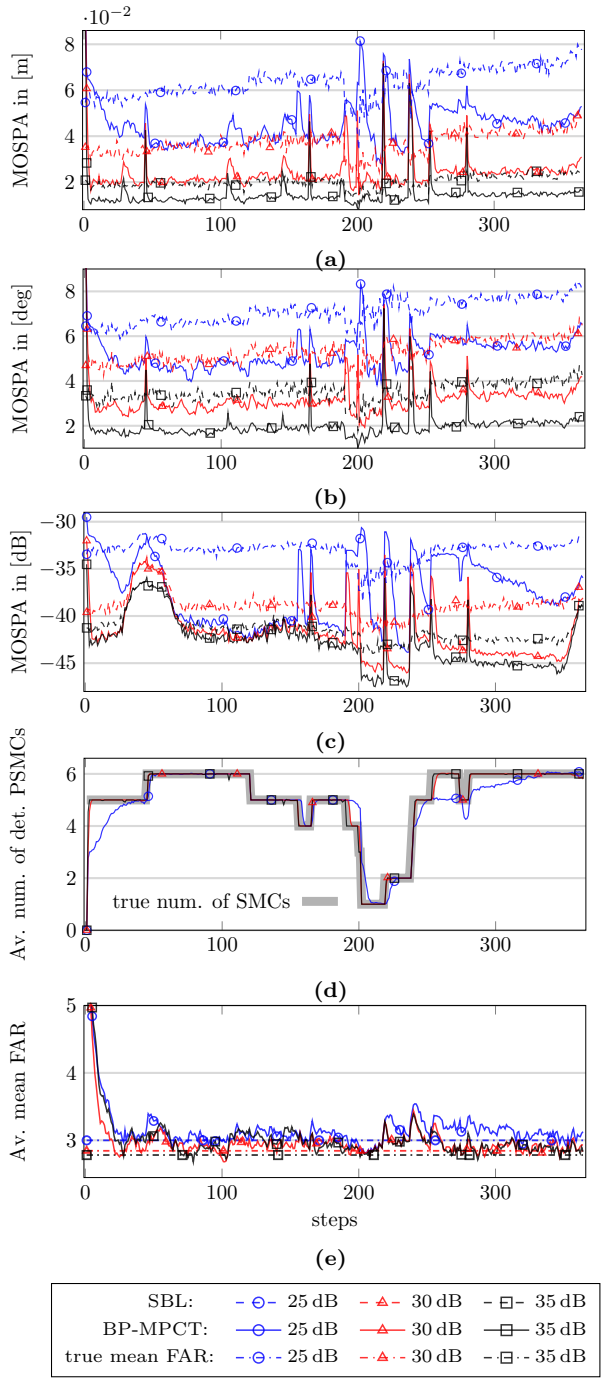

Figure 3: For different $\mathrm{SNR}_{1\mathrm{m}}$, MOSPA errors on (a) distances, (b) AoAs, and (c) amplitudes. (d) Averaged number of detected PSMCs. (e) Averaged estimated mean FAR.

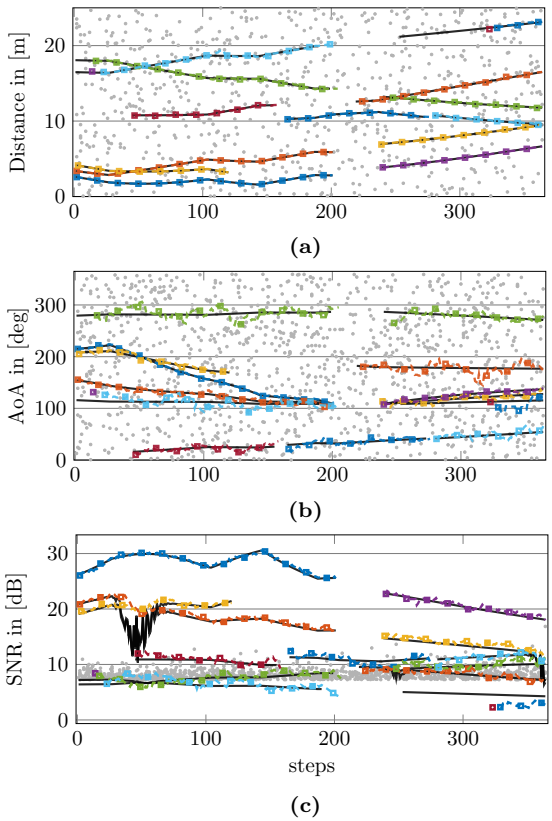

Figure 4: Estimation results of a single simulation run for $\mathrm{SNR}_{1\mathrm{m}} = 25\,\mathrm{dB}$ on (a) distances, (b) AoAs, and (c) SNRs, i.e., the squares of the estimated normalized amplitudes. False alarm measurements are depicted by gray dots, true SMC parameters by black solid lines, and estimates of detected PSMCs by different colors.

The results of an exemplary simulation run given $\mathrm{SNR}_{1\mathrm{m}} = 25\,\mathrm{dB}$ are shown in Fig. 4. As can be seen, the BP-MPCT algorithm shows good ability to distinguish between false alarm measurements and measurements originated from SMCs. The birth-death processes of SMCs are accurately detected and tracks are well reconstructed even for some "weak" SMCs, for example, the estimated track denoted in cyan between time $n = 1$ and $n = 200$, of which the true SNR is mostly below the 8 dB detection threshold. Furthermore, the association of estimates over time in delay and angular subspaces are robust even in the presence of intersections between SMCs.

6 Conclusions

We presented a BP-MPCT algorithm which jointly performs probabilistic DA, detection and tracking of MPC parameters. This algorithm is adaptive to time-varying mean false alarm rate, as well as the detection probabilities by utilizing the amplitude statistics of the MPC estimates. Simulation results showed that the BP-MPCT algorithm has excellent performance regarding the scalability to the time-varying model order, estimation accuracy, and association property over time in a realistic and very challenging scenario.

7 Acknowledgment

This work was supported in part by the Swedish Research Council (VR), in part by the strategic research area ELLIIT and in part by the TU Graz.

References

[1] M. L. Jakobsen, T. Pedersen and B. H. Fleury, "Analysis of stochastic radio channels with temporal birth-death dynamics: A marked spatial point process perspective", *IEEE Trans. Antennas Propag.*, vol. 62, no. 7, pp. 3761–3775, 2014.

[2] J. Flordelis, X. Li, O. Edfors and F. Tufvesson, "Massive MIMO extensions to the COST 2100 channel model: Modeling and validation", *IEEE Trans. Wireless Commun.*, vol. 19, no. 1, pp. 380–394, 2020.

[3] F. Rusek, D. Persson, B. K. Lau, E. G. Larsson, T. L. Marzetta, O. Edfors and F. Tufvesson, "Scaling up MIMO: Opportunities and challenges with very large arrays", *IEEE Signal Process. Mag.*, vol. 30, no. 1, pp. 40–60, 2013.

[4] R. Di Taranto, S. Muppirisetty, R. Raulefs, D. Slock, T. Svensson and H. Wymeersch, "Location-aware communications for 5G networks: How location information can improve scalability, latency, and robustness of 5G", *IEEE Signal Process. Mag.*, vol. 31, no. 6, pp. 102–112, 2014.

[5] S. Hu, F. Rusek and O. Edfors, "Beyond massive MIMO: The potential of data transmission with large intelligent surfaces", *IEEE Trans. Signal Process.*, vol. 66, no. 10, pp. 2746–2758, 2018.

[6] C. Gentner, T. Jost, W. Wang, S. Zhang, A. Dammann and U. C. Fiebig, "Multipath assisted positioning with simultaneous localization and mapping", *IEEE Trans. Wireless Commun.*, vol. 15, no. 9, pp. 6104–6117, 2016.

[7] R. Mendrzik, F. Meyer, G. Bauch and M. Z. Win, "Enabling situational awareness in millimeter wave massive MIMO systems", *IEEE J. Sel. Topics Signal Process.*, vol. 13, no. 5, pp. 1196–1211, 2019.

[8] E. Leitinger, F. Meyer, F. Hlawatsch, K. Witrisal, F. Tufvesson and M. Z. Win, "A belief propagation algorithm for multipath-based SLAM", *IEEE Trans. Wireless Commun.*, vol. 18, no. 12, pp. 5613–5629, 2019.

[9] J. Salmi, A. Richter and V. Koivunen, "Detection and tracking of MIMO propagation path parameters using state-space approach", *IEEE Trans. Signal Process.*, vol. 57, no. 4, pp. 1538–1550, 2009.

[10] X. Li, E. Leitinger, M. Oskarsson, K. Åström and F. Tufvesson, "Massive MIMO-based localization and mapping exploiting phase information of multipath components", *IEEE Trans. Wireless Commun.*, vol. 18, no. 9, pp. 4254–4267, 2019.

[11] M. Haardt, F. Roemer and G. Del Galdo, "Higher-order SVD-based subspace estimation to improve the parameter estimation accuracy in multidimensional harmonic retrieval problems", *IEEE Trans. Signal Process.*, vol. 56, no. 7, pp. 3198–3213, 2008.

[12] D. Shutin and B. H. Fleury, "Sparse variational Bayesian SAGE algorithm with application to the estimation of multipath wireless channels", *IEEE Trans. Signal Proces.*, vol. 59, no. 8, pp. 3609–3623, 2011.

[13] A. Richter, "Estimation of radio channel parameters: Models and algorithms", PhD thesis, Ilmenau University of Technology, 2005.

[14] T. Jost, W. Wang, U. Fiebig and F. Perez-Fontan, "Detection and tracking of mobile propagation channel paths", *IEEE Trans. Antennas Propag.*, vol. 60, no. 10, pp. 4875–4883, 2012.

[15] F. Meyer, Y. Park and P. Gerstoft, "Variational Bayesian estimation of time-varying DOAs", in *Proc. IEEE Fusion-20*, Rustenburg, South Africa, 2020, pp. 1–6.

[16] M. A. Badiu, T. L. Hansen and B. H. Fleury, "Variational Bayesian inference of line spectra", *IEEE Trans. Signal Process.*, vol. 65, no. 9, pp. 2247–2261, 2017.

[17] T. L. Hansen, B. H. Fleury and B. D. Rao, "Superfast line spectral estimation", *IEEE Trans. Signal Process.*, vol. PP, no. 99, pp. 1–1, 2018.

[18] S. Grebien, E. Leitinger, K. Witrisal and B. H. Fleury, "Super-resolution channel estimation including the dense multipath component — A sparse Bayesian approach", 2021, in preperation.

[19] D. Shutin and B. Vexler, "Sparse Bayesian learning with dictionary refinement for super-resolution through time", in *Proc. IEEE CAMSAP-17*, 2017, pp. 1–5.

[20] Y. Bar-Shalom, P. K. Willett and X. Tian, *Tracking and data fusion: a handbook of algorithms*. Storrs, CT, USA: Yaakov Bar-Shalom, 2011.

[21] F. Meyer, T. Kropfreiter, J. L. Williams, R. Lau, F. Hlawatsch, P. Braca and M. Z. Win, "Message passing algorithms for scalable multitarget tracking", *Proc. IEEE*, vol. 106, no. 2, pp. 221–259, 2018.

[22] D. Lerro and Y. Bar-Shalom, "Automated tracking with target amplitude information", in *1990 American Control Conf.*, 1990, pp. 2875–2880.

[23] E. Leitinger, S. Grebien, X. Li, F. Tufvesson and K. Witrisal, "On the use of MPC amplitude information in radio signal based SLAM", in *Proc. IEEE SSP-18*, Freiburg, Germany, 2018, pp. 633–637.

[24] E. Leitinger, S. Grebien and K. Witrisal, "Multipath-based SLAM exploiting AoA and amplitude information", in *Proc. IEEE ICCW-19*, Shanghai, China, 2019, pp. 1–7.

[25] G. Soldi, F. Meyer, P. Braca and F. Hlawatsch, "Self-tuning algorithms for multisensor-multitarget tracking using belief propagation", *IEEE Trans. Signal Process.*, vol. 67, no. 15, pp. 3922–3937, 2019.

[26] T. Wilding, S. Grebien, E. Leitinger, U. Mühlmann and K. Witrisal, "Single-anchor, multipath-assisted indoor positioning with aliased antenna arrays", in *Asilomar-18*, Pacifc Grove, CA, USA, 2018, pp. 525–531.

[27] F. Meyer, P. Braca, P. Willett and F. Hlawatsch, "A scalable algorithm for tracking an unknown number of targets using multiple sensors", *IEEE Trans. Signal Process.*, vol. 65, no. 13, pp. 3478–3493, 2017.

[28] S. M. Kay, *Fundamentals of Statistical Signal Processing: Detection Theory*. Upper Saddle River, NJ, USA: Prentice Hall, 1998.

[29] S. M. Kay, *Fundamentals of Statistical Signal Processing: Estimation Theory*. Upper Saddle River, NJ, USA: Prentice-H, 1993.

[30] F. Kschischang, B. Frey and H.-A Loeliger, "Factor graphs and the sum-product algorithm", *IEEE Trans. Inf. Theory*, vol. 47, no. 2, pp. 498–519, 2001.

[31] D. Schuhmacher, B.-T. Vo and B.-N. Vo, "A consistent metric for performance evaluation of multi-object filters", *IEEE Trans. Signal Process.*, vol. 56, no. 8, pp. 3447–3457, 2008.

[32] Y. Bar-Shalom, T. Kirubarajan and X.-R. Li, *Estimation with Applications to Tracking and Navigation*. New York, NY, USA: Wiley, 2002.

Paper VI

Sequential Detection and Estimation of Multipath Channel Parameters Using Belief Propagation

This paper proposes a BP-based algorithm for sequential detection and estimation of MPC parameters based on radio signals. Under dynamic channel conditions with moving transmitter/receiver, the number of MPCs, the MPC dispersion parameters, and the number of false alarm contributions are unknown and time-varying. We develop a Bayesian model for sequential detection and estimation of MPC dispersion parameters, and represent it by a factor graph enabling the use of BP for efficient computation of the marginal posterior distributions. At each time step, a snapshot-based parametric channel estimator provides parameter estimates of a set of MPCs which are used as noisy measurements by the proposed BP-based algorithm. It performs joint probabilistic data association, and estimation of the time-varying MPC parameters and the mean number of false alarm measurements, by means of the sum-product algorithm rules. The algorithm also exploits amplitude information enabling the reliable detection of "weak" MPCs with very low component SNRs. The performance of the proposed algorithm compares well to state-of-the-art algorithms for high SNR MPCs, but it significantly outperforms them for medium or low SNR MPCs. Results using real radio measurements demonstrate the excellent performance of the proposed algorithm in realistic and challenging scenarios.

X. Li, E. Leitinger, A. Venus, F. Tufvesson,
"Sequential Detection and Estimation of Multipath Channel Parameters Using Belief Propagation,"
IEEE Trans. Wireless Commun., 2022, doi:10.1109/TWC.2022.3165856.
(Xuhong Li and Erik Leitinger are co-first authors.)

1 Introduction

The information of dispersive wireless radio channels and its temporal behavior in dynamic scenarios are of great importance for the development of radio channel models [1], [2], 5G wireless communication technologies [3]–[5], and multipath-based localization and mapping [6]–[10]. The response of a non-static wireless radio channel is typically represented by superimposed weighted Dirac delta distributions with distinct and time-varying locations (or supports) in the respective dispersion domains (delay, AoA, angle-of-departure, Doppler frequency, and combinations thereof). Each component is meant to represent a multipath component (MPC). In general, the channel response can be observed only within a finite aperture leading to some limitations on the ability to resolve MPCs closely spaced in the dispersion domains. The related time-varying MPC parameters are usually estimated from multi-dimensional measurements using antenna arrays and multiple frequencies (wideband or UWB) [11] using super-resolution (SR) algorithms that perform sequential estimation of MPC parameters.

1.1 State-of-the-Art Methods

If the number-of-MPCs (NoM) is known, subspace methods [12]–[14] or maximum likelihood (ML) methods as for example [15] are standard SR methods to estimate time-invariant MPC parameters. Expectation maximization-based methods [16], have been proven a viable approximation of the computationally prohibitive ML methods [17]. In recent years, a channel model has been introduced that also considers DMC [18]. The DMC incorporates MPCs that cannot be resolved due to finite observation aperture. Including the estimation of DMC can improve the accuracy of the parameter estimation of distinct MPCs.

All afore mentioned methods have in common that they do not incorporate the estimation of the NoM into the estimation problem. One classical solution is to extend the methods with an outer stage for NoM detection using for example eigenvalue-based methods, or the generic information theoretic criteria, e.g., the Akaike/Bayesian information criterion, the minimum description length (MDL) principle [19]. The outer stage schemes mostly tend to overestimate the NoM. Inspired by the ideas of sparse estimation and compressed sensing, some SR sparse Bayesian parametric channel estimation algorithms [11], [20]–[22] have recently appeared which aim to reconstruct sparse signals from a reduced set of measurements specified by a sparse weight vector. By introducing a sparsity-promoting prior model for the weights, the estimation of the NoM and MPC parameters can be jointly formulated in a Bayesian framework.

To capture the temporal behaviors of MPC parameters in time-varying scenarios, many sequential estimation methods have been proposed, which can be

grouped into two broad categories. Methods of the first category sequentially estimate the MPC parameters directly based on the radio signals using for example an extended Kalman filter [23]–[26]. Methods of the second category adopt a two-stage structure where the estimates of a snapshot-based channel estimator are used as measurements in a tracking filter [27]. In this work, we focus on the two-stage methods. Due to the finite aperture of measurement systems and the resolution capability of snapshot-based parametric channel estimators, some measurements might not be well resolved hence incorporate contributions from more than one MPCs and false alarms may exist. In this case, to decide which measurement should be used for the update of which MPC (i.e., DA problem) can be complicated. In general, existing sequential channel estimation methods adopt "hard" association which assumes that measurements are fine resolved and each of them originates from single MPC that is specified by metrics such as the global nearest neighbor [28]. Probabilistic DA[28], [29], on the other hand, solves the origin uncertainty problem in a "soft" manner, in which the association probabilities for all current measurements are computed and used to form a mixture PDF for the update of each MPC state.

1.2 Contributions

Here, we propose a belief propagation (BP)-based algorithm for sequential detection of MPCs and estimation of their dispersion parameters that uses the MPC estimates from a snapshot-based parametric SR-sparse-Bayesian learning (SBL) channel estimator (abbreviated as SR-SBL) as measurements [11], [21], [22], [30].[10] To reduce the computational demand and to improve the convergence behavior of the snapshot-based estimator, statistical information of the dispersion parameters of the BP-based algorithm is fed back to the SR-SBL channel estimator. The proposed algorithm jointly performs probabilistic DA and sequential estimation of potential MPC (PMPC) parameters by running the BP-based algorithm, also known as the sum-product algorithm, on a factor graph [8], [29], [33], [34]. Note that independence between MPCs is assumed throughout the work. We use a probabilistic model for MPC existence where each PMPC state is augmented by a binary existence variable and associated with an existence probability, which is also estimated and used for the detection of reliable MPCs modeling the birth and death of these components [8], [35]. The complex amplitudes of MPCs are an integral part of the multipath channel model and must be estimated alongside with the dispersion parameters. Therefore, they are incorporated into the proposed algorithm. More specifically, the

[10] This work is inspired by the BP-based SLAM algorithm presented in [8], [31], [32]. The main novelties of the proposed algorithm over the previous work are threefold: (i) we present more detailed derivations for the joint prior PDFs and joint likelihoods; (ii) we extend the prior work with adaptive estimation of the false alarm rate (FAR); (iii) we apply the prior work successfully to the field of parametric radio channel estimation.

algorithm uses the statistics of MPC amplitudes to determine the unknown and time-varying detection probabilities [31], [32], [36], [37], which improves the detectability and maintenance of low signal-to-noise ratio (SNR) MPCs, and enables a better discrimination against false alarms. Knowing the correct false alarm rate (FAR) is crucial for optimal performance of Bayesian detection and estimation algorithms. However, determining the FAR in advance is not straightforward, especially, if the FAR is time-varying. Using a fixed predefined value of FAR that deviates largely from the true one, can potentially lead to decreased detection performance of MPCs and an increased number of detected false alarms. The proposed algorithm estimates the possibly time-varying FAR to cope with false alarm measurements originating from the preprocessing step and clutter measurements originating from strongly fluctuating scattered MPCs (as for example DMC). The main contributions of this paper are summarized as follows.

- We introduce a Bayesian model for sequential detection and estimation of MPC parameters, which uses the estimates from a snapshot-based channel estimator as measurements. Within this model, the death and birth of MPCs and DAs are formulated probabilistically, and adaptive detection probabilities are incorporated by exploiting amplitude information.
- We further present a BP-based algorithm based on the factor graph representation of the estimation problem, where the PMPC states and the FAR are estimated jointly and sequentially.
- The performance of the proposed algorithm is demonstrated with both synthetic and real measurements. Moreover, the results are compared with the KEST [27] algorithm (a state-of-the-art sequential parametric channel estimation method), and posterior-CRLB (posterior-CRLB).

This paper advances over our preliminary conference publication [38] by (i) presenting a detailed derivations of the factor graph, (ii) including the detailed derivations of the factors related to the FAR, (iii) establishing a particle-based implementation of the proposed algorithm, (iv) validating the performance with additional simulated and real scenarios, and (v) demonstrating a comparison with a state-of-the-art method and the posterior-CRLB.

Notations: Column vectors and matrices are denoted by boldface lowercase and uppercase letters. Random variables are displayed in san serif, upright fonts as for example x and $\mathbf{x}$ and their realizations in serif, italic font as for example x and $\boldsymbol{x}$. $f(\boldsymbol{x})$ denotes the PDF or probability mass function (PMF) of continuous or discrete random vector. $(\cdot)^{\mathrm{T}}$, $(\cdot)^{*}$, and $(\cdot)^{\mathrm{H}}$ denote matrix transpose, complex conjugation and Hermitian transpose, respectively. $\|\cdot\|$ is the Euclidean norm. $|\cdot|$ represents the cardinality of a set. $\mathrm{diag}\{\boldsymbol{x}\}$ denotes a diagonal matrix with entries in $\boldsymbol{x}$. $\mathrm{tr}\{\cdot\}$ denotes the trace of a matrix. $\boldsymbol{I}_{[\cdot]}$

is an identity matrix of dimension given in the subscript. $[\boldsymbol{X}]_{n,n}$ denotes the nth diagonal entry of $\boldsymbol{X}$. $[\boldsymbol{X}]_{1:n}$ denotes a sub-matrix containing $1\!:\!n$ columns and rows of $\boldsymbol{X}$. Furthermore, $\bar{1}(e)$ denotes the function of the event $e = 0$ (i.e., $\bar{1}(e) = 1$ if $e = 0$ and 0 otherwise). $1_{\mathbb{A}}(\boldsymbol{x})$ denotes the indicator function that is $1_{\mathbb{A}}(\boldsymbol{x}) = 1$ if $\mathbf{x} \in \mathbb{A}$ and 0 otherwise. For any function $g(\boldsymbol{x})$ we define the integral $\langle g(\boldsymbol{x})\rangle_{f(\boldsymbol{x})} = \int g(\boldsymbol{x})f(\boldsymbol{x})\mathrm{d}\boldsymbol{x}$. As for example $\langle \boldsymbol{x}\rangle_{f(\boldsymbol{x})} = \int \boldsymbol{x}f(\boldsymbol{x})\mathrm{d}\boldsymbol{x}$ and $\langle f(\boldsymbol{x})\rangle_{1_{\mathbb{A}}(\boldsymbol{x})} = \int_{\mathbb{A}} f(\boldsymbol{x})\mathrm{d}\boldsymbol{x}$ denote the expected value and the integral over $f(\boldsymbol{x})$ of the random vector $\boldsymbol{x}$, respectively.

2 Radio Signal Model

We consider a single-input multiple-output (SIMO) UWB system, where the Tx uses a single antenna, and the Rx is equipped with an antenna array made of H elements located at $\boldsymbol{p}_n^{(h)} \in \mathbb{R}^{2\times 1}$ with $h \in \{1, \ldots, H\}$.[11] We define $d_n^{(h)} = \|\boldsymbol{p}_n^{(h)} - \boldsymbol{p}_n\|$ and $\varphi_n^{(h)} = \angle(\boldsymbol{p}_n^{(h)} - \boldsymbol{p}_n) - \psi$, as the distance of the hth element to the reference location $\boldsymbol{p}_n \in \mathbb{R}^{2\times 1}$, i.e., the array's center of gravity, and its angle relative to the array orientation ψ, respectively. For the sake of brevity, we assume a two-dimensional scenario with horizontal-only propagation.[12]

2.1 Received Signal

Signals are represented by their complex envelopes with respect to a center frequency f_c. The single antenna at the transmitter emits a periodic signal $\tilde{s}(t)$. The received signal at each antenna element h at the discrete observation time n is given as [11], [18], [39]

$$s_{\mathrm{RX},n}^{(h)}(t) = \sum_{l=1}^{L_n} \tilde{\alpha}_{l,n}\, s\big(t; \tilde{d}_{l,n}, \tilde{\varphi}_{l,n}, \boldsymbol{p}_n^{(h)}\big) + \omega_n^{(h)}(t) \tag{1}$$

where the first term comprises L_n MPCs, with each being characterized by its complex amplitude $\tilde{\alpha}_{l,n} \in \mathbb{C}$, distance $\tilde{d}_{l,n} = c\tilde{\tau}_{l,n} \in \mathbb{R}$ to the array's center of gravity directly related to the time delay via the speed of light c, and AoA $\tilde{\varphi}_{l,n} \in [-\pi, \pi)$ w.r.t. the array orientation. Under the far-field plane-wave assumption, the signal $s\big(t; \tilde{d}, \tilde{\varphi}, \boldsymbol{p}^{(h)}\big)$ is given as $s\big(t; \tilde{d}, \tilde{\varphi}, \boldsymbol{p}^{(h)}\big) = \mathrm{e}^{j2\pi f_\mathrm{c} g(\tilde{\varphi}, \boldsymbol{p}^{(h)})}\tilde{s}\big(t - \tilde{d}/c + g\big(\tilde{\varphi}, \boldsymbol{p}^{(h)}\big)\big)$. The function $g\big(\tilde{\varphi}, \boldsymbol{p}^{(h)}\big) = \frac{d^{(h)}\cos(\tilde{\varphi} - \psi - \varphi^{(h)})}{c}$ gives the delay shift of a plane-wave incident with AoA $\tilde{\varphi}$ being measured relatively to the array

[11] Note that the extension of the algorithm to a multiple-input single-output (MISO) or a MIMO system considering an antenna array at the Tx is straightforward.

[12] An extension to three-dimensional scenarios with horizontal and vertical propagation is straightforward, but it would lead to a cumbersome notation and one would not gain any further insights.

orientation ψ, at the hth antenna position w.r.t. the array's center of gravity. We assume that the Tx and Rx are time synchronized and the array orientation is known. The measurement noise process $\omega_n^{(h)}(t)$ in (1) is independent AWGN with double-sided power spectral density $N_0/2$.

The received signal in (1) observed over a duration T is sampled with frequency $f_s = 1/T_s$ at each time n, yielding a length $N_\mathrm{s} = T/T_\mathrm{s}$ sample vector $\mathbf{s}_{\mathrm{RX},n}^{(h)} \in \mathbb{C}^{N_\mathrm{s}\times 1}$ from each array element. By stacking $\mathbf{s}_{\mathrm{RX},n}^{(h)}$ from H array elements, the discrete time signal vector $\mathbf{s}_{\mathrm{RX},n} \triangleq [\mathbf{s}_{\mathrm{RX},n}^{(1)\mathrm{T}} \ \cdots \ \mathbf{s}_{\mathrm{RX},n}^{(H)\mathrm{T}}]^\mathrm{T} \in \mathbb{C}^{N_\mathrm{s}H\times 1}$ is given by

$$\boldsymbol{s}_{\mathrm{RX},n} = \boldsymbol{S}(\tilde{\boldsymbol{\theta}}_n)\tilde{\boldsymbol{\alpha}}_n + \boldsymbol{\omega}_n. \tag{2}$$

In the first summand $\tilde{\boldsymbol{\alpha}}_n \triangleq [\tilde{\alpha}_{1,n} \cdots \tilde{\alpha}_{L_n,n}]^\mathrm{T} \in \mathbb{C}^{L_n\times 1}$, $\tilde{\boldsymbol{\theta}}_n \triangleq [\tilde{\boldsymbol{\theta}}_{1,n}^\mathrm{T} \cdots \tilde{\boldsymbol{\theta}}_{L_n,n}^\mathrm{T}]^\mathrm{T} \in \mathbb{R}^{2L_n\times 1}$ with $\tilde{\boldsymbol{\theta}}_{l,n} \triangleq [\tilde{d}_{l,n}\ \tilde{\varphi}_{l,n}]^\mathrm{T} \in \mathbb{R}^{2\times 1}$ denoting the vector comprising the MPC parameters, and $\boldsymbol{S}(\tilde{\boldsymbol{\theta}}_n) \triangleq [\boldsymbol{s}(\tilde{\boldsymbol{\theta}}_{1,n}) \cdots \boldsymbol{s}(\tilde{\boldsymbol{\theta}}_{L_n,n})] \in \mathbb{C}^{N_\mathrm{s}H\times L_n}$ with columns given by $\boldsymbol{s}(\tilde{\boldsymbol{\theta}}_{l,n}) = [\boldsymbol{s}_1(\tilde{\boldsymbol{\theta}}_{l,n})^\mathrm{T} \ \cdots \ \boldsymbol{s}_H(\tilde{\boldsymbol{\theta}}_{l,n})^\mathrm{T}]^\mathrm{T} \in \mathbb{C}^{N_\mathrm{s}H\times 1}$. The hth entry of $\boldsymbol{s}(\tilde{\boldsymbol{\theta}}_{l,n})$ reads $\boldsymbol{s}_h(\tilde{\boldsymbol{\theta}}_{l,n}) \triangleq [s\big(-[(N-1)/2]T_\mathrm{s}; \tilde{d}_{l,n}, \tilde{\varphi}_{l,n}, \boldsymbol{p}^{(h)}\big) \ \cdots \ s\big([(N-1)/2]T_\mathrm{s}; \tilde{d}_{l,n}, \tilde{\varphi}_{l,n}, \boldsymbol{p}^{(h)}\big)]^\mathrm{T} \in \mathbb{C}^{N_\mathrm{s}\times 1}$. The measurement noise vector $\boldsymbol{\omega}_n \in \mathbb{C}^{N_\mathrm{s}H\times 1}$ is a complex circularly symmetric Gaussian random vector with covariance matrix $\boldsymbol{C} = \sigma^2\boldsymbol{I}_{N_\mathrm{s}H}$, where $\sigma^2 = N_0/T_\mathrm{s}$ is the noise variance. The component SNR of each MPC is $\widetilde{\mathrm{SNR}}_{l,n} = \frac{|\tilde{\alpha}_{l,n}|^2\|\boldsymbol{s}(\tilde{\boldsymbol{\theta}}_{l,n})\|^2}{\sigma^2}$ and the according normalized amplitude equals $\tilde{u}_{l,n} = \sqrt{\widetilde{\mathrm{SNR}}_{l,n}}$. An MPC exists only when its associated geometric feature is visible at the Rx position. The true number L_n of MPCs as well as their individual parameters $\tilde{u}_{l,n}$, $\tilde{d}_{l,n}$, and $\tilde{\varphi}_{l,n}$ are unknown and time-varying in dynamic scenarios. We propose an algorithm to sequentially detect and estimate these parameters.

2.2 Parametric Channel Estimation

Based on the discrete time signal vector in (2), a snapshot-based SR-SBL estimator [11], [20]–[22], [30] provides estimated dispersion parameters of M_n multipath components (MPCs) stacked into the vector $\boldsymbol{z}_n \triangleq [\boldsymbol{z}_{1,n}^\mathrm{T} \cdots \boldsymbol{z}_{M_n,n}^\mathrm{T}]^\mathrm{T} \in \mathbb{R}^{3M_n\times 1}$ at each time n. An entry $\boldsymbol{z}_{m,n} \triangleq [z_{\mathrm{d}m,n}\ z_{\varphi_{m,n}}\ z_{\mathrm{u}m,n}]^\mathrm{T} \in \mathbb{R}^{3\times 1}$ comprises the distance estimate $z_{\mathrm{d}m,n}$, the AoA estimate $z_{\varphi_{m,n}}$, and the normalized amplitude estimate $z_{\mathrm{u}m,n}$ of an MPC. The normalized amplitude estimate is given by $z_{\mathrm{u}m,n} \triangleq |\mu_{\alpha m,n}|/\sigma_{\alpha m,n}$ where $\mu_{\alpha m,n}$ and $\sigma_{\alpha m,n}$ denote, respectively, the estimated mean and standard deviation of the complex amplitudes. Note that all estimated component SNRs given by $z_{\mathrm{u}m,n}^2$ are above a predefined detection threshold u_de. The estimated amplitudes $z_{\mathrm{u}m,n}$ are directly related to the detection probabilities of the corresponding MPCs [31], [32] (see Sec-

tion 3.3). At time $n = 1$, the initial prior PDF of the dispersion parameters considered in the snapshot-based estimator is uniform over the validation region. For each time $n \geq 2$, the snapshot-based estimator is initialized with $\hat{L}_{n-1}$ detected MPCs returned from the BP-based algorithm at time $n-1$ (see Section 4.2). The vector $\boldsymbol{z}_n$ is used as noisy measurement by the proposed algorithm. Note that the snapshot-based estimator decomposes $\boldsymbol{s}_{\mathrm{RX},n}$ into individual, decorrelated components with parameters stacked into $\boldsymbol{z}_n$, reducing the number of dimensions (as M_n is usually much smaller than $N_{\mathrm{s}}H$).

3 System Model

3.1 PMPC States

Following [8], [29], we account for the time-varying and unknown NoM by introducing PMPCs indexed by $k \in \{1, \ldots, K_n\}$. The number of PMPCs K_n is the maximum number of actual MPCs that have produced measurements so far [29]. The existence/non-existence of PMPC k as an actual MPC is modeled by a binary random variable $\mathsf{r}_{k,n} \in \mathbb{B} = \{0, 1\}$ in the sense that a PMPC exists if and only if $r_{k,n} = 1$. Augmented states of PMPCs are denoted as $\mathbf{y}_{k,n} \triangleq [\mathbf{x}_{k,n}^{\mathrm{T}} \ \mathsf{r}_{k,n}]^{\mathrm{T}} \in \mathbb{R}^{5\times 1} \times \mathbb{B}$, where $\mathbf{x}_{k,n} = [\boldsymbol{\theta}_{k,n}^{\mathrm{T}} \ \mathsf{u}_{k,n} \ \mathsf{v}_{\mathrm{d}k,n} \ \mathsf{v}_{\varphi_{k,n}}]^{\mathrm{T}} \in \mathbb{R}^{5\times 1}$, $\boldsymbol{\theta}_{k,n} = [\mathsf{d}_{k,n} \ _{k,n}]^{\mathrm{T}} \in \mathbb{R}^{2\times 1}$, and $\mathsf{v}_{\mathrm{d}k,n}$ and $\mathsf{v}_{\varphi_{k,n}}$ are the distance velocity and angular velocity, respectively.

Formally, PMPC k is also considered even if it is non-existent, i.e., $r_{k,n} = 0$. The states $\mathbf{x}_{k,n}$ of non-existent PMPCs are obviously irrelevant and have no influence on the PMPC detection and state estimation. Therefore, all PDFs defined for PMPC states, $f(\boldsymbol{y}_{k,n}) = f(\boldsymbol{x}_{k,n}, r_{k,n})$, are of the form $f(\boldsymbol{x}_{k,n}, r_{k,n} = 0) = f_{k,n} f_{\mathrm{D}}(\boldsymbol{x}_{k,n})$, where $f_{\mathrm{D}}(\boldsymbol{x}_{k,n})$ is an arbitrary "dummy PDF" and $f_{k,n} \in [0, 1]$ is a constant representing the probability of non-existence [8], [29], [35].

3.2 State-Transition Model

For each PMPC with state $\mathbf{y}_{k,n-1}$ with $k \in \{1, \ldots, K_{n-1}\}$ at time $n-1$, there is one "legacy" PMPC with state $\underline{\mathbf{y}}_{k,n} \triangleq [\underline{\mathbf{x}}_{k,n}^{\mathrm{T}} \ \underline{\mathsf{r}}_{k,n}]^{\mathrm{T}}$ with $k \in \{1, \ldots, K_{n-1}\}$ at time n. Assuming that PMPC states evolve independently across k and n, the corresponding state-transition PDF of the joint states $\mathbf{y}_{n-1} \triangleq [\mathbf{y}_{1,n-1}^{\mathrm{T}} \cdots \mathbf{y}_{K_{n-1},n-1}^{\mathrm{T}}]^{\mathrm{T}}$ and $\underline{\mathbf{y}}_n \triangleq [\underline{\mathbf{y}}_{1,n}^{\mathrm{T}} \cdots \underline{\mathbf{y}}_{K_{n-1},n}^{\mathrm{T}}]^{\mathrm{T}}$ factorizes as [29]

$$f(\underline{\boldsymbol{y}}_n | \boldsymbol{y}_{n-1}) = \prod_{k=1}^{K_{n-1}} f(\underline{\boldsymbol{y}}_{k,n} | \boldsymbol{y}_{k,n-1}) \tag{3}$$

where $f(\underline{\boldsymbol{y}}_{k,n}|\boldsymbol{y}_{k,n-1}) = f(\underline{\boldsymbol{x}}_{k,n}, \underline{r}_{k,n}|\boldsymbol{x}_{k,n-1}, r_{k,n-1})$ is the single PMPC state-transition PDF. If a PMPC did not exist at time n–1, i.e., $r_{k,n-1}=0$, it cannot exist at time n as a legacy PMPC. This means that

$$f(\underline{\boldsymbol{x}}_{k,n}, \underline{r}_{k,n}|\boldsymbol{x}_{k,n-1}, 0) = \begin{cases} f_{\mathrm{D}}(\underline{\boldsymbol{x}}_{k,n}), & \underline{r}_{k,n} = 0 \\ 0, & \underline{r}_{k,n} = 1\,. \end{cases} \tag{4}$$

If a PMPC existed at time $n-1$, i.e., $r_{k,n-1} = 1$, at time n it either dies i.e., $\underline{r}_{k,n} = 0$ or it still exists i.e., $\underline{r}_{k,n} = 1$, with the survival probability denoted as p_{s}. If it does survive, the state $\underline{\mathbf{x}}_{k,n}$ is distributed according to the state-transition PDF $f(\underline{\boldsymbol{x}}_{k,n}|\boldsymbol{x}_{k,n-1})$. Thus,

$$f(\underline{\boldsymbol{x}}_{k,n}, \underline{r}_{k,n}|\boldsymbol{x}_{k,n-1}, 1) = \begin{cases} (1-p_{\mathrm{s}}) f_{\mathrm{D}}(\underline{\boldsymbol{x}}_{k,n}), & \underline{r}_{k,n} = 0 \\ p_{\mathrm{s}} f(\underline{\boldsymbol{x}}_{k,n}|\boldsymbol{x}_{k,n-1}), & \underline{r}_{k,n} = 1. \end{cases} \tag{5}$$

We also define the state vector for all times up to n of legacy PMPCs as $\underline{\mathbf{y}}_{1:n} \triangleq [\underline{\mathbf{y}}_1^{\mathrm{T}} \cdots \underline{\mathbf{y}}_n^{\mathrm{T}}]^{\mathrm{T}}$.

3.3 Measurement Model

Before the current measurements $\mathbf{z}_n$ are observed, the number of measurements M_n is a random variable. The vector collecting the number of measurements is defined as $\mathbf{m}_{1:n} \triangleq [\mathsf{M}_1 \cdots \mathsf{M}_n]^{\mathrm{T}}$. The conditional PDF $f(\boldsymbol{z}_{m,n}|\boldsymbol{x}_{k,n})$ of $\mathbf{z}_n$ assumes that the individual measurements $\mathbf{z}_{m,n}$ are conditionally independent given the state $\mathbf{x}_{k,n}$. At each time n, a snapshot-based channel estimator provides the current observed measurement vector $\boldsymbol{z}_n = [\boldsymbol{z}_{1,n}^{\mathrm{T}} \cdots \boldsymbol{z}_{M_n,n}^{\mathrm{T}}]^{\mathrm{T}}$ (see Section 2), which is not random anymore and with fixed M_n. If $\boldsymbol{z}_{m,n}$ is a PMPC-oriented measurement, we assume that the conditional PDF $f(\boldsymbol{z}_{m,n}|\boldsymbol{x}_{k,n})$ is conditionally independent across $z_{\mathrm{d}m,n}$, $z_{\varphi_{m,n}}$, and $z_{\mathrm{u}m,n}$ given the states $\mathsf{d}_{k,n}$, $_{k,n}$, and $\mathsf{u}_{k,n}$, thus it factorizes as

$$f(\boldsymbol{z}_{m,n}|\boldsymbol{x}_{k,n}) = f(z_{\mathrm{d}m,n}|d_{k,n}, u_{k,n}) f(z_{\varphi_{m,n}}|\varphi_{k,n}, u_{k,n}) f(z_{\mathrm{u}m,n}|u_{k,n}) \tag{6}$$

where the individual likelihood functions of the distance measurement $f(z_{\mathrm{d}m,n}|$ $d_{k,n}, u_{k,n})$ and the AoA measurement $f(z_{\varphi_{m,n}}|\varphi_{k,n}, u_{k,n})$ are modeled by Gaussian PDFs, i.e.,

$$f(z_{\mathrm{d}m,n}|d_{k,n}, u_{k,n}) = \left(2\pi\sigma_{\mathrm{d}k,n}^2\right)^{-\frac{1}{2}} \mathrm{e}^{\frac{-(z_{\mathrm{d}m,n}-d_{k,n})^2}{2\sigma_{\mathrm{d}k,n}^2}} \tag{7}$$

and

$$f(z_{\varphi_{m,n}}|\varphi_{k,n},u_{k,n}) = \left(2\pi\sigma^2_{\varphi_{k,n}}\right)^{-\frac{1}{2}} \mathrm{e}^{\frac{-(z_{\varphi_{m,n}}-\varphi_{k,n})^2}{2\sigma^2_{\varphi_{k,n}}}}. \tag{8}$$

The variances depend on $u_{k,n}$ and are determined based on the Fisher information, respectively, given by $\sigma^2_{\mathrm{d}k,n}=c^2/(8\pi^2\beta^2_{\mathrm{bw}}u^2_{k,n})$ and $\sigma^2_{\varphi_{k,n}}=c^2/(8\pi^2 f_{\mathrm{c}}^2 u^2_{k,n} \times D^2(\varphi_{k,n}))$, where the latter is a function of the PMPC state ${}_{k,n}$ [32], [40]. Here, β^2_{bw} is the mean square bandwidth of the signal $\tilde{s}(t)$ and $D^2(\varphi_{k,n})$ is the squared array aperture. The likelihood function $f(z_{\mathrm{u}m,n}|u_{k,n})$ of the normalized amplitude measurement $z_{\mathrm{u}m,n}$ is modeled by a truncated Rician PDF [28, Ch. 1.6.7], i.e.,

$$f(z_{\mathrm{u}m,n}|u_{k,n}) = \frac{\frac{z_{\mathrm{u}m,n}}{\sigma^2_{\mathrm{u}k,n}}\mathrm{e}^{\left(\frac{-(z^2_{\mathrm{u}m,n}+u^2_{k,n})}{2\sigma^2_{\mathrm{u}k,n}}\right)}\mathrm{I}_0\left(\frac{z_{\mathrm{u}m,n}u_{k,n}}{\sigma^2_{\mathrm{u}k,n}}\right)}{p_{\mathrm{d}}(u_{k,n})} \tag{9}$$

for $z_{\mathrm{u}m,n} > \sqrt{u_{\mathrm{de}}}$, where the squared scale parameter $\sigma^2_{\mathrm{u}k,n}$ depends on $u_{k,n}$ and is determined based on the Fisher information given by $\sigma^2_{\mathrm{u}k,n} = \frac{1}{2} + \frac{1}{4N_{\mathrm{s}}H}u^2_{k,n}$, $\mathrm{I}_0(\cdot)$ represents the 0th-order modified first-kind Bessel function, and u_{de} is the detection threshold of the snapshot-based estimator. The derivation of the squared scale parameter is given in Appendix D. The detection probability (i.e., the probability that a PMPC $\mathbf{y}_{k,n}$ generates a measurement $\boldsymbol{z}_{m,n}$) is modeled by a Rician cummulative distribution function (CDF), i.e., $p_{\mathrm{d}}(u_{k,n}) = Q_1(u_{k,n}/\sigma_{\mathrm{u}k,n}, \sqrt{u_{\mathrm{de}}}/\sigma_{\mathrm{u}k,n})$ [31], [32], [36], where the CDF $Q_1(\cdot,\cdot)$ denotes the Marcum Q-function [28, Ch. 1.6.7]. Note that $p_{\mathrm{d}}(u_{k,n})$ is directly related to the MPC's visibility and the component SNR as well as to the snapshot-based estimator.

False alarm measurements originating from the snapshot-based parametric channel estimator are assumed statistically independent of PMPC states. They are modeled by a Poisson point process with mean ${}_{\mathrm{fa}n}$ and PDF $f_{\mathrm{fa}}(\boldsymbol{z}_{m,n})$, which is assumed to factorize as $f_{\mathrm{fa}}(\boldsymbol{z}_{m,n}) = f_{\mathrm{fa_d}}(z_{\mathrm{d}m,n})f_{\mathrm{fa}_\varphi}(z_{\varphi_{m,n}})f_{\mathrm{fa_u}}(z_{\mathrm{u}m,n})$, where $f_{\mathrm{fa_d}}(z_{\mathrm{d}m,n})=1/d_{\max}$ and $f_{\mathrm{fa}_\varphi}(z_{\varphi_{m,n}})=1/2\pi$ are assumed to be uniform on $[0, d_{\max}]$ and on $[0, 2\pi)$, respectively. With noise only, the Rician PDF in (9) degenerates to a Rayleigh PDF, thus the false alarm PDF $f_{\mathrm{fa_u}}(z_{\mathrm{u}m,n})$ of the normalized amplitude is given as $f_{\mathrm{fa_u}}(z_{\mathrm{u}m,n})=2z_{\mathrm{u}m,n}\exp(-z^2_{\mathrm{u}m,n})/p_{\mathrm{fa}}$ for $z_{\mathrm{u}m,n} > \sqrt{u_{\mathrm{de}}}$ where $p_{\mathrm{fa}} = \exp(-u_{\mathrm{de}})$ denotes the false alarm probability [28, Ch. 1.6.7]. The amplitude information can significantly improve the detectability of MPCs with low component SNRs as shown in Section 7.2 using very challenging simulation setups (see Fig. 5).

The FAR ${}_{\mathrm{fa}n}$ is assumed unknown, time-varying, and automatically adapted online in the proposed algorithm. It evolves across time according to the state-

transition PDF $f(\mu_{\mathrm{fa}n}|\mu_{\mathrm{fa}n-1})$. The state vector for all times up to n is given as $\boldsymbol{\mu}_{\mathrm{fa}1:n} \triangleq [{}_{\mathrm{fa}1} \cdots {}_{\mathrm{fa}n}]^{\mathrm{T}}$.

3.4 New PMPCs

Newly detected PMPCs at time n, i.e., PMPCs that generate measurements for the first time at time n, are modeled by a Poisson point process with mean ${}_{\mathrm{n}}$ and PDF $f_{\mathrm{n}}(\overline{\boldsymbol{x}}_{m,n})$. The mean ${}_{\mathrm{n}}$ is assumed to be a known constant. Following [8], [29], newly detected PMPCs are represented by new PMPC states $\overline{\mathbf{y}}_{m,n} \triangleq [\overline{\mathbf{x}}_{m,n}^{\mathrm{T}}\ \overline{\mathsf{r}}_{m,n}]^{\mathrm{T}}$, $m \in \{1,\ldots,M_n\}$. Each new PMPC $\overline{\mathbf{y}}_{m,n}$ corresponds to a measurement $\boldsymbol{z}_{m,n}$, thus the number of new PMPCs at time n equals to the number of measurements M_n. Here, $\overline{r}_{m,n} = 1$ means that the measurement $\boldsymbol{z}_{m,n}$ was generated by a newly detected PMPC. The state vector of all new PMPCs at time n is given by $\overline{\mathbf{y}}_n \triangleq [\overline{\mathbf{y}}_{1,n}^{\mathrm{T}} \cdots \overline{\mathbf{y}}_{\mathsf{M}_n,n}^{\mathrm{T}}]^{\mathrm{T}}$ and state vector for all times up to n by $\overline{\mathbf{y}}_{1:n} \triangleq [\overline{\mathbf{y}}_1^{\mathrm{T}} \cdots \overline{\mathbf{y}}_n^{\mathrm{T}}]^{\mathrm{T}}$. The new PMPCs become legacy PMPCs at time $n+1$, accordingly the number of legacy PMPCs is updated as $K_n = K_{n-1} + M_n$. (The number of PMPCs is bounded by a pruning operation as it is detailed in Section 4.2.) The vector containing all PMPC states at time n is given by $\mathbf{y}_n \triangleq [\underline{\mathbf{y}}_n^{\mathrm{T}}\ \overline{\mathbf{y}}_n^{\mathrm{T}}]^{\mathrm{T}}$, where $\mathbf{y}_{k,n}$ with $k \in \{1,\ldots,K_n\}$, and state vector for all times up to n by $\mathbf{y}_{1:n} \triangleq [\mathbf{y}_1^{\mathrm{T}} \cdots \mathbf{y}_n^{\mathrm{T}}]^{\mathrm{T}}$.

3.5 Data Association Uncertainty

Estimation of multiple PMPC states is complicated by the DA uncertainty, i.e., it is unknown which measurement $\mathbf{z}_{m,n}$ originated from which PMPC. Furthermore, it is not known if a measurement did not originate from a PMPC (false alarm), or if a PMPC did not generate any measurement (missed detection). The associations between measurements and legacy PMPCs are described by the PMPC-oriented association vector $\mathbf{a}_n \triangleq [\mathsf{a}_{1,n} \cdots \mathsf{a}_{\mathsf{K}_{n-1},n}]^{\mathrm{T}}$ with entries $a_{k,n} \triangleq m \in \{1,\ldots,M_n\}$, if legacy PMPC k generates measurement m, or $a_{k,n} \triangleq 0$, if legacy PMPC k does not generate any measurement. In line with [8], [29], [41], the associations can be equivalently described by a measurement-oriented association vector $\mathbf{b}_n \triangleq [\mathsf{b}_{1,n} \cdots \mathsf{b}_{\mathsf{M}_n,n}]^{\mathrm{T}}$ with entries $b_{m,n} \triangleq k \in \{1,\ldots,K_{n-1}\}$, if measurement m is generated by legacy PMPC k, or $b_{m,n} \triangleq 0$, if measurement m is not generated by any legacy PMPC. Furthermore, we assume that at any time n, each PMPC can generate at most one measurement, and each measurement can be generated by at most one PMPC [8], [29], [41]. This is enforced by the exclusion functions $\Psi(\boldsymbol{a}_n, \boldsymbol{b}_n)$ and $\Gamma_{\boldsymbol{a}_n}(\overline{r}_{m,n})$. The function $\Psi(\boldsymbol{a}_n, \boldsymbol{b}_n) = \prod_{k=1}^{K_{n-1}} \prod_{m=1}^{M_n} \psi(a_{k,n}, b_{m,n})$ is defined as $\psi(a_{k,n}, b_{m,n}) = 0$, if $a_{k,n} = m$ and $b_{m,n} \neq k$ or $b_{m,n} = k$ and $a_{k,n} \neq m$, otherwise it equals 1. The function $\Gamma_{\boldsymbol{a}_n}(\overline{r}_{m,n}) = 0$, if $\overline{r}_{m,n} = 1$ and $a_{k,n} = m$, otherwise it equals 1. The "redundant formulation" of using $\mathbf{a}_n$ together with

$\mathbf{b}_n$ is the key to make the algorithm scalable for large numbers of PMPCs and measurements. The association vectors for all times up to n are given by $\mathbf{a}_{1:n} \triangleq [\mathbf{a}_1^{\mathrm{T}} \cdots \mathbf{a}_n^{\mathrm{T}}]^{\mathrm{T}}$ and $\mathbf{b}_{1:n} \triangleq [\mathbf{b}_1^{\mathrm{T}} \cdots \mathbf{b}_n^{\mathrm{T}}]^{\mathrm{T}}$. A figure that conceptually illustrates the DAs between measurements and PMPCs is given in [42].

4 Joint Posterior PDF and Problem Formulation

4.1 Joint Posterior PDF and Factor Graph

Here, we assume that the measurements $\boldsymbol{z}_{1:n} \triangleq [\boldsymbol{z}_1^{\mathrm{T}}, \ldots, \boldsymbol{z}_n^{\mathrm{T}}]^{\mathrm{T}}$ for all times up to n are observed and thus fixed. By using common assumptions [8], [28], [29], the joint posterior PDF of $\mathbf{y}_{1:n}$, $\mathbf{a}_{1:n}$, $\mathbf{b}_{1:n}$, $\boldsymbol{\mu}_{\mathrm{fa}\,1:n}$, and $\mathbf{m}_{1:n}$ conditioned on the observed measurement vector $\boldsymbol{z}_{1:n}$ is given by

$$\begin{aligned} &f(\boldsymbol{y}_{1:n}, \boldsymbol{a}_{1:n}, \boldsymbol{b}_{1:n}, \boldsymbol{\mu}_{\mathrm{fa}\,1:n}, \boldsymbol{m}_{1:n} | \boldsymbol{z}_{1:n}) \\ &\quad = f(\underline{\boldsymbol{y}}_{1:n}, \overline{\boldsymbol{y}}_{1:n}, \boldsymbol{a}_{1:n}, \boldsymbol{b}_{1:n}, \boldsymbol{\mu}_{\mathrm{fa}\,1:n}, \boldsymbol{m}_{1:n} | \boldsymbol{z}_{1:n}) \\ &\quad \propto f(\boldsymbol{z}_{1:n} | \underline{\boldsymbol{y}}_{1:n}, \overline{\boldsymbol{y}}_{1:n}, \boldsymbol{a}_{1:n}, \boldsymbol{b}_{1:n}, \boldsymbol{m}_{1:n}) f(\underline{\boldsymbol{y}}_{1:n}, \overline{\boldsymbol{y}}_{1:n}, \boldsymbol{a}_{1:n}, \boldsymbol{b}_{1:n}, \boldsymbol{\mu}_{\mathrm{fa}\,1:n}, \boldsymbol{m}_{1:n}). \end{aligned} \tag{10}$$

After inserting the expressions (42) and (52) and performing some simple manipulations, the joint posterior PDF in (10) can be rewritten as

$$\begin{aligned} &f(\underline{\boldsymbol{y}}_{1:n}, \overline{\boldsymbol{y}}_{1:n}, \boldsymbol{a}_{1:n}, \boldsymbol{b}_{1:n}, \boldsymbol{\mu}_{\mathrm{fa}\,1:n}, \boldsymbol{m}_{1:n} | \boldsymbol{z}_{1:n}) \\ &\quad \propto f(\mu_{\mathrm{fa}\,1}) \prod_{l=1}^{M_1} h(\overline{\boldsymbol{y}}_{l,1}, b_{l,1}, \mu_{\mathrm{fa}\,1}; \boldsymbol{z}_1) \prod_{n'=2}^{n} f(\mu_{\mathrm{fa}\,n'} | \mu_{\mathrm{fa}\,n'-1}) \\ &\qquad \times \left(\prod_{k'=1}^{K_{n'-1}} f(\underline{\boldsymbol{y}}_{k',n'} | \boldsymbol{y}_{k',n'-1}) \right) \left(\prod_{k=1}^{K_{n'-1}} g(\underline{\boldsymbol{y}}_{k,n'}, a_{k,n'}, \mu_{\mathrm{fa}\,n'}; \boldsymbol{z}_{n'}) \right. \\ &\qquad \left. \times \prod_{m=1}^{M_{n'}} \psi(a_{k,n'}, b_{m,n'}) \right) \left(\prod_{m'=1}^{M_{n'}} h(\overline{\boldsymbol{y}}_{m',n'}, b_{m',n'}, \mu_{\mathrm{fa}\,n'}; \boldsymbol{z}_{n'}) \right) \end{aligned} \tag{11}$$

where the functions $g(\underline{\boldsymbol{y}}_{k,n}, a_{k,n}, \mu_{\mathrm{fa}\,n}; \boldsymbol{z}_n)$ and $h(\overline{\boldsymbol{y}}_{m,n}, b_{m,n}, \mu_{\mathrm{fa}\,n}; \boldsymbol{z}_n)$ will be discussed next.

The pseudo likelihood functions $g(\underline{\boldsymbol{y}}_{k,n}, a_{k,n}, \mu_{\mathrm{fa}\,n}; \boldsymbol{z}_n) = g(\underline{\boldsymbol{x}}_{k,n}, \underline{r}_{k,n}, a_{k,n}, \mu_{\mathrm{fa}\,n}; \boldsymbol{z}_n)$ and $h(\overline{\boldsymbol{y}}_{m,n}, b_{m,n}, \mu_{\mathrm{fa}\,n}; \boldsymbol{z}_n) = h(\overline{\boldsymbol{x}}_{m,n}, \overline{r}_{m,n}, b_{m,n}, \mu_{\mathrm{fa}\,n}; \boldsymbol{z}_n)$ are given

by

$$g(\underline{\boldsymbol{x}}_{k,n}, \underline{r}_{k,n} = 1, a_{k,n}, \mu_{\mathrm{fa}n}; \boldsymbol{z}_n) = \begin{cases} \dfrac{n(\mu_{\mathrm{fa}n}) f(\boldsymbol{z}_{m,n}|\underline{\boldsymbol{x}}_{k,n}) p_{\mathrm{d}}(\underline{u}_{k,n})}{\mu_{\mathrm{fa}n} f_{\mathrm{fa}}(\boldsymbol{z}_{m,n})}, & a_{k,n} = m \\ n(\mu_{\mathrm{fa}n})\big(1 - p_{\mathrm{d}}(\underline{u}_{k,n})\big), & a_{k,n} = 0 \end{cases} \tag{12}$$

and $g(\underline{\boldsymbol{x}}_{k,n}, \underline{r}_{k,n} = 0, a_{k,n}, \mu_{\mathrm{fa}n}; \boldsymbol{z}_n) = \bar{1}(a_{k,n}) n(\mu_{\mathrm{fa}n})$ with a factor related to FAR $n(\mu_{\mathrm{fa}n}) \triangleq (e^{-\mu_{\mathrm{fa}n}} \mu_{\mathrm{fa}n}^{M_n})^{1/(K_{n-1}+M_n)}$ and by

$$h(\overline{\boldsymbol{x}}_{m,n}, \overline{r}_{m,n} = 1, b_{m,n}, \mu_{\mathrm{fa}n}; \boldsymbol{z}_n) = \begin{cases} 0, & b_{m,n} = k \\ \dfrac{n(\mu_{\mathrm{fa}n}) \mu_{\mathrm{n}} f_{\mathrm{n}}(\overline{\boldsymbol{x}}_{m,n}) f(\boldsymbol{z}_{m,n}|\overline{\boldsymbol{x}}_{m,n})}{\mu_{\mathrm{fa}n} f_{\mathrm{fa}}(\boldsymbol{z}_{m,n})}, & b_{m,n} = 0 \end{cases} \tag{13}$$

and $h(\overline{\boldsymbol{x}}_{m,n}, \overline{r}_{m,n} = 0, b_{m,n}, \mu_{\mathrm{fa}n}; \boldsymbol{z}_n) = n(\mu_{\mathrm{fa}n})$, respectively. The factor graph [43], [44] representing the factorization in (11) is shown in Fig. 1. The detailed derivations of the joint posterior PDF in (11) and the pseudo likelihood functions in (12) and (13) are provided in the Appendix in Section A, Section B, and Section C.

4.2 PMPC Detection and State Estimation

The problem considered is the sequential detection of PMPCs and estimation of their states $\mathbf{y}_{k,n}$, $k \in \{1, \ldots, K_{n-1} + M_n\}$ along with the estimation of the FAR $_{\mathrm{fa}n}$ based on the measurement vector $\boldsymbol{z}_{1:n}$. This relies on the marginal posterior existence probabilities $p(r_{k,n} = 1|\boldsymbol{z}_{1:n})$, the marginal posterior PDFs $f(\boldsymbol{x}_{k,n}|r_{k,n} = 1, \boldsymbol{z}_{1:n})$ and $f(\mu_{\mathrm{fa}n}|\boldsymbol{z}_{1:n})$. More specifically, a PMPC is detected if $p(r_{k,n} = 1|\boldsymbol{z}_{1:n}) > p_{\mathrm{de}}$ [45], where p_{de} is the existence probability threshold not to be confused with u_{de} the detection threshold of the snapshot-based estimator. The probabilities $p(r_{k,n} = 1|\boldsymbol{z}_{1:n})$ are obtained from the marginal posterior PDFs of the PMPC states, $f(\boldsymbol{y}_{k,n}|\boldsymbol{z}_{1:n}) = f(\boldsymbol{x}_{k,n}, r_{k,n}|\boldsymbol{z}_{1:n})$, according to

$$p(r_{k,n} = 1|\boldsymbol{z}_{1:n}) = \big\langle f(\boldsymbol{x}_{k,n}, r_{k,n} = 1|\boldsymbol{z}_{1:n}) \big\rangle_{1_{\mathbb{R}^{5\times 1}}(\boldsymbol{x}_{k,n})} \tag{14}$$

and the marginal posterior PDFs $f(\boldsymbol{x}_{k,n}|r_{k,n} = 1, \boldsymbol{z}_{1:n})$ are obtained from $f(\boldsymbol{x}_{k,n}, r_{k,n}|\boldsymbol{z}_{1:n})$ as

$$f(\boldsymbol{x}_{k,n}|r_{k,n} = 1, \boldsymbol{z}_{1:n}) = \frac{f(\boldsymbol{x}_{k,n}, r_{k,n} = 1|\boldsymbol{z}_{1:n})}{p(r_{k,n} = 1|\boldsymbol{z}_{1:n})}. \tag{15}$$

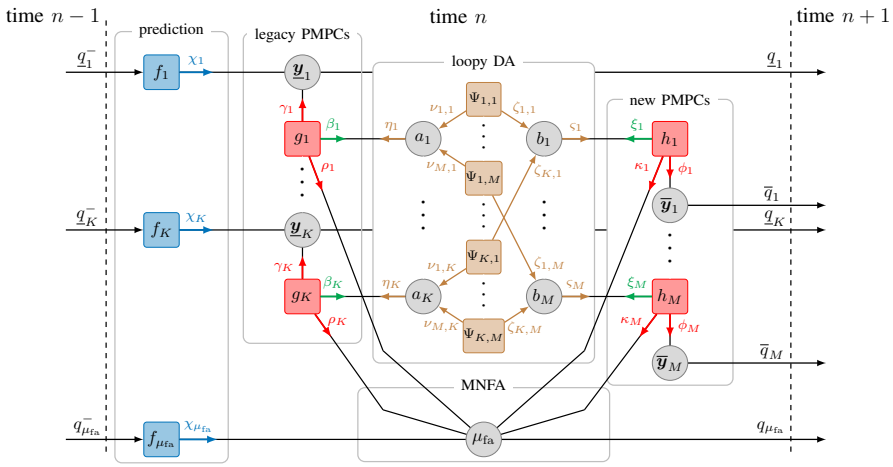

Figure 1: Factor graph representation of the factorized joint posterior PDF (11). For simplicity, the following short notations are used: $K \triangleq K_{n-1}$, $M \triangleq M_n$; *variable nodes*: $a_k \triangleq a_{k,n}$, $b_m \triangleq b_{m,n}$, $\mu_{\text{fa}} \triangleq \mu_{\text{fa}_n}$, $\underline{\boldsymbol{y}}_k \triangleq \underline{\boldsymbol{y}}_{k,n}$, $\overline{\boldsymbol{y}}_m \triangleq \overline{\boldsymbol{y}}_{m,n}$; *factor nodes*: $f_k \triangleq f(\underline{\boldsymbol{y}}_{k,n}|\boldsymbol{y}_{k,n-1})$, $g_k \triangleq g(\underline{\boldsymbol{x}}_{k,n}, \underline{r}_{k,n}, a_{k,n}, \mu_{\text{fa}_n}; \boldsymbol{z}_n)$, $h_m \triangleq h(\overline{\boldsymbol{x}}_{m,n}, \overline{r}_{m,n}, b_{m,n}, \mu_{\text{fa}_n}; \boldsymbol{z}_n)$, $f_{\mu_{\text{fa}}} \triangleq f(\mu_{\text{fa}_n}|\mu_{\text{fa}_{n-1}})$, $\Psi_{k,m} \triangleq \Psi(a_{k,n}, b_{m,n})$; *prediction*: $\chi_k \triangleq \chi(\underline{\boldsymbol{x}}_{k,n}, \underline{r}_{k,n})$, $\chi_{\mu_{\text{fa}}} \triangleq \chi(\mu_{\text{fa}_n})$; *measurement evaluation*: $\beta_k \triangleq \beta(a_k)$, $\xi_m \triangleq \xi(b_m)$; *loopy DA*: $\nu_{m,k} \triangleq \nu_{m\to k}(a_{k,n})$, $\zeta_{k,m} \triangleq \zeta_{k\to m}(b_{m,n})$, $\eta_k \triangleq \eta(a_k)$, $\varsigma_m \triangleq \varsigma(b_m)$; *measurement update*: $\gamma_k \triangleq \gamma(\underline{\boldsymbol{x}}_{k,n}, \underline{r}_{k,n})$, $\rho_k \triangleq \rho_k(\mu_{\text{fa}_n})$, $\phi_m \triangleq \phi(\overline{\boldsymbol{x}}_{m,n}, \overline{r}_{m,n})$, $\kappa_m \triangleq \kappa_m(\mu_{\text{fa}_n})$; belief calculation: $\underline{q}_k^- \triangleq \underline{q}(\boldsymbol{x}_{k,n-1}, r_{k,n-1})$, $\underline{q}_k \triangleq \underline{q}(\underline{\boldsymbol{x}}_{k,n}, \underline{r}_{k,n})$, $\overline{q}_m \triangleq \overline{q}(\overline{\boldsymbol{x}}_{m,n}, \overline{r}_{m,n})$, $q_{\mu_{\text{fa}}}^- \triangleq q(\mu_{\text{fa}_{n-1}})$, $q_{\mu_{\text{fa}}} \triangleq q(\mu_{\text{fa}_n})$.

The number of detected PMPCs represents the estimated NoM given by $\hat{L}_n$. The states $\mathsf{u}_{k,n}$ and $\boldsymbol{\theta}_{k,n}$ of the detected PMPCs are estimated by means of the MMSE estimator [46], i.e.,

$$u_{k,n}^{\text{MMSE}} \triangleq \left\langle u_{k,n} \right\rangle_{f(\boldsymbol{x}_{k,n}|r_{k,n}=1,\boldsymbol{z}_{1:n})} \tag{16}$$

$$\boldsymbol{\theta}_{k,n}^{\text{MMSE}} \triangleq \left\langle \boldsymbol{\theta}_{k,n} \right\rangle_{f(\boldsymbol{x}_{k,n}|r_{k,n}=1,\boldsymbol{z}_{1:n})} \tag{17}$$

with $\boldsymbol{\theta}_{k,n}^{\text{MMSE}} = [d_{k,n}^{\text{MMSE}}\ \varphi_{k,n}^{\text{MMSE}}]^{\text{T}} \in \mathbb{R}^{2\times 1}$, respectively. Note that the estimated component SNRs is given by $\text{SNR}_{k,n}^{\text{MMSE}} = \left(u_{k,n}^{\text{MMSE}}\right)^2$. Finally, the estimate of the FAR $_{\text{fa}n}$ is given by

$$\mu_{\text{fa}_n}{}^{\text{MMSE}} \triangleq \left\langle \mu_{\text{fa}_n} \right\rangle_{f(\mu_{\text{fa}_n}|\boldsymbol{z}_{1:n})}. \tag{18}$$

To initialize the dispersion parameters of the snapshot-based channel es-

timator (see Section 2.2), the prior PDF is assumed to be Gaussian with vector-valued mean given by the MMSE estimate $\boldsymbol{\theta}_{k,n-1}^{\mathrm{MMSE}} \in \mathbb{R}^{2\times 1}$ and covariance matrix $\boldsymbol{\Sigma}_{k,n-1} = \mathrm{diag}\{\sigma_{\mathrm{d}\,k,n-1}^{\mathrm{MMSE}}\ \sigma_{\varphi\,k,n-1}^{\mathrm{MMSE}}\} \in \mathbb{R}^{2\times 2}$ of the parameters with $k \in \{1,\ldots,\hat{L}_{n-1}\}$, where $\sigma_{\mathrm{d}\,k,n}^{\mathrm{MMSE}} = \left(\left\langle (d_{k,n} - d_{k,n}^{\mathrm{MMSE}})^2 \right\rangle_{f(\boldsymbol{x}_{k,n}|r_{k,n}=1,\boldsymbol{z}_{1:n})}\right)^{\frac{1}{2}}$ and $\sigma_{\varphi\,k,n}^{\mathrm{MMSE}} = \left(\left\langle (\varphi_{k,n} - \varphi_{k,n}^{\mathrm{MMSE}})^2 \right\rangle_{f(\boldsymbol{x}_{k,n}|r_{k,n}=1,\boldsymbol{z}_{1:n})}\right)^{\frac{1}{2}}$.

As the number of PMPCs grows with time n (at each time by $K_n = K_{n-1} + M_n$), PMPCs with $p(r_{k,n} = 1|\boldsymbol{z}_{1:n})$ below a threshold p_{pr} are removed from the state space ("pruned").

5 The Proposed Sum-Product Algorithm

The posterior PDFs $f(\underline{\boldsymbol{x}}_{k,n}, \underline{r}_{k,n}|\boldsymbol{z}_{1:n})$, $f(\overline{\boldsymbol{x}}_{m,n}, \overline{r}_{m,n}|\boldsymbol{z}_{1:n})$, and $f(\mu_{\mathrm{fa}\,n}|\boldsymbol{z}_{1:n})$ involved in (14), (15) and (18) are marginal PDFs of the joint posterior PDF $f(\boldsymbol{y}_{1:n}, \boldsymbol{a}_{1:n}, \boldsymbol{b}_{1:n}, \boldsymbol{\mu}_{\mathrm{fa}\,1:n}, \boldsymbol{m}_{1:n}|\boldsymbol{z}_{1:n})$. Since direct marginali- zation of the joint posterior PDF is infeasible, we use loopy (iterative) BP [43] by means of the sum-product algorithm rules [43], [44] on the factor graph shown in Fig. 1. Due to the loops inside the factor graph, the resulting beliefs $\underline{q}(\underline{\boldsymbol{y}}_{k,n}) = \underline{q}(\underline{\boldsymbol{x}}_{k,n}, \underline{r}_{k,n})$, $\overline{q}(\overline{\boldsymbol{y}}_{m,n}) = \overline{q}(\overline{\boldsymbol{x}}_{m,n}, \overline{r}_{m,n})$, and $q(\mu_{\mathrm{fa}\,n})$ are only approximations of the respective posterior marginal PDFs, and there is no canonical order in which the messages should be computed [43]. For the proposed algorithm, we specify the following order: (i) messages are not sent backward in time; (ii) iterative message passing is only performed for probabilistic DA at each time n. Combining the specified order with the generic BP rules for calculating messages and beliefs yields the following calculations at each time n (which are in parts in line with [8], [29, Ch. III]):

1. *Prediction*: First, a prediction step is performed. The prediction for the FAR is given by

$$\chi(\mu_{\mathrm{fa}\,n}) = \left\langle f(\mu_{\mathrm{fa}\,n}|\mu_{\mathrm{fa}\,n-1}) \right\rangle_{q(\mu_{\mathrm{fa}\,n-1})} \tag{19}$$

and for all the legacy PMPCs is given by

$$\begin{aligned}&\chi(\underline{\boldsymbol{x}}_{k,n}, \underline{r}_{k,n})\\ &= \sum_{r_{k,n-1}\in\{0,1\}} \left\langle f(\underline{\boldsymbol{x}}_{k,n}, \underline{r}_{k,n}|\boldsymbol{x}_{k,n-1}, r_{k,n-1}) \right\rangle_{\underline{q}(\boldsymbol{x}_{k,n-1}, r_{k,n-1})}\end{aligned} \tag{20}$$

where $q(\mu_{\mathrm{fa}\,n-1})$ and $\underline{q}(\boldsymbol{x}_{k,n-1}, r_{k,n-1})$ were calculated at the previous time $n-1$. After substituting the PMPC state-transition PDFs in (20) with (4) and (5), respectively, we obtain the prediction messages for leg-

acy PMPCs as

$$\chi(\underline{\boldsymbol{x}}_{k,n},1)=p_{\mathrm{s}}\big\langle f(\underline{\boldsymbol{x}}_{k,n}|\boldsymbol{x}_{k,n-1})\big\rangle_{\underline{q}(\boldsymbol{x}_{k,n-1},1)} \tag{21}$$

and $\chi(\underline{\boldsymbol{x}}_{k,n},0)=\chi_{k,n}f_{\mathrm{D}}(\underline{\boldsymbol{x}}_{k,n})$ with

$$\chi_{k,n}=(1-p_{\mathrm{s}})\big\langle \underline{q}(\boldsymbol{x}_{k,n-1},1)\big\rangle_{1_{\mathbb{R}^{5\times1}}(\boldsymbol{x}_{k,n-1})}+\underline{q}_{k,n-1} \tag{22}$$

where $\chi_{k,n}\triangleq\big\langle\chi(\underline{\boldsymbol{x}}_{k,n},0)\big\rangle_{1_{\mathbb{R}^{5\times1}}(\underline{\boldsymbol{x}}_{k,n})}$ and $\underline{q}_{k,n-1}\triangleq\big\langle\underline{q}(\boldsymbol{x}_{k,n-1},0)\big\rangle_{1_{\mathbb{R}^{5\times1}}(\boldsymbol{x}_{k,n-1})}$. After the prediction step, the following steps are performed for all legacy and new PMPCs in parallel:

2. *Measurement Evaluation*: For legacy PMPCs, the messages $\beta(a_{k,n})$ passed from the factor nodes $g(\underline{\boldsymbol{x}}_{k,n},\ \underline{r}_{k,n},a_{k,n},\mu_{\mathrm{fa}n};\boldsymbol{z}_n)$ to the PMPC-oriented DA variable nodes $a_{k,n}$ are calculated by

$$\begin{aligned}\beta(a_{k,n})=&\Big\langle\big\langle g(\underline{\boldsymbol{x}}_{k,n},1,a_{k,n},\mu_{\mathrm{fa}n};\boldsymbol{z}_n)\big\rangle_{\chi(\underline{\boldsymbol{x}}_{k,n},1)}\Big\rangle_{\chi(\mu_{\mathrm{fa}n})}\\&+\bar{1}(a_{k,n})\Big\langle\big\langle\chi(\underline{\boldsymbol{x}}_{k,n},0)n(\mu_{\mathrm{fa}n})\big\rangle_{1_{\mathbb{R}^{5\times1}}(\underline{\boldsymbol{x}}_{k,n})}\Big\rangle_{\chi(\mu_{\mathrm{fa}n})}.\end{aligned} \tag{23}$$

For new PMPCs, the messages $\xi(b_{m,n})$ passed from the factor nodes $h(\overline{\boldsymbol{x}}_{m,n},\overline{r}_{m,n},\ b_{m,n},\mu_{\mathrm{fa}n};\boldsymbol{z}_n)$ to the measurement-oriented DA variable nodes $b_{m,n}$ are calculated according to

$$\xi(b_{m,n})=\sum_{\overline{r}_{m,n}\in\{0,1\}}\Big\langle\big\langle h(\overline{\boldsymbol{x}}_{m,n},\overline{r}_{m,n},b_{m,n},\mu_{\mathrm{fa}n};\boldsymbol{z}_n)\big\rangle_{1_{\mathbb{R}^{5\times1}}(\overline{\boldsymbol{x}}_{m,n})}\Big\rangle_{\chi(\mu_{\mathrm{fa}n})}. \tag{24}$$

More specifically, for $b_{m,n}=k$ it becomes $\xi(b_{m,n})=\big\langle n(\mu_{\mathrm{fa}n})\chi(\mu_{\mathrm{fa}n})\big\rangle_{1_{\mathbb{R}}(\mu_{\mathrm{fa}n})}$ and for $b_{m,n}=0$ it becomes

$$\begin{aligned}\xi(b_{m,n})=&\big\langle n(\mu_{\mathrm{fa}n})\chi(\mu_{\mathrm{fa}n})\big\rangle_{1_{\mathbb{R}}(\mu_{\mathrm{fa}n})}+\Big\langle\Big\langle\frac{\mu_{\mathrm{n}}f_{\mathrm{n}}(\overline{\boldsymbol{x}}_{m,n})n(\mu_{\mathrm{fa}n})}{\mu_{\mathrm{fa}n}}\\&\times\frac{f(\boldsymbol{z}_{m,n}|\overline{\boldsymbol{x}}_{m,n})}{f_{\mathrm{fa}}(\boldsymbol{z}_{m,n})}\Big\rangle_{1_{\mathbb{R}^{5\times1}}(\overline{\boldsymbol{x}}_{m,n})}\Big\rangle_{\chi(\mu_{\mathrm{fa}n})}.\end{aligned} \tag{25}$$

3. *Iterative Probabilistic DA*: With the messages $\beta(a_{k,n})$ and $\xi(b_{m,n})$, the probabilistic DA messages $\eta(a_{k,n})$ and $\varsigma(b_{m,n})$ are obtained with an effi-

cient loopy BP-based algorithm as shown in [8], [35], [41]

$$\eta(a_{k,n}) = \prod_{m=1}^{M_n} \nu^{(p)}_{\psi_{m\to k}}(a_{k,n}) \tag{26}$$

$$\varsigma(b_{m,n}) = \prod_{k=1}^{K_{n-1}} \zeta^{(p)}_{\psi_{k\to m}}(b_{m,n}) \tag{27}$$

where $\nu^{(p)}_{\psi_{m\to k}}(a_{k,n})$ and $\zeta^{(p)}_{\psi_{k\to m}}(b_{m,n})$ denote the messages passed from $\psi(a_{k,n}, b_{m,n})$ to the variable nodes $a_{k,n}$ and $b_{m,n}$ at each iteration $p \in \{1, \ldots, P\}$, respectively.

4. *Measurement Update*: For legacy PMPCs, the messages $\gamma(\underline{\boldsymbol{x}}_{k,n}, \underline{r}_{k,n})$ passed from the factor nodes $g(\underline{\boldsymbol{x}}_{k,n}, \underline{r}_{k,n}, a_{k,n}, \mu_{\mathrm{fa}n}; \boldsymbol{z}_n)$ to the variable nodes $\underline{\boldsymbol{y}}_{k,n}$ are calculated by

$$\gamma(\underline{\boldsymbol{x}}_{k,n}, 1) = \sum_{a_{k,n}=0}^{M_n} \eta(a_{k,n}) \big\langle g(\underline{\boldsymbol{x}}_{k,n}, 1, a_{k,n}, \mu_{\mathrm{fa}n}; \boldsymbol{z}_n) \big\rangle_{\chi(\mu_{\mathrm{fa}n})} \tag{28}$$

and $\gamma(\underline{\boldsymbol{x}}_{k,n}, 0) = \gamma_{k,n} f_{\mathrm{D}}(\underline{\boldsymbol{x}}_{k,n})$ with

$$\begin{aligned} \gamma_{k,n} &= \big\langle \gamma(\underline{\boldsymbol{x}}_{k,n}, 0) \big\rangle_{1_{\mathbb{R}^{5\times 1}}(\underline{\boldsymbol{x}}_{k,n})} \\ &= \eta(0) \big\langle n(\mu_{\mathrm{fa}n}) \big\rangle_{\chi(\mu_{\mathrm{fa}n})}. \end{aligned} \tag{29}$$

For new PMPCs, the messages $\phi(\overline{\boldsymbol{x}}_{m,n}, \overline{r}_{m,n})$ passed from the factor nodes $h(\overline{\boldsymbol{x}}_{m,n}, \overline{r}_{m,n}, b_{m,n}, \mu_{\mathrm{fa}n}; \boldsymbol{z}_n)$ to the variable nodes $\overline{\boldsymbol{y}}_{m,n}$ are calculated by

$$\phi(\overline{\boldsymbol{x}}_{m,n}, 1) = \varsigma(0) \big\langle h(\overline{\boldsymbol{x}}_{m,n}, 1, b_{m,n}, \mu_{\mathrm{fa}n}; \boldsymbol{z}_n) \big\rangle_{\chi(\mu_{\mathrm{fa}n})} \tag{30}$$

and $\phi(\overline{\boldsymbol{x}}_{m,n}, 0) = \phi_{m,n} f_{\mathrm{D}}(\overline{\boldsymbol{x}}_{m,n})$ with

$$\begin{aligned} \phi_{m,n} &\triangleq \big\langle \phi(\overline{\boldsymbol{x}}_{m,n}, 0) \big\rangle_{1_{\mathbb{R}^{5\times 1}}(\overline{\boldsymbol{x}}_{m,n})} \\ &= \sum_{b_{m,n}=0}^{K_{n-1}} \varsigma(b_{m,n}) \big\langle n(\mu_{\mathrm{fa}n}) \big\rangle_{\chi(\mu_{\mathrm{fa}n})}. \end{aligned} \tag{31}$$

For the FAR $_{\mathrm{fa}n}$, the messages $\rho_k(\mu_{\mathrm{fa}n})$ and $\kappa_m(\mu_{\mathrm{fa}n})$ passed from the factor nodes $g(\underline{\boldsymbol{x}}_{k,n}, \underline{r}_{k,n}, a_{k,n}, \mu_{\mathrm{fa}n}; \boldsymbol{z}_n)$ and $h(\overline{\boldsymbol{x}}_{m,n}, \overline{r}_{m,n}, b_{m,n}, \mu_{\mathrm{fa}n}; \boldsymbol{z}_n)$,

respectively, to the variable node $\mu_{\mathrm{fa}n}$ are calculated by

$$\rho_k(\mu_{\mathrm{fa}n}) = \sum_{a_{k,n}=0}^{M_n} \eta(a_{k,n}) \sum_{\underline{r}_{k,n}\in\{0,1\}} \left\langle g(\underline{\boldsymbol{x}}_{k,n}, \underline{r}_{k,n}, a_{k,n}, \mu_{\mathrm{fa}n}; \boldsymbol{z}_n)\right\rangle_{\chi(\underline{\boldsymbol{x}}_{k,n},\underline{r}_{k,n})} \tag{32}$$

and

$$\kappa_m(\mu_{\mathrm{fa}n}) = n(\mu_{\mathrm{fa}n})\varsigma(0)\left\langle \frac{\mu_{\mathrm{n}} f(\boldsymbol{z}_{m,n}|\overline{\boldsymbol{x}}_{m,n})}{\mu_{\mathrm{fa}n} f_{\mathrm{fa}}(\boldsymbol{z}_{m,n})}\right\rangle_{f_{\mathrm{n}}(\overline{\boldsymbol{x}}_{m,n})} + \sum_{b_{m,n}=0}^{K_{n-1}} \varsigma(b_{m,n}) n(\mu_{\mathrm{fa}n}). \tag{33}$$

5. *Belief Calculation*: With all the messages above, the approximations of the marginal posterior PDFs needed for the MMSE estimations in Section 4.2 are calculated as follows. The beliefs $\underline{q}(\underline{\boldsymbol{y}}_{k,n}) = \underline{q}(\underline{\boldsymbol{x}}_{k,n}, \underline{r}_{k,n})$ approximating the marginal posterior PDFs $f(\underline{\boldsymbol{y}}_{k,n}|\boldsymbol{z}_{1:n}) = f(\underline{\boldsymbol{x}}_{k,n}, \underline{r}_{k,n}|\boldsymbol{z}_{1:n})$ for legacy PMPCs are obtained as

$$\underline{q}(\underline{\boldsymbol{x}}_{k,n}, 1) = \frac{1}{\underline{C}_{k,n}} \chi(\underline{\boldsymbol{x}}_{k,n}, 1)\gamma(\underline{\boldsymbol{x}}_{k,n}, 1) \tag{34}$$

and $\underline{q}(\underline{\boldsymbol{x}}_{k,n}, 0) = \underline{q}_{k,n} f_{\mathrm{D}}(\underline{\boldsymbol{x}}_{k,n})$ with $\underline{q}_{k,n} = \dfrac{1}{\underline{C}_{k,n}} \chi_{k,n}\gamma_{k,n}$. The normalization constant is given as $\underline{C}_{k,n} = \left\langle \gamma(\underline{\boldsymbol{x}}_{k,n}, 1)\right\rangle_{\chi(\underline{\boldsymbol{x}}_{k,n},1)} + \chi_{k,n}\gamma_{k,n}$. The beliefs $\overline{q}(\overline{\boldsymbol{y}}_{m,n}) = \overline{q}(\overline{\boldsymbol{x}}_{m,n}, \overline{r}_{m,n})$ approximating the marginal posterior PDFs $f(\overline{\boldsymbol{y}}_{m,n}|\boldsymbol{z}_{1:n}) = f(\overline{\boldsymbol{x}}_{m,n}, \overline{r}_{m,n}|\boldsymbol{z}_{1:n})$ for new PMPCs are obtained as

$$\overline{q}(\overline{\boldsymbol{x}}_{m,n}, 1) = \frac{1}{\overline{C}_{m,n}} \phi(\overline{\boldsymbol{x}}_{m,n}, 1) \tag{35}$$

and $\overline{q}(\overline{\boldsymbol{x}}_{m,n}, 0) = \overline{q}_{m,n} f_{\mathrm{D}}(\overline{\boldsymbol{x}}_{m,n})$ with $\overline{q}_{m,n} = \dfrac{1}{\overline{C}_{m,n}} \phi_{m,n}$. The normalization constant is given as $\overline{C}_{m,n} = \left\langle \phi(\overline{\boldsymbol{x}}_{m,n}, 1)\right\rangle_{1_{\mathbb{R}^{5\times 1}}(\overline{\boldsymbol{x}}_{m,n})} + \phi_{m,n}$. Finally, the belief $q(\mu_{\mathrm{fa}n})$ approximating the marginal posterior PDF $f(\mu_{\mathrm{fa}n}|\boldsymbol{z}_{1:n})$ for the FAR is obtained as

$$q(\mu_{\mathrm{fa}n}) = \chi(\mu_{\mathrm{fa}n}) \prod_{k=1}^{K_{n-1}} \rho_k(\mu_{\mathrm{fa}n}) \prod_{m=1}^{M_n} \kappa_m(\mu_{\mathrm{fa}n}). \tag{36}$$

6 Particle-based Implementation

Since integrations involved in the calculations of the messages and beliefs cannot be obtained analytically, we use a computationally efficient sequential particle-based message passing implementation which provides approximate computation. In what follows, we present particle-based implementations for FAR related steps (19), (32), (33) and (36). The implementation of all other steps in Section 5, and the calculation of posterior existence probabilities of PMPCs are performed in line with [35, Section VI]. Similarly to [8], our implementation uses a "stacked state" [47] comprising the PMPC states and the FAR state.

1. *Prediction*: The belief $q(\mu_{\mathrm{fa}n-1})$ calculated at the previous time $n-1$ is represented by J particles and weights, i.e., $\{\hat{\mu}_{\mathrm{fa}n-1}^{(j)}, \hat{w}_{\mathrm{fa}n-1}^{(j)}\}_{j=1}^{J}$. At time n, for each particle $\hat{\mu}_{\mathrm{fa}n-1}^{(j)}$, $j \in \{1,\ldots,J\}$ one particle $\mu_{\mathrm{fa}n}^{'(j)}$ with corresponding weight $w_{\mathrm{fa}n}^{'(j)} = \hat{w}_{\mathrm{fa}n-1}^{(j)}$ is drawn from $f(\mu_{\mathrm{fa}n}|\mu_{\mathrm{fa}n-1})$, and $\{\mu_{\mathrm{fa}n}^{'(j)}, w_{\mathrm{fa}n}^{'(j)}\}_{j=1}^{J}$ represent the prediction message $\chi(\mu_{\mathrm{fa}n})$ in (19). Note that the proposal distribution underlying the weight calculation is $f(\mu_{\mathrm{fa}n}|\mu_{\mathrm{fa}n-1})$.

2. *Measurement Update*: The non-normalized weights corresponding to the messages for legacy PMPCs $\rho_k(\mu_{\mathrm{fa}n})$ in (32) and new PMPCs $\kappa_m(\mu_{\mathrm{fa}n})$ in (33) are calculated by

$$\begin{aligned}\underline{w}_{\mathrm{fa}k,n}^{(j)} = &\sum_{a_{k,n}=0}^{M_n} \eta(a_{k,n}) g(\underline{\boldsymbol{x}}_{k,n}^{(j)}, 1, a_{k,n}, \mu_{\mathrm{fa}n}^{(j)}; \boldsymbol{z}_n) w_{k,n}^{(j)} \\ &+ n(\mu_{\mathrm{fa}n}^{(j)}) \frac{(1 - \sum_{j=0}^{J} w_{k,n}^{(j)})}{J}\end{aligned} \tag{37}$$

and

$$\overline{w}_{\mathrm{fa}m,n}^{(j)} = n(\mu_{\mathrm{fa}n}^{(j)}) \frac{\mu_{\mathrm{n}} f(\boldsymbol{z}_{m,n}|\overline{\boldsymbol{x}}_{m,n}^{(j)})}{\mu_{\mathrm{fa}n}^{(j)} f_{\mathrm{fa}}(\boldsymbol{z}_{m,n})} f_{\mathrm{n}}(\overline{\boldsymbol{x}}_{m,n}^{(j)}) + \sum_{b_{m,n}=0}^{K_{n-1}} \varsigma(b_{m,n}) n(\mu_{\mathrm{fa}n}^{(j)}) \tag{38}$$

respectively. The weighted particles $\{\underline{\boldsymbol{x}}_{k,n}^{(j)}, \underline{w}_{k,n}^{(j)}\}_{j=1}^{J}$ represent the prediction messages $\chi(\underline{\boldsymbol{x}}_{k,n}, \underline{r}_{k,n})$ of legacy PMPCs in (20), thus their predicted existence probabilities can be approximated as $\sum_{j=0}^{J} \underline{w}_{k,n}^{(j)}$, and $(1-\sum_{j=0}^{J} \underline{w}_{k,n}^{(j)})/J$ is the weight of particles representing $\chi(\underline{\boldsymbol{x}}_{k,n}, 0)$. Moreover,

the weighted particles $\{\overline{\boldsymbol{x}}_{m,n}^{(j)}, \overline{w}_{k,n}^{(j)} = 1/J\}_{j=1}^{J}$ with equal weights represent the states of new PMPCs.

3. *Belief Calculation and State Estimation*: The above approximate messages are further used for calculating the non-normalized weights corresponding to the belief $q(\mu_{\mathrm{fa}n})$ in (36), given by

$$w_{\mathrm{fa}n}^{(j)} = w_{\mathrm{fa}n}^{'\,(j)} \prod_{k=1}^{K_{n-1}} \underline{w}_{\mathrm{fa}k,n}^{(j)} \prod_{m=1}^{M_n} \overline{w}_{\mathrm{fa}m,n}^{(j)}. \tag{39}$$

After normalization $w_{\mathrm{fa}n}^{(j)} = w_{\mathrm{fa}n}^{(j)} / \sum_{j=0}^{J} w_{\mathrm{fa}n}^{(j)}$, an approximation of the MMSE state estimate $\mu_{\mathrm{fa}n}^{\mathrm{MMSE}}$ in (18) is given by

$$\mu_{\mathrm{fa}n}^{\mathrm{MMSE}} \approx \sum_{j=0}^{J} w_{\mathrm{fa}n}^{(j)} \mu_{\mathrm{fa}n}^{'\,(j)}. \tag{40}$$

To avoid the particle degeneracy effect, a resampling step [35] is performed as a final preparation for the next time $n+1$ leading to $\{\hat{\mu}_{\mathrm{fa}n}^{(j)}, \hat{w}_{\mathrm{fa}n}^{(j)} = 1/J\}_{j=1}^{J}$ representing the belief $q(\mu_{\mathrm{fa}n})$. Assuming a fixed number P of message passing iterations for DA, the computational complexity of calculating the (approximate) marginal posterior PDFs scales only linearly in the number of particles. Moreover, the complexity of the iterative DA given by the operations in (26) and (27) scales as $O(K_{n-1}M_n)$, i.e., quadratically in the number of PMPCs [29], [35], [41].

7 Experimental Results

The performance of the proposed algorithm is validated using both synthetic and real radio measurements. For synthetic measurements, the performance is further compared with the posterior-CRLB [48] and that of the KEST algorithm [27].

7.1 Analysis Setup

Common Simulation Setup

For synthetic and real measurements, the following setups and parameters are commonly used. We assume that MPC dispersion parameters with according velocities and normalized amplitudes evolve independently across time and to each other. More specifically, the state-transition PDF of $\underline{\boldsymbol{\theta}}_{k,n}$ (with according velocities $\underline{\mathrm{v}}_{\mathrm{d}k,n}$ and $\underline{\mathrm{v}}_{\varphi k,n}$) is chosen to be a nearly-constant velocity model.

The state-transition PDF of the normalized amplitude $\underline{\mathrm{u}}_{k,n}$ is chosen to be $\underline{u}_{k,n} = u_{k,n-1} + \epsilon_{\mathrm{u}\,k,n}$, where the noise $_{\mathrm{u}\,k,n}$ is iid across k and n, zero-mean, and Gaussian with variance $\underline{\sigma}^2_{\mathrm{u}\,k,n}$. Based on the models above, the state-transition PDF of legacy PMPC state $\underline{\mathbf{x}}_{k,n}$ is collectively given as $\underline{\boldsymbol{x}}_{k,n} = \boldsymbol{F}\boldsymbol{x}_{k,n-1} + \boldsymbol{\Gamma}\boldsymbol{\epsilon}_n$, where the transition matrices $\boldsymbol{F} \in \mathbb{R}^{5\times5}$ and $\boldsymbol{\Gamma} \in \mathbb{R}^{5\times3}$ are formulated as in [23], [49, Section 6.3.2] with sampling period $\Delta T = 1\,\mathrm{s}$. The driving process $\boldsymbol{\epsilon}_n \in \mathbb{R}^{3\times1}$ is iid across k and n, zero-mean and Gaussian with covariance matrix $\mathrm{diag}\{\sigma^2_{\mathrm{d}}, \sigma^2_{\varphi}, \underline{\sigma}^2_{\mathrm{u}\,k,n}\}$. In addition, the state-transition PDF of the FAR $_{\mathrm{fa}n}$ is given as $\mu_{\mathrm{fa}n} = \mu_{\mathrm{fa}n-1} + \epsilon_{\mathrm{fa}n}$, where $_{\mathrm{fa}n}$ is iid across n, zero-mean, and Gaussian with variance σ^2_{fa}.[13] For computational efficiency of the particle-based implementation, the likelihood function (9) of the normalized amplitude is approximated by a truncated Gaussian PDF, i.e.,

$$f(z_{\mathrm{u}\,m,n}|u_{k,n}) = \frac{\frac{1}{\sigma_{\mathrm{u}\,k,n}\sqrt{2\pi}} \exp\left(\frac{-(z_{\mathrm{u}\,m,n}-u_{k,n})^2}{2\sigma^2_{\mathrm{u}\,k,n}}\right)}{p_{\mathrm{d}}(u_{k,n})} \tag{41}$$

for $z_{\mathrm{u}\,m,n} > \sqrt{u_{\mathrm{de}}}$, where $p_{\mathrm{d}}(u_{k,n}) = Q((\sqrt{u_{\mathrm{de}}} - u_{k,n})/\sigma_{\mathrm{u}\,k,n})$ is the CDF of Gaussian distribution. The birth PDF of a new PMPCs $f_{\mathrm{n}}(\overline{\boldsymbol{x}}_{m,n}) = 1/(2\pi d_{\max})$ is assumed to be uniform on $[0,\, 2\pi d_{\max})$. The particles for the initial state $\overline{\mathbf{x}}_{m,n}$ of a new PMPC are drawn from a 5-D Gaussian PDF with means $[z_{\mathrm{d}\,m,n}\, z_{\varphi_{m,n}}\, z_{\mathrm{u}\,m,n}\, 0\, 0]^{\mathrm{T}}$ and variances $[\sigma^2_{\mathrm{d}\,m,n}\sigma^2_{\varphi_{m,n}}\sigma^2_{\mathrm{u}\,m,n}\sigma^2_{\mathrm{v_d}}\sigma^2_{\mathrm{v}_\varphi}]^{\mathrm{T}}$, where $\sigma^2_{\mathrm{d}\,m,n}$, $\sigma^2_{\varphi_{m,n}}$ and $\sigma^2_{\mathrm{u}\,m,n}$ are calculated using the amplitude measurements $z_{\mathrm{u}\,m,n}$ (see Section 3.3). The particles for the initial FAR $_{\mathrm{fa}n}$ state are drawn from a Gaussian PDF with mean $M_1/2$ and variance $\sigma^2_{\mathrm{fa_{ini}}}$. The other simulation parameters are as follows: the survival probability $p_{\mathrm{s}} = 0.999$, the existence probability threshold $p_{\mathrm{de}} = 0.5$, the pruning threshold $p_{\mathrm{pr}} = 10^{-4}$, the mean number of newly detected MPCs $\mu_{\mathrm{n}} = 0.008$, the maximum number of message passing iterations for DA $P = 5000$ and the PDFs of the states are represented by $J = 10000$ particles each.

For each simulation run, AWGN is generated with noise variance σ^2 specified by the SNR output defined as $\mathrm{SNR}_{1\mathrm{m}} = 10\log_{10}\left(\frac{|\alpha_{\mathrm{LoS}}|^2\|\boldsymbol{s}_{\mathrm{LoS}}\|^2}{\sigma^2}\right)$, where the amplitude α_{LoS} and the signal vector $\boldsymbol{s}_{\mathrm{LoS}}$ of the line-of-sight (LoS) path are computed at 1 m distance. For comparability with other papers presenting parametric channel estimation methods as for example [21], [25], [27], we also define the input SNR, i.e., $\mathrm{SNR}^{\mathrm{in}}_{1\mathrm{m}} = \mathrm{SNR}_{1\mathrm{m}} - 10\log_{10}(N_{\mathrm{s}}H)$, the input component SNRs $\mathrm{SNR}^{\mathrm{in}}_{l,n} = 10\log_{10}\left(\widetilde{\mathrm{SNR}}_{l,n}/(N_{\mathrm{s}}H)\right)$ and the input detection threshold $u^{\mathrm{in}}_{\mathrm{de}} = 10\log_{10}\left(u_{\mathrm{de}}/(N_{\mathrm{s}}H)\right)$ excluding the array and frequency sample gain.

[13] Incorporating the interacting multiple model (IMM) [37] into the algorithm can help to resolve the motion uncertainties of the unknown variable states, therefore the demand on presetting and tunning of noise variances for the state-transition PDFs can be relaxed. However, it is out of the scope of this paper and can be considered as a future extension.

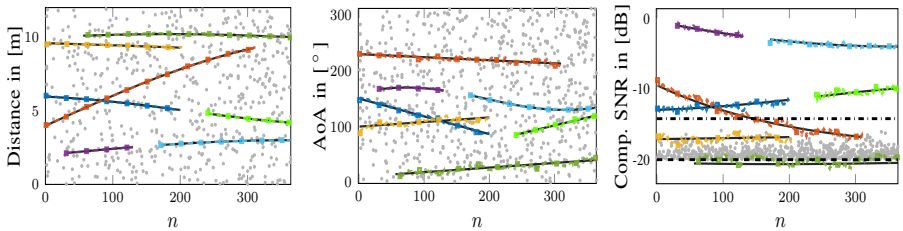

Figure 2: Results for fully synthetic measurements with the proposed algorithm given $\mathrm{SNR}_{\mathrm{lm}}^{\mathrm{in}} = 5.4\,\mathrm{dB}$. The estimates of (a) distances, (b) AoAs, and (c) input component SNRs. The black solid lines denote the true MPC parameters. The gray dots denote the false alarm measurements. The estimates of different MPCs are denoted with densely-dashed lines with square markers in different colors. The horizontal dashed and dash-dotted lines in (c) indicate the detection thresholds of $-20\,\mathrm{dB}$ and $-14.4\,\mathrm{dB}$, respectively.

Metrics

The performance of different methods is measured using the OSPA metric [50], which can efficiently capture the estimation errors of the NoM and MPC states when comparing with the true MPC states at each time. We use OSPA metric order 2 and cutoff parameters 0.1 m and 10° for distance and AoA respectively, where cutoff parameters denote the weightings of how the metric penalizes the NoM estimation errors as opposed to MPC state estimation errors. In addition, we compute the posterior-CRLB [48] as a performance benchmark. The error bounds for distance and AoA at time n are given as $\varepsilon_{\mathrm{d}n} = \left(\frac{\mathrm{tr}[\boldsymbol{J}_{\mathrm{p}n}^{-1}]_{1:L_n}}{L_n}\right)^{\frac{1}{2}}$ and $\varepsilon_{\varphi_n} = \left(\frac{\mathrm{tr}[\boldsymbol{J}_{\mathrm{p}n}^{-1}]_{L_n+1:2L_n}}{L_n}\right)^{\frac{1}{2}}$, where $\boldsymbol{J}_{\mathrm{p}n}$ denotes the posterior FIM. The mean OSPA (MOSPA) errors, mean error bounds (MEBs), and the mean estimate of each unknown variable are obtained by averaging over all simulation runs.

7.2 Performance for Synthetic Measurements

We assume that the static single-antenna Tx transmits $\tilde{s}(t)$ to the Rx equipped with a 3×3 uniform rectangular array with inter-element spacing of 2 cm. Over 364 time steps, 7 MPCs with different lifetimes and time-varying distances and AoAs were synthesized. The amplitude of each MPC is assumed to follow free-space pathloss and is attenuated by 3 dB after each reflection. Furthermore, we have designed two intersections between MPCs in their distance and AoA parameters at time $n = 83$ and $n = 125$, respectively. For the intersection at time $n = 83$, the distances intersect simultaneously with the amplitudes. For the transmit signal $\tilde{s}(t)$, we use a root-raised-cosine pulse with

a roll-off factor of 0.6 and pulse duration of $T_\mathrm{p} = 2\,\mathrm{ns}$ (bandwidth of 500 MHz) at center frequency of $f_\mathrm{c} = 6\,\mathrm{GHz}$. With sampling period $T_\mathrm{s} = 1.25\,\mathrm{ns}$, the number of samples per array element is $N_\mathrm{s} = 46$. In [11], [39], a detection threshold $u_\mathrm{de}^\mathrm{in}$ is determined for SR-SBL channel estimation algorithms for single-snapshot wideband MIMO measurements. Given the signal parameters, number of antennas, and array-layout as defined above, this detection threshold $u_\mathrm{de}^\mathrm{in}$ for a chosen false alarm probability of 10^{-2} is given as $-14.4\,\mathrm{dB}$. MPCs below $u_\mathrm{de}^\mathrm{in}$ are mostly miss detected and therefore barely utilized as measurements in the proposed algorithm. To support the detection and estimation of low SNR MPCs, the detection threshold can be relaxed. This will inevitably bring more false alarm measurements, but the proposed algorithm can efficiently filter them out even under low $\mathrm{SNR}_\mathrm{1m}^\mathrm{in}$ conditions as shown in the following experimental results. We performed 100 simulation runs for each $\mathrm{SNR}_\mathrm{1m}^\mathrm{in} \in \{-0.6, 2.4, 3.9, 5.4, 8.4, 13.4, 15.4, 18.4\}\,\mathrm{dB}$ with parameters: $d_\mathrm{max} = 17\,\mathrm{m}$, $\sigma_{\mathrm{fa}_\mathrm{ini}} = 0.5$, $\sigma_\mathrm{fa} = 0.15$, $\sigma_\mathrm{d} = 0.002\,\mathrm{m/s^2}$, $\sigma_\varphi = 0.17°/\mathrm{s}^2$, $\underline{\sigma}_{\mathrm{u}k,n} = 0.02\,u_{k,n-1}^\mathrm{MMSE}$, $\sigma_{\mathrm{v_d}} = 0.01\,\mathrm{m/s}$, $\sigma_{\mathrm{v}_\varphi} = 0.6°/\mathrm{s}$.[14] Note that the first four $\mathrm{SNR}_\mathrm{1m}^\mathrm{in}$ values represent extreme testing setups, where the true component SNRs (output) of some MPCs are even below or close to 0 dB SNR output.

Fully Synthetic Measurements

First, we present the simulation results using fully synthetic measurements without involving the snapshot-based channel estimator. In each simulation run, MPC-oriented measurements were generated by adding Gaussian noises to the true MPC parameters, where the noise variances were state-dependent and computed as in Section 3.3. In addition, false alarm measurements were generated with increasing FAR $\mu_{\mathrm{fa}n}$ from 1.5 to 3. More specifically, the distances and AoAs of false alarm measurements were drawn from uniform distributions in the validation region, and the norm amplitudes were generated with Rayleigh distribution with squared scale parameter 1/2 using a detection threshold of $u_\mathrm{de}^\mathrm{in} = -20\,\mathrm{dB}$.

Fig. 2 shows the results of an exemplary simulation run given $\mathrm{SNR}_\mathrm{1m}^\mathrm{in} = 5.4\,\mathrm{dB}$. It is seen that the proposed algorithm exhibits high detection and estimation accuracy for medium and high SNR MPCs. The "weakest" MPC—with component SNR below the detection threshold of $-20\,\mathrm{dB}$—is stably detected shortly after the beginning although the related measurements are mostly miss detected in the SR-SBL. In addition, the proposed algorithm excellently copes with intersecting MPCs. Fig. 3 further presents the MOSPA errors and the mean estimates of the NoM and the FAR given $\mathrm{SNR}_\mathrm{1m}^\mathrm{in} = \{5.4, 13.4, 18.4\}\,\mathrm{dB}$. Given medium and high $\mathrm{SNR}_\mathrm{1m}^\mathrm{in}$ values, the NoM is accurately estimated and

[14] The heuristic approach to scale the standard deviation $\underline{\sigma}_{\mathrm{u}k,n}$ by the MMSE estimates $u_{k,n-1}^\mathrm{MMSE}$ was chosen since the range of normalized amplitude values tends to be very large.

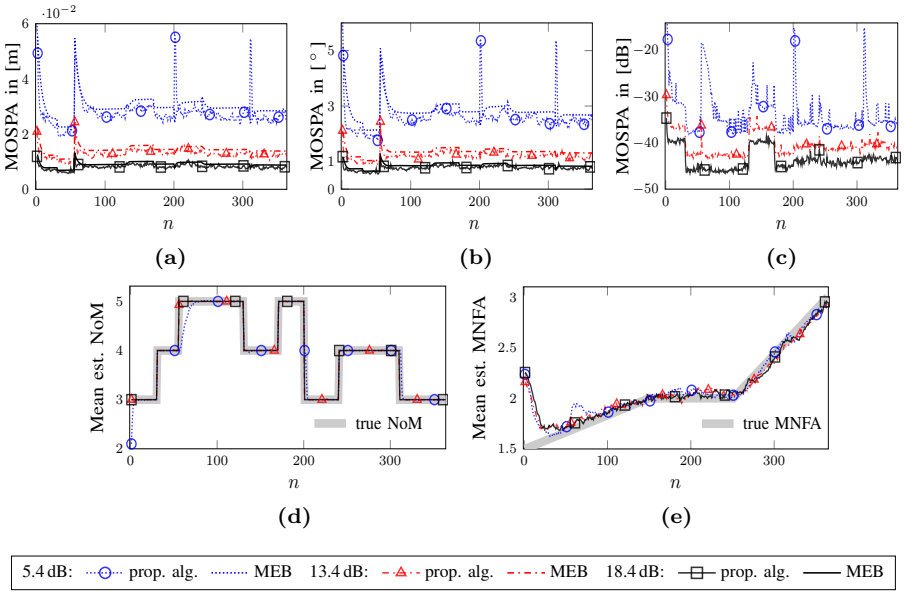

Figure 3: Results for fully synthetic measurements with the proposed algorithm (prop. alg.) given $\mathrm{SNR}_{1\mathrm{m}}^{\mathrm{in}} = \{5.4, 13.4, 18.4\}$ dB. MOSPA errors of the estimated (a) distances, (b) AoAs, and (c) input component SNRs. Mean estimates of the NoM (d) and the FAR (e).

the MOSPA errors attain the MEBs. For distance, AoA and component SNR, the MOSPA errors are mostly below 2 cm, 2° and −35 dB, respectively. Given $\mathrm{SNR}_{1\mathrm{m}}^{\mathrm{in}} = 5.4$ dB, the MOSPA errors remain on the MEB-levels mostly, despite a few peaks due to the underestimated NoM. Furthermore, the FAR is accurately estimated for all conditions.

Synthetic Radio Measurements

Next, we show the overall performance of the proposed two-stage algorithm by involving the snapshot-based channel estimator. In each simulation run, radio measurements were synthesized by applying true MPC parameters to the radio signal model (2) with given $\mathrm{SNR}_{1\mathrm{m}}^{\mathrm{in}}$. The measurements $\boldsymbol{z}_{m,n}$ at each time n were provided by a snapshot-based SR-SBL channel estimator in line with the implementation in [30]. We relaxed the detection threshold to $u_{\mathrm{de}}^{\mathrm{in}} = -18$ dB for $\mathrm{SNR}_{1\mathrm{m}}^{\mathrm{in}}$ values above 5 dB and $u_{\mathrm{de}}^{\mathrm{in}} = -20$ dB otherwise. For comparison, we implemented the KEST algorithm according to [19] and [27] which performs detection of MPCs and sequential estimation of their distances, AoAs and amplitudes. For NoM estimation in the KEST algorithm, the penalty factor

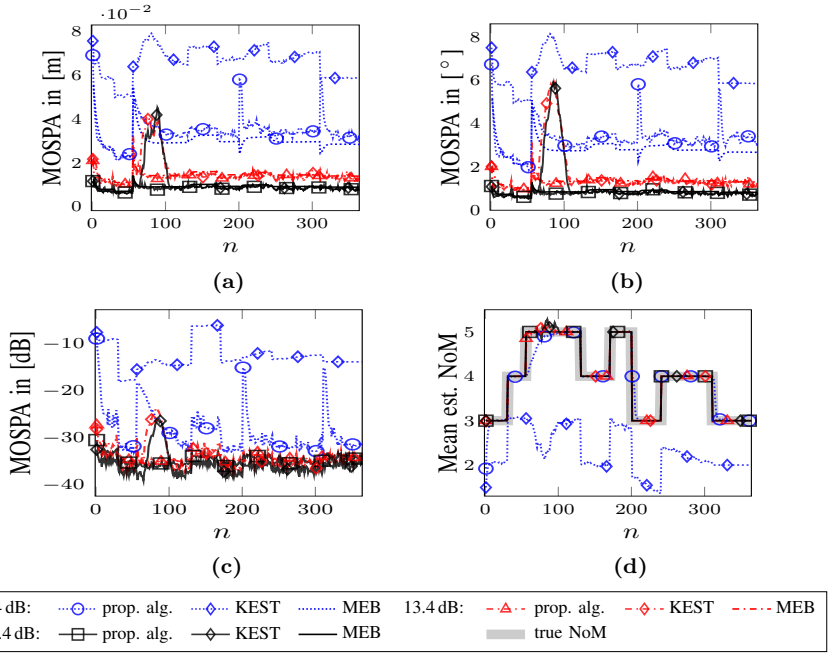

Figure 4: Results for synthetic radio measurements given $\mathrm{SNR}_{1\mathrm{m}}^{\mathrm{in}} = \{5.4, 13.4, 18.4\}$ dB. MOSPA errors of the estimated (a) distances, (b) AoAs, and (c) input component SNRs. Mean estimates of the NoM (d).

for a NoM change was set to $p_{\mathrm{chg}} = 0.1$, and the penalty p_{ord} for a higher NoM was chosen according to the MDL principle [19], [27].

For comparison between the proposed algorithm and the KEST algorithm of an exemplary simulation run, the reader is referred to Appendix E in [42]. Fig. 4 shows the MOSPA errors, MEBs and the mean estimate of the NoM for each $\mathrm{SNR}_{1\mathrm{m}}^{\mathrm{in}} \in \{5.4, 13.4, 18.4\}$ dB. The peaks of MOSPA errors indicate the NoM estimation errors which mostly happen when there is MPC birth or death. For medium and high $\mathrm{SNR}_{1\mathrm{m}}^{\mathrm{in}}$, it shows that the MOSPA errors of the proposed algorithm are mostly below 2 cm, 2° and −35 dB respectively for distance, AoA and input component SNR. The KEST algorithm shows comparable results except for the high error peaks around the intersecting MPCs at time $n = 83$. At low SNR, the MOSPA errors versus time n of the proposed algorithm are slightly above the MEBs since the "weakest" MPCs—with component SNRs well below the relaxed detection thresholds—are occasionally not detected, however, the KEST algorithm has much larger MOSPA errors, since it almost never detects these MPCs.

Finally, Fig. 5 shows component SNRs of the MPCs, the mean cardinality

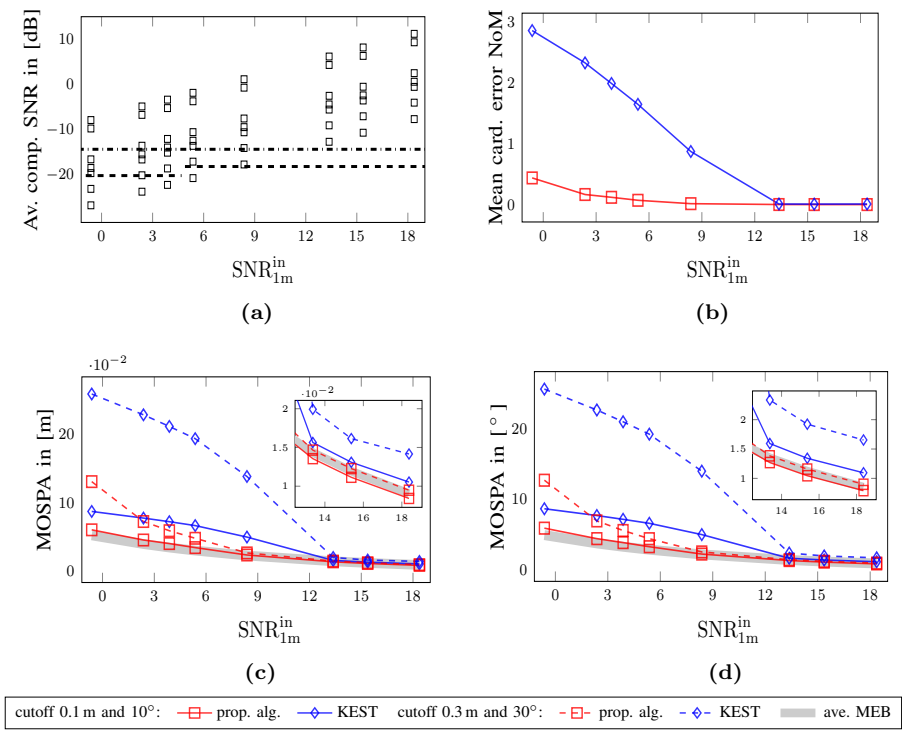

Figure 5: Results for synthetic radio measurements: The average (averaged over all time steps) (a) true input component SNRs of 7 MPCs, (b) mean cardinality error of the NoM, and (c) and (d) MOSPA errors and MEBs. In (a), the dash-dotted line indicates the theoretical detection threshold of $-14.4\,\text{dB}$, and the dashed lines indicate the relaxed detection thresholds of $-20\,\text{dB}$ and $-18\,\text{dB}$, respectively.

error [50] in the NoM, and MOSPA errors averaged over all time steps versus SNR ($\text{SNR}^{\text{in}}_{\text{1m}} \in \{-0.6, 2.4, 3.9, 5.4, 8.4, 13.4, 15.4, 18.4\}\,\text{dB}$). Fig. 5a shows that quite a few of the MPCs have component SNRs that are below the relaxed detection thresholds (some even far below the theoretical threshold) for the first five $\text{SNR}^{\text{in}}_{\text{1m}}$ values. These MPCs are mostly miss detected by the KEST algorithm, leading to a much higher mean cardinality error [50] as shown in Fig. 5b and therefore also to much higher MOSPA errors, as shown in Fig. 5c and Fig. 5d, than that of the proposed algorithm. By setting the cutoff parameters to larger values, i.e., 0.3 m and 30°, the mean cardinality error and MOSPA errors are better visualized. At high $\text{SNR}^{\text{in}}_{\text{1m}}$ values both algorithms mostly detected all MPCs. However, the proposed algorithm still outperforms the KEST algorithm since its MOSPA errors are lower when MPCs are inter-

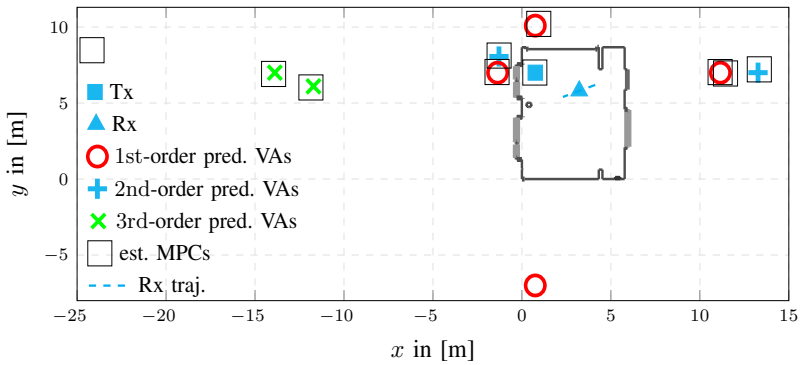

Figure 6: Floor plan of the measurement environment and the results of the proposed algorithm using real radio measurements of *setup*-2 (1 GHz bandwidth, 5×5 array) at time $n = 50$. For each of the 10 detected MPCs, the estimated state is transformed into a two-dim. coordinate and associated with a geometrically calculated VA.

secting. In summary, the proposed algorithm outperforms the KEST algorithm in all testing conditions and attains the MEBs for $\mathrm{SNR}_{1\mathrm{m}}^{\mathrm{in}}$ above 5 dB. A study of the runtimes for both algorithms can be found in Appendix E in [42]. For instance, the runtimes per time step (for MATLAB implementations) of both algorithms for $\mathrm{SNR}_{1\mathrm{m}}^{\mathrm{in}} = 18.4\,\mathrm{dB}$, obtained by averaging over all simulation runs and time steps, are both approximately 2 s / step.

7.3 Performance for Real UWB Radio Measurements

For further validation of the proposed algorithm, we use real radio measurements collected in a seminar room at TU Graz, Austria. The floor plan is depicted in Fig. 6, including the positions of the static Tx and a few mirror images of the Tx, i.e., VAs, which model the MPCs due to specular reflections. More details about the measurement environment and VA calculations can be found in [8], [51], [52]. On the Tx side, a dipole-like antenna with an approximately uniform radiation pattern in the azimuth plane and zeros in the floor and ceiling directions was used. At each Rx position, a same antenna was mounted on a plotter and moved yielding a virtual uniform rectangular array with an inter-element spacing of 2 cm. The UWB signals are measured at 100 Rx positions along a 2 m trajectory using an M-sequence correlative channel sounder with frequency range 3.1–10.6 GHz. We selected a subband with bandwidth $B = 1/T_{\mathrm{p}}$ using filtering with a root-raised-cosine pulse with a roll-off factor of 0.6 and pulse duration T_{p} at center frequency of $f_{\mathrm{c}} = 6\,\mathrm{GHz}$. The following two measurement setups are used: (i) *setup*-1: $T_{\mathrm{p}} = 2\,\mathrm{ns}$, $B = 0.5\,\mathrm{GHz}$, $N_{\mathrm{s}} = 94$, 3×3 array, $\mathrm{SNR}_{1\mathrm{m}}^{\mathrm{in}} = 0.7\,\mathrm{dB}$, $u_{\mathrm{de}}^{\mathrm{in}} = -16\,\mathrm{dB}$; (ii) *setup*-2: $T_{\mathrm{p}} = 1\,\mathrm{ns}$, $B = 1\,\mathrm{GHz}$, $N_{\mathrm{s}} = 187$, 5×5 array, $\mathrm{SNR}_{1\mathrm{m}}^{\mathrm{in}} = -6.7\,\mathrm{dB}$, $u_{\mathrm{de}}^{\mathrm{in}} = -20\,\mathrm{dB}$. Since no significant

AWGN was observed from the filtered signal, artificial AWGN generated with $\mathrm{SNR}_{1\mathrm{m}}$ was added. The simulation parameters are as follows: $d_{\max} = 30\,\mathrm{m}$, $\sigma_{\mathrm{d}} = 0.03\,\mathrm{m/s^2}$, $\sigma_{\varphi} = 1^\circ/\mathrm{s}^2$, $\underline{\sigma}_{\mathrm{u}k,n} = 0.1\,u^{\mathrm{MMSE}}_{k,n-1}$, $\sigma_{\mathrm{fa}} = 1$, $\sigma_{\mathrm{v_d}} = 0.1\,\mathrm{m/s}$, $\sigma_{\mathrm{v}_\varphi} = 6^\circ/\mathrm{s}$.

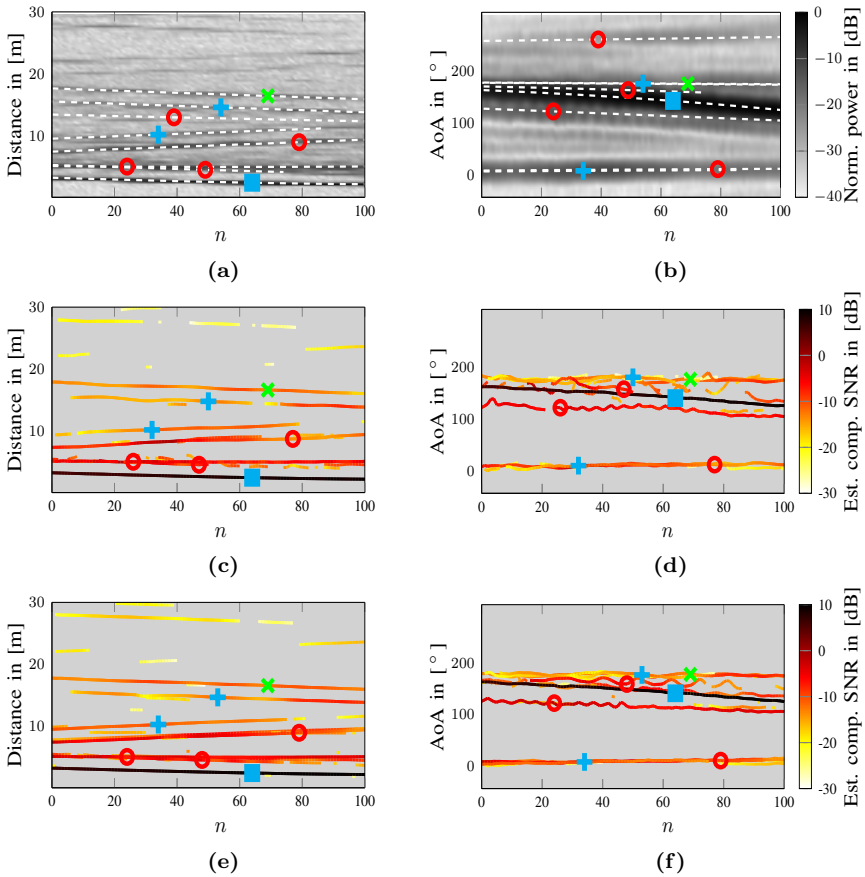

Figure 7: Results for real radio measurements. (a) and (b) depict the delay and angular power spectra versus time for *setup*-2. Corresponding to the distinct peaks and their variations in the spectra, a few exemplary distance and AoA paths (white dashed lines) are calculated with geometrically expected VAs, of which the orders are highlighted with markers listed in Fig. 6. The distance and AoA estimates of the detected MPCs are shown for *setup*-1 in (c) and (d), and for *setup*-2 in (e) and (f), among which the estimates associated with the geometrically calculated paths in (a) and (c) are highlighted with markers.

Fig. 7 shows the estimated delays and AoAs of the detected MPCs for *setup*-1 and *setup*-2. The backgrounds of Fig. 7a and Fig. 7b are the delay and angular power spectra versus time respectively for *setup*-2, where the peaks and variations representing individual MPC paths are readily visible in delay domain with good resolution capability of UWB signals, but hardly resolved in angular domain with limited array aperture. As can be observed, some distinct peaks align with the MPC paths predicted with up to 3rd-order geometrically expected VAs, and related to the estimated MPC paths highlighted with markers in Fig. 7c and Fig. 7d for *setup*-1 and in Fig. 7e and Fig. 7f for *setup*-2. The intersecting 1st-order MPCs and a few short-lived MPCs around 5 m are nearby in both delay and angular domains. They are better resolved for *setup*-2 with larger signal bandwidth and array size, however oscillation on the estimates still exist especially in the angular domain as for *setup*-1. Fig. 6 zooms into the performance of a single snapshot for *setup*-2, where the MMSE estimates of the detected MPC states at time $n = 50$ after being transformed into two-dimensional coordinates are shown. Within the 10 detected MPCs, the LoS component and MPCs related to the three 1st-order VAs w.r.t. surrounding walls are accurately estimated. Most of the other detected MPCs are also well explained by some higher order VAs (up to order five). However, due to imperfect antenna-calibration leading to time-dispersive system response, "ghost" components are sometimes detected alongside significant MPCs. The estimated MPCs associated with the 2nd and the upper 3rd-order VAs are related to the complex room structure in the left-upper corner. Note that the lower wall has high attenuation coefficient and therefore no related MPCs are detected (as for example the MPC related to the 1st-order VA of the lower wall which has parameters around 14 m and 270°). The estimated FARs for both measurement setups converge rapidly and remain around one over time. The small and stable values can be explained by the high detection threshold $u_{\mathrm{de}}^{\mathrm{in}}$ used in the SBL channel estimator and the static measurement scenario. More details can be found in Appendix E in [42]. The proposed algorithm is capable of detecting MPCs and estimating their parameters that very well resemble the geometry, and capturing their dynamic behaviors related to the surrounding environment.

8 Conclusions

We proposed a BP-based algorithm for sequential detection and estimation of MPC parameters based on radio signals, which adopts a two-stage structure combining a snapshot-based SR-SBL channel estimator with a BP-based sequential detection and estimation algorithm. Using amplitude information and the augmentation of PMPC states with a binary existence variable enable the reliable detection of "weak" MPCs with very low component SNRs. Simula-

tion results using synthetic measurements show that the algorithm excellently copes with a high number of false alarm measurements and intersecting MPCs with parameters nearby in the dispersion space. It is capable of estimating the parameters of MPCs on posterior-CRLB-levels even for low SNR MPCs. We have shown that the performance of the proposed algorithm compares well to existing state-of-the-art algorithms for high SNR MPCs, but it significantly outperforms them for medium and low SNR MPCs. The results using real radio measurements show that the algorithm demonstrates excellent performance in challenging indoor-environments by detecting many geometry-related MPCs up to reflection-order five and estimating their dispersion parameters with high accuracy. Possible directions for future research include extending the proposed algorithm to a more general inhomogeneous false alarm intensity [53] coping with false alarms resulting from model mismatches in the radio signal such as DMC or incorporating correlations between measurements [54].

9 Acknowledgment

The authors would like to thank Dr. Florian Meyer and Prof. Bernard H. Fleury for carefully reading the manuscript and insightful comments.

This work was supported in part by the Swedish Research Council (VR), in part by the Strategic Research Area Excellence Center at Linköping–Lund in Information Technology (ELLIIT), in part by the Christian Doppler Research Association, and in part by the TU Graz.

Appendix

We provide derivations of the joint prior PDF and the joint likelihood function in Section A and Section B respectively, which lead to the factorized expressions of the joint posterior PDF (11) and the pseudo likelihood functions (12) and (13) in Section C. In Section D, we derive the squared scale parameter of the truncated Rician PDF in (9).

A Joint Prior PDF

Before presenting derivations, we first define a few sets as follows: $\mathcal{D}_{\boldsymbol{a}_n,\underline{\boldsymbol{r}}_n} \triangleq \{k \in \{1,\ldots,K_{n-1}\} : \underline{r}_{k,n} = 1, a_{k,n} \neq 0\}$ denotes the existing legacy PMPCs set, and $\mathcal{N}_{\overline{\boldsymbol{r}}_n} \triangleq \{m \in \{1,\ldots,M_n\} : \overline{r}_{m,n} = 1, b_{m,n} = 0\}$ denotes the existing new PMPCs set. Correspondingly, the sets of non-existing legacy PMPCs are given by $\overline{\mathcal{D}}_{\boldsymbol{a}_n,\underline{\boldsymbol{r}}_n} \triangleq \{1,\ldots,K_{n-1}\} \setminus \mathcal{D}_{\boldsymbol{a}_n,\underline{\boldsymbol{r}}_n}$, and the sets of non-existing new PMPCs are given as $\overline{\mathcal{N}}_{\overline{\boldsymbol{r}}_n} \triangleq \{1,\ldots,M_n\} \setminus \mathcal{N}_{\overline{\boldsymbol{r}}_n}$. Hence, the number of

false alarm measurements can be represented with the sets as $k_{\mathrm{fa}n} = M_n - |\mathcal{D}_{\boldsymbol{a}_n,\underline{\boldsymbol{r}}_n}| - |\mathcal{N}_{\overline{\boldsymbol{r}}_n}|$, and the number of PMPCs states is given as $K_{n-1} + M_n = |\mathcal{D}_{\boldsymbol{a}_n,\underline{\boldsymbol{r}}_n}| + |\overline{\mathcal{D}}_{\boldsymbol{a}_n,\underline{\boldsymbol{r}}_n}| + |\mathcal{N}_{\overline{\boldsymbol{r}}_n}| + |\overline{\mathcal{N}}_{\overline{\boldsymbol{r}}_n}|$.

Assuming that the new PMPCs states $\overline{\mathbf{y}}_n$ and the PMPC-oriented association variables $\mathbf{a}_n$ are conditionally independent given the legacy PMPCs state $\underline{\mathbf{y}}_n$, the joint prior PDF of $\underline{\mathbf{y}}_{1:n}$, $\overline{\mathbf{y}}_{1:n}$, $\mathbf{a}_{1:n}$, $\mathbf{b}_{1:n}$, $\mathrm{fa}_{1:n}$, and the number of the measurements $\mathbf{m}_{1:n}$ factorizes as

$$
\begin{aligned}
&f(\boldsymbol{y}_{1:n}, \boldsymbol{a}_{1:n}, \boldsymbol{b}_{1:n}, \boldsymbol{\mu}_{\mathrm{fa}1:n}, \boldsymbol{m}_{1:n}) \\
&\quad = f(\underline{\boldsymbol{y}}_{1:n}, \overline{\boldsymbol{y}}_{1:n}, \boldsymbol{a}_{1:n}, \boldsymbol{b}_{1:n}, \boldsymbol{\mu}_{\mathrm{fa}1:n}, \boldsymbol{m}_{1:n}) \\
&\quad = f(\mu_{\mathrm{fa}1}) f(\overline{\boldsymbol{x}}_1|\overline{\boldsymbol{r}}_1, M_1) p(\overline{\boldsymbol{r}}_1, \boldsymbol{a}_1, \boldsymbol{b}_1, M_1|\mu_{\mathrm{fa}1}) \prod_{n'=2}^{n} f(\mu_{\mathrm{fa}n'}|\mu_{\mathrm{fa}n'-1}) \\
&\qquad \times \left(\prod_{k=1}^{K_{n'-1}} f(\underline{\boldsymbol{y}}_{k,n'}|\boldsymbol{y}_{k,n'-1}) \right) f(\overline{\boldsymbol{x}}_{n'}|\overline{\boldsymbol{r}}_{n'}, M_{n'}) p(\overline{\boldsymbol{r}}_{n'}, \boldsymbol{a}_{n'}, \boldsymbol{b}_{n'}, M_{n'}|\mu_{\mathrm{fa}n'}, \underline{\boldsymbol{y}}_{n'})
\end{aligned}
\tag{42}
$$

where $p(\overline{\boldsymbol{r}}_1, \boldsymbol{a}_1, \boldsymbol{b}_1, M_1|\mu_{\mathrm{fa}1}, \underline{\boldsymbol{y}}_1) = p(\overline{\boldsymbol{r}}_1, \boldsymbol{a}_1, \boldsymbol{b}_1, M_1|\mu_{\mathrm{fa}1})$ since no legacy PMPCs exist at time $n = 1$. We determine the prior PDF of new PMPCs $f(\overline{\boldsymbol{x}}_n|\overline{\boldsymbol{r}}_n, M_n)$ and the joint conditional prior PMF $p(\overline{\boldsymbol{r}}_n, \boldsymbol{a}_n, \boldsymbol{b}_n, M_n|\mu_{\mathrm{fa}n}, \underline{\boldsymbol{y}}_n)$ as follows.

Before the current measurements are observed, the number of measurements M_n is random. The Poisson PMF of the number of existing new PMPCs evaluated at $|\mathcal{N}_{\overline{\boldsymbol{r}}_n}|$ is given by $p(|\mathcal{N}_{\overline{\boldsymbol{r}}_n}|) = \mu_{\mathrm{n}}^{|\mathcal{N}_{\overline{\boldsymbol{r}}_n}|}/|\mathcal{N}_{\overline{\boldsymbol{r}}_n}|! \mathrm{e}^{\mu_{\mathrm{n}}}$. The prior PDF of the new PMPC state $\overline{\mathbf{x}}_n$ conditioned on $\overline{\mathbf{r}}_n$ and M_n is expressed as

$$
f(\overline{\boldsymbol{x}}_n|\overline{\boldsymbol{r}}_n, M_n) = \prod_{m \in \mathcal{N}_{\overline{\boldsymbol{r}}_n}} f_{\mathrm{n}}(\overline{\boldsymbol{x}}_{m,n}) \prod_{m' \in \overline{\mathcal{N}}_{\overline{\boldsymbol{r}}_n}} f_{\mathrm{D}}(\overline{\boldsymbol{x}}_{m',n}). \tag{43}
$$

The PMF for the number of false alarm measurements is given by $p(k_{\mathrm{fa}n}) = \mu_{\mathrm{fa}n}^{k_{\mathrm{fa}n}}/k_{\mathrm{fa}n}! \mathrm{e}^{\mu_{\mathrm{fa}n}}$. The joint conditional prior PMF of the binary existence variables of new PMPCs $\overline{\mathbf{r}}_n \triangleq [\overline{\mathsf{r}}_{1,n} \cdots \overline{\mathsf{r}}_{\mathsf{M}_n,n}]$, the DA vectors $\mathbf{a}_n$ and $\mathbf{b}_n$ and the number of the measurements M_n conditioned on fa_n and $\underline{\mathbf{y}}_n$ is obtained as

[8], [28], [29]

$$
\begin{aligned}
&p(\overline{\boldsymbol{r}}_n, \boldsymbol{a}_n, \boldsymbol{b}_n, M_n | \mu_{\mathrm{fa}n}, \underline{\boldsymbol{y}}_n) \\
&= \chi_{\overline{\boldsymbol{r}}_n, \boldsymbol{a}_n, M_n} \left(\prod_{m \in \mathcal{N}_{\overline{\boldsymbol{r}}_n}} \Gamma_{\boldsymbol{a}_n}(\overline{r}_{m,n}) \right) \left(\prod_{k \in \mathcal{D}_{\boldsymbol{a}_n, \underline{\boldsymbol{r}}_n}} p_{\mathrm{d}}(\underline{u}_{k,n}) \right) \\
&\quad \times \Psi(\boldsymbol{a}_n, \boldsymbol{b}_n) \left(\prod_{k' \in \overline{\mathcal{D}}_{\boldsymbol{a}_n, \underline{\boldsymbol{r}}_n}} \left(1(a_{k',n}) - \underline{r}_{k',n} p_{\mathrm{d}}(\underline{u}_{k',n}) \right) \right).
\end{aligned} \tag{44}
$$

The normalization constant $\chi_{\overline{\boldsymbol{r}}_n, \boldsymbol{a}_n, M_n}$ combining the two Poisson PMFs above is given by

$$
\chi_{\overline{\boldsymbol{r}}_n, \boldsymbol{a}_n, M_n} = \left(\mathrm{e}^{-\mu_{\mathrm{n}}} / M_n! \right) \left((\mu_{\mathrm{n}} / \mu_{\mathrm{fa}n})^{|\mathcal{N}_{\overline{\boldsymbol{r}}_n}|} \mu_{\mathrm{fa}n}^{-|\mathcal{D}_{\boldsymbol{a}_n, \underline{\boldsymbol{r}}_n}|} \right) \left(\mathrm{e}^{-\mu_{\mathrm{fa}n}} \mu_{\mathrm{fa}n}^{M_n} \right) \tag{45}
$$

where the first part (the terms in the first brackets) is fixed after observing the current measurements given the assumption that the mean number of newly detected PMPCs $_{\mathrm{n}}$ is a known constant. The second part can be merged with factors in the sets $\mathcal{N}_{\overline{\boldsymbol{r}}_n}$ and $\mathcal{D}_{\boldsymbol{a}_n, \underline{\boldsymbol{r}}_n}$, respectively. The third part equals to $n(\mu_{\mathrm{fa}n})^{(K_{n-1}+M_n)}$ where $n(\mu_{\mathrm{fa}n}) \triangleq (\mathrm{e}^{-\mu_{\mathrm{fa}n}} \mu_{\mathrm{fa}n}^{M_n})^{1/(K_{n-1}+M_n)}$ is the FAR-related normalization constant. The two exclusion functions $\Psi(\boldsymbol{a}_n, \boldsymbol{b}_n)$ and $\Gamma_{\boldsymbol{a}_n}(\overline{r}_{m,n}) = 0$ ensure that $p(\overline{\boldsymbol{r}}_n, \boldsymbol{a}_n, \boldsymbol{b}_n, M_n | \mu_{\mathrm{fa}n}, \underline{\boldsymbol{y}}_n) \neq 0$ if and only if a measurement is generated by only one PMPC (either a legacy or a new one), and a PMPC generates no more than one measurement.

The product of the prior PDF of new PMPCs (43) and the joint conditional prior PMF (44) after merging factors can be written up to the normalization constant as

$$
\begin{aligned}
&p(\overline{\boldsymbol{r}}_n, \boldsymbol{a}_n, \boldsymbol{b}_n, M_n | \mu_{\mathrm{fa}n}, \underline{\boldsymbol{y}}_n) f(\overline{\boldsymbol{x}}_n | \overline{\boldsymbol{r}}_n, M_n) \\
&\propto \left(\psi(\boldsymbol{a}_n, \boldsymbol{b}_n) \prod_{k \in \mathcal{D}_{\boldsymbol{a}_n, \underline{\boldsymbol{r}}_n}} \frac{n(\mu_{\mathrm{fa}n}) p_{\mathrm{d}}(\underline{u}_{k,n})}{\mu_{\mathrm{fa}n}} \right. \\
&\quad \left. \times \prod_{k' \in \overline{\mathcal{D}}_{\boldsymbol{a}_n, \underline{\boldsymbol{r}}_n}} n(\mu_{\mathrm{fa}n}) \left(\bar{1}(a_{k',n}) - \underline{r}_{k',n} p_{\mathrm{d}}(\underline{u}_{k',n}) \right) \right) \\
&\quad \times \left(\prod_{m \in \mathcal{N}_{\overline{\boldsymbol{r}}_n}} \frac{n(\mu_{\mathrm{fa}n}) \mu_{\mathrm{n}} f_{\mathrm{n}}(\overline{\boldsymbol{x}}_{m,n})}{\mu_{\mathrm{fa}n}} \Gamma_{\boldsymbol{a}_n}(\overline{r}_{m,n}) \prod_{m' \in \overline{\mathcal{N}}_{\overline{\boldsymbol{r}}_n}} n(\mu_{\mathrm{fa}n}) f_{\mathrm{D}}(\overline{\boldsymbol{x}}_{m',n}) \right).
\end{aligned} \tag{46}
$$

With some simple manipulations using the definitions of exclusion functions $\Psi(\boldsymbol{a}_n, \boldsymbol{b}_n)$ and $\Gamma_{\boldsymbol{a}_n}(\overline{r}_{m,n})$ (see Section 3.5), Eq. (46) can be rewritten as the product of factors related to the legacy PMPCs and to the new PMPCs, respectively, i.e.,

$$\begin{aligned} &p(\overline{\boldsymbol{r}}_n, \boldsymbol{a}_n, \boldsymbol{b}_n, M_n | \mu_{\mathrm{fa}n}, \underline{\boldsymbol{y}}_n) f(\overline{\boldsymbol{x}}_n | \overline{\boldsymbol{r}}_n, M_n) \\ &\propto \left(\prod_{k=1}^{K_{n-1}} g_1(\underline{\boldsymbol{y}}_{k,n}, a_{k,n}, \mu_{\mathrm{fa}n}; M_n) \prod_{m=1}^{M_n} \psi(a_{k,n}, b_{m,n}) \right) \\ &\quad \times \left(\prod_{m'=1}^{M_n} h_1(\overline{\boldsymbol{y}}_{m',n}, b_{m',n}, \mu_{\mathrm{fa}n}; M_n) \right) \end{aligned} \tag{47}$$

with $g_1(\underline{\boldsymbol{y}}_{k,n}, a_{k,n}, \mu_{\mathrm{fa}n}; M_n) = g_1(\underline{\boldsymbol{x}}_{k,n}, \underline{r}_{k,n}, a_{k,n}, \mu_{\mathrm{fa}n}; M_n)$ given by

$$g_1(\underline{\boldsymbol{x}}_{k,n}, \underline{r}_{k,n} = 1, a_{k,n}, \mu_{\mathrm{fa}n}; M_n) \triangleq \begin{cases} \dfrac{n(\mu_{\mathrm{fa}n}) p_{\mathrm{d}}(\underline{u}_{k,n})}{\mu_{\mathrm{fa}n}}, & a_{k,n} = m \\ n(\mu_{\mathrm{fa}n})\big(1 - p_{\mathrm{d}}(\underline{u}_{k,n})\big), & a_{k,n} = 0 \end{cases} \tag{48}$$

and $g_1(\underline{\boldsymbol{x}}_{k,n}, \underline{r}_{k,n} = 0, a_{k,n}, \mu_{\mathrm{fa}n}; M_n) \triangleq \bar{1}(a_{k,n}) n(\mu_{\mathrm{fa}n})$, and $h_1(\overline{\boldsymbol{y}}_{m,n}, b_{m,n}, \mu_{\mathrm{fa}n}; M_n) = h_1(\overline{\boldsymbol{x}}_{m,n}, \overline{r}_{m,n}, b_{m,n}, \mu_{\mathrm{fa}n}; M_n)$ is given by

$$h_1(\overline{\boldsymbol{x}}_{m,n}, \overline{r}_{m,n} = 1, b_{m,n}, \mu_{\mathrm{fa}n}; M_n) \triangleq \begin{cases} 0, & b_{m,n} = k \\ \dfrac{n(\mu_{\mathrm{fa}n}) \mu_{\mathrm{n}} f_{\mathrm{n}}(\overline{\boldsymbol{x}}_{m,n})}{\mu_{\mathrm{fa}n}}, & b_{m,n} = 0 \end{cases} \tag{49}$$

and $h_1(\overline{\boldsymbol{x}}_{m,n}, \overline{r}_{m,n} = 0, b_{m,n}, \mu_{\mathrm{fa}n}; M_n) \triangleq n(\mu_{\mathrm{fa}n})$.

Finally, by inserting (47) into (42), the joint prior PDF can be rewritten as

$$\begin{aligned} &f(\underline{\boldsymbol{y}}_{1:n}, \overline{\boldsymbol{y}}_{1:n}, \boldsymbol{a}_{1:n}, \boldsymbol{b}_{1:n}, \boldsymbol{\mu}_{\mathrm{fa}1:n}, \boldsymbol{m}_{1:n}) \\ &\propto f(\mu_{\mathrm{fa}1}) \prod_{l=1}^{M_1} h_1(\overline{\boldsymbol{y}}_{l,1}, b_{l,1}, \mu_{\mathrm{fa}1}; M_1) \prod_{n'=2}^{n} f(\mu_{\mathrm{fa}n'} | \mu_{\mathrm{fa}n'-1}) \\ &\quad \times \left(\prod_{k'=1}^{K_{n'-1}} f(\underline{\boldsymbol{y}}_{k',n'} | \boldsymbol{y}_{k',n'-1}) \right) \left(\prod_{k=1}^{K_{n'-1}} g_1(\underline{\boldsymbol{y}}_{k,n'}, a_{k,n'}, \mu_{\mathrm{fa}n'}; M_{n'}) \right. \\ &\quad \left. \times \prod_{m=1}^{M_{n'}} \psi(a_{k,n'}, b_{m,n'}) \right) \left(\prod_{m'=1}^{M_{n'}} h_1(\overline{\boldsymbol{y}}_{m',n'}, b_{m',n'}, \mu_{\mathrm{fa}n'}; M_{n'}) \right). \end{aligned} \tag{50}$$

B Joint Likelihood Function

Assume that the measurements $\mathbf{z}_n$ are independent across n, the conditional PDF of $\mathbf{z}_{1:n}$ given $\underline{\mathbf{y}}_{1:n}$, $\overline{\mathbf{y}}_{1:n}$, $\mathbf{a}_{1:n}$, $\mathbf{b}_{1:n}$, and the number of measurements $\mathbf{m}_{1:n}$ is given by

$$f(\boldsymbol{z}_{1:n}|\underline{\boldsymbol{y}}_{1:n},\overline{\boldsymbol{y}}_{1:n},\boldsymbol{a}_{1:n},\boldsymbol{b}_{1:n},\boldsymbol{m}_{1:n}) = \prod_{n'=1}^{n} f(\boldsymbol{z}_{n'}|\underline{\boldsymbol{y}}_{n'},\overline{\boldsymbol{y}}_{n'},\boldsymbol{a}_{n'},\boldsymbol{b}_{n'},M_{n'}). \quad (51)$$

Note that $f(\boldsymbol{z}_1|\underline{\boldsymbol{y}}_1,\overline{\boldsymbol{y}}_1,\boldsymbol{a}_1,\boldsymbol{b}_1,M_1) = f(\boldsymbol{z}_1|\overline{\boldsymbol{y}}_1,\boldsymbol{a}_1,\boldsymbol{b}_1,M_1)$ since no legacy PMPCs exist at time $n=1$. The conditional PDF $f(\boldsymbol{z}_{m,n}|\boldsymbol{x}_{k,n})$ characterizing the statistical relation between the measurements $\mathbf{z}_{m,n}$ and the PMPC states $\mathbf{x}_{k,n}$ is a central element in the conditional PDF of the measurement vector $\mathbf{z}_n$ given $\underline{\mathbf{y}}_n$, $\overline{\mathbf{y}}_n$, $\mathbf{a}_n$, $\mathbf{b}_n$, and the number of the measurements M_n. Assuming that the measurements $\mathbf{z}_{m,n}$ are conditionally independent across m given $\underline{\mathbf{y}}_{k,n}$, $\overline{\mathbf{y}}_{m,n}$, $\mathsf{a}_{k,n}$, $\mathsf{b}_{m,n}$, and M_n [28], Eq. (51) factorizes as

$$\begin{aligned} &f(\boldsymbol{z}_{1:n}|\underline{\boldsymbol{y}}_{1:n},\overline{\boldsymbol{y}}_{1:n},\boldsymbol{a}_{1:n},\boldsymbol{b}_{1:n},\boldsymbol{m}_{1:n}) \\ &\quad = C(\boldsymbol{z}_1)\left(\prod_{m\in\mathcal{N}_{\overline{\boldsymbol{r}}_1}} \frac{f(\boldsymbol{z}_{m,1}|\overline{\boldsymbol{x}}_{m,1})}{f_{\mathrm{fa}}(\boldsymbol{z}_{m,1})}\right)\prod_{n'=2}^{n} C(\boldsymbol{z}_{n'}) \\ &\qquad \times \left(\prod_{k\in\mathcal{D}_{\boldsymbol{a}_{n'},\underline{\boldsymbol{r}}_{n'}}} \frac{f(\boldsymbol{z}_{a_{k,n'},n'}|\underline{\boldsymbol{x}}_{k,n'})}{f_{\mathrm{fa}}(\boldsymbol{z}_{a_{k,n'},n'})}\right)\left(\prod_{m\in\mathcal{N}_{\overline{\boldsymbol{r}}_{n'}}} \frac{f(\boldsymbol{z}_{m,n'}|\overline{\boldsymbol{x}}_{m,n'})}{f_{\mathrm{fa}}(\boldsymbol{z}_{m,n'})}\right), \end{aligned} \quad (52)$$

and the conditional PDF at each time $n \geq 2$ factorizes as [28]

$$\begin{aligned} &f(\boldsymbol{z}_n|\underline{\boldsymbol{y}}_n,\overline{\boldsymbol{y}}_n,\boldsymbol{a}_n,\boldsymbol{b}_n,M_n) \\ &\quad = C(\boldsymbol{z}_n)\left(\prod_{k\in\mathcal{D}_{\boldsymbol{a}_n,\underline{\boldsymbol{r}}_n}} \frac{f(\boldsymbol{z}_{a_{k,n},n}|\underline{\boldsymbol{x}}_{k,n})}{f_{\mathrm{fa}}(\boldsymbol{z}_{a_{k,n},n})}\right)\left(\prod_{m\in\mathcal{N}_{\overline{\boldsymbol{r}}_n}} \frac{f(\boldsymbol{z}_{m,n}|\overline{\boldsymbol{x}}_{m,n})}{f_{\mathrm{fa}}(\boldsymbol{z}_{m,n})}\right). \end{aligned} \quad (53)$$

Since the normalization factor $C(\boldsymbol{z}_n) = \prod_{m=1}^{M_n} f_{\mathrm{fa}}(\boldsymbol{z}_{m,n})$ depending on $\boldsymbol{z}_n$ and M_n is fixed after the current measurement $\boldsymbol{z}_n$ is observed, the likelihood function in (53) can be rewritten up to the normalization constant as

$$\begin{aligned} &f(\boldsymbol{z}_n|\underline{\boldsymbol{y}}_n,\overline{\boldsymbol{y}}_n,\boldsymbol{a}_n,\boldsymbol{b}_n,M_n) \\ &\quad \propto \left(\prod_{k=1}^{K_{n-1}} g_2(\underline{\boldsymbol{y}}_{k,n},a_{k,n};\boldsymbol{z}_n)\right)\left(\prod_{m=1}^{M_n} h_2(\overline{\boldsymbol{y}}_{m,n},b_{m,n};\boldsymbol{z}_n)\right) \end{aligned} \quad (54)$$

where the factor related to legacy PMPC states $g_2(\underline{\boldsymbol{y}}_{k,n}, a_{k,n}; \boldsymbol{z}_n) = g_2(\underline{\boldsymbol{x}}_{k,n}, \underline{r}_{k,n}, a_{k,n}; \boldsymbol{z}_n)$ is given by

$$g_2(\underline{\boldsymbol{x}}_{k,n}, \underline{r}_{k,n} = 1, a_{k,n}; \boldsymbol{z}_n) \triangleq \begin{cases} \dfrac{f(\boldsymbol{z}_{m,n}|\underline{\boldsymbol{x}}_{k,n})}{f_{\text{fa}}(\boldsymbol{z}_{m,n})}, & a_{k,n} = m \\ 1, & a_{k,n} = 0 \end{cases} \tag{55}$$

and $g_2(\underline{\boldsymbol{x}}_{k,n}, \underline{r}_{k,n} = 0, a_{k,n}; \boldsymbol{z}_n) \triangleq 1$. The factor related to new PMPC states $h_2(\overline{\boldsymbol{y}}_{m,n}, b_{m,n}; \boldsymbol{z}_n) = h_2(\overline{\boldsymbol{x}}_{m,n}, \overline{r}_{m,n}, b_{m,n}; \boldsymbol{z}_n)$ is given by

$$h_2(\overline{\boldsymbol{x}}_{m,n}, \overline{r}_{m,n} = 1, b_{m,n}; \boldsymbol{z}_n) \triangleq \begin{cases} 1, & b_{m,n} = k \\ \dfrac{f(\boldsymbol{z}_{m,n}|\overline{\boldsymbol{x}}_{m,n})}{f_{\text{fa}}(\boldsymbol{z}_{m,n})}, & b_{m,n} = 0 \end{cases} \tag{56}$$

and $h_2(\overline{\boldsymbol{x}}_{m,n}, \overline{r}_{m,n} = 0, b_{m,n}; \boldsymbol{z}_n) \triangleq 1$. Inserting (54) (55) and (56) into (51), the conditional PDF can be rewritten as the joint likelihood function

$$\begin{aligned} &f(\boldsymbol{z}_{1:n}|\underline{\boldsymbol{y}}_{1:n}, \overline{\boldsymbol{y}}_{1:n}, \boldsymbol{a}_{1:n}, \boldsymbol{b}_{1:n}, \boldsymbol{m}_{1:n}) \\ &\quad \propto \left(\prod_{m=1}^{M_1} h_2(\overline{\boldsymbol{x}}_{m,1}, \overline{r}_{m,1}, b_{m,1}; \boldsymbol{z}_1) \right) \prod_{n'=2}^{n} \left(\prod_{k=1}^{K_{n'-1}} g_2(\underline{\boldsymbol{x}}_{k,n'}, \underline{r}_{k,n'}, a_{k,n'}; \boldsymbol{z}_{n'}) \right) \\ &\quad \times \left(\prod_{m'=1}^{M_{n'}} h_2(\overline{\boldsymbol{x}}_{m',n'}, \overline{r}_{m',n'}, b_{m',n'}; \boldsymbol{z}_{n'}) \right). \end{aligned} \tag{57}$$

C Joint Posterior PDF

Finally, by substituting the joint prior PDF with (50) and the joint likelihood function with (57), the joint posterior PDF (10) can be rewritten as

$$
\begin{aligned}
&f(\boldsymbol{y}_{1:n}, \boldsymbol{a}_{1:n}, \boldsymbol{b}_{1:n}, \boldsymbol{\mu}_{\mathrm{fa}\,1:n}, \boldsymbol{m}_{1:n} | \boldsymbol{z}_{1:n}) \\
&\quad \propto f(\mu_{\mathrm{fa}\,1}) \left(\prod_{l=1}^{M_1} h_1(\overline{\boldsymbol{y}}_{l,1}, b_{l,1}, \mu_{\mathrm{fa}\,1}; M_1) h_2(\overline{\boldsymbol{y}}_{l,1}, b_{l,1}; \boldsymbol{z}_1) \right) \\
&\quad \times \prod_{n'=2}^{n} f(\mu_{\mathrm{fa}\,n'} | \mu_{\mathrm{fa}\,n'-1}) \left(\prod_{k'=1}^{K_{n'-1}} f(\underline{\boldsymbol{y}}_{k',n'} | \boldsymbol{y}_{k',n'-1}) \right) \\
&\quad \times \left(\prod_{k=1}^{K_{n'-1}} g_1(\underline{\boldsymbol{y}}_{k,n'}, a_{k,n'}, \mu_{\mathrm{fa}\,n'}; M_{n'}) g_2(\underline{\boldsymbol{y}}_{k,n'}, a_{k,n'}; \boldsymbol{z}_{n'}) \prod_{m=1}^{M_{n'}} \psi(a_{k,n'}, b_{m,n'}) \right) \\
&\quad \times \left(\prod_{m'=1}^{M_{n'}} h_1(\overline{\boldsymbol{y}}_{m',n'}, b_{m',n'}, \mu_{\mathrm{fa}\,n'}; M_{n'}) h_2(\overline{\boldsymbol{y}}_{m',n'}, b_{m',n'}; \boldsymbol{z}_{n'}) \right) . \qquad (58)
\end{aligned}
$$

The factors related to the legacy PMPCs and to the new PMPCs can be simplified as $g(\underline{\boldsymbol{y}}_{k,n}, a_{k,n}, \mu_{\mathrm{fa}\,n}; \boldsymbol{z}_n) \triangleq g_1(\underline{\boldsymbol{y}}_{k,n}, a_{k,n}, \mu_{\mathrm{fa}\,n}; M_n) g_2(\underline{\boldsymbol{y}}_{k,n}, a_{k,n}; \boldsymbol{z}_n)$ and $h(\overline{\boldsymbol{y}}_{m,n}, b_{m,n}, \mu_{\mathrm{fa}\,n}; \boldsymbol{z}_n) \triangleq h_1(\overline{\boldsymbol{y}}_{m,n}, b_{m,n}, \mu_{\mathrm{fa}\,n}; M_n) h_2(\overline{\boldsymbol{y}}_{m,n}, b_{m,n}; \boldsymbol{z}_n)$, respectively (see Fig. 1).

D Squared Scale Parameter of the Truncated Rician PDF

Here, we derive the squared scale parameter of the truncated Rician PDF in (9) in Section 3.3. We follow [46, Ch. 3.8] and approximate the squared scale parameter using the Fisher information which is sufficiently accurate for large amplitudes and large $N_{\mathrm{s}} H$.[15] For simplicity, we assume that the MPCs are well separated in dispersion space, so that their mutual correlations are negligible. We first determine the FIM for $\boldsymbol{\xi}_{l,n} = [\Re\{\tilde{\alpha}_{l,n}\}\ \Im\{\tilde{\alpha}_{l,n}\}\ \sigma^2]^{\mathrm{T}}$, where $\Re\{\tilde{\alpha}_{l,n}\}$ and $\Im\{\tilde{\alpha}_{l,n}\}$ denote the real and imaginary parts of the complex amplitudes $\tilde{\alpha}_{l,n}$, and then apply the chain rule [46] to get the FIM for $\tilde{u}_{l,n}$. According to

[15] Note that for unknown noise variance the distribution of the normalized amplitude measurement $z_{\mathrm{u}\,m,n}$ is not described by a Rician distribution anymore. More specifically, the statistic of two times the squared PMPC-oriented normalized amplitude measurements $2z^2_{\mathrm{u}\,m,n}$ is described by a non-central Fisher distribution [55], [56, Ch. 15.10.3]. For large $N_{\mathrm{s}} H$, the statistic of $2z^2_{\mathrm{u}\,m,n}$ can be well approximated by a non-central χ^2 distribution [45, Ch. 2.2] and therefore the statistic of the normalized amplitude measurement $z_{\mathrm{u}\,m,n}$ by a Rician distribution. However, the proof and the details are out-of-scope of this paper.

[46], the elements of the FIM for $\tilde{\boldsymbol{\xi}}_{l,n}$ are given by

$$[\boldsymbol{J}_{l,n}(\boldsymbol{\xi}_{l,n})]_{i,j} = 2\Re\left\{\frac{\partial\,\tilde{\alpha}_{l,n}\boldsymbol{s}^{\mathrm{H}}(\tilde{\boldsymbol{\theta}}_{l,n})}{\partial[\xi_{l,n}]_i}\boldsymbol{C}^{-1}\frac{\partial\boldsymbol{s}(\tilde{\boldsymbol{\theta}}_{l,n})\tilde{\alpha}_{l,n}}{\partial[\xi_{l,n}]_j}\right\} + \mathrm{tr}\left\{\boldsymbol{C}^{-1}\frac{\partial\boldsymbol{C}^{-1}}{\partial[\xi_{l,n}]_i}\boldsymbol{C}^{-1}\frac{\partial\boldsymbol{C}^{-1}}{\partial[\xi_{l,n}]_j}\right\} \tag{59}$$

where $i,j \in \{1,2,3\}$. After some straightforward calculations (59) can be rewritten as

$$\boldsymbol{J}_{l,n}(\boldsymbol{\xi}_{l,n}) = \mathrm{diag}\left\{\frac{2\|\boldsymbol{s}(\tilde{\boldsymbol{\theta}}_{l,n})\|^2}{\sigma^2}, \frac{2\|\boldsymbol{s}(\tilde{\boldsymbol{\theta}}_{l,n})\|^2}{\sigma^2}, \frac{N_{\mathrm{s}}H}{\sigma^4}\right\}. \tag{60}$$

The CRLB for $\tilde{u}_{l,n}$ is obtained by applying the chain rule, i.e.,

$$\sigma^2_{\mathrm{u}l,n} \triangleq J^{-1}_{\tilde{\mathrm{u}}l,n}(\tilde{u}_{l,n}) = \boldsymbol{t}^{\mathrm{H}}_{l,n}\boldsymbol{J}^{-1}_{l,n}(\boldsymbol{\xi}_{l,n})\boldsymbol{t}_{l,n} = \frac{1}{2} + \frac{\tilde{u}^2_{l,n}}{4N_{\mathrm{s}}H} \tag{61}$$

where the Jacobian $\boldsymbol{t}_{l,n}$ containing the partial derivatives is

$$\begin{aligned}\boldsymbol{t}_{l,n} &\triangleq \left[\frac{\partial\tilde{u}_{l,n}}{\partial\Re\{\tilde{\alpha}_{l,n}\}} \quad \frac{\partial\tilde{u}_{l,n}}{\partial\Im\{\tilde{\alpha}_{l,n}\}} \quad \frac{\partial\tilde{u}_{l,n}}{\partial\sigma^2}\right]^{\mathrm{T}} \\ &= \left[\frac{\Re\{\tilde{\alpha}_{l,n}\}\|\boldsymbol{s}(\tilde{\boldsymbol{\theta}}_{l,n})\|}{|\tilde{\alpha}_{l,n}|\,\sigma} \quad \frac{\Im\{\tilde{\alpha}_{l,n}\}\|\boldsymbol{s}(\tilde{\boldsymbol{\theta}}_{l,n})\|}{|\tilde{\alpha}_{l,n}|\,\sigma} \quad \frac{-|\tilde{\alpha}_{l,n}|\,\|\boldsymbol{s}(\tilde{\boldsymbol{\theta}}_{l,n})\|}{2\,\sigma^3}\right]^{\mathrm{T}}.\end{aligned} \tag{62}$$

Note that the second term $\frac{\tilde{u}^2_{l,n}}{4N_{\mathrm{s}}H}$ in (61) characterizes the effect of the noise variance estimation, which becomes significant for high component SNRs, and converges to zero for low component SNRs or a large $N_{\mathrm{s}}H$. Thus, for PMPC-oriented measurements the squared scale parameter of the truncated Rician PDF in (9) is given by (61) and for false alarm measurements the squared scale parameter of the Rayleigh PDF is given by 1/2.

References

[1] M. L. Jakobsen, T. Pedersen and B. H. Fleury, "Analysis of stochastic radio channels with temporal birth-death dynamics: A marked spatial point process perspective", *IEEE Trans. Antennas Propag.*, vol. 62, no. 7, pp. 3761–3775, 2014.

[2] J. Flordelis, X. Li, O. Edfors and F. Tufvesson, "Massive MIMO extensions to the COST 2100 channel model: Modeling and validation", *IEEE Trans. Wireless Commun.*, vol. 19, no. 1, pp. 380–394, 2020.

[3] F. Rusek, D. Persson, B. K. Lau, E. G. Larsson, T. L. Marzetta, O. Edfors and F. Tufvesson, "Scaling up MIMO: Opportunities and challenges with very large arrays", *IEEE Signal Process. Mag.*, vol. 30, no. 1, pp. 40–60, 2013.

[4] R. Di Taranto, S. Muppirisetty, R. Raulefs, D. Slock, T. Svensson and H. Wymeersch, "Location-aware communications for 5G networks: How location information can improve scalability, latency, and robustness of 5G", *IEEE Signal Process. Mag.*, vol. 31, no. 6, pp. 102–112, 2014.

[5] S. Hu, F. Rusek and O. Edfors, "Beyond massive MIMO: The potential of data transmission with large intelligent surfaces", *IEEE Trans. Signal Process.*, vol. 66, no. 10, pp. 2746–2758, 2018.

[6] C. Gentner, T. Jost, W. Wang, S. Zhang, A. Dammann and U. C. Fiebig, "Multipath assisted positioning with simultaneous localization and mapping", *IEEE Trans. Wireless Commun.*, vol. 15, no. 9, pp. 6104–6117, 2016.

[7] E. Leitinger, F. Meyer, F. Tufvesson and K. Witrisal, "Factor graph based simultaneous localization and mapping using multipath channel information", in *IEEE Int. Conf. on Commun. Workshops (ICCW)*, Paris, France, 2017, pp. 652–658.

[8] E. Leitinger, F. Meyer, F. Hlawatsch, K. Witrisal, F. Tufvesson and M. Z. Win, "A belief propagation algorithm for multipath-based SLAM", *IEEE Trans. Wireless Commun.*, vol. 18, no. 12, pp. 5613–5629, 2019.

[9] R. Mendrzik, F. Meyer, G. Bauch and M. Z. Win, "Enabling situational awareness in millimeter wave massive MIMO systems", *IEEE J. Sel. Topics Signal Process.*, vol. 13, no. 5, pp. 1196–1211, 2019.

[10] E. Leitinger and F. Meyer, "Data fusion for multipath-based SLAM", in *Proc. Asilomar-20*, Pacifc Grove, CA, USA, 2020, pp. 934–939.

[11] S. Grebien, E. Leitinger, K. Witrisal and B. H. Fleury, "Super-resolution channel estimation including the dense multipath component — A sparse Bayesian approach", 2021, in preperation.

[12] R. Schmidt, "Multiple emitter location and signal parameter estimation", *IEEE Trans. Antennas Propag.*, vol. 34, no. 3, pp. 276–280, 1986.

[13] R. Roy and T. Kailath, "ESPRIT-estimation of signal parameters via rotational invariance techniques", *IEEE Trans. Acoust., Speech, Signal Process.*, vol. 37, no. 7, pp. 984–995, 1989.

[14] M. Haardt, F. Roemer and G. Del Galdo, "Higher-order SVD-based subspace estimation to improve the parameter estimation accuracy in multidimensional harmonic retrieval problems", *IEEE Trans. Signal Process.*, vol. 56, no. 7, pp. 3198–3213, 2008.

[15] B. Ottersten, M. Viberg, P. Stoica and A. Nehorai, "Exact and large sample maximum likelihood techniques for parameter estimation and detection in array processing", in *Radar Array Processing*, Springer, 1993, pp. 99–151.

[16] J. A. Fessler and A. O. Hero, "Space-alternating generalized expectation-maximization algorithm", *IEEE Trans. Signal Process.*, vol. 42, no. 10, pp. 2664–2677, 1994.

[17] B. H. Fleury, M. Tschudin, R. Heddergott, D. Dahlhaus and K. Ingeman Pedersen, "Channel parameter estimation in mobile radio environments using the SAGE algorithm", *IEEE J. Sel. Areas Commun.*, vol. 17, no. 3, pp. 434–450, 1999.

[18] A. Richter, "Estimation of radio channel parameters: Models and algorithms", PhD thesis, Ilmenau University of Technology, 2005.

[19] P. Stoica and Y. Selen, "Model-order selection: A review of information criterion rules", *IEEE Signal Process. Mag.*, vol. 21, no. 4, pp. 36–47, 2004.

[20] D. Shutin and B. H. Fleury, "Sparse variational Bayesian SAGE algorithm with application to the estimation of multipath wireless channels", *IEEE Trans. Signal Proces.*, vol. 59, no. 8, pp. 3609–3623, 2011.

[21] M. A. Badiu, T. L. Hansen and B. H. Fleury, "Variational Bayesian inference of line spectra", *IEEE Trans. Signal Process.*, vol. 65, no. 9, pp. 2247–2261, 2017.

[22] T. L. Hansen, B. H. Fleury and B. D. Rao, "Superfast line spectral estimation", *IEEE Trans. Signal Process.*, vol. PP, no. 99, pp. 1–1, 2018.

[23] J. Salmi, A. Richter and V. Koivunen, "Detection and tracking of MIMO propagation path parameters using state-space approach", *IEEE Trans. Signal Process.*, vol. 57, no. 4, pp. 1538–1550, 2009.

[24] X. Li, E. Leitinger, M. Oskarsson, K. Åström and F. Tufvesson, "Massive MIMO-based localization and mapping exploiting phase information of multipath components", *IEEE Trans. Wireless Commun.*, vol. 18, no. 9, pp. 4254–4267, 2019.

[25] D. Shutin and B. Vexler, "Sparse Bayesian learning with dictionary refinement for super-resolution through time", in *Proc. IEEE CAMSAP-17*, 2017, pp. 1–5.

[26] F. Meyer, Y. Park and P. Gerstoft, "Variational Bayesian estimation of time-varying DOAs", in *Proc. IEEE Fusion-20*, Rustenburg, South Africa, 2020, pp. 1–6.

[27] T. Jost, W. Wang, U. Fiebig and F. Perez-Fontan, "Detection and tracking of mobile propagation channel paths", *IEEE Trans. Antennas Propag.*, vol. 60, no. 10, pp. 4875–4883, 2012.

[28] Y. Bar-Shalom, P. K. Willett and X. Tian, *Tracking and data fusion: a handbook of algorithms*. Storrs, CT, USA: Yaakov Bar-Shalom, 2011.

[29] F. Meyer, T. Kropfreiter, J. L. Williams, R. Lau, F. Hlawatsch, P. Braca and M. Z. Win, "Message passing algorithms for scalable multitarget tracking", *Proc. IEEE*, vol. 106, no. 2, pp. 221–259, 2018.

[30] D. Shutin, W. Wang and T. Jost, "Incremental sparse Bayesian learning for parameter estimation of superimposed signals", in *Proc. SAMPTA-2013*, 2013, pp. 6–9.

[31] E. Leitinger, S. Grebien, X. Li, F. Tufvesson and K. Witrisal, "On the use of MPC amplitude information in radio signal based SLAM", in *Proc. IEEE SSP-18*, Freiburg, Germany, 2018, pp. 633–637.

[32] E. Leitinger, S. Grebien and K. Witrisal, "Multipath-based SLAM exploiting AoA and amplitude information", in *Proc. IEEE ICCW-19*, Shanghai, China, 2019, pp. 1–7.

[33] F. Meyer and J. L. Williams, "Scalable detection and tracking of geometric extended objects", *IEEE Trans. Signal Process.*, vol. 69, pp. 6283–6298, 2021.

[34] F. Meyer and K. L. Gemba, "Probabilistic focalization for shallow water localization", *J. Acoust. Soc. Am.*, 2021.

[35] F. Meyer, P. Braca, P. Willett and F. Hlawatsch, "A scalable algorithm for tracking an unknown number of targets using multiple sensors", *IEEE Trans. Signal Process.*, vol. 65, no. 13, pp. 3478–3493, 2017.

[36] D. Lerro and Y. Bar-Shalom, "Automated tracking with target amplitude information", in *1990 American Control Conf.*, 1990, pp. 2875–2880.

[37] G. Soldi, F. Meyer, P. Braca and F. Hlawatsch, "Self-tuning algorithms for multisensor-multitarget tracking using belief propagation", *IEEE Trans. Signal Process.*, vol. 67, no. 15, pp. 3922–3937, 2019.

[38] X. Li, E. Leitinger and F. Tufvesson, "Detection and tracking of multipath channel parameters using belief propagation", in *Proc. Asilomar-20*, Pacifc Grove, CA, USA, 2020, pp. 1083–1089.

[39] E. Leitinger, S. Grebien, B. H. Fleury and K. Witrisal, "Detection and estimation of a spectral line in MIMO systems", in *Proc. Asilomar-20*, Pacifc Grove, CA, USA, 2020, pp. 1090–1095.

[40] T. Wilding, S. Grebien, E. Leitinger, U. Mühlmann and K. Witrisal, "Single-anchor, multipath-assisted indoor positioning with aliased antenna arrays", in *Asilomar-18*, Pacifc Grove, CA, USA, 2018, pp. 525–531.

[41] J. Williams and R. Lau, "Approximate evaluation of marginal association probabilities with belief propagation", *IEEE Trans. Aerosp. Electron. Syst.*, vol. 50, no. 4, pp. 2942–2959, 2014.

[42] X. Li, E. Leitinger, A. Venus and F. Tufvesson, "Sequential detection and estimation of multipath channel parameters using belief propagation", 2021, arXiv:2109.05623.

[43] F. Kschischang, B. Frey and H.-A Loeliger, "Factor graphs and the sum-product algorithm", *IEEE Trans. Inf. Theory*, vol. 47, no. 2, pp. 498–519, 2001.

[44] H.-A Loeliger, "An introduction to factor graphs", *IEEE Signal Process. Mag.*, vol. 21, no. 1, pp. 28–41, 2004.

[45] S. M. Kay, *Fundamentals of Statistical Signal Processing: Detection Theory*. Upper Saddle River, NJ, USA: Prentice Hall, 1998.

[46] S. M. Kay, *Fundamentals of Statistical Signal Processing: Estimation Theory*. Upper Saddle River, NJ, USA: Prentice-H, 1993.

[47] F. Meyer, O. Hlinka, H. Wymeersch, E. Riegler and F. Hlawatsch, "Distributed localization and tracking of mobile networks including noncooperative objects", *IEEE Trans. Signal Inf. Process. Net.*, vol. 2, no. 1, pp. 57–71, 2016.

[48] P. Tichavsky, C. Muravchik and A. Nehorai, "Posterior Cramer-Rao bounds for discrete-time nonlinear filtering", *IEEE Trans. Signal Process.*, vol. 46, no. 5, pp. 1386–1396, 1998.

[49] Y. Bar-Shalom, T. Kirubarajan and X.-R. Li, *Estimation with Applications to Tracking and Navigation*. New York, NY, USA: Wiley, 2002.

[50] D. Schuhmacher, B.-T. Vo and B.-N. Vo, "A consistent metric for performance evaluation of multi-object filters", *IEEE Trans. Signal Process.*, vol. 56, no. 8, pp. 3447–3457, 2008.

[51] P. Meissner, E. Leitinger, M. Lafer and K. Witrisal, *MeasureMINT UWB database*, 2013.

[52] E. Leitinger, P. Meissner, C. Rudisser, G. Dumphart and K. Witrisal, "Evaluation of position-related information in multipath components for indoor positioning", *IEEE J. Sel. Areas Commun.*, vol. 33, no. 11, pp. 2313–2328, 2015.

[53] A. Venus, E Leitinger, S. Tertinek and K. Witrisal, "A message passing based adaptive PDA algorithm for robust radio-based localization and tracking", in *IEEE RadarConf21*, 2021, pp. 1–6.

[54] M. Beard, B.-T. Vo and B.-N. Vo, "Bayesian multi-target tracking with merged measurements using labelled random finite sets", *IEEE Trans. Signal Process.*, vol. 63, no. 6, pp. 1433–1447, 2015.

[55] K. J. Worsley, "Local maxima and the expected euler characteristic of excursion sets of χ^2, f and t fields", *Adv. Appl. Probab.*, vol. 26, no. 1, pp. 13–42, 1994.

[56] R. J. Adler and J. E. Taylor, *Random Fields and Geometry*. New York, NY, USA: Springer, 2007.